IAEA-TECDOC-1699

Dense Magnetized Plasmas

Report of a Coordinated Research Project
2001–2006

IAEA
International Atomic Energy Agency

DENSE MAGNETIZED PLASMAS

The following States are Members of the International Atomic Energy Agency:

AFGHANISTAN
ALBANIA
ALGERIA
ANGOLA
ARGENTINA
ARMENIA
AUSTRALIA
AUSTRIA
AZERBAIJAN
BAHRAIN
BANGLADESH
BELARUS
BELGIUM
BELIZE
BENIN
BOLIVIA
BOSNIA AND HERZEGOVINA
BOTSWANA
BRAZIL
BULGARIA
BURKINA FASO
BURUNDI
CAMBODIA
CAMEROON
CANADA
CENTRAL AFRICAN REPUBLIC
CHAD
CHILE
CHINA
COLOMBIA
CONGO
COSTA RICA
CÔTE D'IVOIRE
CROATIA
CUBA
CYPRUS
CZECH REPUBLIC
DEMOCRATIC REPUBLIC OF THE CONGO
DENMARK
DOMINICA
DOMINICAN REPUBLIC
ECUADOR
EGYPT
EL SALVADOR
ERITREA
ESTONIA
ETHIOPIA
FIJI
FINLAND
FRANCE
GABON
GEORGIA
GERMANY
GHANA
GREECE
GUATEMALA
HAITI
HOLY SEE
HONDURAS
HUNGARY
ICELAND
INDIA
INDONESIA
IRAN, ISLAMIC REPUBLIC OF
IRAQ
IRELAND
ISRAEL
ITALY
JAMAICA
JAPAN
JORDAN
KAZAKHSTAN
KENYA
KOREA, REPUBLIC OF
KUWAIT
KYRGYZSTAN
LAO PEOPLE'S DEMOCRATIC REPUBLIC
LATVIA
LEBANON
LESOTHO
LIBERIA
LIBYA
LIECHTENSTEIN
LITHUANIA
LUXEMBOURG
MADAGASCAR
MALAWI
MALAYSIA
MALI
MALTA
MARSHALL ISLANDS
MAURITANIA
MAURITIUS
MEXICO
MONACO
MONGOLIA
MONTENEGRO
MOROCCO
MOZAMBIQUE
MYANMAR
NAMIBIA
NEPAL
NETHERLANDS
NEW ZEALAND
NICARAGUA
NIGER
NIGERIA
NORWAY
OMAN
PAKISTAN
PALAU
PANAMA
PAPUA NEW GUINEA
PARAGUAY
PERU
PHILIPPINES
POLAND
PORTUGAL
QATAR
REPUBLIC OF MOLDOVA
ROMANIA
RUSSIAN FEDERATION
RWANDA
SAUDI ARABIA
SENEGAL
SERBIA
SEYCHELLES
SIERRA LEONE
SINGAPORE
SLOVAKIA
SLOVENIA
SOUTH AFRICA
SPAIN
SRI LANKA
SUDAN
SWAZILAND
SWEDEN
SWITZERLAND
SYRIAN ARAB REPUBLIC
TAJIKISTAN
THAILAND
THE FORMER YUGOSLAV REPUBLIC OF MACEDONIA
TOGO
TRINIDAD AND TOBAGO
TUNISIA
TURKEY
UGANDA
UKRAINE
UNITED ARAB EMIRATES
UNITED KINGDOM OF GREAT BRITAIN AND NORTHERN IRELAND
UNITED REPUBLIC OF TANZANIA
UNITED STATES OF AMERICA
URUGUAY
UZBEKISTAN
VENEZUELA
VIETNAM
YEMEN
ZAMBIA
ZIMBABWE

The Agency's Statute was approved on 23 October 1956 by the Conference on the Statute of the IAEA held at United Nations Headquarters, New York; it entered into force on 29 July 1957. The Headquarters of the Agency are situated in Vienna. Its principal objective is "to accelerate and enlarge the contribution of atomic energy to peace, health and prosperity throughout the world''.

IAEA-TECDOC-1699

DENSE MAGNETIZED PLASMAS

REPORT OF A COORDINATED RESEARCH PROJECT 2001–2006

INTERNATIONAL ATOMIC ENERGY AGENCY
VIENNA, 2013

Marketing and Sales Unit, Publishing Section
International Atomic Energy Agency
Vienna International Centre
PO Box 100
1400 Vienna, Austria
fax: +43 1 2600 29302
tel.: +43 1 2600 22417
email: sales.publications@iaea.org
http://www.iaea.org/books

For further information on this publication, please contact:

Physics Section
International Atomic Energy Agency
Vienna International Centre
PO Box 100
1400 Vienna, Austria
Email: Official.Mail@iaea.org

Printed by the IAEA in Austria
April 2013

IAEA Library Cataloguing in Publication Data

Dense magnetized plasmas : report of a coordinated research project 2001–2006. — Vienna : International Atomic Energy Agency, 2013.
p.; 30 cm. — (IAEA-TECDOC series, ISSN 1011-4289; no. 1699)
ISBN 978-92-0-139110-0
Includes bibliographical references.

1. Plasma (Ionized gases) — Research. 2. Dense plasma focus. I. International Atomic Energy Agency. II. Series.

IAEAL 13-00804

FOREWORD

The IAEA strives to promote the development and utilization of nuclear technologies offering research opportunities for the growth of industrial applications in various domains. The Coordinated Research Project (CRP) on Dense Magnetized Plasmas (DMPs) was intended to coordinate the development of compact and low cost sources for the generation of charged particle beams, neutrons, X rays and plasma streams. Intense short bursts of neutrons are required for testing and calibrating neutron based diagnostics. Intense particle beams and plasma streams from DMP sources find applications in various research fields and technology, for instance, high heat load testing of candidate materials for the first wall of future fusion reactors. On-site detection of illicit and explosive materials using high rep-rate neutron bursts from compact DMP devices is of great interest. Soft and hard X ray beams produced from such sources have potential applications in biology and enzymology.

The overall objective of this CRP was to stimulate and promote investigation of DMPs through synergistic international cooperation. Specific objectives were: (i) to coordinate complementary research efforts related to DMPs by experts in developed and developing Members States, (ii) to speed up the progress in DMP applications by sharing knowledge, expertise and costs, (iii) to promote technology transfer among Member States, and (iv) to contribute to knowledge preservation by involving additional scientists from developing Member States who are not yet experts in DMPs.

The three major components of DMP devices are the driver (power supply, electrode system and its associated switch), the target and the target chamber. Engineering fields related to DMP system design include vacuum technology, radiation resistant material development, ablation hydrodynamics and neutronics. In each case, the integration of the components must account for the unique interfaces and constraints of the particular application. Therefore, while much of the technological development could be conducted in parallel, close coordination was deemed necessary for effective system integration. This CRP has helped accomplish this by giving broader exposure to the design challenges.

This publication covers the discussion of crucial issues relevant to the design and construction of DMP devices held by the participants from eight Member States. This is an ongoing activity coordinated by the IAEA and continues to be of interest to the Member States. The vital issues in design and fabrication of the DMP devices and the main findings summarized in this report are technically valuable for the non-experts planning to initiate research on the topic in their own country. This report on the technical knowhow will provide assistance for further progress in the application of this technology in developing countries.

The IAEA officers responsible for the publication were R. Kamendje and T. Desai of the Division of Physical and Chemical Sciences.

EDITORIAL NOTE

This publication has been prepared from the original material as submitted by the authors. The views expressed do not necessarily reflect those of the IAEA, the governments of the nominating Member States or the nominating organizations.

The use of particular designations of countries or territories does not imply any judgement by the publisher, the IAEA, as to the legal status of such countries or territories, of their authorities and institutions or of the delimitation of their boundaries.

The mention of names of specific companies or products (whether or not indicated as registered) does not imply any intention to infringe proprietary rights, nor should it be construed as an endorsement or recommendation on the part of the IAEA.

The authors are responsible for having obtained the necessary permission for the IAEA to reproduce, translate or use material from sources already protected by copyrights.

CONTENTS

SUMMARY

Overall objectives

The overall objective of this Coordinated Research Project (CRP) was to stimulate and promote investigation of dense magnetized plasmas (DMPs) through synergistic international cooperation. Specific objectives were: (i) to coordinate complementary research efforts related to DMPs by experts in developed and developing Members States, (ii) to speed up the progress in DMP applications by sharing knowledge, expertise and costs, (iii) to promote technology transfer among Member States, and (iv) to contribute to knowledge preservation by involving additional scientists from developing Member States who are not yet experts in DMPs.

The three major components of all DMP devices are the driver (power supply, electrode system and its associated switch), the target and the target chamber. Related engineering fields for DMP system design include vacuum technology, radiation resistant material development, ablation hydrodynamics, and neutronics. It should be noted that there is not yet a single optimal way to make choices among the various technologically possible components for power supplies, switches, etc. For example, the switch in one application might be based on solid state technology, whereas in another application on a pseudo spark. In each case, the integration of the components must account for the unique interfaces and constraints of the particular application. Therefore, while much of the technological development could be conducted in parallel, close coordination was deemed to be necessary for effective system integration. It was expected that this CRP on DMPs would help accomplish this by giving broader exposure to the design challenges.

CRP participating institutes

This CRP was undertaken by 11 institutes from eight Member States listed below:

- Institute of Plasma Physics and Laser Microfusion, Warsaw, Poland;
- Pollution Free Sources of Ionizing Radiation Laboratory, Moscow, Russian Federation;
- Tsingua University, Beijing, China;
- Korea Atomic Energy Research Institute, Daejeon, Republic of Korea;
- A.A. Baikov Institute of Metallurgy and Material Science, Moscow, Russian Federation;
- International Centre for Dense Magnetized Plasmas, Warsaw, Poland;
- Nanyang Technological University, Singapore;
- Ferrara University, Ferrara, Italy;
- University of Bucharest, Bucharest, Romania;
- Tallinn Pedagogical University, Tallinn, Estonia;
- Physics Technical Institute, St. Petersburg, Russian Federation.

Overall results of the CRP

The outputs delivered during the CRP activities cover the construction of several new devices, new testing chambers and innovative diagnostics and the new contributions to fusion and plasma physics science, all materialized in scientific publications:

- New Devices: Conception, design and construction of several dense magnetized plasma devices (Plasma Focus 6.0, Plasma Focus 10.0, Volume Reflex Plasma Chamber,

Positive Ion Source, Plasma Gun, a small and a large Z-pinch Plasma Focus (under construction) and chambers optimized for different applications. Moreover, several upgrades of the largest plasma focus operating with the DD reaction, PF-1000, were accomplished.

- New Diagnostics: Upgrade and design of various diagnostic systems (fast optical diagnostics, Laser induced photo-detachment diagnostics, X ray diagnostics, neutron spectrometers, proton track detectors, etc.).
- Material tests: Irradiation, diagnosis and modelling of materials relevant for fusion reactors and biological applications.
- Publications: The CRP results obtained utilizing new devices in 135 individual research activities and in 14 large international joint activities have been communicated to the worldwide fusion community through 94 journal publications and 47 proceedings presented at international and national conferences and meetings. The results of CRP activities developed up to 2005 were published in the journal Nukleonika in a Special Issue (Jan. 2006, No 1.) and a few selected papers were published in 2007 in Nukleonika Supplement.

Assessment of the work performed

During the first year (2002) the projects were focused on assessing the status of present devices involved in the CRP and develop the requirements for new plasma focus devices to be used in material research for fusion. Designs for new devices and components were developed aiming to upgrade and build new facilities in participating laboratories. Initial equipment was manufactured/ purchased and was transported to the recipient laboratories. Also a specific action was conducted to gather more participants involved in DMP to join the CRP. The initial five contracts were extended to eight contracts plus two agreements. The second year (2003) was devoted mainly to putting into operation two recent devices, the plasma focus 10.0 and the plasma focus 6.0. In parallel, diagnostic systems were developed to measure the plasma properties and control the operation of the devices. This work was conducted on a strong basis of international collaboration, with the teams from different laboratories.

For the third year (2004) the results were obtained in the utilization of the DPF devices to measure properties of fusion grade materials under irradiation of neutrons, X rays and deuterium plasma jets. Also a contribution for biology by irradiating enzymes was made by one laboratory. Theoretical work on modelling the experimental conditions and interpretation of results was also conducted. An important result of the experiments in material science was obtained by showing “proof of principle” that DPF can be used to treat materials for fusion applications and improve their specific characteristics, in particular their micro-hardness. This was a topic that called for further investigations.

The CRP also explored other applications for DMP devices. This is for instance the development of very intense ion beam sources and plasma jets for tokamak plasma fuelling and heating. These were conducted under an individual contract and a CRP agreement. Application of DMPs in support of fusion research was mainly addressed in the extension period of the CRP (2005–2006), where most of the new devices and upgrades could be fully utilized. The activities in this area are summarized below:

- Intense streams of plasma and fast ions generated in plasma accelerators (PA) and dense plasma focus (DPF) applied in testing materials intended for use as first wall and/or divertor elements in the existing and future fusion devices. Such tests using DMPs were and are being carried out intensively in the Russian Federation (DPF, PA), Poland

(DPF) and Ukraine (PA). For example, preliminary comparative round-robin tests of low activating steels of various types, tungsten, carbon composites, and other ceramic and optical materials, were performed in 2006 with financial support from the IAEA (TC project POL/1013).

- Intense, short duration, neutron pulses from DPF used to calibrate neutron diagnostics (activation counters) for existing and planned fusion devices (e.g. W7-X). This kind of activity is performed at present within the EURATOM frame work.
- Plasma gun technology developed for tokamak fuelling and improving initial stage of tokamak discharge. Experimental results obtained in GLOBUS-M are very positive and promising for scaling to larger devices.
- Dense plasma sources developed for production of neutral beam systems for application in magnetic confinement devices for plasma heating and current drive.

Outcomes

The CRP was successful in delivering the following outcomes:

- Established network among the CRP participating laboratories in planning and implementing research activities.
- Contribution to capacity building through the education of several students (awarding Master and PhD degrees) who participated in the CRP activities.
- Served as an umbrella for the organization of several Fellowships (at national and international level), Schools, Joint experiments, and Workshops used to exchange expertise, transfer knowledge, discuss new results and plan combined activities.
- Helped to establish links between CRP and non-CRP members, for instance, the membership on an international consortium established to test candidate materials for fusion in a round-robin experimental approach.
- Accompanied the establishment of a plasma focus laboratory at ICTP, Trieste, supported by CRP members, for training purposes.
- Helped a CRP member (POL1013) to develop the experimental conditions to conduct a TC project during 2005–2006 to establish a laboratory for material testing based on dense plasma focus devices (DPF).
- Spinoffs: Research activities based on the application of Plasma focus devices as generators of ion, electron and neutron beams, hard and soft X rays have large potential for future applications in fusion, medicine, hidden material detection and semiconductor industry.

Conclusions

The results of this CRP (F13009) on Dense Magnetized Plasmas have established a sound basis in view of initiating and integrating the research activity of the DMP community towards mainstream fusion programmes. The main achievements that support this improved capability can be highlighted as follows:

- State of the art research infrastructures have been established among the CRP participating institutes.
- Modern diagnostic systems necessary to carry out advanced experiments have been elaborated and tested.
- New knowledge of the physical mechanisms occurring in DMP devices and irradiation of sample materials has been gained and exchanged within the community.

- Methodologies and procedures for organizing international experiments have been developed and implemented, starting from the preparatory phase and proceeding through the experiments up to the elaboration of scientific reports.
- Preparatory activities towards the effective utilization of DMPs in fusion research have been initiated, including the establishment of links to groups working in magnetic and inertial confinement fusion programmes.

COUNTRY REPORTS

REPETITIVE PLASMA FOCUS AS A SOURCE OF IONIZING RADIATION AND PLASMA STREAMS FOR APPLICATION IN MATERIAL TECHNOLOGY, BIOLOGY AND MEDICINE

V. GRIBKOV, S. JEDNOROG
Department of Dense Magnetized Plasma
Institute of Plasma Physics and Laser Microfusion
Warsaw, Poland

Abstract

The dense plasma focus device PF-6 was newly installed in cooperation with Moscow Physical Society (MPS). With this particular device — PF-6 — we have reached record parameters in the field of DPF technology: for 7 kJ stored energy we have a 760 kA peak current and a 10^9 average neutron yield per a single shot (for pure deuterium as a working gas). This device can now operate with a repetition rate close to 1 cps and produce a set of shots of about 100 in a single sequence. Other installations, viz. PF-1000, PF-150, PF-60, PF-10, and PF-5M, have been modified and installed also in the frame of the same coordinated program. These devices were used with different gases and in various irradiation modes to carry out experimental investigations of interaction of pulsed electron, ion, neutron, X rays, and high-temperature plasma beams with different materials for the goals of radiation material sciences, biology and medicine. In particular they were applied for investigations in the fields of radio-enzymology, Positron Emission Tomography, neutron/X ray therapy of malignant tumors, structural and functional changes produced in components perspective for use in thermonuclear fusion devices with magnetic and inertial plasma confinement, as well as for a single-shot technique of characterization of different materials by neutron activation analysis based on a time-of-flight method.

1. INTRODUCTION

Dense magnetized plasmas (DMP) produced by a number of different devices (various plasma accelerators, pinch facilities, high-voltage/high-current fast energy storage systems of the waterline type with wire loads, etc.) occupies a niche between the inertial plasma fusion devices (e.g. of the laser produced plasma types) and installations with the magnetic plasma confinement (for example of the tokamak type) because of the characteristic times of their physical processes and their main plasma parameters.

Besides its own intrinsic fusion perspectives discussed in 50's and now re-emerging due to new concepts put forward during the last few years, installations based on plasma of this type can serve as very powerful sources of various types of ionizing radiation for a number of important applications. In this CRP we used the sub-class of dense plasma focus (DPF) devices. DPF installation is a type of plasma accelerator that produces directed hot ($T \sim 1$ keV) fast ($v > 10^7$ cm/s) dense ($n_{pl} \approx 10^{16}$ to 10^{19} cm^{-3}) plasma streams, high energy ion ($E_i \approx 0.01$ to 100 MeV) and electron ($E_e \approx 0.01$ to 1.0 MeV) beams in addition to soft ($E_{h\nu} \sim 0.1$ to 10 keV) and hard ($E_{h\nu} \sim 10$ to 1000 keV) X rays and fusion neutrons ($E_n \sim 2.45$ and 14 MeV).

These streams and beams have characteristic parameters that exist in present day accelerators and space vehicles, but in particular, in thermonuclear fusion devices employing inertial and magnetic plasma confinement, e.g. at plasma facing components of future fusion pilot reactors such as the ITER and NIF facilities. They can also be used for a large number of applications where one needs short powerful pulses of radiation of the above mentioned types.

Dense plasma focus (DPF) devices, compared with other thermonuclear devices, have a number of important advantages:

- These devices provide an opportunity to expose different materials and objects to pulsed directed beams of various types — ion, electron, plasma, X ray, neutron and shock

wave — of high-power flux density (up to 1013 W/cm2 for fast electrons, 1010 W/cm2 for fast ions, plasma streams and X ray photons and up to 109 n/cm2 for neutrons) with pulse duration in the range 10-9 to 10-6 s.

- Because all types of radiation generated by DPF are of penetrating nature these devices can produce important volumetric effects (in contrast to lasers).
- They enable the experimenter to choose the specific distribution of pulsed energy between all the above mentioned types of ionizing radiation — soft and hard X rays, neutrons, electron, ion and plasma beams: energy flux density may be significantly different for each type of radiation depending on the mode of irradiation.
- These beams in DPF devices can be separated in time due to their different velocities
- These beams in DPF devices can also be separated in space due to different angular distributions and by application of a magnetic field as well as because of their dissimilar Linear Energy Transfer (LET).
- Very high brightness of radiation of the above types gives important opportunities for new and sometimes unusual applications in pulsed radiation physics and chemistry, biology and medicine, as well as in different branches of material sciences (radiation material science, nano-technologies, neutron activation analysis, etc.).
- The physics of interaction of high-power pulses of radiation generated in different fusion devices with materials is especially important for study of damage produced in elements of these installations including the discharge chamber of the DPF itself, but in particular the plasma-facing walls of thermonuclear fusion installations with inertial (laser, wire-array Z-pinches and heavy ion fusion) and magnetic (tokamak and stellarator) plasma confinement; in the latter case DPF devices can simulate radiation loads which are typical of special regimes of the reactor's operation (ELMs, disruption instability, etc.).

Most of laboratories use for a DPF device construction an elemental base elaborated in the 60's of the previous century. These elements (capacitors, master spark, switches, DPF discharge chambers, etc.) are not well suited to a long device lifetime (typically restricted by a thousand of shots), or to reliable and reproducible operation, in particular with a high repetition rate. At the start of the CRP just a few DPF devices of high efficiency were in operation. These devices have been constructed using modern technologies. Namely in literature one might find only ING-103 (All-Russian Institute of Automation, Moscow, Russian Federation) and NX1 (National Institute of Education, Nanyang Technological University, Singapore) devices. But they had very narrow specializations — neutron production (ING-103) and soft X ray generation (NX1). Thus the demand for a broad spectrum of small and medium size DPF devices fitted to a wide variety of applications was an issue of the day.

During the last few years we manufactured several DPF devices of small and medium sizes, in particular the PF-6 device, fitted to the above demands. We also modernized the biggest facility in the world: the PF-1000. We performed investigations on material technology, biology and medicine, including a wide range of material damage tests, executed at pulsed ion, electron and high temperature plasma (HTP) beams, generated by different DPF devices in the frame of national and international scientific programs. The results obtained show that the above mentioned types of radiation may result in a number of synergetic effects.

Dense plasma focus (DPF) devices have a number of important and specific features compared with other dense magnetized plasma (DMP) installations. It is a very powerful source of a number of types of penetrating radiation (fast electron and ion beams, plasma

streams and shock waves, soft and hard X ray photons, neutrons and charged fusion products), and this source occupies a unique niche in the field of various applications. In particular it is superior where a very short (of nanosecond range) and extremely bright flashes of the above types of radiation are needed.

But to be useful in real applications (especially in those related to medicine or industry, i.e. not only for scientific purposes) these devices have to gain several new qualities. The most important among them are: long lifetime of elements, reliable and reproducible operation with a high repetition rate, and high efficiency of generation of the above mentioned types of ionizing radiation as well.

2. APPARATUS

To reach the above aims in this CRP project, we decided to use three new elements for our device, which appear to have been very successful. They are the capacitors of the KMK-30-7 type manufactured by Polytechnic Institute (Technical University), St. Petersburg, Russian Federation, switches of the pseudo-spark type (thyratrons with cold cathode) of the TDI1-150k/25 made for us by Scientific Production Company "Pulsed Technology Ltd", Ryazan, Russian Federation, and sealed gas discharge chambers designed and manufactured by VNIIA. All characteristics of these systems were given in previous Progress reports on this Project. Constructing this device we collaborated with MPS, VNIIA and NIE/NTU. Here we shall mention only the fact that the expected lifetime of these elements and systems is 1 through 10 million of shots, with a repetition rate tested up to 50 Hz.

The first variant of the PF-6 device gave a possibility to work in a mode when each shot could be done in every 10 min. It was so due to a very low power of our charger. To ensure higher rate of "firing" the discharges we designed and manufacture a new powerful system for energy supply fulfilled during the reporting period (2005–2007). It gave us a possibility to work in the regime up to 1 cps. Figure 1 shows an exterior of the PF-6 device whereas the new charger is presented in Fig. 2.

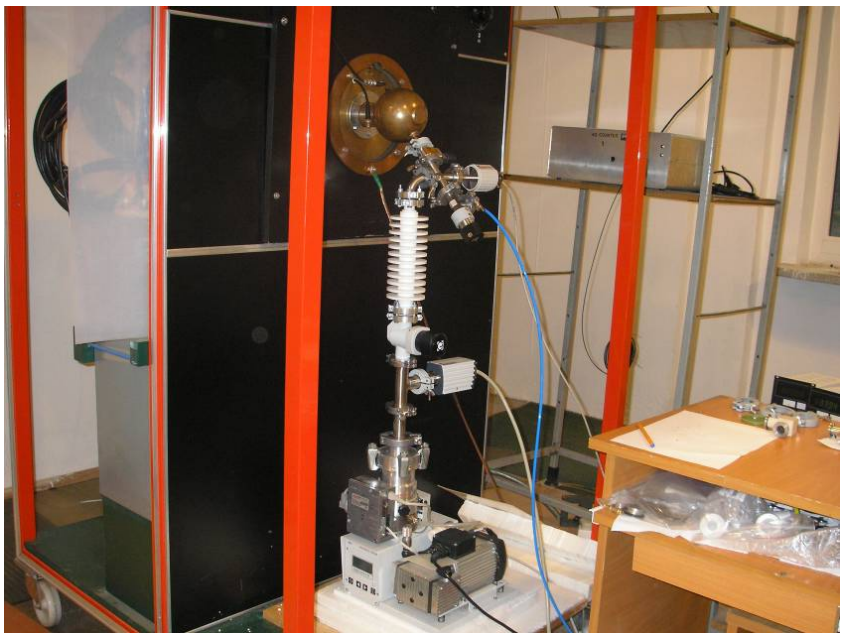

FIG. 1. Transportable device PF-6: 7 kJ, 750 kA, 10^9 D2 n/pulse, weight — 400 kg (IPPLM + MPS).

For the same time we have elaborated a new design for a master trigger used for initiation of the switches of pseudo-spark type. Before we used a spark made in our laboratory and based on four charging/discharging coaxial cables by means of a field distortion spark-gap. It gave us a jitter of our four capacitors switching time about 10 ns. Now we elaborated a new scheme based on cryotrons. It has the following advantages:

(1) Cryotron is an industrial product, i.e. a device working with high reproducibility, a few ns switching time and long lifetime; it can work with a high repetition rate
(2) Scheme based on cryotrons can be multiplied ad infinitum; it is very important for large DPF devices working with many capacitors.

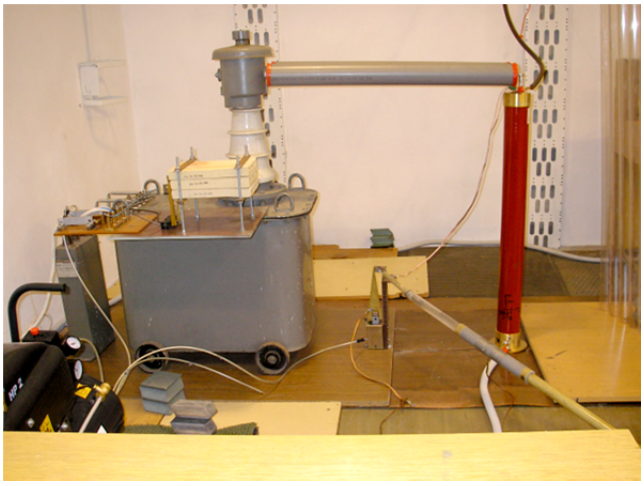

FIG. 2. Improved (powerful) charger making operation of the PF-6 device with a rep rate of ~ 1 cps.

Figure 3 shows an oscilloscope trace of the triggering pulse of the new scheme. It can be seen that the rise time of the pulse is about 15 ns, which is good for a large condenser bank.

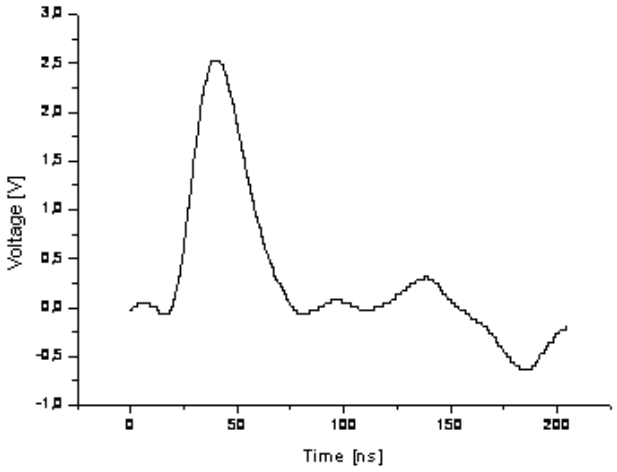

FIG. 3. Initiation pulse for the PF-6's master spark produced by a new system of the pseudo-spark triggering based on cryotrons.

A key element of a DPF is a discharge chamber. In cooperation with MPS and VNIIA we designed and manufacture a set of such chambers. Each of them is optimized respectively on neutron production (two types — working up to 16 kV and in the range 16-23 kV), soft X ray irradiation, hard X ray photon beam and fast ion beam generation for applications in radiation material science. These chambers are presented in Fig. 4.

Side by side with the PF-6 device we took part in modernization of the IPPLM main facility PF-1000 — the biggest in the world DPF (1.2 MJ) operating with deuterium as a working gas. In particular we found that the actual length of the anode of the discharge chamber is too long and should be decreased. Such a procedure made a few months ago with the anode (shortening of it by about 25%) resulted in an increase of neutron yield by 3 times. At present moment the device produces $6x10^{11}$ neutrons per pulse. Further optimization works with electrodes and the current collector of the device must be provided. As it will be described later this device was used for several experiments in the field of radiation material science. For these aims we designed and manufactured several special fasteners for samples to be irradiated. These experiments were performed in cooperation with MPS, Tallinn University, Estonia (TU) and the A.A. Baikov Institute of Metallurgy and Material Sciences, Russ. Ac. Sci., Moscow Russian Federation (IMET).

Besides PF-6 and PF-1000 we used a number of other DPF devices for various experiments — PF-150 (20 kJ, IPPLM), PF-60 (30 kJ), ING-103 (2.5 kJ, VNIIA) and ING-102 (0.2 kJ, VNIIA).

3. DIAGNOSTICS

Being invented in the 50's DPF is the most well diagnosed plasma device at present time. To have data on parameters of the fast electron and ion beams (including charged fusion reactions products), plasma streams, soft and hard X ray radiation, and neutrons (current magnitude, velocity, spectrum, angular distribution, absolute yields, fluence, power flux density, etc.) we use a number of diagnostics, having about 1 ns temporal resolution, a few micrometers spatial resolution, high spectral and angular resolution. These diagnostics are:

- Rogowski coils, magnetic probes, voltage dividers for current I, voltage V, magnetic field B measurements
- Multi-frame visual and soft X ray cameras, laser interferometry, shlieren and shadowgraphy for plasma and ion beams dynamics
- Hard and soft X ray, UV and optical spectroscopy, calorimetry, dosimetry and metrology, temporal and spatial monitoring of these radiations for electromagnetic radiation in a broad wavelength range.
- Track detectors, electrostatic and electromagnetic (e.g. Thomson-parabola, etc.) analyzers for fast ions, including those with a use of PMT tube of 5 ns temporal resolution
- Electrostatic and electromagnetic analyzers, Čerenkov detectors, Rogowski coils, magnetic probes, Faraday cage for fast electrons
- Activation counters, bubble detectors, multichannel PMT-based spectrometer for neutron emission parameters measurements, etc.

4. PARAMETERS

DPF usually operates with deuterium or deuterium–tritium mixture as a working gas. Measurements have shown that in any well working DPF we have about the same parameters for all radiation types except of their pulse duration and geometrical factors, e.g. a surface, which can be irradiated by them at the same power flux density of the radiation type. These two latter parameters are increased with the energy stored in the capacitor bank. Thus we may have in a DPF the parameters of the radiations with their upper limits as it follows in Table 1.

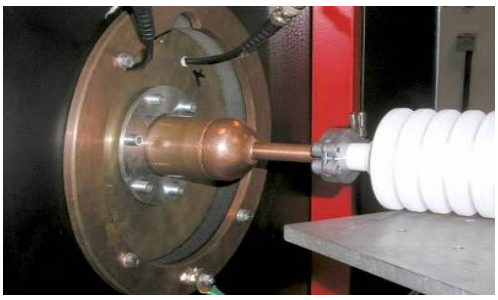

(a)

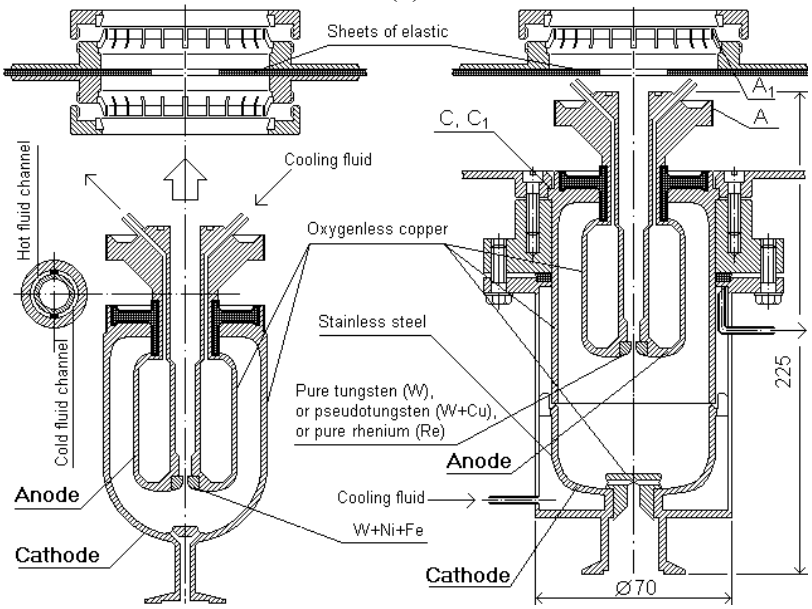

(b)

(c)

(d)

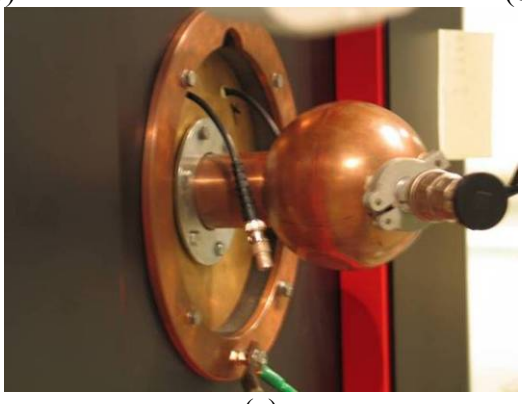

(e)

FIG. 4. A set of DPF chambers optimized for neutrons (a) up to 16 kV and (e) 16-23 kV), (b) for soft X ray radiation, (c) for hard X ray photons, (d) for a beam of fast ions.

5. PHYSICS OF DENSE MAGNETIZED PLASMA IN DPF

Plasma dynamics was investigated by us with a help of 5-frame laser interferometry (Fig. 5), streak camera and two 4-frame cameras taking 1 ns exposure images of plasma's self-luminosity in visible (Fig. 6) and soft X ray (Fig. 7) ranges.

Dynamics of different types of radiation was investigated by various techniques including PMT with fast scintillators, Čerenkov detectors, activation counters, PIN diodes, etc. Typical set of results received in a single shot of the PF-1000 facility is presented in Fig. 8. Temporal correlation of signals received with these detectors gave us the possibility to investigate mechanisms of fast particles (including fusion neutrons) and plasma streams production, and to measure their main parameters, such as energy and angular distributions.

Same types of diagnostics were applied not only to characterize plasma and ionizing radiations of DPF itself, but also for investigation of conditions produced during target irradiation as well as parameters of secondary plasma, produced by these streams. In Fig. 9 one may see formation of: (a) shock wave plasma stream, (b) beam of fast ions, and (c) secondary plasma, produced by these plasma and ion streams.

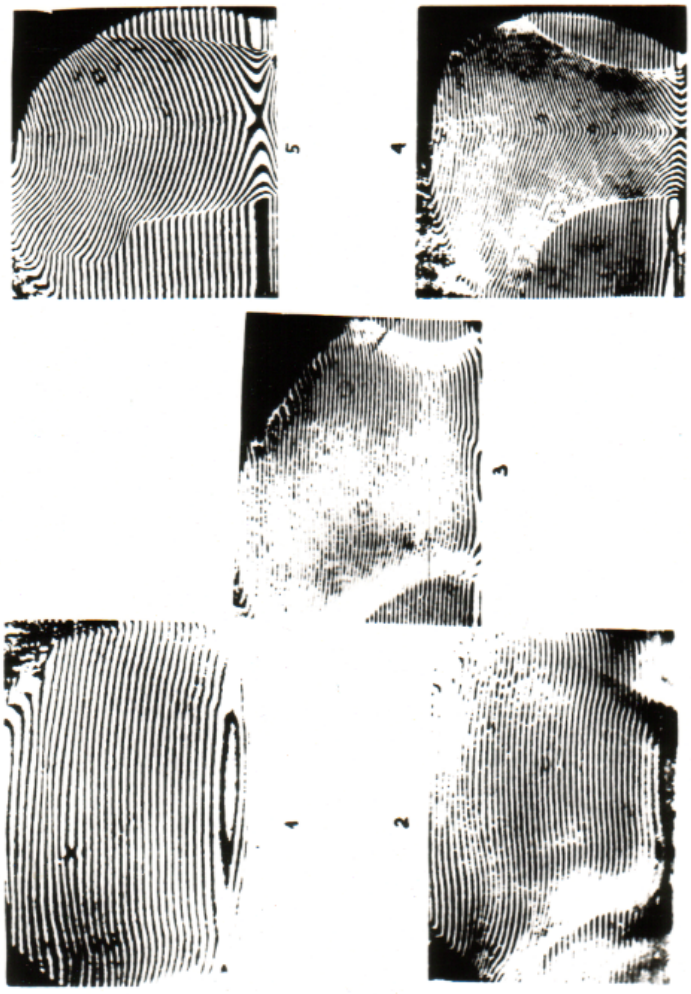

FIG. 5. The 5-frame laser interferometry of the pinch plasma (PF-60, IPPLM+MPS) (time of exposure — 1 ns, time interval between frames — 16 ns.

TABLE 1. DPF THE PARAMETERS OF THE RADIATIONS WITH THEIR UPPER LIMITS

Plasma streams	
Density	$N = 10^{18}$ cm^{-3}
Velocity	$v = 5\times10^{7}$ cm/s
Efficiency	$k = 10\%$
Power flux density	$P = 10^{8}$ MW/m^2
Fast electron beam	
Energy range of fast electrons	$E_e = 0.02…1.0$ *MeV*
Power flux density of the beam	$P = 10^{14}$ *MW/m*^{2}
Efficiency	$k = 10\%$
Fast ion beam *(D* or *T)*	
Energy range of fast ions	$E_i = 0.02…10.0$ *MeV*
Power flux density of the beam	$P = 10^{12}$ *MW/m*^{2}
Efficiency	$k = 10\%$
Soft X rays (1…10 keV)	
Power flux density	$P = 10^{10}$ *MW/m*^{2}
Efficiency	$k = 10\%$
Hard X rays (0.02…1.0 MeV)	
Power flux density	$P = 10^{9}$ *MW/m*^{2}
Efficiency	$k = 1\%$
Neutrons (2.5, 14.0 MeV in 4π)	
Neutron yield	10^{12} (10^{14}) neutrons/pulse
Efficiency	$k = 0.1\%$

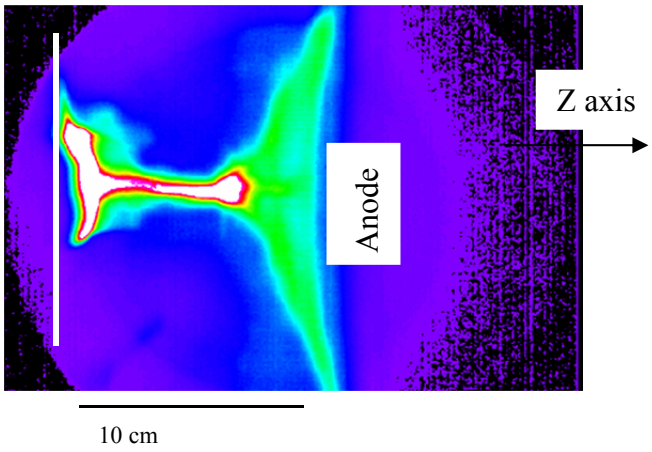

FIG. 6. Frame picture taken in visible light with exposure time 1 ns (PF-1000, IPPLM + ICDMP).

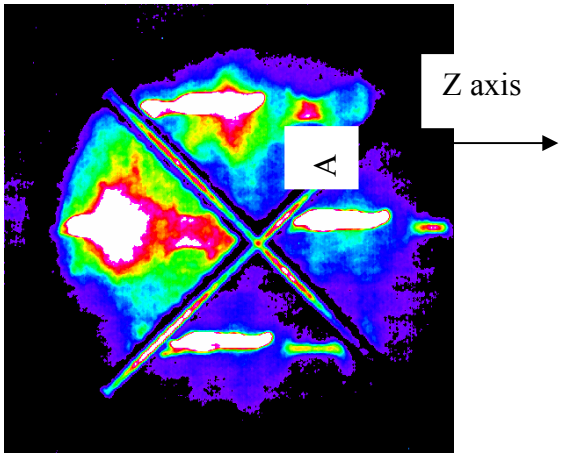

FIG. 7. 4-frame 1-ns soft x ray picture of pinch plasma (IPPLM + ICDMP).

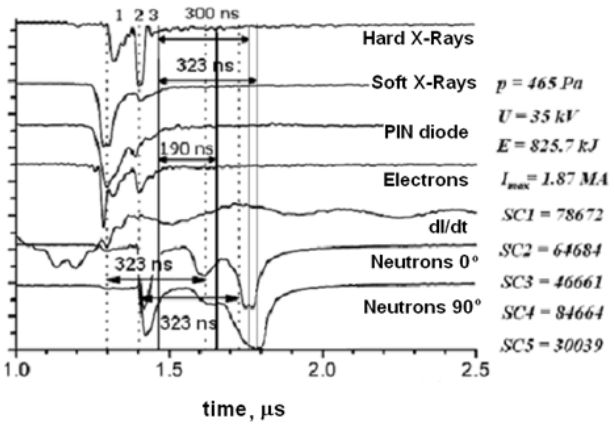

FIG. 8. Collection of the data from 5 neutron counters, 4 PM tubes, PIN diode, Čerenkov detector, and Rogowski coil (IPPLM + ICDMP.

Spectroscopic technique having temporal resolution about 0.5 μs applied in visible range of wavelengths for secondary plasma enabled us to study the temporal evolution of temperature and density (Fig. 10 — spectrum and temporal evolution of main parameters of secondary plasma). It appears in particular that in spite of the fact that primary ion/plasma streams irradiate our test samples during a few microseconds this secondary plasma exists and thus ensure a heat load upon the specimens for about 100 μs. It has a very important consequence, namely it means that the heat load at the irradiation of test samples in PF-1000 facility may lasts about the same time interval as it is in large tokamak devices during such unstable events like ELMs and disruptions.

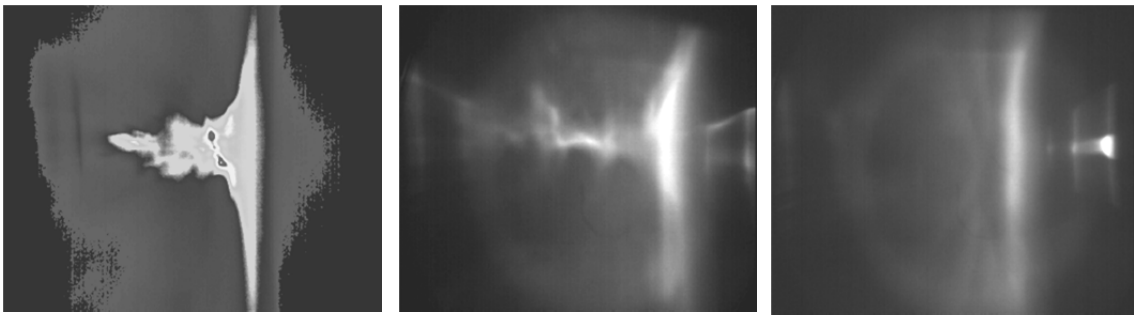

FIG. 9. Plasma shock wave (a), beam of fast ions (b) and secondary plasma, produced near the surface of the target under irradiation (c).

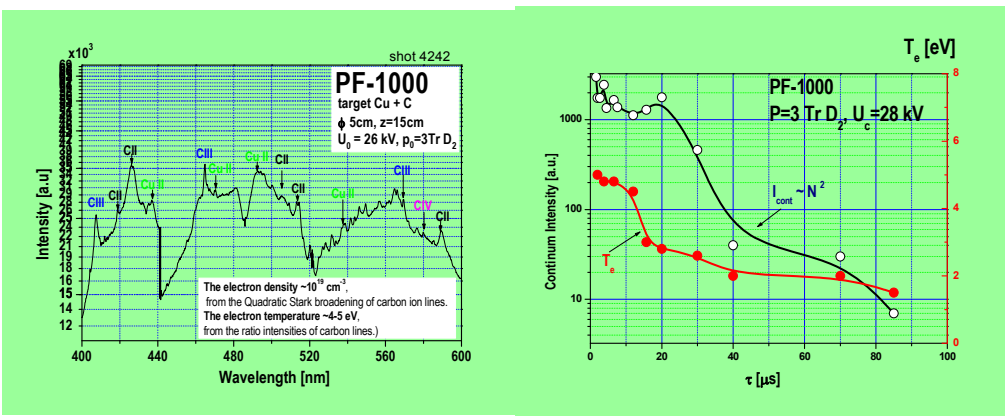

FIG. 10. Spectrum (a) and temporal evolution of main parameters (b) of secondary plasma.

6. RADIATION CHEMISTRY/BIOLOGY: RADIOENZYMOLOGY

In these experiments performed by IPPLM in close cooperation with MPS and MSU several types of enzymes (ATC, peroxidase, etc.) were irradiated *in vitro* with various doses, dose power and spectral range of X ray photons. We have found here a very large (4 orders (!) of magnitude) difference in doses for the enzyme activation/inactivation by their irradiation with X rays from DPF compared with the same procedure using an isotope source (^{137}Cs). However with DPF the effects appear at power flux density difference in these two types of irradiation experiments about 7 to 8 orders of magnitude in favor of DPF.

We found that the proper characteristic of the short pulse radiation action is a product "dose × dose power": D×P. One may see it comparing Fig. 11 where activation/inactivation is plotted in dependence on dose (quite chaotic picture representing however the above data) with Fig. 12 were the same data are rearranged versus the product of D×P. Indeed in this very case almost all data received in experiments with low-intensity high dose irradiation (^{137}Cs, classical X ray tube, ^{90}Sr-^{90}Y isotope source) and contrary with high intensity low dose devices having short powerful X ray pulse (DPFs) are collected around the magnitude of $10^{-1} < D \times P < 10^{1}$ [Gy^2/s]. It is true except two points — "1" and "2". We believe that the point "1" is connected with so-called triggering effects found in the frame of a "problem of low doses".

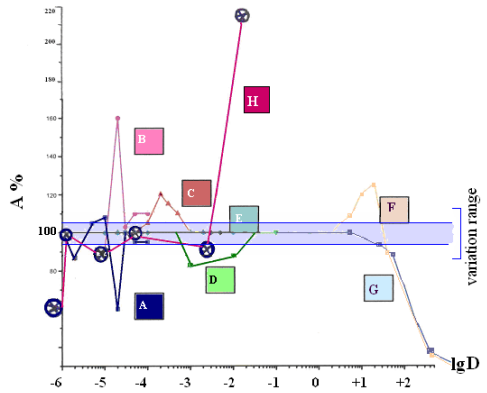

A, B – "PF -0.2", Cu filter; ***C*** – "PF-2", Cu filter;
D – X-ray tube: U = 50.0 kV, $E_{hv.\,max} \leq$ 35.0 keV;
E – isotope β -source Sr -Y: 8 keV > E_{hv} > 2000 KeV; and
"PF -0.2", Al filter: 8 keV > E_{hv} > 100 keV;
F, G – γ-source ^{137}Cs for different enzymes: $E_{hv.\,max}$ = 662 keV

FIG. 11. Activity of enzymes versus irradiation dose.

More interesting result is demonstrated by the point "2". In previous experiments nobody ever saw such a tremendous activation of an enzyme (2.3 times!). But here we have overcome the magnitude of D ´ P by 4 orders of magnitude also at first time in experiments of such a kind.

At the same time it is important to mark that even for data within the above range 10-1< D´P < 101 [Gy2/s] it is not clear why the same effects of activation/inactivation take place for certain sorts of sources (DPF, 137Cs) and do not fulfilled for another (e.g. medical X ray tube).

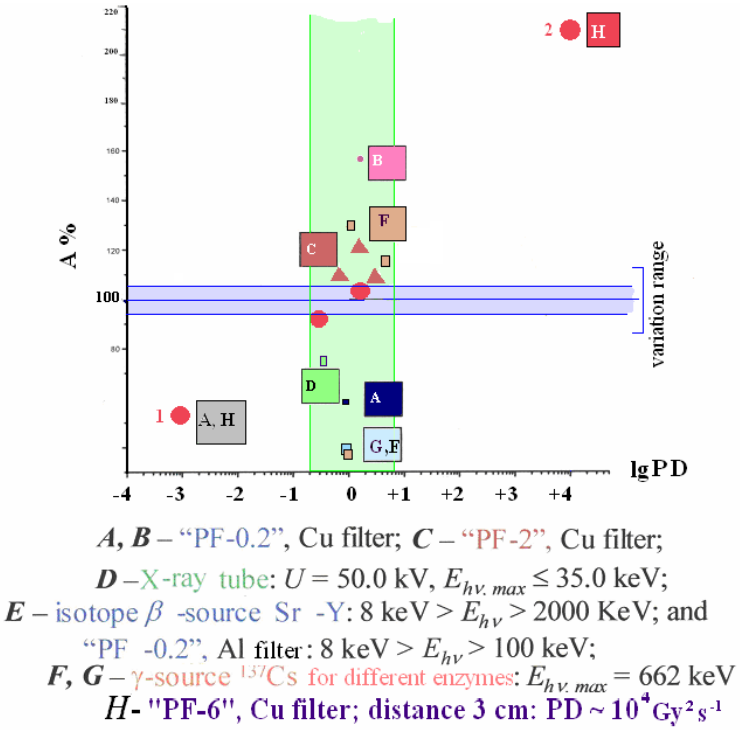

FIG. 12. Activity of enzymes versus a product of D×P.

In these experiments we changed distances between source and test-tubes with enzymes, a number of irradiating shots as well as filters on the DPF chamber window, which screened pulses of X rays. We interpret these data on the base of saturation and synergetic effects taking into consideration the power flux density and spectrum of irradiating X ray photons from one side and absorption spectrum of the enzyme molecules from the other. Our preliminary conclusion is that in this case we have the abovementioned synergetic effect achieved due to simultaneously produced a high concentration of free radicals in the vicinity of an enzyme molecule and an excitation of metallic ions within this molecule.

Thus we believe that by these experiments we have shown that in pulsed radiation regime a product of dose and dose power is crucial.

It is interesting to mark here that as it will be seen in the chapter devoted to radiation material science in those field a so-called "damage parameter" F plays a very important role. It gives a possibility to estimate damage of materials under their irradiation provided that the penetrating radiation has high power P and short pulse duration τ. It appears that this factor has the following form: $F = P \times \tau^{0.5}$. As one can see this factor coincides with the product of dose and dose power.

7. RADIATION MEDICINE

7.1. Fast ions in positron emission tomography (IPPLM)

Positron emission tomography (PET) is one of several methods currently exploiting nuclear physics principles for health — so-called "nuclear medicine" (NM); generally PET consists of three elements: production of positron emitting isotopes, synthesis of biological molecules labeled with the above positron emitters, and scanning of a human body.

The most commonly used at present time as PET tracers are the isotopes ^{11}C, ^{13}N, ^{15}O and ^{18}F ($T_{1/2}$ = 20.03 min, 9.97 min, 2.03 min and 109 min, respectively), because they can be introduced into biological molecules without altering the composition of these molecules.

DPF, in which ions are accelerated by collective effects, may prove attractive as alternative to cyclotrons for the production of positron emitting isotopes, in particular because of its potentially lower cost and lower level of complexity.

We made experiments on production of the ^{13}N isotope by fast ions generated by the DPF discharge using the reaction:

^{12}C (d,n)^{13}N

The threshold for this reaction is 328 keV, but the cross-section remains very small below ~ 600 keV. The main objectives of our work were:

(1) To determine activity induced by fast deuterons impinging into the solid target
(2) To calculate production of positron emitting isotope ^{13}N using a DPF.

For the purpose of ion beam measurements as well as diagnostic nuclear reaction with deuterons, the $^{12}C(d,n)^{13}N$ reaction with a carbon target seems to be very attractive. The target was based on soot imbedded in polyurethane, and it results in flexibility and durability as well as recitation of the shock wave, which produced by cumulative plasma streams in DPF. When the above threshold is passed, the cross section of the reaction rapidly increases and has many resonances. The maximum value of the isotope production probability occurs for deuterons with energy about 1.5 MeV; but in the case of deuterons within energy range 0.7–0.9 MeV the cross section of the reaction is only 3–5 times lower than in the previous case.

Our first results received with PF-150 operated at the 20-kJ energy level (PF-150, IPPLM) are shown in Fig. 13.

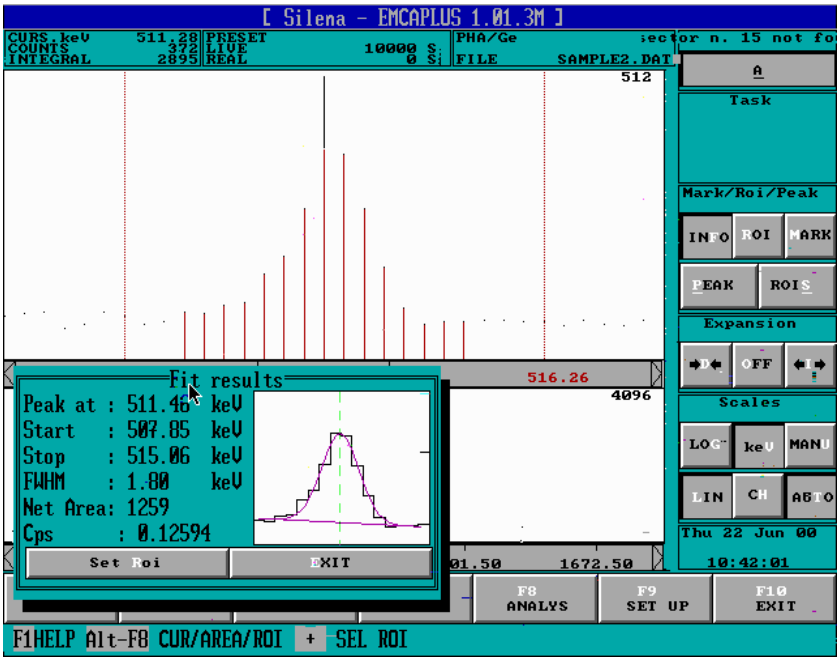

FIG. 13. X ray spectrum of annihilation of the electron/positron pair.

Figure 13 shows a gamma-ray spectrum measured using an HPGe detector having a peak at 511.4 keV. These are annihilation gamma-rays from the positron emitting isotope ^{13}N. The number of fast ions N_i ejected from DPF with energy enough for production of the measured number of atoms of the nitrogen isotope ^{13}N and calculated using the equation for activity was found to be $N_i \sim 10^{13}$. This result has shown that the DPF of the level of energy about 20 kJ (not optimized for ion production in these our experiments) if working with a frequency of 10 Hz can produce for the time period of 100 seconds (1/6 of the half-life time) an amount of the isotope ^{13}N having total activity circa 30 MBq. Note that for the tomography diagnostics of a human head with the help of this method the necessary quantity of the isotope determined by its activity is 10 MBq.

7.2. Thermal and fast neutrons and X rays in Boron Neutron Capture Therapy (Ferrara University *(FU)* + *IPPLM* + International Centre for Theoretical Physics (ICTP)

Beginning from the 1930's when Chadwick discovered the neutron, it was suggested that neutron beams could be used for cancer treatment, in particular making use of the large thermal-neutron capture cross-section of boron. At present this method of therapy of various tumors with use of Boron Neutron Capture Therapy (BNCT) (glioma and gliosarcoma of brain, carcinoma of prostate, etc., including those with multiple dispersed metastases when neoplastic cells cannot be removed by surgery because of their diffusive character of distribution) is under a development in various clinics and laboratories. The main idea of this method is to irradiate within a neutron field of thermal or epithermal ($E_n \geq 1$ eV) neutrons a neoplasm saturated beforehand by a boron containing substance. At the present time two chemicals are widely used — BPA and DSH.

Therapeutic effects are attained due to a very high Linear Energy Transfer (LET) of the nuclear reaction products, which produced at the interaction of thermal neutrons with Boron atoms ^{10}B:

$$^{10}B_5 + {}^{1}n_0\ (\sigma = 3{,}838\ \text{barn}) \rightarrow {}^{4}He_2 + {}^{7}Li_3 + 2.79\ \text{MeV}\ (6.3\%)\ \text{and}$$
$$\rightarrow {}^{4}He_2 + [{}^{7}Li_3]^* + 2.31\ \text{MeV}\ (93.7\%)$$
$$\downarrow$$
$$^{7}Li_3 + \gamma\ (478\ \text{keV})$$

Mean-free-paths (MFP) of lithium nuclei and alpha-particles within human tissues are equal to 6 and 9 μm respectively, what makes a release of their energy to be practically local in the vicinity of a zone of neutron's absorption (size of a cell is about 10 μm).

Our analysis has shown that DPF presents the following opportunities:

(1) DPF devices of the medium size (5–10 kJ) can ensure the necessary dose in about three hours working with a moderator (i.e. at the production of epithermal neutrons) if it will be operated with a rep rate of 100 cps with D_2 or with 1 cps with D-T mixture.
(2) One can expect here a synergetic effect if DPF will be used either with just fast neutrons of the ns pulse duration or at the combined application of fast neutrons and hard X rays for a suppression of malignant cells; the reason for this is a simultaneous rupture of both spirals of DNA during the ns period of time.

Both the opportunities open ways for low dose therapy of cancer by usage of DPF devices.

8. RADIATION MATERIAL SCIENCE

8.1. Preface

The DPF, being the oldest device studied at nuclear fusion facilities (a 50 year history), is a very well diagnosed apparatus. As it was shown above it is usually supplied with a number of instruments monitoring the main characteristics of its radiation types during an irradiation process with ns time resolution and with high angle, spatial, and spectral precision. The same is true for the process of the interaction of generated by it various types of radiation with samples under tests. These data can be cross-correlated with the results received a posteriori by analytical instrumentation under the investigations of irradiated specimens.

In our material science experiment performed in cooperation with IMET, MSU, FU, ITEP, and MSU the morphology of the irradiated sample's surfaces after the irradiation was investigated by optical, electron and atomic force microscopes, as well as by an optical refractometer. We applied also tribology instrumentation, weighing samples after irradiation, profilometry, elastic recoil detection analysis (ERDA), X ray microprobe (i.e. elemental), structural and diffraction analysis, etc.

Side by side with the systematic activity in this field with the abovementioned institutions we took part during the year under report in round robin tests of samples prepared for us by Forschungszentrum Jülich (FJ), Germany, using materials candidate for a divertor of Iter, namely carbon-fiber composite (CFC) with a tungsten (W) core placed in the central part of samples. Besides us and the above German Centre the following institutes were the participants in these experiments: laser department of IPPLM (Poland), TRINITI (Troitsk, RF), IPP-U, NSC KIPT (Khar'kov, Ukraine), and Sandia Laboratories (USA). Comparative characteristics of those devices used in these experiments are presented in Table 2. In particular in this table one can see that DPF are much closer (or even much higher) to the real situations expected in the NIF by all parameters and to Iter by almost all parameters except plasma/beams pulse duration. But duration of heat load reached in PF-1000 due to long existence of secondary plasma can also be used for simulation of a number of effects in Iter. The idea of the tests was to irradiate these samples with plasma, and fast electron and ion streams in regimes below and above melting point on various devices having different parameters (pulse durations, energy of fast particles, velocities and densities of plasma bunches, etc.). A thorough comparison of the results obtained by different groups will be made at later time.

8.2. Materials

Besides the above specimens used in round robin tests the following materials were chosen for the experiments: austenitic chromium-manganese steels, ferritic steels, pure vanadium, tungsten, graphite, copper, aluminum, as well as several alloys of the above metals.

We irradiate also samples of optical materials used for windows in chambers of fusion reactors and several sorts of ceramics. Selection of specimens was determined by their known characteristic to withstand high heat and radiation loads and by their low activation ability.

8.3. Experimental conditions

In the framework of the current CRP Project we investigate influence of pulsed high energy ($E_i \geq 100$ keV) ion beams and high temperature plasma streams (HTP, particle velocity ~ 5×10^7 cm/s) on a target material. We found that the results are in a remarkable

distinction in radiation and thermal effects in dependence of irradiation conditions. The features of physical and chemical processes, structure phase transformations and elemental distribution in irradiated materials are also different. All of that lead to the different material damage and change of its properties and chemical content.

In Fig. 14 one can see the geometry of specimens positioning inside the chamber of PF-1000 facility whereas Fig. 15 represents the plasma and fast ion beam spatial distribution. Note that the ion beam is emitted about 180 ns after the starting moment of the movement of plasma (shock wave) stream. But having an order magnitude higher speed it outruns the plasma stream at a certain moment and after this it converts from a conical structure beam into a hemispherical outflow.

8.4. Analysis methods

The irradiated samples were investigated by optical and scanning electron microscopy, X ray diffraction analysis, X ray spectral analysis and atomic force microscopy. In addition we used optical refractometry, weighing of samples before and after irradiation and some other methods. Examples are presented in Figs 16 and 17.

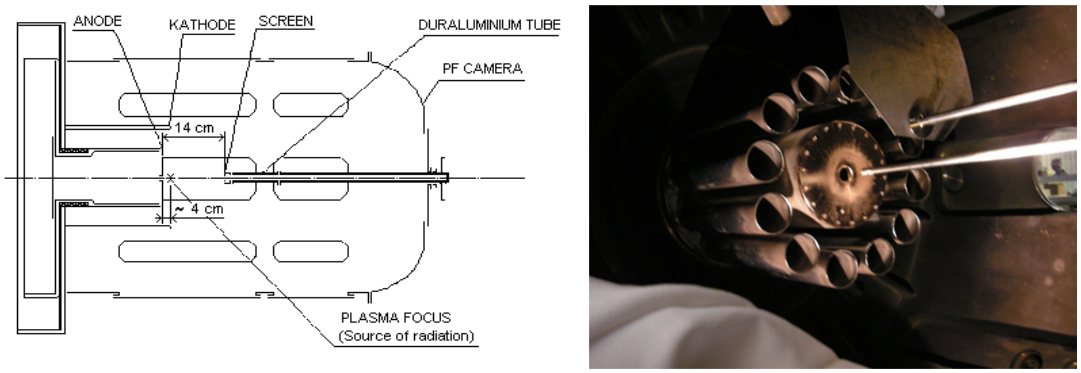

FIG. 14. Scheme of specimen's positioning (a) and picture of this assembling (b) together with the protective screen.

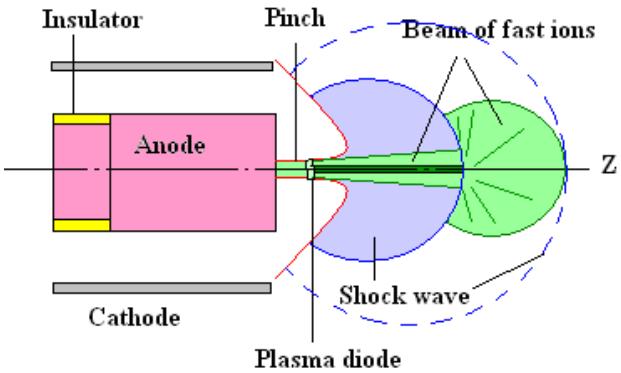

FIG. 15. Schematic view of plasma stream, shock wave (SW) and fast ion beam propagation.

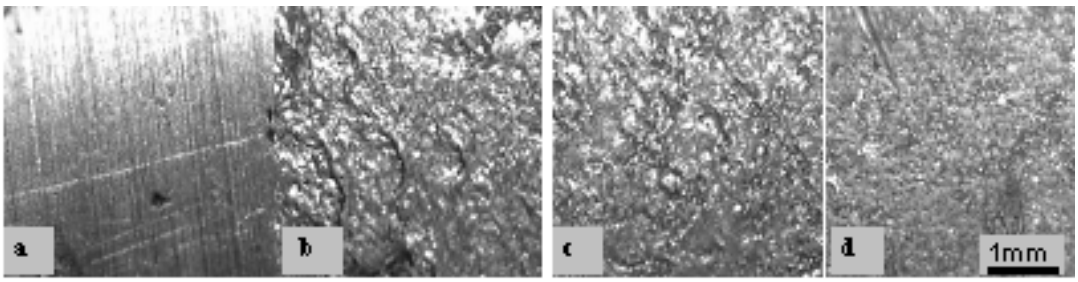

FIG. 16. Optical microscopy of the topographic structure of the surface of a duralumin tube in the original state (a) and after 13-fold DP pulses: (b) the part nearest to the anode; (c) central part; (d) the part which was the farthest from the anode.

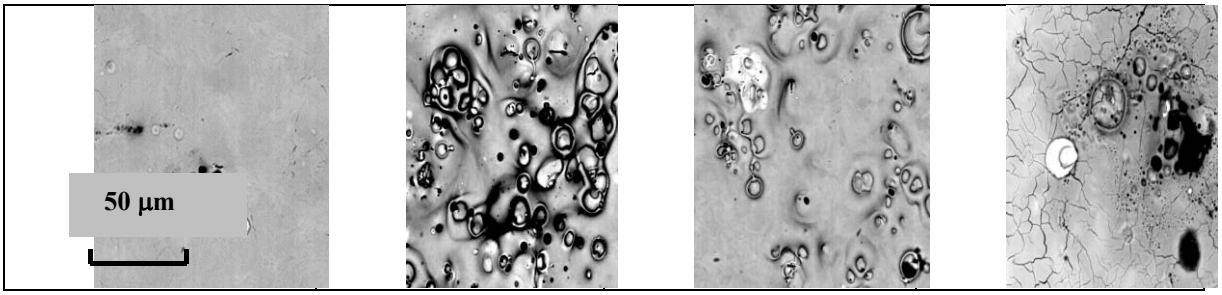

FIG. 17. Scanning electron microscopy of the surfaces of austenitic steels irradiated in PF-1000 device by deuterium plasma: (a) 10Cr12Mn20W (8 pulses), (b) 25Cr12Mn20W (8 pulses), (c) 10Cr12Mn20W+0,05Sc (5 pulses) (d) 10Cr12Mn20W+0,05La (5 pulses).

Elastic Recoil Detection Analysis (ERDA) was used to trace the deuterium atoms scattering profile within the irradiated specimens. In this method the He+ ion beam of the energy 1.9 MeV irradiated test sample at an angle of 15° to its surface. The recoil deuterons were registered at an angle of 30° to the incident beam direction. The method provides the integral characteristics of the deuterium concentration profile on the part of the surface investigated.

The thickness of the layer evaporated during the sample irradiation was determined by means of weighing specimens before and after irradiation taking into account the square of irradiated area and density of the material.

8.5. Experiments

During previous years our main advantages were as follows:

- Three typical regimes of the impact of ion and plasma beams upon the target material depending on power flux densities were found:

"Implantation mode" — $q \approx 10^5$–10^7 W/cm^2;

"Detachment regime" (screening of the surface by a secondary plasma cloud) — $q \approx 10^7$–10^8 W/cm^2;

"Explosive rupture mode" (violent detachment with strong evaporation of the material under irradiation) — $q \approx 10^8$–10^{11} W/cm^2.

- It was found that concentration of implanted deuterium strongly exceeded the limit of its solubility in steel whereas their distribution profiles by depth had different character. These facts found its explanation on the base of pulsed radiation physics in its perfect sense (see later) and non-stationary diffusion (in cooperation with TU).

- In certain cases a redistribution of the elements in the surface layer of austenitic chromium-manganese steels was found. A remarkable increase of Mn content and a reduction of Fe content took place near the blister-like bubbles formed on the irradiated surface.
- It was found that damages of the surface layer of ferritic steels (10Cr9WV and Eurofer97 types) under realized conditions were remarkably lower in comparison with those in austenitic steels. Phase compositions of ferritic steels remained steady under the pulsed action of high power density (up to 10^{10} W/cm^2) and pulse durations up to 1 μs.
- The surface layer of tungsten after a 10-fold action of pulsed irradiation under harsh conditions ($q \approx 10^{10}$ W/cm^2, $\tau \approx 1$ μs) was rather strongly damaged. Elongated surface cracks and significant erosion of the material were observed: mean thickness of the layer evaporated per single pulse was 2 μm.

TABLE 2. COMPARATIVE CHARACTERISTICS OF THE DEVICES USED IN THE EXPERIMENTS

Table 2	**ITER Cadarache, France**	**NIF LLNL, USA**	**PF-1000 IPPLM, Poland**	**PF-10, ITEP, RF,kPF-5M, IMET, RF, PF ICTP, Italy**	**QSPA Kh-50 Ukraine**	**MK-200 Troitsk, RF**	**RHEPP-1 Sandia Lab USA**	**JUDITH Jülich, Germany**
Peak heat flux, P [W/m^2]: norm. oper. disruptions VDEs ELMs	**10^6 10^{11} 10^9 10^7**	**10^{13}**	*** 10^{11}-10^{16} (10^{18} for fast electrons)**	*** 10^{10}-10^{13} (10^{17} for fast electrons)**	**$0.6\cdot10^{10}$ $1.1\cdot10^{10}$**	**10^{11}**	**10^{12}**	**10^{10}**
Duration of heat load [s]	**10^{-4}-10^3**	**10^{-7}-- 10^{-6} (?!)**	***10^{-4}**	**$3\cdot10^{-5}$**	**≥10^{-4}**	**$2\cdot10^{-5}$**	**$2\cdot10^{-7}$ (?!)**	**10^{-4}-10^3**
T_{pl} (surface) [eV]	**10^3**	**10^2-10^3**	***10^3**	***10^3**	**10^2**	**10^2**	-	-
Duration T_{pl}[s]	**10^{-4}-10^{-1}**	**$2\cdot10^{-6}$**	**$2\cdot10^{-7}$**	**$2\cdot10^{-8}$**	**≥10^{-4}**		-	-
E_i, D fast [eV]	**10^5**	**10^2/10^6**	***10^5(10^7)**	***10^5**	-	**~10^3**	**$8\cdot10^5$**	-
Duration E_i [s]	**≥10^{-4}**	**$2\cdot10^{-6}$**	**$2\cdot10^{-7}$**	**$2\cdot10^{-8}$**	-	**$2\cdot10^{-5}$**	**$2\cdot10^{-7}$**	-
E_e, fast [eV]	**10^5-10^7**	**?**	***10^5(10^6)**	**10^5**	-	-	-	**$1.5\cdot10^5$**
Duration E_e [s]	**≥10^{-4}**	**?**	**$2\cdot10^{-7}$**	**$2\cdot10^{-8}$**	-	-	-	**10^{-4}-10^3**
Irrad. surface [cm^2]	**~10^7**	**~10^6**	**10^1-10^3 (0,1)**	**1 (0.01)**	**10^2**	**1-30**	**10^2**	**0.04-10^2**
X rays [eV]	**10^5-10^7**	**10^1**	***10^0-10^6**	**10^0-10^5**	-	-	-	**$1.5\cdot10^5$**
Neutrons [eV]	**$1.4\cdot10^7$**	**$1.4\cdot10^7$**	**$2.5\cdot10^6$**	***$1.4\cdot10^7$**	-	-	-	-
Neutrons/ cm^2	**10^{13}**	**10^{14}**	**10^{10}**	***10^{10}**	-	-	-	-

Comparison of radiation resistance of three optical materials — quartz, sapphire and topaz — irradiated in similar conditions has shown that quartz is much more resistant than others (see optical and atomic force microscopy results presented Figs. 18 and 19).

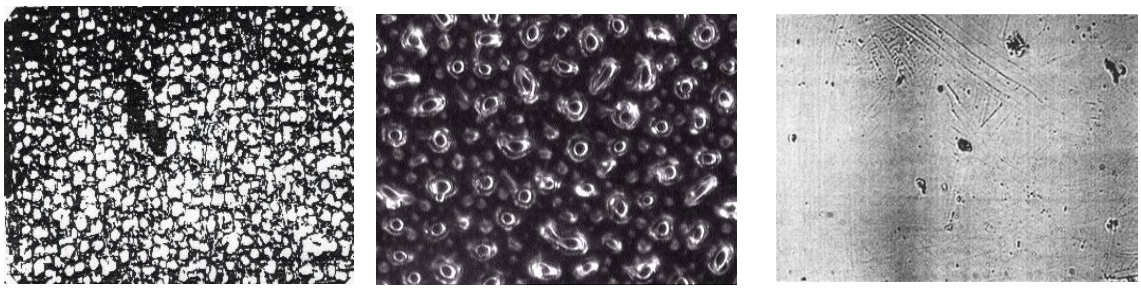

a) *b)* *c)*

FIG. 18. Optical microscopy of sapphire (a), topaz (b) and quartz (c).

Four typical defect sizes — 50 nm, 0.3 μm, 3 μm, and 10 μm — were found by atomic force microscopy (Fig. 19). Measurements of three of them (0.3 μm, 3 μm, and 10 μm) have been independently supported by optical microscopy (Fig. 18) and reflectometry (see Fig. 20). These reflection dependences on the wavelength of the light illuminating the irradiated surfaces of specimens (in fact characteristics of light scattered by surface imperfections) has been analyzed using the Mie theory of light scattering.

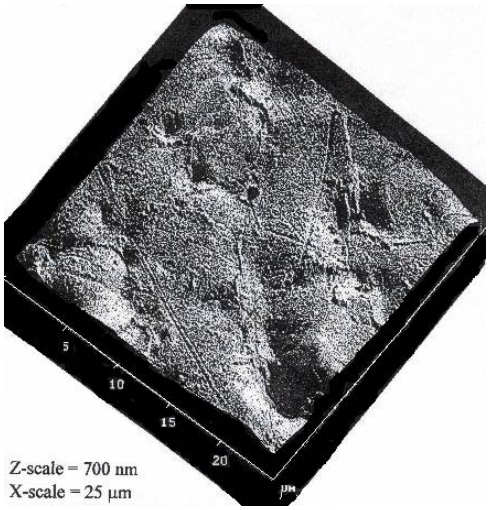

FIG. 19. Atomic force microscopy of the irradiated surface of sapphire.

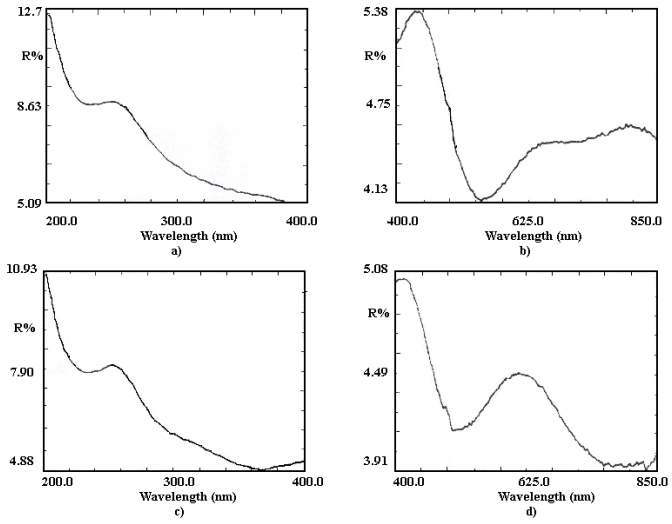

FIG. 20. Reflection (scattering) coefficient of a sapphire sample surface versus wavelength.

During the last year we performed two important experiments — simulation of material damage produced under plasma disruptions in thermonuclear fusion reactor (an irradiation of a tube positioned along the Z-axis of the device) and the above mentioned round robin experiment.

Irradiation conditions for the first case are presented in the Table 3. As can be seen from the Table the time of interaction between an irradiation pulse and the tube surface increased by about 2 times while the value q decreases by approximately 5 times when the distance from the source to the sample $L(A)$ increased from 20 to 36 cm. At the same time the thickness of the melted surface layer d decreased by about 3.5 times. Besides, it is evident that application of a protective screen provided a decrease of q by approximately 2 to 3 orders of magnitude in comparison with the value of $q = 10^9$ W/cm^2 for the screen surface (no protection). The data concerning of the plasma disruption in ITER reactor and interaction conditions of the pulsed deuterium plasma with the tube material in our experiment are presented in Table 4. Damage factor $F = q\tau^{1/2}$ in the Table 4 is parameter, which allows comparing a surface damage under different irradiation conditions. From the table it is seen that the damage factor of the material in our experiments conformed to the one for plasma disruption conditions in Iter within one order of magnitude.

TABLE 3. IRRADIATION CONDITIONS FOR THE FIRST CASE

No. of the tube specimen	1	2	3	4	5
Distance between the specimen and the anode $L(A)$, cm	20	24	28	32	36
Duration of interaction between the specimen and the plasma stream τ, μs	1.9	2.4	2.8	3.3	3.9
Thickness of the melted surface layer d, μm	23.8	17.9	12.6	11.2	7.1
Power density of the plasma stream q, 10^6 W/cm^2	5.0	2.5	1.6	1.2	0.8

TABLE 4. EXPERIMENTAL CONDITIONS

Damage factor $F = q\tau^{0,5}$ [W· cm^{-2}· s^{0,5}]			
Plasma disruption in reactor ITER [13, 14]		Influence of pulsed plasma upon the tube material in PF-1000 device	
The first wall	Divertor plate	The nearest to the anode part	The outermost from the anode part
~ (10^3 – 10^4)	~ (10^3 –10^5)	~ 10^4	~ 10^3

In a round robin tests we used samples presented in Fig. 21.

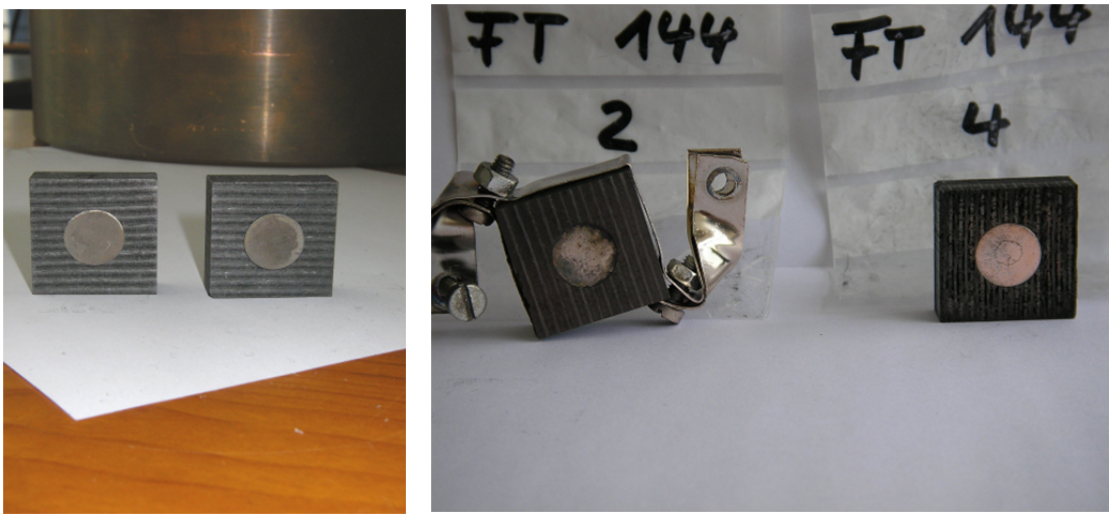

FIG. 21. Samples made of CFC and W before (left) and after (right) irradiation in PF-1000

Electron microscopy has shown cracks in tungsten, spattering of CFC and production of nanostructures on a surface of tungsten (see Figs 22–25).

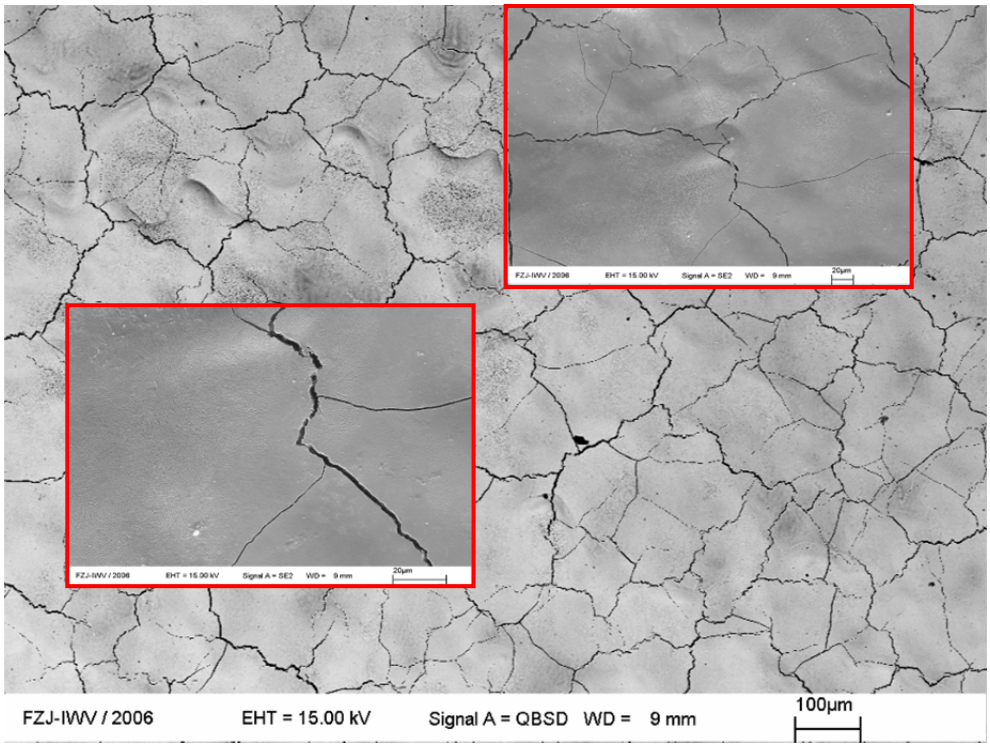

FIG. 22. Tungsten after 1 pulse of irradiation at a distance of 60 cm from the anode.

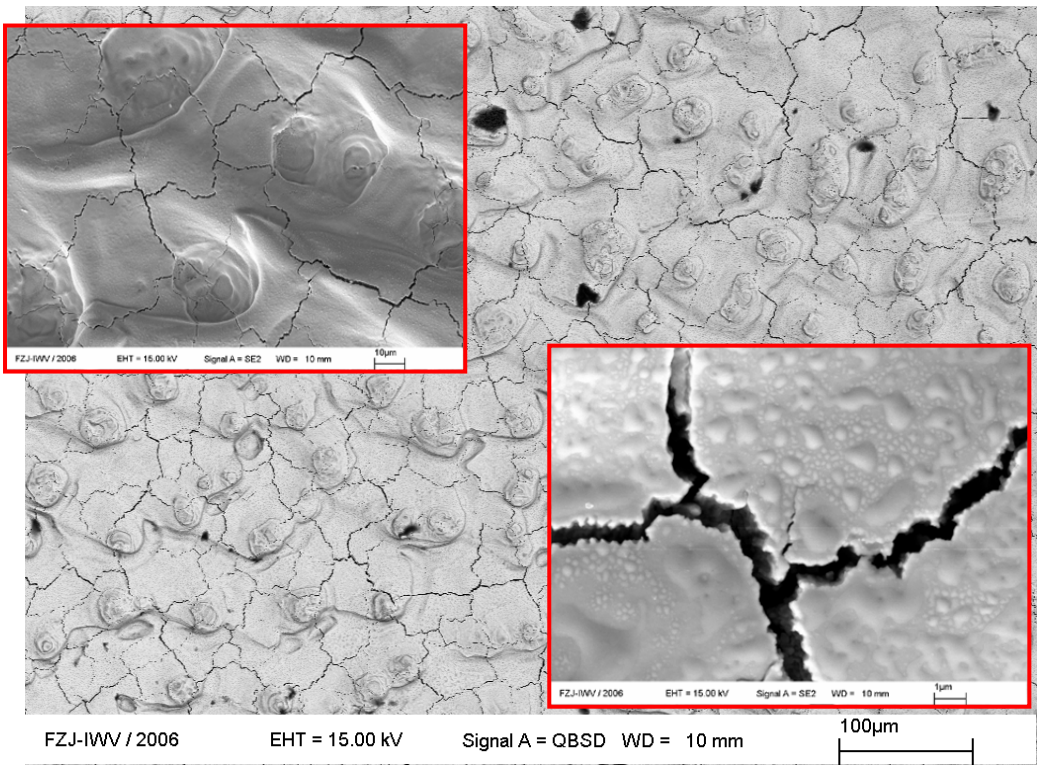

FIG. 23. Tungsten after 4 pulses of irradiation at a distance of 15 cm from the anode.

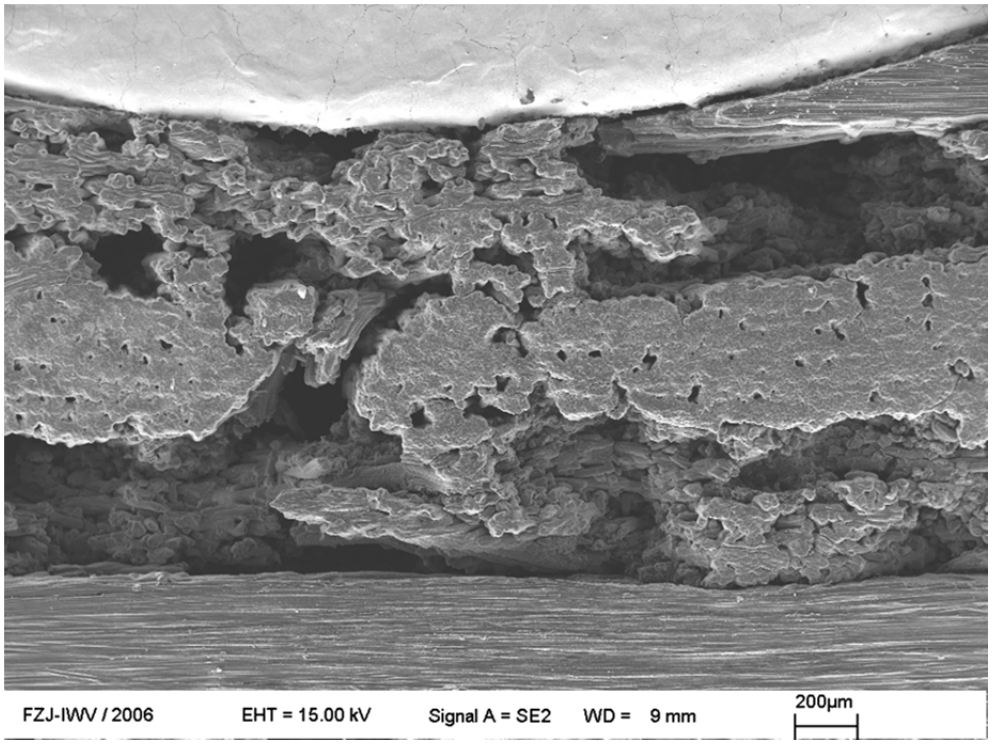

FIG. 24. Border between tungsten (up) and CFC (bottom).

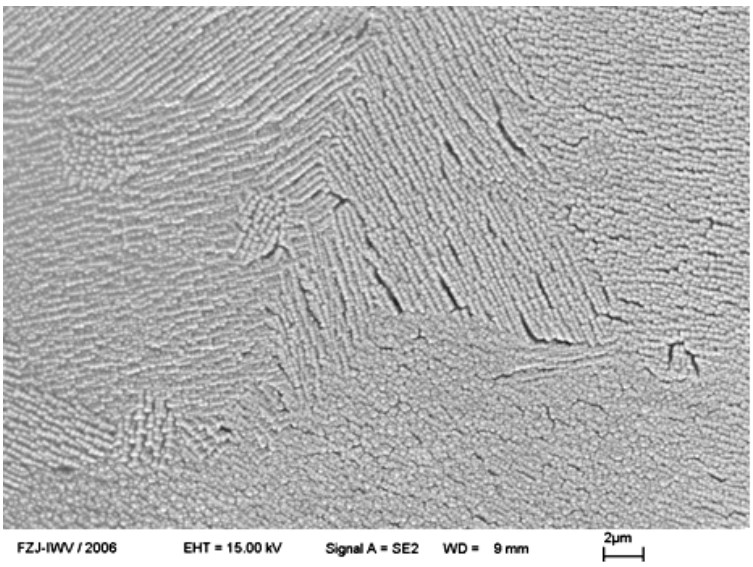

FIG. 25. Nanostructure produced on the surface of tungsten in harsh conditions.

As it was mentioned above detailed analysis of the results received here will be done later.

But as for the experiments with the tube we have reached an important consequence (see Fig. 26). As it was shown by measurements of the micro-hardness of the material outside and inside the tube it was increased by about 1.5 times. It opens perspectives for material treatment by DPF in hard to reach compartments (in our case — an internal surface of tubes).

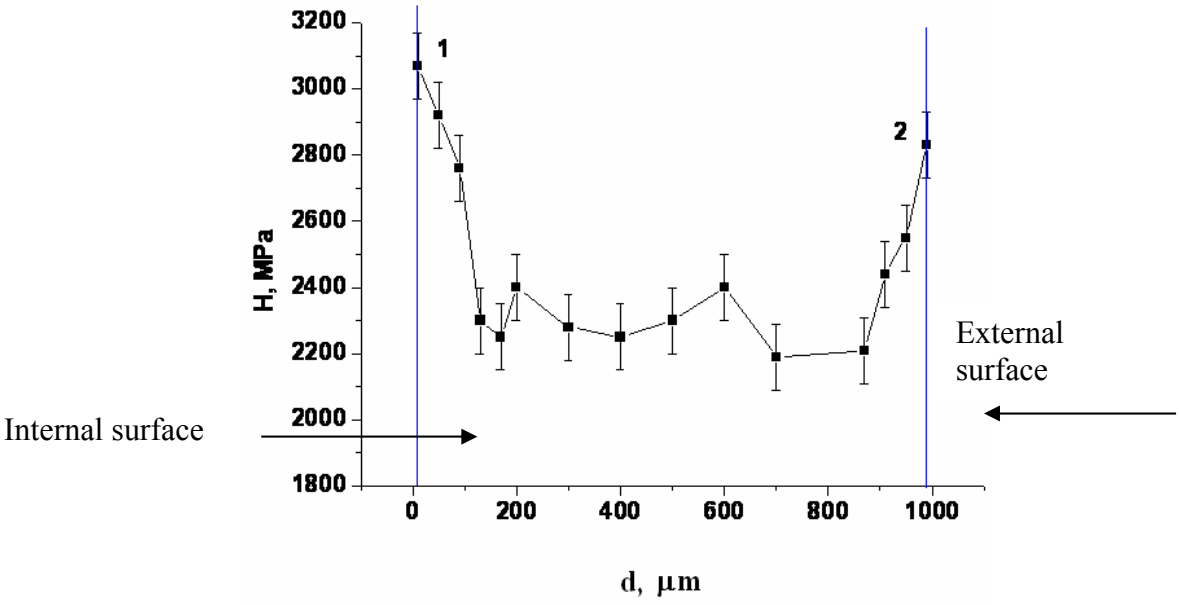

FIG. 26. Micro-hardness increase of the hard to reach compartment.

Beside the above results it was found that at a certain condition of irradiation of aluminum it is possible to produce on its surface a regular nanostructure of the type shown in Fig. 27.

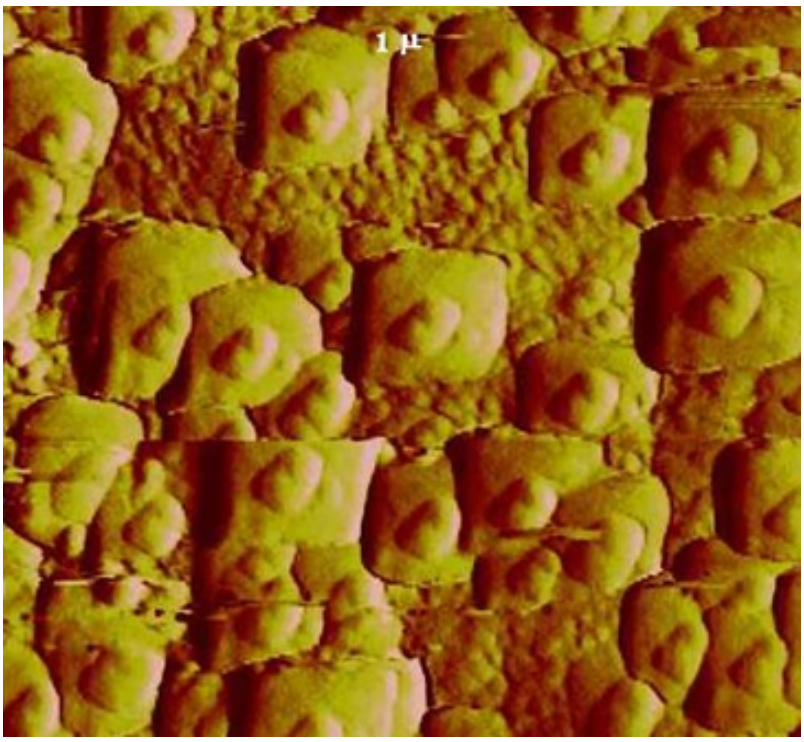

FIG. 27. Regular nanostructure produced by DPF on the surface of aluminum sample.

This work opens perspectives in application of DPF in nano-technologies.

9. SINGLE-SHOT NANOSECOND NEUTRON ACTIVATION ANALYSIS — $(SNA)^2$

Two important issues encountered in the non-intrusive characterization of unknown materials by neutron activation analysis methods with using isotopes or classical accelerators:

- Low signal-to-background ratio;
- Long duration of measurements at a characterization procedure.

That is why these methods demand to produce a huge number of shots of classical accelerators or a long irradiation of a sample by radiation from isotope. Due to this fact a "signal to noise" ratio is still rather poor for each of the technique whereas activation of the interrogated sample is very high.

We have proposed to bring into play a neutron source based on a plasma focus (DPF), which generates very powerful pulses of neutrons of the nanosecond (ns) duration and can convert the procedure into a "Single-Shot Nanosecond Neutron Activation Analysis — (SSNNAA) = $(SNA)^2$" in case of elastically scattered neutron analysis or in a rather short procedure if gamma-rays are investigated in case of inelastic neutron scattering.

In our first experiments elastically scattered neutron radiation has been investigated by two activation counters and two fast photomultipliers with scintillators (S+PM) (see Fig. 28). During this experiment it appeared to be possible to characterize a 1-litre bottle of methanol in a single DPF shot. In the case of inelastic scattering of neutrons the whole procedure to characterize a piece of a gold ore with the gold content of the level of 1 g would take about one minute at the rep rate of DPF of 1 cps.

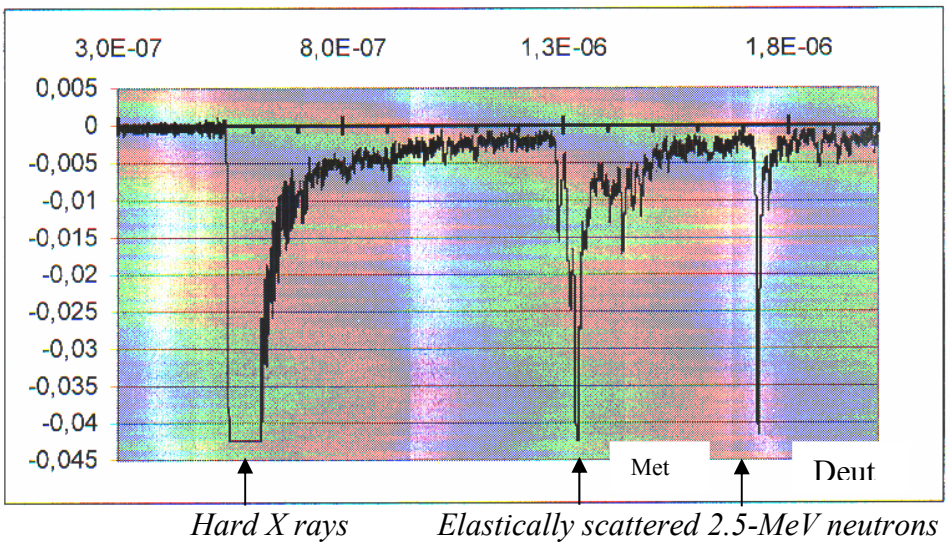

FIG. 28. Hard X ray pulse and pulses of neutrons elastically scattered from a 1-litre bottle of methanol and from a high-pressure cylinder filled with deuterium.

10. DISCUSSIONS

So we have in DPF high radiation power of SXR, HXR, electron, ion and plasma streams, and neutrons as well. Classical "pulsed radiation physics and chemistry" usually deal with relatively "weak" beams of radiation (low power flux density), and they operate by terms of "dose" (D); in this case only the absolute number of ionizing particles or photons interacting with the object is important. The primary assumption is that each fast particle or X ray photon interacts with the object independently of each other.

At the same time during the last four decades physics of high energy density (and corresponding chemistry) was born and extended from laser light into penetrating radiation of various types. With this feature a new quality is created, which ensures an action of the powerful pulses upon the corresponding physical and chemical processes during the time interval short compared with the duration of the processes themselves. Power of the modern sources is so high, that a very high concentration of individual micro-volumes of interaction can be created (e.g. spurs and blobs at water radiolysis), so they may overlap each other (see Fig. 29). It is important that this overlapping will be executed in time interval short in comparison with a reciprocal physical process or chemical reaction (e.g. reaction with free radicals). In this case we may expect — and already received a number of collective effects of synergetic nature (see Fig. 30). Of course these effects are of non-stationary and non-steady state character. In our papers we have proved that these effects can be explained on this basis.

11. CONCLUSIONS

Our experiments made throughout the five years of the CRP has shown that DPF side by side with its own fusion perspectives can successfully be used right now in a number of important applications in biology, medicine, material sciences, express NAA, etc.

It can also simulate many damage features existed in fusion devices and accelerators such as phase changes, brittle destruction and cracks, melting, evaporation and re-deposition of materials under tests, etc. and they are produced namely by the same plasma and ion streams that existed in modern fusion devices and expected to be in fusion reactors.

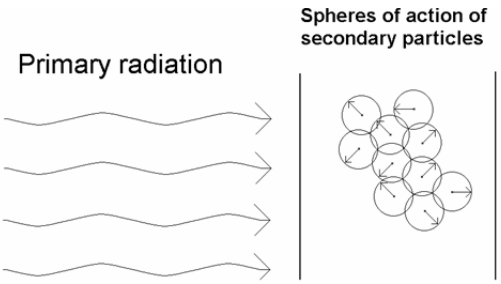

FIG. 29. Overlapping of spheres of action of secondary particles.

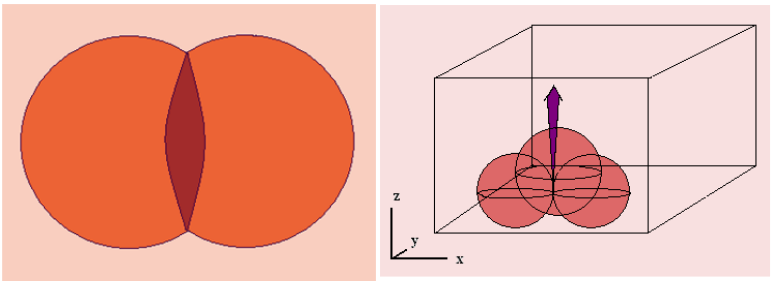

a) *b)*

FIG. 30. Collision of two shock waves with the parameters' increase in the collision zone (a) and 3-D collision of 3 shock waves with a formation of a cumulative stream (jet) (b).

DPF can be used in a single-shot nanosecond neutron activation analysis for characterization of unknown materials just in a single ns shot of the device that shorten the whole procedure, in particular in the cases of registration of elastic and inelastic scattering of neutrons. It is promising to apply DPF for irradiation of malignant tumors in BCNT and in a therapy by fast neutrons, in particular in combination with hard X ray photons generated by it that opens perspectives in a low dose therapy.

Dense plasma foci have good opportunities in a production of short lived isotopes for the aims of Positron Emission Tomography. Our experiments in radio-enzymology have demonstrated an urgent necessity to change a main parameter in radiation dosimetry from Dose into a product of Dose and Dose Power.

Future perspectives of DPF are connected with small sealed DPF chambers giving opportunities to investigate such complicated problems as tritium inventory and beryllium re-deposition taking place under typical thermonuclear fusion conditions in a very cheap and efficient way. DPF devices based on the modern high power pulsed technology can produce "instantaneous" powerful impact upon materials and may help in investigation of transient phenomena.

Their application in pulsed radiation physics and chemistry and in radiation material science in particular, gave already promising results, which have to be verified in mutual experiments with the same materials but other radiation devices such as ion and electron beam accelerators, plasma guns, etc., but most importantly with the real fusion devices — especially of the ICF type.

ACKNOWLEDGEMENTS

We express our thanks for fruitful mutual works to our partners on the current CRP from the following organizations:

Institute of Plasma Physics and Laser Microfusion (IPPLM), Warsaw, Poland; Tallinn University (TU), Tallinn, Estonia; A.A. Baikov Institute of Metallurgy and Material Science (IMET), Russ. Ac. Sci., Moscow, Russian Federation; National Institute of Education (NIE), Nanyang Technological University, Singapore; Ferrara University (FU), Ferrara, Italy; International Centre for Dense Magnetized Plasma (ICDMP), Warsaw, Poland; A.F. Ioffe Physics-Technical Institute (PTI), Russ. Ac. Sci., Sankt-Petersburg, Russian Federation, and the Moscow Physical Society (MPS), Moscow, Russian Federation.

Besides the above participants of the CRP during this Project we collaborated with:
The Andrzej Soltan Institute for Nuclear Studies (INS), Otwock-Swierk, Poland; Institute of Plasma Physics (IPP-U), NSC KIPT, Khar'kov, Ukraine; Institute of Plasma Physics (IPP-Cz), ASCR, Prague, Czech Republic; A.I. Alikhanov Institute for Theoretical and Experimental Physics (ITEP), Rosatom, Moscow, Russian Federation; The Abdus Salam International Centre for Theoretical Physics (ICTP), UNESCO, Trieste, Italy; N.L. Dukhov All-Russian Research Inst. for Automation (VNIIA), Rosatom, Moscow, Russian Federation; Forschungszentrum Jülich (FJ), Germany, and Moscow State University (MSU), Moscow, Russian Federation.

REFERENCES

[1] BERNARD, A., BRUZZONE, H., CHOI, P., CHUAQUI, H., GRIBKOV, V.A., et al., Journal of the Moscow Phys. Soc. 8, No. 2 (1998) 93–170.

[2] E.B. BURLAKOVA (Ed.), "Low Doses of Radiation: Are They Dangerous?" Nova Scientific Publishers, Inc., New York (2000).

[3] V.A. GRIBKOV, M.A. ORLOVA et al., On the Possible Mechanisms of Enzyme Activation Changes at Their Pulsed Irradiation, J. Russ. Laser Research, 24, No. 4, Plenum Press, New York (2003) 289–300.

[4] GRIBKOV, V.A., DUBROVSKY, A.V., ORLOVA, M.A., SCHOLZ, M., Opportunities Afforded by New Generation of Pulsed Radiation Sources in Flash Radiation Physics and Chemistry, Research Journal of Chemistry and Environment, 9, No. 4 (2005) 11–19.

[5] IVANOV, L.I., PLATOV, YU.M., Radiation physics of metals and applications, Intercontact Nauka, Moscow, Russian Federation (in Russian).

[6] PIMENOV, V.N., MASLYAEV, S.A., IVANOV, L.I., et al., Surface and bulk processes in materials induced by pulsed ion and plasma beams at Dense Plasma Focus devices, Nukleonika 51, No. 1 (2006) 71–78.

[7] GRIBKOV, V., DUBROVSKY, A., KARPIŃSKI, L., MIKLASZEWSKI, R., PADUCH, M., SCHOLZ, M., STRZYŻEWSKI, P., TOMASZEWSKI, K., The Dense Plasma Focus Opportunities in Detection of Hidden Objects by Using Nanosecond Impulse Neutron Inspection System (NINIS), AIP Conference Proceedings Series, Vol. 875, Plasma and Fusion Science, 16th IAEA Technical Meeting on Research using Small Fusion Devices and XI Latin American Workshop on Plasma Physics, J.E. Herrera-Velázquez (Ed.) (2006) 415–418.

[8] Bogoljubov, E.P., Gribkov, V.A., Dubrovsky, A.V., Ivanov, Yu.P., Rizhkov, V.I., Samarin, V.A., et al., Application of "Plasma Focus" type devices for the material science, Proceedings of Inter-Industrial Scientific and Technological Conference "Portable Neutron Generators and Generator-Based Technologies" (23–30 May 2003) Moscow, Russian Federation, N.L. Dukhov VNIIA (2004) 81–98.
[9] GRIBKOV, V.A., Dense Plasma Focus as a Tool for Material Science and Technology, Journal of the Moscow Phys. Soc. 3, No. 3 (1993) 231–239.
[10] LEE, S., LEE, P., ZHANG, G., FENG, X., GRIBKOV, V.A., LIU, M., SERBAN, A., AND WONG, T.K.S., IEEE Transactions on PLASMA SCIENCE 26, No. 4 (1998) 1119–1126.
[11] KODENTSOV, A.A., UGASTE, Yu.E., PIMENOV, V.N., et al., Influence of dense deuterium plasma pulses on Fe and Fe-Mn alloy specimens in a plasma focus device, Proc. of the Tallinn Univ. of Social and Educational Sciences, Tallinn, Estonia, B2 (2003) 51–56.
[12] IVANOV, L.I., UGASTE, YU.E., PIMENOV, V.N., GRIBKOV, V.A., MEZZETTI, F., Mass transport of hydrogen from iron-based alloys to outside environment, Perspektivnye Materialy (Perspective materials), No. 2 (2000) 18–25 (in Russian).
[13] MASLYAEV, S.A., PIMENOV, V.N., PLATOV, YU.M., et al., Influence of deuterium plasma pulses generated in plasma focus device on the materials for thermonuclear fusion reactor, Perspektivnye Materialy (Perspective materials) No. 3 (1998) 39–46 (in Russian).
[14] HASSANEIN, A., KONKASHBAEV, I., Erosion of plasma-facing materials during a tokamak disruption, Nucl. Fusion 5 (1994) Supplement: 193–224.
[15] MARTYNENKO, YU.V., MOSKOVKIN, P.G., KOLBASOV, B.N., Accumulation and penetration of tritium in the first wall of tokamak ITER in disruption regime, "The questions of atomic science and technique", Nucl. Fusion 3 (2001) 65–72.

ELABORATION OF A SERIES OF 2–4 KJ MULTIPURPOSE DENSE PLASMA FOCUS DEVICES

A. DUBROVSKI
Pollution Free Sources of Ionizing Radiation Laboratory
Moscow, Russian Federation

Abstract

Under this CRP contract, the design for three new dense plasma focus (DPF) installations has been realized in Moscow Physical Society (MPS). These are DPF-10 (W = 10.0 kJ), PF-5M (W = 5 kJ, rep. rate regime in cooperation with IPPLM, Poland) and DPF-6 (stored energy W = 6.0 kJ in cooperation with IPPLM, Poland). Starting from zero level at the commencement of this CRP, the three mentioned DPF devices are now in operation. Two of them (DPF-6 and PF-5M) yield first experimental results. A series of joint experiments on the PF-1000 device has been carried out in the course of this reporting period. The analysis of the irradiated test samples was carried out in cooperation with other CRP participants.

1. INTRODUCTION

Dense plasma focus (DPF) device is a remarkable source of copious X rays (soft and hard), neutrons, fast electrons and ions and plasma streams as well. Because it has the same energy density (unlike tokamak devices) at any stored energy level (at least in the range 0.10 through 1 MJ) it has a predictable yield of these types of radiation. And due to its very short pulsed character and small sizes of the sources of the radiation it has an extremely high brightness making it very well suited to different applications.

At present the work on the DPF technology have shown that DPF can be formed in devices with stored energy from tens J to hundreds kJ with a discharge current from tens of kA to several MA. Here 2.5 MeV D-D neutron yield is 10^4–10^{12} n/pulse with pulse duration from 5 to 300 ns. For D-T gas mixture neutron yield increases by 102 times with neutron energy of ~14 MeV. It has also been demonstrated that the DPF is a powerful X rays source with photon energies ranging from hundreds of eV to hundreds of keV (and even several MeV), in addition to being a source of fast electrons and ions with particle energy within the range specific for each working gas, electrode configuration and operational regime. A number of works have shown that the fast particle current can replace total discharge current of the device for tens of nanoseconds. DPF so is one of the most intensive sources of the specified radiation having rather high efficiency [1–6].

DPF as ionizing radiation source is more acceptable from ecological point of view in comparison with isotopes, fission reactors and conventional accelerators. This is so since it uses relatively low voltage and becomes a source of hard radiation only within a short period of time of the discharge period, when pulsed electromagnetic energy converts into energy of beams of fast particles. At other times it is safe and does not require special storage or guarding [1, 2–4].

The study of DPF irradiation factors effect on the surface layer of the different materials had constituted a general scientific interest of the team of four IAEA Research Contractors configured in Dense Magnetized Plasmas Program. Moscow Physical Society (this CRP) as well as IPPLM (CRP No. 11940 R) has moreover another task, which has become a general subject of our researches: to create a number of new small scale DPF devices in order to expand the experimental base for material science.

2. ACTIVITIES

2.1. Elaboration of three multipurpose dense plasma focus devices

As a result of MPS activity under this CRP during the complete accounting period the design of three new DPF installations have been realized: DPF-6 (in cooperation with CRP No. 11940/R and CRP No. 11941/R, energy store W = 6.0 kJ, rep rate regime of operation in prospect), DPF-10 (independently, W = 10.0 kJ), and PF-5M (in cooperation with CRP No. 11940/R and CRP No. 11943/R, W = 5 kJ, rep rate regime of operation in prospect). Named small scale plasma focus devices have common peculiarity — every replaceable DPF chamber for a special purpose, which is designed by MPS fits to each device.

Starting from zero level at the commencement of this CRP, three mentioned DPF devices are put into operation now. Two of them (DPF-6.0 as well as PF-5M) yield the first experimental results.

2.2. DPF-6 device

The DPF device named as DPF-6, which is represented here according common MPS — IPPLM (Institute of Plasma Physics and Laser Microfusion (Warsaw, Poland), (IAEA Research Contract No. 11940/R3)) decision is situated in IPPLM. The installation is planned to be able operate in repetitive mode. This condition noticeably has assigns its elements selection. The electric circuit of the device is shown in our previous reports. The installation is now tested. A number of experiments have been carried out with the device. The DPF-6 device is able to operate now in single shot regime. The parameters of the device projected are presented in the Table 1.

TABLE 1. GENERAL DPF-6.0 DEVICE PARAMETERS

Bank capacitance	28 μF
Actuating voltage	12–20 kV
Energy storage	2.0–6.0 kJ
DPF chamber type	Exchangeable
Rep rate	1–10 Hz
Lifetime of the DPF systems	More than 1 million shots

Two photographs of the DPF-6.0 device are presented in Figs 1 and 2.

At the present time, a new more powerful high voltage charger has been designed and is now being assembled by Polish collaborators. The charger will guarantee the frequency regime of DPF-6 device operation on $\omega \cong 1$ cps at least.

An alternative DPF device trigger system using high voltage krytrons now is designed in order to carry the device to repetitive mode of operation as well. New trigger system has been tested within the last joined experiment on DPF-6 device (according the work plans of the experiment participants).

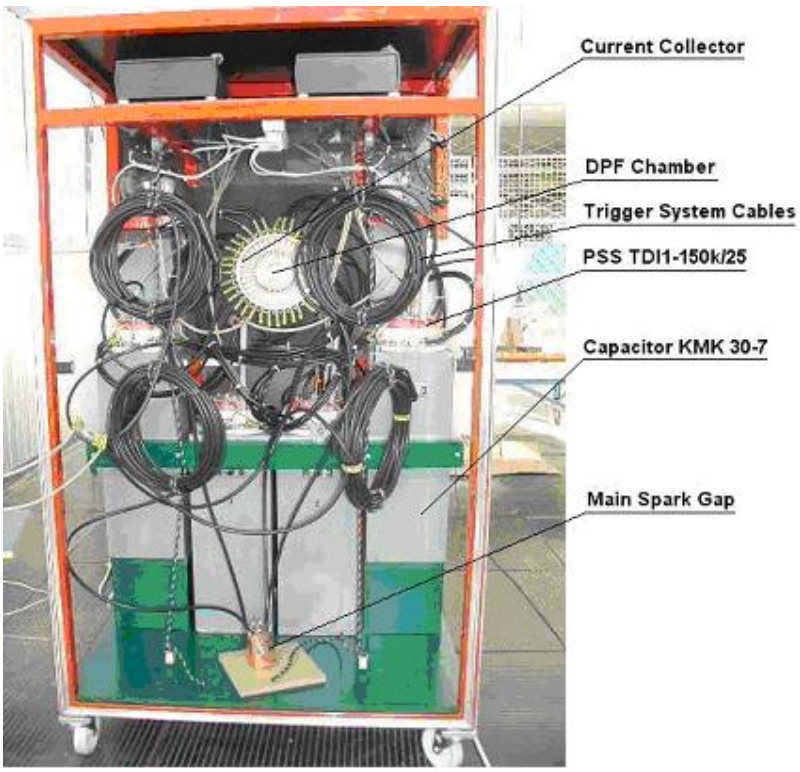

FIG. 1. Photo of DPF-6 device (back).

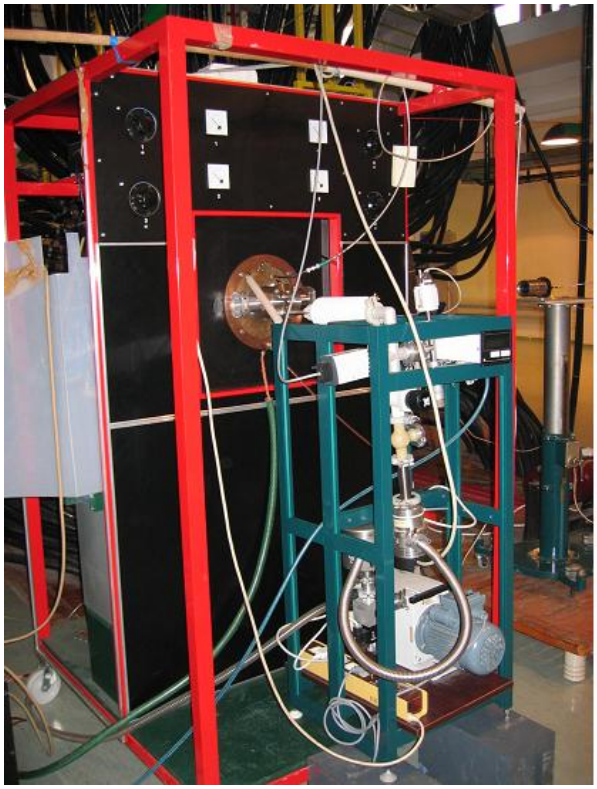

FIG. 2. Photo of DPF-6 device (front face).

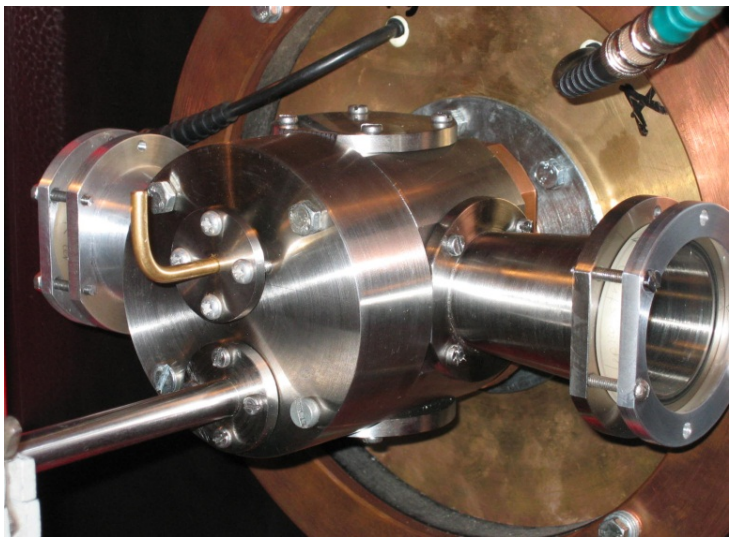

FIG. 3. Target set used in DPF-6 device.

A number of experimental investigations have been carried out on DPF-6 operating in single-shot regime up to this time. Among them:

- Experiment aimed at studying relevant aspects of material science. The target set of a special construction (Fig. 3) has been successfully tested at the experiment. The jet of hot nitrogen as well as deuterium plasmas irradiated numbers of different metallic test samples.
- Hard X ray irradiation of biologic samples;
- Precision measurements of neutron yield and neutron flux space distribution. Time-of-flight neutron experiment.
- Determination of a hard X ray pulse duration using scintillation detectors.

The abovementioned investigations were carried out as joint experiments as part of a collaboration formed by participants in CRP 11940/R, 11941/R, 11942/R, 11943/R, and 12062/R. Analytic results of these investigations are contained within progress reports and publications of the named participants.

2.3. DPF-10 device

DPF-10 device has been realized and tested at the Institute for Theoretical and Experimental Physics (ITEP), B. Cheremushkinskaya str. 25, 117259, Moscow, Russian Federation, where MPS has its operating floor. The parameters of the device are presented in the Table 2.

TABLE 2. GENERAL DPF-10 DEVICE PARAMETERS

Bank capacitance	48 μF
Actuating voltage	15–20 kV
Energy storage	5.0–10.0 kJ
DPF chamber type	Exchangeable
Rep. rate	Operation conditions of single shots
Lifetime of the DPF systems	More than 10000 shots

The photograph in Fig. 4 shows DPF-10 installation at the place of testing.

FIG. 4. Photo of DPF-10 device at the place of testing.

Now the installation DPF-10 is decided to apply as pulse neutron source for the experiment with time-of-flight measurements. The device has been moved to the long room at ITEP (more than 30 m in length (see Fig. 5) in order to provide an acceptable flight path. This time an erection of the device on the new position is executed. DPF-10 is now at inoperable condition for a while.

FIG. 5. DPF-10.0 device (background scene) situated at the long room.

2.4. PF-5M — the device for material science

The decision to create new plasma focus device within "a series of 2–4 kJ multipurposes dense plasma focus devices" (as it is formulated in a title of this contract) had been made at the end of 2004. The place of the device location is A.A. Baikov Institute of Metallurgy and Material Science, RAS (Moscow). The letter "M" of the device name means that PF-5M is assigned in general for the material science purposes. The parameters of the device projected are presented in the Table 3.

TABLE 3. GENERAL PF-5M DEVICE PARAMETERS

Battery capacity	16 μF
Actuating voltage	15–20 kV
Energy storage	1.8–3.2 kJ
DPF chamber type	Exchangeable
Rep. rate	Operation conditions of single shots 1 Hz
Lifetime of the DPF systems	More than 100 000 shots

The flow block of the device is shown in Fig. 6. The assembling of the energy store with vacuum system standing on the movable platform provides the possibility of some displacement of PF-5M device within the room. Current collector of the general type makes it possible to use every DPF chamber, which was described in detail at our previous reports. But the main destination of PF-5M device is to operate in combination with the open type DPF chamber provided by a special sample holder set.

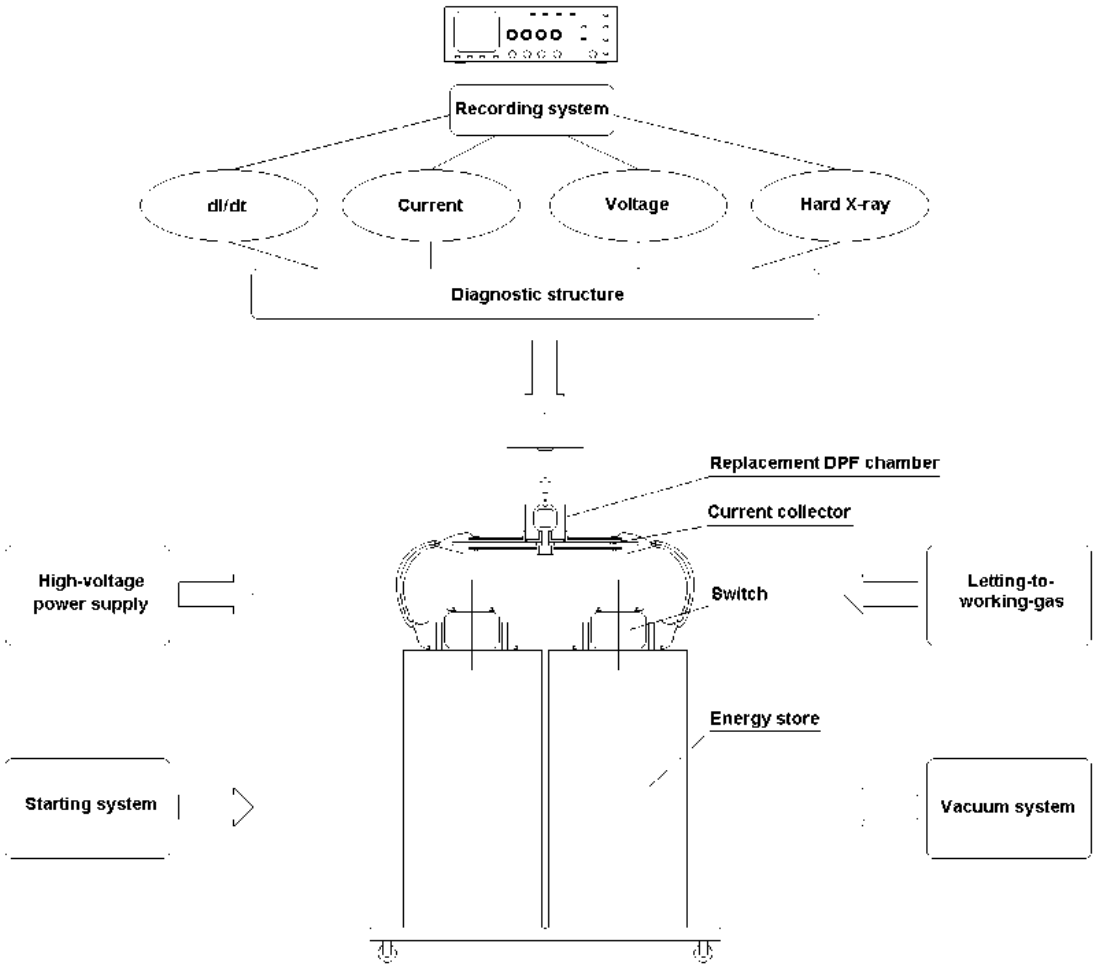

FIG. 6. Block diagram of the PF-5M device.

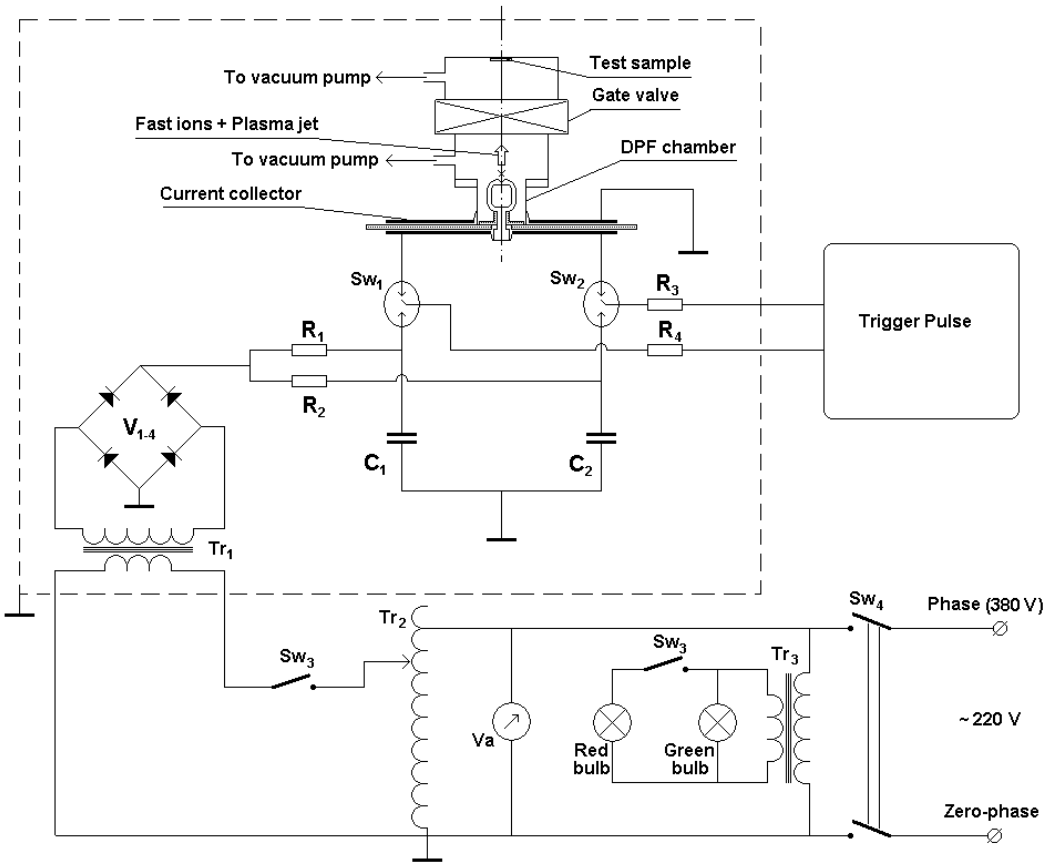

FIG. 7. The electric circuit of the PF-5M device.

The electric circuit of the device is shown in Fig. 7. Two high voltage capacitors of the type KMK 30-8 manufactured by Saint-Petersburg State Technical University (SPSTU) are used as the energy store. This time we use two vacuum spark-gaps realized from Plexiglas as current commutators. At the same time we have a few purchased pseudo-spark switches TDI1-150k/25 elaborated and produced by "Pulse Technology Ltd", Ryazan, Russian Federation, proposing to convert the device into rep-rate machine. See the details of high voltage pseudo-spark switches in our previous reports.

Starting from the zero level we have fulfilled the next stages up to the moment of our last report (April 2006):

- The design of the flow block and the electric circuit;
- The instrumentation of the operating room;
- Assembling of the device as a unit;
- Physical launching of the device (combined testing of high-voltage as well as trigger systems);
- Complete launching of the device equipped with X ray DPF chamber.

This reporting period MPS activity was generally concentrated on final adjustment of plan to use the device as an instrument for material science. We decided not to use a special DPF chamber of the open type as was realized at DPF-6.0 device, but to remodel any sealed off chamber, which we have into the open type one (see Fig. 8).

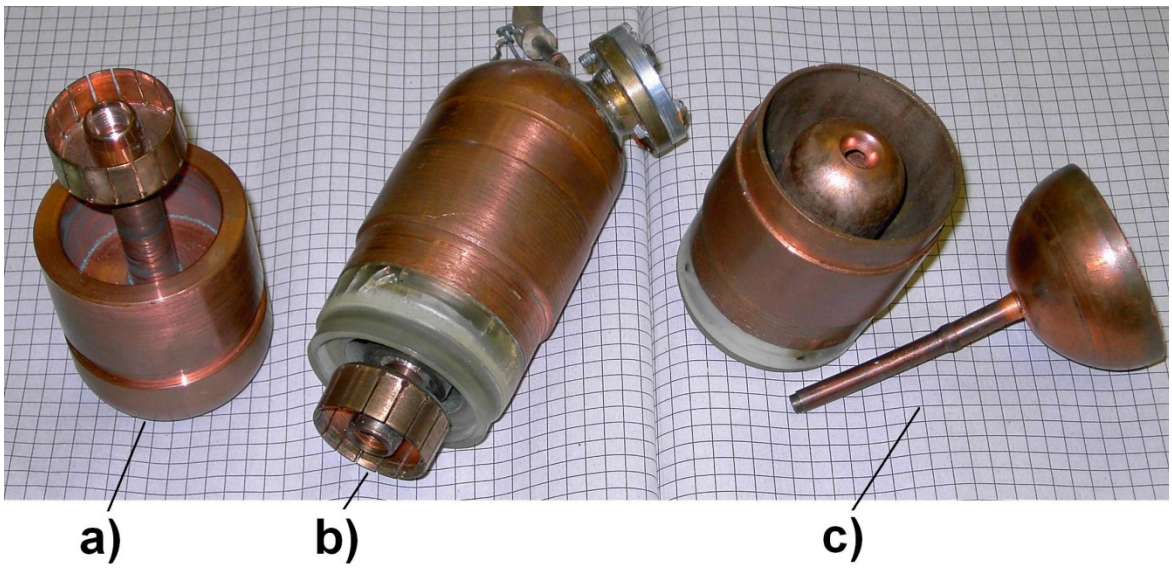

FIG. 8. Three different objects fit to described devices: (a) DPF chamber blank-stimulation, (b) X ray DPF chamber, (c) re-modelled (truncated) chamber with its cover.

The schematic diagram of the PF-5M device chamber with the target set is presented in Fig. 9.

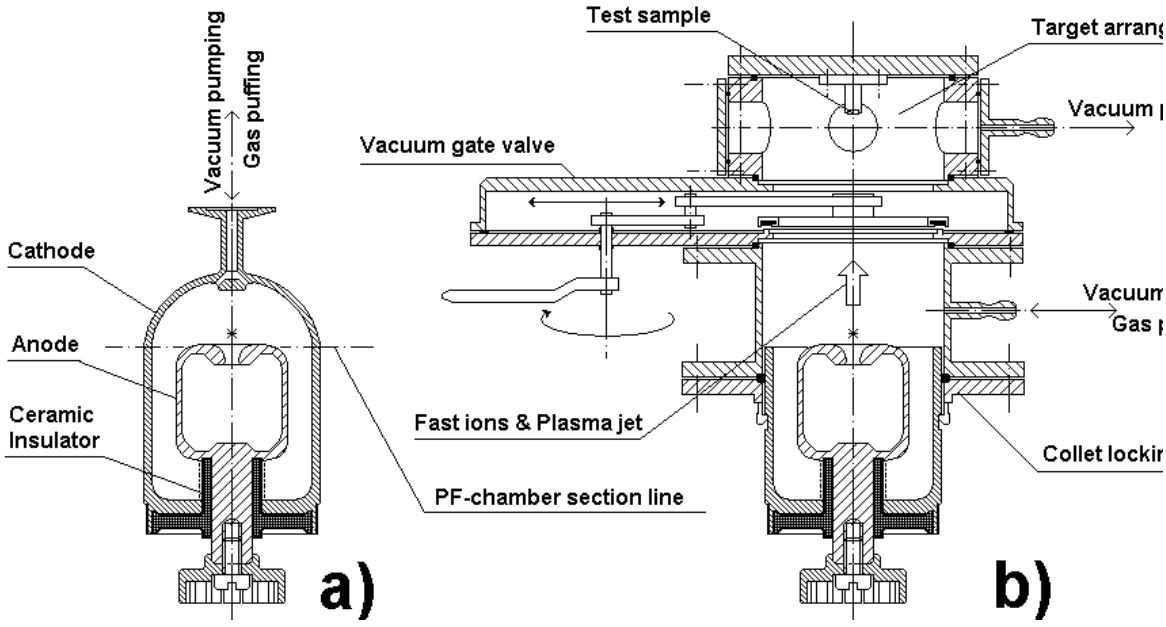

FIG. 9. (a) DPF chamber, (b) Schematic diagram of the PF-5M device chamber with the target set.

Using of the vacuum gate-valve, which is able to separate a target set volume from DPF chamber itself keeping vacuum conditions within the last one, considerably enhances the experiment conditions.

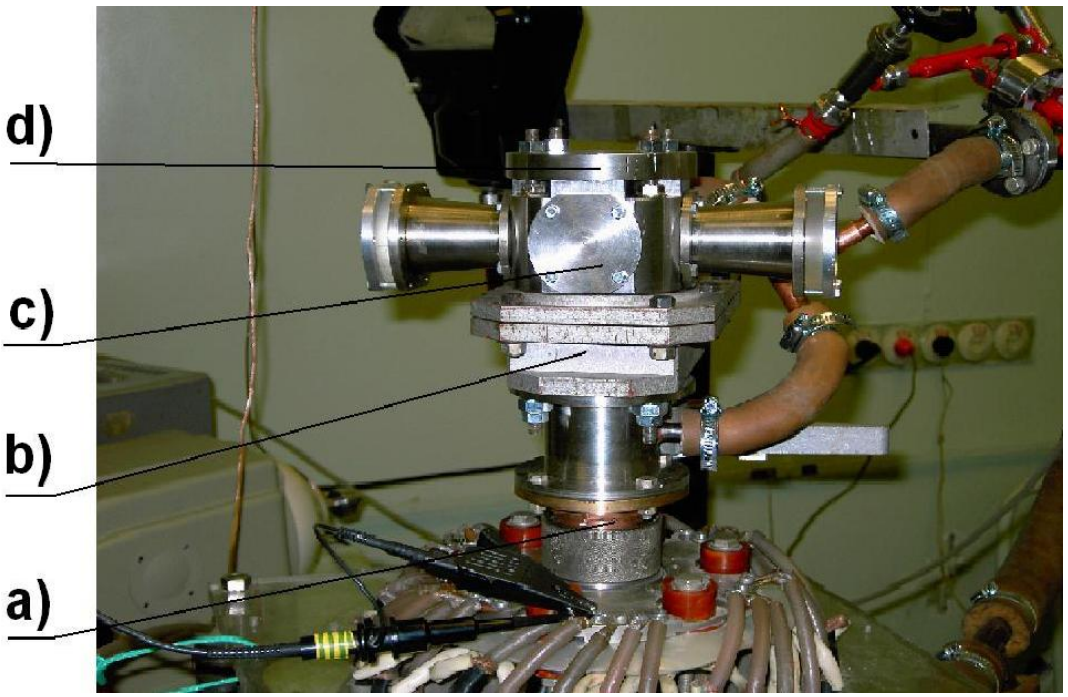

FIG. 10. PF-5M device with the target set readyassembled:(a) Small visible edge of DPF chamber,(b) Vacuum gate valve, (c) Target set, (d) Target set cover with the sample holder.

The PF-5M device with the target set ready-assembled is shown in Fig. 10. The first experimental irradiation of the metallic test sample has been carried out at the described installation 2007-03-23. Nitrogen of 1.6 Torr pressure was selected as a working gas for the first experiment. After 20 conditioning shots at 15 kV of charging high voltage the oscillograms of voltage and current began to look to that shown in Fig. 11. Then three valuable shots were fired to irradiate the test sample number one. No analytical study of the sample is performed for the time being.

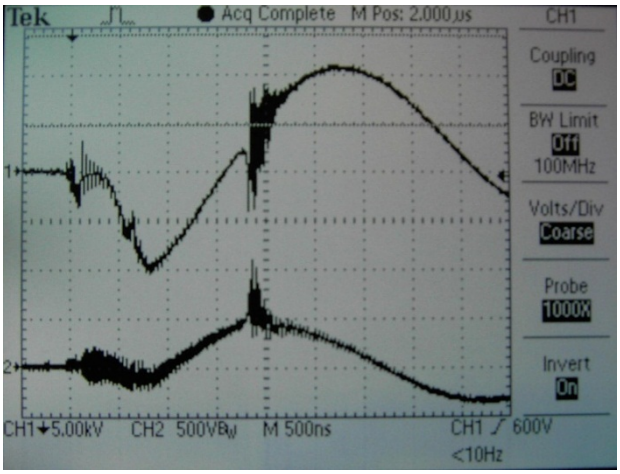

FIG. 11. Oscillograms of high voltage signal (top) and current signal (bottom).

Next follows a number of photos (see Figs 12–14), which demonstrate some sequential stages of the first irradiative experiment. The captions contain appropriate comments.

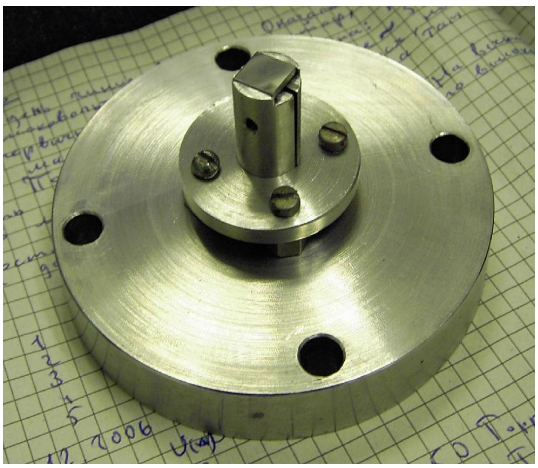

FIG. 12. The test sample No. 1 in this sample holder before the irradiation.

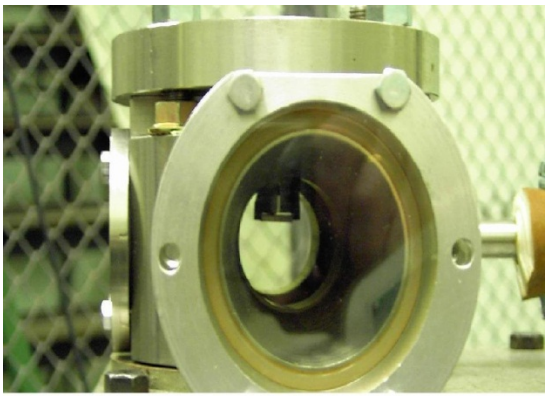

FIG. 13. Test sample ready for irradiation.

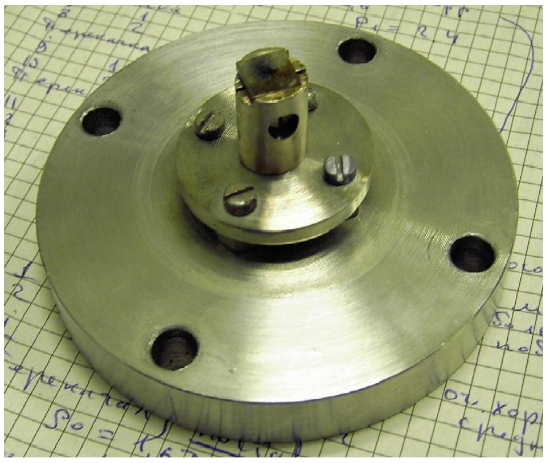

FIG. 14. The test sample No. 1 in this sample holder just after the irradiation.

2.5. The experiments on PF-150 and PF-1000 installations

An experiment on PF-150 (IPPLM, Warsaw) as well as the range of joined experiments on PF-1000 device had been carried out in the course of reporting period. The task of MPS (CRP #11942/R) was in main the engineering decision of the irradiative experiment. The analytical procedure of formerly irradiated test samples was the task of other participants of the researches. The findings are prepared for common publications. [10–14]

3. CONCLUSION

- As a result of MPS activity we have now three new plasma focus installations: DPF-6, DPF-10, and PF-5M devices practically ready for the material science experiment carrying out.
- The range of experimental researches not only for the material science was carried out on DPF-6 device.
- The irradiation of the first metallic test sample has been carried out on the PF-5M device.
- The MPS took part in the series of joined experimental study in the field of material science using DPF devices PF-150 and PF-1000.

ACKNOWLEDGEMENTS

The work was carried out in close cooperation with the Russian Federation and foreign scientists outside the Moscow Physical Society:

- A.A.Baikov Institute of metallurgy and material science RAS, Leninsky pr. 49, 119991 Moscow, Russian Federation (IAEA Research Contract No 11943);
- Institute of Plasma Physics and Laser Microfusion, Hery str. 23, 00–908 Warsaw, Poland (IAEA Research Contract No 11940);
- Pedagogical University of Tallinn, Narva Road 25, 10120 Tallinn, Estonia (IAEA Research Contract No 12062);
- Institute for Theoretical and Experimental Physics ITEP, B. Cheremushkinskaya str. 25, 117259, Moscow, Russian Federation;
- University of Ferrara, Via Paradiso, 12, 144100, Ferrara, Italy;
- Institute of Plasma Physics ASCR, Za Slovankou 3, P.O.Box 17, 18221 Prague 8, Czech Republic;
- The Andrzej Soltan Institute for Nuclear Studies, 05–400 Swierk by Warsaw, Poland.

REFERENCES

[1] DUBROVSKY, A.V., GRIBKOV, V.A., Installation based on high efficiency high repetition rate miniature DPF chambers for material science, Nukleonika 45(3) (2000) 159–162.

[2] BOGOLYUBOV, E.P., BOCHKOV,V.D., VERETENNIKOV,V.A., VEKHOREVA, L.T., GRIBKOV, V.A., DUBROVKY, A.V., IVANOV, YU.P., ISAKOV,A.I., KROKHIN,O.N., LEE,P. LEE,S., NIKULIN, V.YA., SERBAN, A., SILIN, P.V., FENG,X., ZHANG,G.X., A Powerful Soft X ray Source for X ray Lithography Based on Plasma Focusing, Physica Scripta 57(1998) 488–494.

[3] DUBROVSKY, A.V., GRIBKOV, V.A., IVANOV, Y.P., LEE, P., LEE, S., LIU, M., SAMARIN, V.A., 0.2-kJ and 2-kJ high rep rate Dense Plasma foci: their design, technology and applications, Nukleonika 46 (2001) S107-S111.
[4] GRIBKOV, V.A., BOGOLJUBOV, E.P., DUBROVSKY, A.V., IVANOV, YU.P., LEE, P., LEE, S., LIU, M., SAMARIN, V.A., Wide Pressure Range Deuterium and Neon Operated DPF as Soft and Hard X ray Source for Radiobiology and Microlithography, Proc. 1st IAEA Technical Committee Meeting on Application of Fusion Energy Research to Science and Technology, 30 October to 3 November 2000, Chengdu, P.R. China 2001.
[5] GRIBKOV, V.A., LEE, S., et al., Dense Plasma Focus Radiation Source for Microlithography & Micromachining, ISMA-2000: International Symposium on Microelectronics and Assembly, 27 November to 2 December 2000, Singapore.
[6] LEE, S., LEE, P., ZHANG, G., FENG, X., GRIBKOV, V., LIU, M., SERBAN, A., and WONG, T., High rep rate high performance Plasma Focus as a radiation source, IEEE Trans. Plasma Sci. 26 (1998) 1119–1126.
[7] DUBROVSKY, A.V., GRIBKOV, V.A., IVANOV, YU.P., KARPINSKI, L., ORLOVA, M.A., et al., Dense Plasma Focus as a powerful source of monochromatic X ray radiation, Nukleonika 51(1) (2006) 21–28.
[8] GRIBKOV, V.A., DUBROVSKY, A.V., SCHOLZ, M., JEDNOROG, S., KARPIŃSKI, L., TOMASZEWSKI, K., PADUCH, M., MIKLASZEWSKI, R., PIMENOV, V.N., IVANOV, et al., PF-6 — an effective plasma focus as a source of ionizing radiation and plasma treams for application in material technology, biology and medicine, Nukleonika 51(1) (2006) 55–62.
[9] GRIBKOV, V.A., DUBROVSKY, A., ORLOVA, M.A., SCHOLZ, M., Opportunities Afforded by New Generation of Pulsed Radiation Sources in Flash Radiation Physics and Chemistry, Research Journal Of Chemistry And Environment 9(4) (2005) 11–19.
[10] MASLYAEV, S.A., PIMENOV, V.N., PLATOV, YU.M., DYOMINA, E.V., BETSOFEN, S.YA., GRIBKOV, V.A., DUBROVSKY, A.V., Influence of deuterium plasma pulses generated in plasma focus device on materials for thermonuclear fusion reactor, Perspektivnye materialy (J. of Advanced materials), 3 (1998) 39–46 (in Russian).
[11] BOROWETSKI, M., CHIARA, P.DE, DUBROVSKY, A.V., DYOMINA, E.V., GRIBKOV, V.A., IVANOV, L.I., MASLYAEV, S.A., MEZZETTI, F., PIMENOV, V.N., PIZZO, L., SCHOLZ, M., SZYDLOWSKI, A., UGASTE, YU.E., VOLOBUEV, I.V., Experimental study of a powerful energy flow effect on materials in PF-1000 installation, Nukleonika 46 (2001) 117–122.
[12] PIMENOV, V.N., GRIBKOV, V.A., DOUBROVSKY, A.V., MEZZETTI, F., SCHOLZ, M., UGASTE, Y.E., DYOMINA, E.V., IVANOV, L.I., MASLYAEV, S.A., et al., Influence of powerful pulses of hydrogen plasma upon materials in PF-1000 device, Nukleonika 47(7) (2002) 155–162.
[13] PIMENOV, V.N., DYOMINA, E.V., IVANOV, L.I., MASLYAEV, S.A., GRIBKOV, V.A., MIKLASZEWSKI, R., SCHOLZ, M., DOUBROVSKY, A.V., VOLOBUEV, I.V., UGASTE, YU.E., MEZZETTI, F., DECHIARA, P., PIZZO, L., KOLMAN, B., et al., Damage of Structural materials for fusion devices under pulsed ion and high temperature plasma beams, Journal of Nuclear Materials 307–311(1) (2002) 95–99.
[14] GRIBKOV, V.A., PIMENOV, V.N., IVANOV, L.I., DYOMINA, E.V., MASLYAEV, S.A., MIKLASZEWSKI, R., SCHOLZ, M., UGASTE, U.E., DOUBROVSKY, A.V., et al., Interaction of High Temperature Deuterium Plasma Streams and Fast Ion Beams with Condensed Materials in Dense Plasma Focus Device, Journal of Physics D, Applied Physics 36 (2003) 1817–1825.

EXPERIMENTAL STUDY ON SMALL Z-PINCH PLASMA DEVICES

C.M. LUO, X.X. WANG, X.B. ZOU, G.X. ZHANG
The Department of Electrical Engineering and Applied Electronic Technology
Tsinghua University
Beijing, China

Abstract

In the first two and a half years of the project, a small gas puff Z-pinch plasma device has been constructed and investigated. The device has the following parameters: capacitor bank 16 μF, charging voltage 22 kV; peak current 210 kA; the duration of discharge current 9.6 μs. The evolution of plasma sheath movement and electron density profile during Z-pinch implosions was determined with a three frame Mach-Zehnder interferometer. The smallest radius of the pinched plasma was about 0.7 mm at the pinch moment; the speed of plasma sheath movement was about 9×10^6 cm/s, the average electron density was $\geq 5.4 \times 10^{19}/cm^3$ in the pinch phase. The energy spectra $dN/dT/d\omega$ for Ne^+, Ne^{2+}, Ne^{3+} and Ne^{4+} ions emitted from plasma were determined. The highest energies of Ne^+, Ne^{2+}, Ne^{3+} and Ne^{4+} are below 1.3 MeV. The energy spectra of K-shell and L-shell radiation from the gas-puff Z-pinch plasma were measured with a soft X ray spectrometer. In the last one and a half years of the project, a fast Z-pinch plasma device was installed. It is a 500 kV/400 kA/100 ns pulsed power generator, which is composed of a 1.2 MV Marx generator, a 1.25 Ohm pulse forming line, a pressurized sulfur hexafluoride spark switch (V/N switch), a 1.25 Ohm pulse transmission line, and load. The new generator will be used for X-pinch experiments. The trial of the generator was conducted, the voltage and current probe were calibrated, and the electrode system in the load section was calculated and designed.

1. SMALL GAS PUFF Z-PINCH PLASMA

1.1. Experiment facility

Gas-puff Z-pinch plasma device is a typical magnetized plasma device and an excellent soft X ray generator; applications for X rays emitted from the device can be found in many scientific and technical fields, such as X ray lithography, X ray microscopy, etc . The scheme and picture of the gas puff Z-pinch plasma device in our laboratory is shown in Figs 1 and 2. The capacitor bank consisted of four capacitors of 4 μF. The capacitor bank was charged to 22 kV. The peak discharge current was about 210 kA. A hollow gas shell was produced by gas injection through a supersonic nozzle from a fast acting electromagnetic valve. The mass of the gas shell can be varied using different plenum pressure and changing the time delay between the beginning of gas injection and the initiation of the discharge. The nozzle is also used as one of electrodes. Neon gas was used as the working gas; the most suitable gas shell is 10 mm in outer radius, 4 mm in thickness and 6 μg/cm in line mass density.

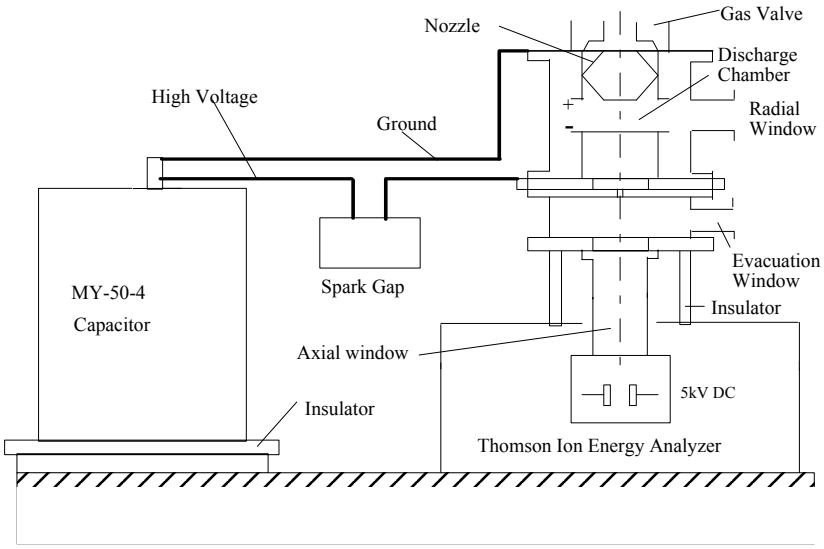

FIG. 1. Layout of Z-pinch plasma experiment.

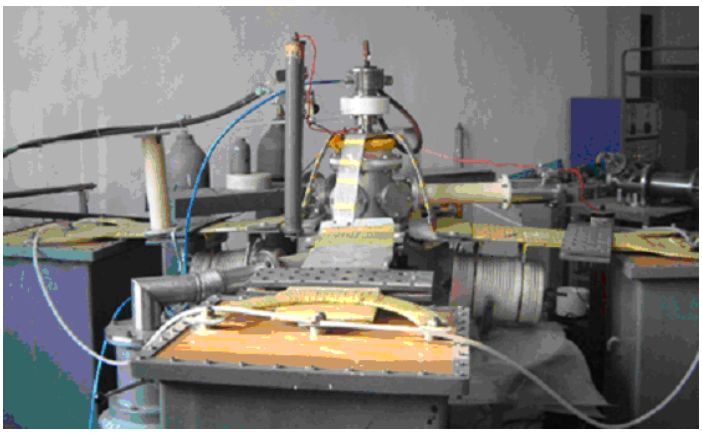

FIG. 2. Picture of gas-puff Z-pinch plasma device.

1.2. DIAGNOSTICS AND RESULTS

1.2.1. Three-frame Mach-Zehnder interferometer

A three-frame Mach-Zehnder interferometer was used for taking three pictures (5 ns exposure and 13 ns time interval between pictures) of the imploding plasma in one Z-pinch shot, which provided us with a series of three interferograms showing the evolution of electron density profile during Z-pinch implosions.

The layout of the three-frame Mach-Zehnder interferometer is shown in Fig. 3. It consisted of a neodymium doped yttrium aluminum garnet (Nd:YAG) laser, a beam splitter and a Mach-Zehnder interferometer. The YAG laser and the beam splitter were mounted on a heavy optical bench of 1.2×2.4 m in area. The YAG laser was Q-switched and its frequency was doubled to deliver on the wavelength 532 nm a 35 mJ pulse in 5 ns. The laser beam was expanded and collimated to 40 mm diameter by a combination of negative and positive lenses. The broadened beam was directed to a fully reflecting mirror M3, and beam splitter B3. A part of this beam passed through B3 to produce beam 1; another part of the beam was reflected by B3 towards mirror M4 and beam splitter B4. In the same way, beams 2 and 3 were produced. Because of the difference of light path, there were time delays of 13 ns between beams 1 and 2, and 2 and 3. Three reference beams were produced with B1 and M2. When probing light beams 1, 2 and 3 with different delay passed through the plasma, they were combined on B2 with three reference beams creating a sequence of three frames of plasma interferogram that were recorded with a CCD camera.

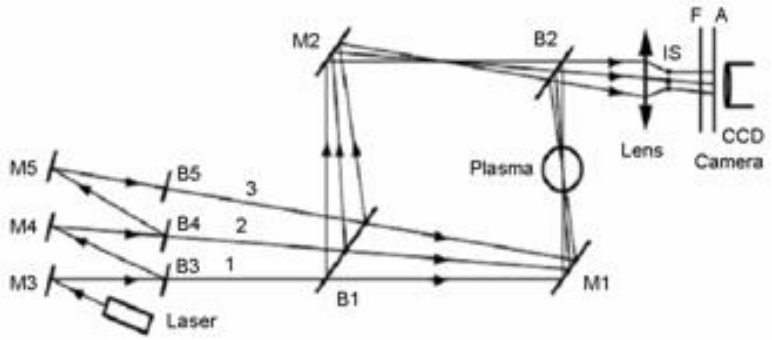

FIG. 3. A scheme of multi-frame interferometer. M1.M5. fully reflecting mirror; B1.B5. partially reflecting mirror; IS . spectroscopic prism; F . interferometric filter; A . attenuator.

Provided the influence of collisions and magnetic field, and the non-linearity can be neglected, the fringe shift ΔN on the interferogram is related to electron density $n_e(r)$ via the equation:

$$\Delta N = \frac{e^2 \lambda}{2\pi m_e c} \int n_e(r)\, dy \tag{1}$$

where: e and m_e are the electron charge and mass, respectively; c is the light speed; λ is the wavelength of the probing light; y is the propagation direction of laser light. Using the Abel inversion method and the known values of the parameters, the electron density profiles of the plasma shell can be derived. For a rough estimate of the electron density, it is assumed that $n_e(r)$ along the detecting light path is constant. Thus, the expression for electron density $n_e(r)$ in cm^{-3} can be simplified to

$$n_e(x) = 4.215 \times 10^{17} \times \Delta N / \Delta Y \tag{2}$$

where Y is the chord length of plasma shell in cm.

The most significant period of plasma movement is in the time interval around pinch formation. Figure 4 shows the interferograms that were taken around the final pinch stage of the imploding plasma. For taking these interferograms, the zero field of the interferogram (interference pattern without any plasma) was adjusted to have fringe spacing in image plane 0.8 mm. The moment of the final pinch was set as the instant of t = 0. From these interferograms, we could see the movement of plasma shell. Figure 4(a) shows the situation 13 ns prior to the pinch. The smallest radius (0.7 mm) of the plasma shell is seen in the interferogram, Fig. 4(b), taken at the pinch time t = 0. At t = 13 ns (Fig. 4(c)), the plasma shell was already expanding. From the interferograms mentioned above, it was estimated that the speed of plasma sheath movement was about 9×10^6 cm/s, the average electron density was $\geq 5.4\times10^{19}$ cm^{-3}.

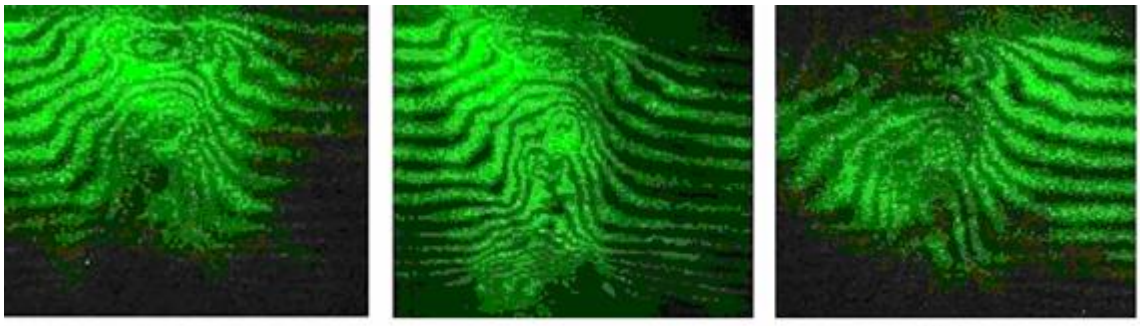

FIG. 4. Interferograms taken at the final pinch of the imploding plasma (a) t = -13 ns, (b) t = 0 ns, and (c) t = 13 ns.

1.2.2. Thomson ion energy analyser

The Thomson ion energy analyzer is a simple and efficient tool to determine the characteristics of ion beams. It can provide information of ion energy, ion momentum and the ratio of charge to mass simultaneously. In this work, the structure of the analyzer is shown in Fig. 5. The analyzer consisted of an iron shell to enhance the magnetic field and to prevent the disturbance from outer electromagnetic field, two permanent magnets made of Sm-Co to

produce magnetic field of 0.564 T, a pinhole with the diameter of 40 μm, a CR-39 plastic target and insulators. The two magnets also functioned as a pair of electrodes.

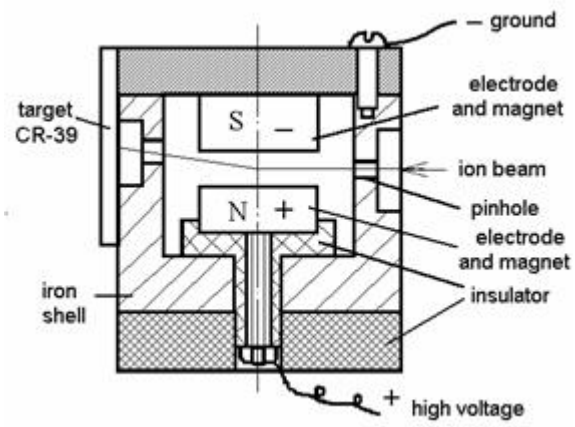

FIG. 5. The structure of Thomson ion energy analyser.

In the experiment, the angles of ion beam deflection by the electric and magnetic fields were small. The deflection angles of ion beam in *x* direction (direction of electrical field $\vec{E}$) and in *y* direction (direction of $\vec{v}\times\vec{B}$, $\vec{v}$- the velocity of ion, $\vec{B}$-magnetic field) can be expressed, respectively as:

$$\theta_x = \frac{q}{2T}\int_0^l E(z)\,dz \tag{3}$$

$$\theta_y = \frac{q}{\sqrt{2mT}}\int_0^l B(z)\,dz \tag{4}$$

where: $T = mv^2/2$ is the kinetic energy of ion; l is the field spread length; q and m is the charge and mass of ion, respectively; θ_x is corresponding to ion energy and θ_y is corresponding to ion momentum. According to Eqs. (3), and (4), the ion energy spectrum can be obtained experimentally. When the ions have a different ratio of charge to mass, or different energy, they experience different deflections in the electromagnetic field, and then they will hit the target (CR-39 plastic) at different positions forming parabolic tracks. Ions with the same charge-to-mass ratio, but different energies will lie on the same parabola but at different positions. Ions with different charge-to-mass ratios will be on different parabolas.
The magnetic field distribution was measured with a gauss-meter. The integration of E and B in Eqs. (3) and (4) were determined as 3.34×10^4 V and 0.012 Tesla-meter, respectively. According to Eqs. (3) and (4), the energy and the momentum of an ion particle could be determined, if θ_x and θ_y of the ion on the parabolic tracks are measured.

Figure 6 is a picture of parabolas produced by ion beams bombarding CR-39 plastic target. On the picture up to five parabolas can be recognized, which are formed by ions with different charge-to-mass ratios. According to Eq. (5), if *m* is constant, the vertical spacing of the parabolas (*y*-direction) at the fixed horizontal (*x*) coordinate is proportional to the square root of the ion charge *q*. In our case, the ratios of θ_y at the fixed θ_x for different parabolas are 1:√2:√3… According to the reading from the picture, these parabolas are identified to belong to Ne^+, Ne^{2+}, Ne^{3+} and Ne^{4+} ions. The energy and the momentum of an ion can be determined, when θ_x and θ_y of the ion on the parabolic tracks are measured. Figure 7 shows the energy

spectra $dN/dTd\omega$ for Ne^{+}, Ne^{2+}, Ne^{3+} and Ne^{4+} ions, where T is the energy of neon ions; N is the number of ions, ω is the solid angle at plasma center subtended by entrance pinhole. From the ion energy spectra, it is concluded that the highest energies of Ne^{+}, Ne^{2+}, Ne^{3+} and Ne^{4+} ions emitted from our Z-pinch plasma are below 1.3 MeV. But it is observed that the ions in higher charge states have higher energy in the low end of the energy spectra.

FIG. 6. Parabolas of Ne ion beams.

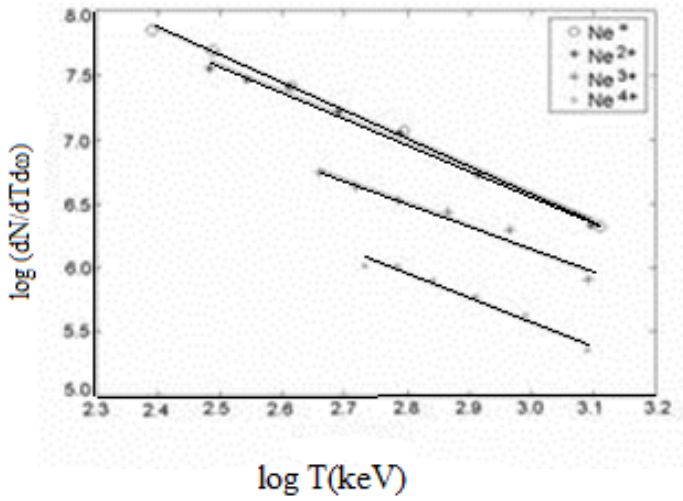

FIG. 7. Relationship between log (dN/dTdω) and log T.

1.2.3. X ray measurement

A soft X ray (0.28 keV ~ 1.56 keV) spectrometer has been designed for measuring the time resolved neon K-shell and L-shell radiation from the small gas-puff Z-pinch device. The spectrometer consists of 10 PINs; each was covered with a filter. The material and thickness of the filters were carefully matched so that every two filters construct a Ross filter pair, as shown in Table 1. Figure 8 is the measured X ray energy spectrum.

TABLE 1. PARAMETERS OF ROSS FILTERS PIN X RAY SPECTROMETER

	Filter 1 Material（μm）	Filter 2 Material（μm）	Photon Energy （keV）
1	V (0.60)	C (0.36) + V (0.56)	0.283 ~ 0.512
2	Fe (0.73)	V (0.62) + Fe (0.40)	0.512 ~ 0.708
3	Ni (0.80)	Fe (0.28) + Ni (0.60)	0.708 ~ 0.853
4	Zn (1.20)	Ni (0.19) + Zn (1.00)	0.853 ~ 1.022
5	Al (8.00)	Zn (0.30) + Al (7.00)	1.022 ~ 1.559

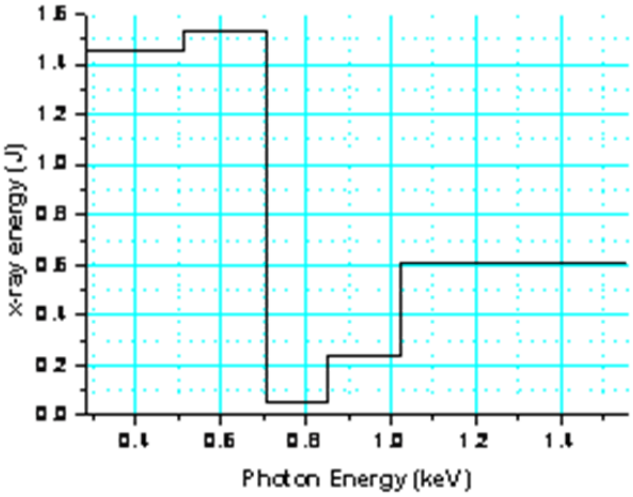

FIG. 8. The measured X ray energy spectrum.

2. FAST Z-PINCH PLASMA DEVICE.

2.1. Facility design and structure

2.1.1. General description of the PPG-I

In the last phase of the project, a ~500kV/400kA/100ns pulsed power generator (PPG-I) was designed and constructed. The new device is a consequent update of an older unit, to follow the development tendency of Z-pinch plasma research and aimed at X ray backlighting for exploding wires and wire array implosions. The PPG-I is composed of a Marx generator, a combined pulse forming line (PFL), a gas filled V/N field distortion switch, a pulse transfer line (PTL), and a resistive load of copper sulphate. The circuit block diagram and a picture of the generator are shown in Figs 9 and 10.

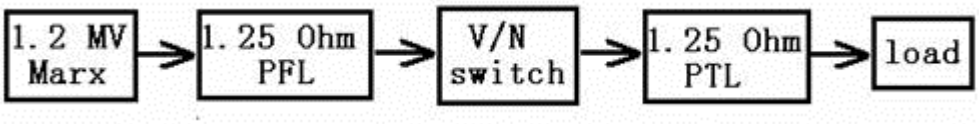

FIG. 9. Block diagram of PPG-I.

FIG. 10. View of the PPG-I.

For X-pinch experiments, two or more wires crossing and touching at a single point constitute an "X"-shaped load. The cross point explodes firstly and then pinches axially to form a so-called X-pinch plasma by the magnetic pressure as pulsed-power generator delivers a suitable current to the "X"- shaped wires. The X-pinch radiating intense X ray pulse is an effective point source for X ray backlighting in radiographing high-density Z-pinch plasma. In addition to X ray backlighting, PPG-I is also intended to drive a puff-gas load, such as neon cylindrical load with a linear density about 10μg/cm. An applicable soft X ray source will also be pursued on the PPG-I.

The normal output voltage VM from Marx generator in the PPG-I is 1.2 MV. When Triggering pulse arrives, the Marx generator discharges in series and charges the combined PFL synchronously. As the PFL reaches to its peak voltage VF of about 1.09 MV (the voltage transfer efficiency between Marx and PFL is simulated to be about 91%), the auxiliary gap of V/N switch breaks down. Being distorted greatly with the electrical field between the main electrodes, the V/N switch swiftly breaks down in multichannel mode and then about VF /2 pulsed voltage is delivered to the matched pulse transfer line. Then, the pulse voltage ultimately fed to the load is about 500 kV. In the PPG-I, the combined PFL and transfer line both have 1.25 Ω characteristic impedance and 167 cm length, which are fixed on by the output parameters of 400 kA peak current, 500 kV peak voltage and 100 ns duration time.

2.1.2.Marx generator

A Marx generator was used as the first stage energy storage unit of PPG-I. The Marx generator comprises 16 stages of energy storage capacitors: a 0.66 μF/100 kV capacitor at each stage. Once erected, the total series capacitance CM is 41 nF (Fig. 11).

Bipolar charge configuration was adopted in the Marx generator. Two capacitors connected with a gas-filled spark gap constitute a charge and discharge module; there are 8 such modules in the Marx generator. A triggering pulse of -160 kV with the rise time of 20 ns fires the first two spark gaps, and the rest of spark gaps are then fired due to resistance coupling. All the capacitors are charged to +75kV or -75 kV in parallel, thus the normal output voltage of the Marx generator is negatively 1.2 MV.

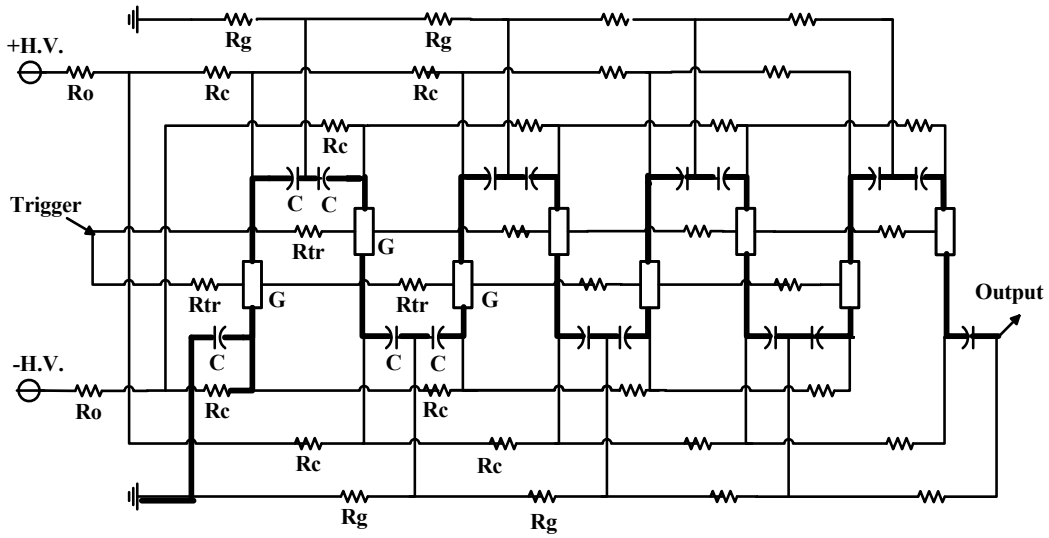

FIG. 11. Circuit of Marx generator C: storage capacitor; R_0: current limiting resistor; R_{tr}: triggering resistor; R_C: charge resistor; R_g: grounding resistor; G: spark gap.

2.1.3. Main switch, pulse forming line-PFL and transfer line-PTL

A pressurized gas filled self-break V/N switch shown in Fig. 12 was employed in the PPG-1. The auxiliary gap self-breaks down first, and then greatly distorted and enhanced fields at the edges of the mid-plate leads to discharge across the main electrodes.
To shrink the size of the generator, de-ionized water was used as insulation substance in both of pulse forming line-PFL and pulse transfer line-PTL. For 100ns pulse duration in PPG-I, the length of all waterlines was determined as 167 cm. Based on insulation consideration the inner and outer radii of waterlines were 7.3 cm and 14.45 cm, respectively.

In the PPG-I, the structure of PFLs have a novel design: four pieces of waterline with impedance 5 Ω in parallel constitute a combined PFL with 1.25 Ω and incorporate each other by a common self-break V/N switch on a matched 1.25 Ω transfer line (Figs 12 and 13). The 1.25 Ω transfer line, with 25.6 cm inner and 30.9 cm outer diameters, delivers electric power from the combined PFL to the load. The 1.25 Ω transfer line was also employed to reduce the prepulse voltage reaching the load as the PFL is charged.

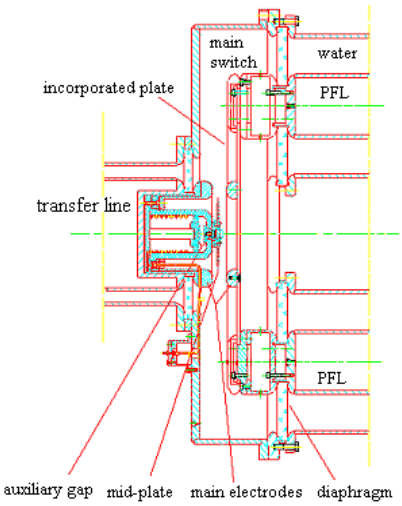

FIG. 12. Connection of the combined PFL and the transfer line through the V/N switch.

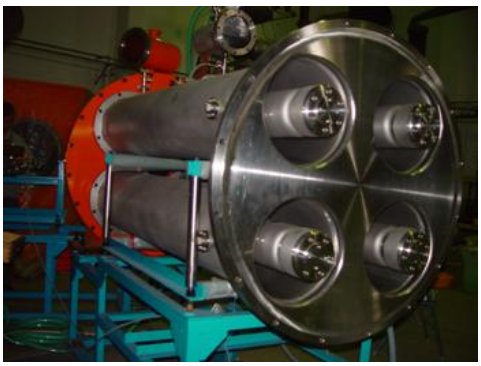

FIG. 13. A unique structure of pulse forming line.

2.2. The trial of the generator

An adjustable copper sulphate resistive load was used to scale the output of the PPG-I. By varying the gas pressures in the main gap and auxiliary gap, respectively, the V/N switch can be tuned to break down near the peak voltage in multichannel or single channel discharge mode. Extensive tests have been made to study the relationship between the rise time of the output voltage pulse and the number of spark channels inside the V/N switch. Figure 14 shows the typical multichannel and single channel photographs observed by a digital camera. The output voltage and current waveforms corresponding to Figs 14 and 15 are shown in Figs 16 and 17. In the experiments, the operating voltage of Marx generator keeps 75 kV, and the load is adjusted to ~1.25 Ω. In Figs 14 and 15, the cathode (high voltage electrode) is at the right side and the anode at the left. The image of mid-plate (self-break plate) is a dim line near the anode and across all the spark channels.

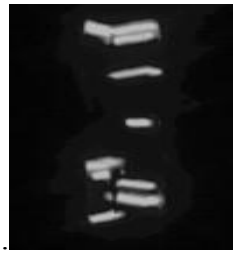

FIG. 14. V/N switch works in multi-channel mode with pressures of 0.46 MPa in the main gap and 0.27 MPa in the auxiliary gap.

FIG. 15. V/N switch works in single-channel mode with pressures of 0.46 MPa in main gap and 0.34 MPa in auxiliary gap.

From the charging voltage trace of the PFL in Figs 16 and 17, it can be seen that the V/N switch breaks down at about 700 ns related to the start of the charging voltage, and the load voltage and current of the PPG-I are respectively 460 kV and 380 kA with about 110 ns

FWHM. Results based on a series of experiments show that the rise time of the output voltage pulse is closely related to the number of the spark channels, ~70 ns for one spark channel and ~30 ns for six to seven spark channels.

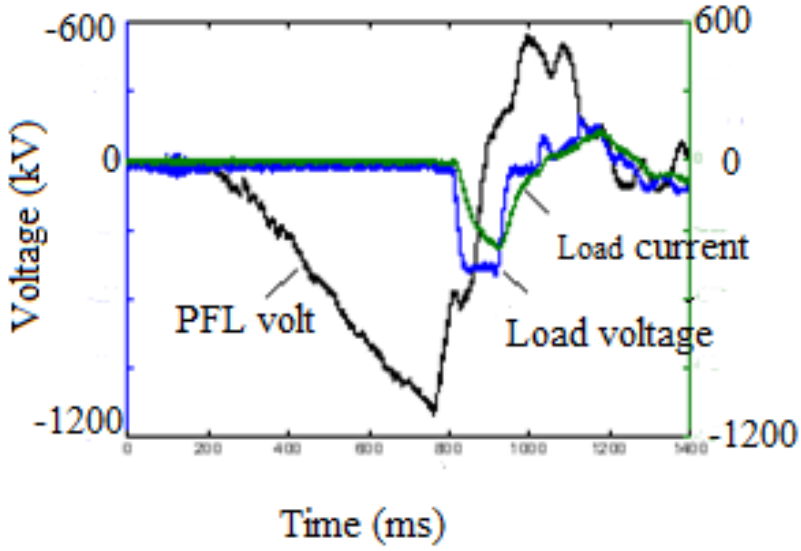

FIG. 16. The output voltage and current waveforms on a ~1.25 Ω load (multi-channel mode).

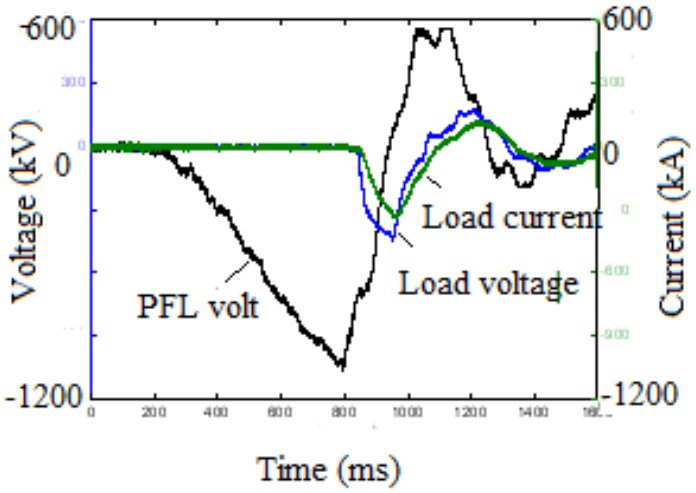

FIG. 17. The output voltage and current waveforms on a ~1.25 Ω load (single channel mode).

2.3. The design of electrode system

The electrode system in load section of the generator was calculated and designed. In order to reduce the inductance of the electrode system so as to attain fast and high current for the X-pinch, the electrode system should be made as compact as possible in the condition without surface flashover and breakdown in vacuum. The design of load section is to figure out the size and details of the electrode system by calculating its electric field with a realistic applied voltage pulse to the electrode system. After measuring the forward going voltage wave, estimating the inductance of the X-shape wire load and the backward going voltage wave from the load, we have calculated the voltage actually applied on the load, and then simulated the electric field with a finite element method.

The design of the electrode system is a procedure of step-by-step and recycles as below: making a small change in the structure and size of electrode system to reduce inductance → calculating the inductance of the load → calculating the load voltage applied on the load → simulating the electric field in this system → checking whether any surface flashover and/or breakdown in vacuum happens or not. In one of our concrete design for an applied pulse voltage of 100 ns in FWHM and 500 kV in amplitude, according to the formula and data given in the vacuum breakdown field and the pulsed flashover field should be 300 kV/cm and 128 kV/cm, respectively. Based on the procedures mentioned above, the calculated highest field on the surface was 113 kV/cm and the highest field in the vacuum was 298 kV/cm. Both of them are below the value of the surface flashover and breakdown voltage in vacuum, respectively. The structure of the load section is shown in Fig. 18.

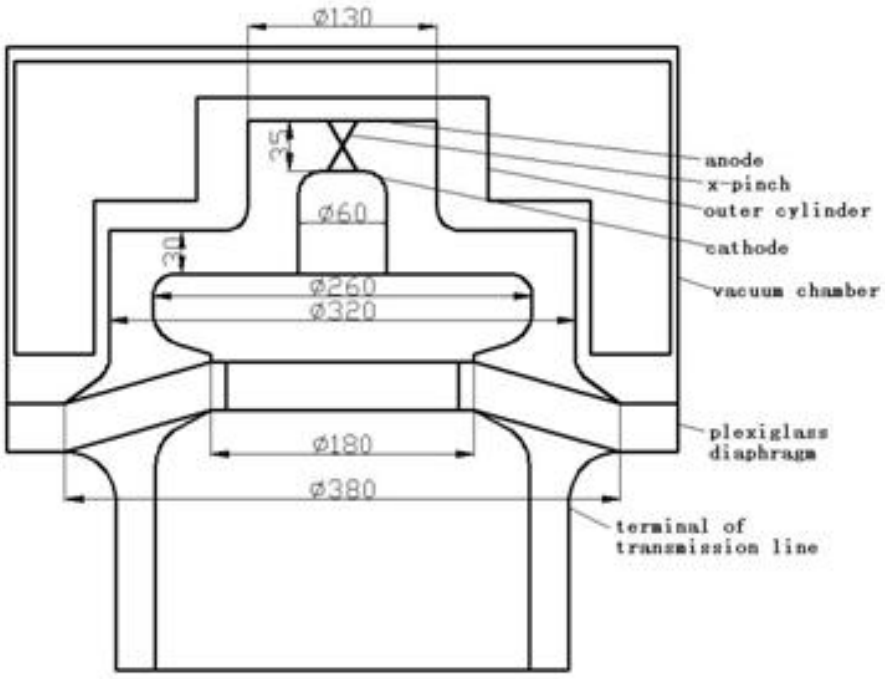

FIG. 18. The structure of the load section.

3. OVERALL CRP CONTRIBUTIONS

At the beginning of the project our group had 3 persons. We had only a few incomplete diagnostic instruments, including a laser interferometer and ion energy magnetic analyzer. During the implementation of the project, our small gas puff Z-pinch device was upgraded and its vacuum condition was improved substantially. After completing the diagnostics mentioned above and developing a soft X ray spectrometer, we were able to conduct more experiments on the device. Some data for the Z-pinch plasma were obtained, including: the size of the pinched plasma and implosion velocity of the plasma sheath at the time of maximum compression; the energy spectra of neon ion beams emitted from the plasma; X ray yield; X ray production efficiency and the energy spectra of soft X rays emitted from the plasma. Having completed these experimental tasks, we shutdown the small gas-puff Z-pinch plasma device.

We have now constructed a fast Z-pinch device driven with a pulse generator. The generator has the parameters of 500 kV/400 kA/100 ns and will be used for X-pinch in

backlighting of Z-pinch plasma. The device will provide a good working stage for further Z-pinch plasma research.

We deliver several courses related to plasma research: Gas Discharge and Plasma, Pulsed Power Technology and High Voltage Engineering for students and graduate students. The size of our group has increased to 8 persons: 5 faculty members and 3 graduate students. To enhance the diagnostics for X-pinch experiments, a Monochromator / Spectrograph, a fast ICCD camera, several high speed digital storage oscilloscopes and diamond radiation detectors have been recently installed.

International collaboration has been enhanced. We have joined the ICDMP community (International Center for Dense Magnetized Plasmas), located in Warsaw, Poland. The major effort of the center is dedicated to the theory, experiment and application of plasma focus and Z-pinch plasmas, especially the application of the neutron pulses produced by these devices. The CRP has given new impetus for our group to take part in the activities of ICDMP. The members of our group periodically attend ICDMP Workshops, and to exchange experience and technical knowledge with ICDMP members. And in September of 2006, we invited Dr. K. Tomaszewski (Institute of Plasma Physics and Laser Micro fusion, Warsaw, Poland) to visit our university and exchange knowledge of high speed photography in plasma experiment.

4. CONCLUSION

A small gas puff Z-pinch plasma device has been installed. The device has the following parameters: capacitance of energy storage capacitors 14 μF, charging voltage 22 kV, peak current 210 kA and a quarter of current period 2.4 μs. The device has been operated successfully, and it was used for diagnostic research and student training.

A three-frame Mach-Zehnder interferometer was developed for Z-pinch plasma experiments. According to interferograms, the electron density n_e of the plasma right before pinch instant is larger than $5.4\times10^{19}/cm^3$, the corresponding velocity v of collapsing plasma sheath is 9.0 cm/μs.

A compact Thomson ion energy analyzer was developed for determining ion energy spectra in Z-pinch plasma device. Clear parabolas produced by neon ions Ne^+, Ne^{2+}, Ne^{3+} and Ne^{4+} on CR-39 target have been observed. The energy spectra $dN/dTd\omega$ for Ne^+, Ne^{2+}, Ne^{3+} and Ne^{4+} ions were determined. The highest energies of Ne^+, Ne^{2+}, Ne^{3+} and Ne^{4+} ions emitted from our Z-pinch plasma are below 1.3 MeV.

Based on the principle of Ross filter, a soft X ray spectrometer has been designed for measuring the time resolved neon K-shell and L-shell radiation from the small gas-puff Z-pinch device. The spectrometer consists of 10 PIN semiconductor detectors; each was covered with a filter. Therefore, five Ross filter pairs were matched. An X ray energy spectrum in the energy range of 0.4 keV to 1.4 keV for X ray photons was obtained. The energy spectrum was rather rough because the number of Ross filter pairs was too small, and it was quite difficult to get well matched Ross filter pairs in the sub-keV energy range.

A 500kV/400kA/100ns pulsed power generator (PPG-I) for X-pinch experiments was designed and constructed. It is based on an oil insulated 16-stages Marx generator, which stores 29 kJ at 75 kV operating voltage. After being erected, the Marx produces a 1.2 MV pulse to charge a combined 1.25 Ω PFL composed of four 5 Ω coaxial waterlines in parallel in

about 700 ns. A pressurized self-break V/N switch working in multichannel discharge mode connects the combined PFL to a matched 1.25 Ω transfer line. Capacitive voltage dividers and current wall monitor were located on different points of the lines to measure the voltage and current pulses. Extensive tests have been made to scale the output of the PPG-I when operating with an adjustable copper sulphate resistive load. From the calibrated monitors the load voltage and current of the PPG-I are respectively 460 kV and 380 kA with about 110 ns FWHM. The electrode system in road section of the generator was calculated and designed. In one of our concrete design for an applied pulse voltage of 100 ns in FWHM and 500 kV in amplitude, the calculated highest field on the surface was 113 kV/cm and the highest field in the vacuum was 298 kV/cm. Both of them are below the value of the surface flashover and breakdown voltage in vacuum, respectively.

ACKNOWLEDGEMENTS

The authors would like to sincerely thank V. Nikulin of the Lebedev Physics Institute and A. Dubrovsky of the Moscow Physical Society, the Russian Federation, for their help during the early stage of constructing the laser interferometer. The work was partially supported over the long period by the International Atomic Energy Agency under contract No. 12409 and the NSC of China under contract No. 19975029.

REFERENCES

[1] DU, J., OHADA, T., SHIMODA, K., HIRANO, K., Characterization of soft X ray Generated in Gas-puff Z-pinch, J Phys Society of Japan 64 (1995) 4185.
[2] ZOU, X.B., WANG, X.X., LUO, C.M., HAN, M., Measuring the Gas Flow from a Supersonic. Nozzle used in a 1.5-MA Gas Puff Z-pinch, IEEE Trans. on Plasma Sci. 30 (2002) 482.
[3] WANG, X.X., ZOU, X.B., LIU, Z., HAN, M., LUO, C.M., MA, R., A Three-Frame Mach-Zehnder. Interferometer for Measuring Dense Magnetized Plasmas, Rev Sci Instrum 74 (2003) 1328.
[4] GUO, X.M., LUO, C.M., Experimental Study of Energy Spectra of Ion Beam from Gas-Puff Z-pinch Plasma, J Phys D Appl Phys 29 (1996) 388.
[5] SCHNEIDER, R.F., LUO, C.M., RHEE, M.J., Resolution of the Thomson Spectrometer, J Appl. Phys. 57 (1985) 1.
[6] SPIELMAN, R.B., DEENEY, C., et al., Phys. Plasmas 5 (1998) 2105.
[7] DEENEY, C., DOUGLAS, M.R., et al., Phys. Rev. Lett. 81 (1998) 4883.
[8] SHELKOVENKO, T.A., PIKUZ, S.A, et al., Physics of Plasma 6 (1999) 2840.
[9] KALANTAR, D.H., Ph.D. thesis, Cornell University (1993).
[10] MITCHELL, I.H., BAYLEY, J.M., CHITTENDEN, J.P., et al., Rev. Sci. Instrum. 67 (1996) 1533.
[11] KALANTARA, D.H., HAMMER, D.A., Rev. Sci. Instrum. 66 (1995) 79.
[12] LIU, R., ZENG, N.G., WANG, X.X., et al., Proceedings of the 12th Asian Conference on Electrical Discharge, China, Nov. (2004) 678.
[13] RICHARD, J.A., “Pulse Power Folmulary”, North Star Research Corp., Albuquerque, NM, USA, (1991).
[14] RICHARD, J.A., http://northstar-research.com/PDF/Formweb1.pde, (2002).

DEVELOPMENT OF A LARGE BEAM FACILITY FOR THE APPLICATION OF HIGH POWER ION BEAMS

BYUNG-HOON OH
Korean Atomic Energy Research Institute
Nuclear Fusion Lab
Daejeon, Republic of Korea

Abstract

A large beam facility for the application of high power ion beams has been developed at the Korean Atomic Energy Research Institute (KAERI). The primary usage of this facility is to develop an 8 MW neutral beam heating system for a tokamak, but other applications using a large beam would also be possible in the near future. The facility is composed of a bucket ion source (100 kV, 55 A), related beam line components including a large vacuum chamber (3 m × 4 m × 5 m), power supplies for the ion source, control and DAS system (PXI based), beam diagnostics system (optical multichannel analyzer), and a water circulation system (2 MW) for cooling of the beam line components. The maximum beam parameters at present are a beam energy of 95 keV and a beam current of 36 A with the beam size of 13×45 cm^2. A maximum pulse length of 200 seconds can be achieved with a 1 MW beam power. The beam power with hydrogen ions will be increased up to 5.5 MW during 20 seconds.

1. INTRODUCTION

High power and/or large ion beams have a large potential for applications in various areas such as fusion energy generation, material sciences, surface physics, semiconductor processes, intensive heat flux engineering, and others. A large ion beam facility, which has been designed and constructed at the Korean Atomic Energy Research Institute to test the Neutral Beam Injection System for the KSTAR tokamak, could be applied to other areas with little additional efforts at any time.

The beam facility consists of an ion source, beam line components, power supplies, cooling circuits, control & DAS system, and beam diagnostics system. The ion source was designed to extract a 100 keV and 55 A deuterium beam with a rectangular beam size of 13×45 cm^2 at the exit grids. Beam divergence is less than 1°. Beam line components include a vacuum chamber, a neutralizer, a bending magnet, ion dumps, a calorimeter, and cryosorption pumps. They limit the beam size to less than 20×55 cm^2 at a distance of 5.2 m from the ion source. Depending on the experimental conditions a neutral beam can be made by filling hydrogen gas into the neutralizer and activating the bending magnet. In addition, cryopumps are necessary to minimize the number of re-ionized ions during beam transport, and to maintain a constant pressure at the ion source. An acceleration power supply, an arc power supply, a filament power supply, and a deceleration power supply deliver the required powers with proper timings for the ion source. Optical multichannel analyzer (OMA) system is used for measuring the beam divergence and ratio of the beam species (H^+:H_2^+:H_3^+), and an IR camera is used for measuring the beam profile and temperature distributions in the target.

Water flow rates and water temperatures at the points of the inlet and outlet of all the components are measured to calculate the dissipated energies within them. Also there are many thermocouples on every beam line component to measure the temperature profile on the target surface. PXI modules controlled by LabView acquire the data from the thermocouples and flow meters. The capacity of the cooling system is 2 MW during continuous operation. Figure 1 shows the schematic diagram of the layout of the vacuum components including the ion source. In the sections from two to five the fabricated system will be described, and in section 6 the experimental results will be described.

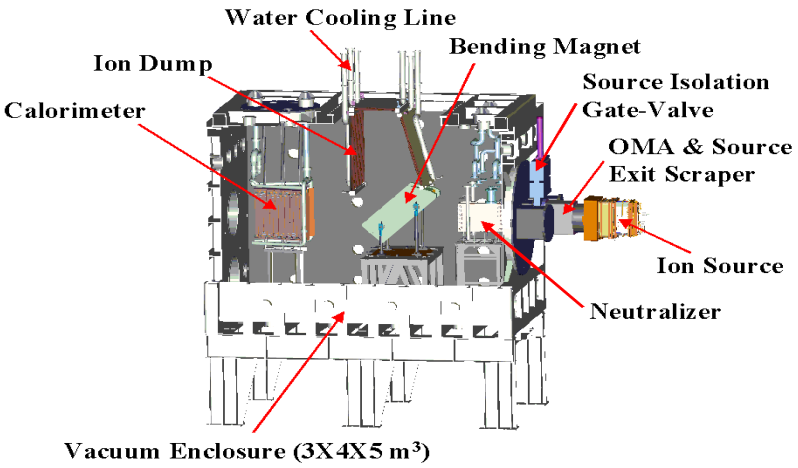

FIG. 1. Inner structure of the large beam facility system.

2. ION SOURCE

The ion source developed for the KSTAR Neutral Beam (NB) system is composed of a plasma generator and a beam accelerator. The type of plasma generator is a multi-cusp chamber where the arrangement of the magnets is set to form magnetic cusp fields to contain the plasma. The multi-cusp source is capable of producing large volumes of uniform, quiescent and high density plasmas with high gas and electrical efficiencies. The plasma chamber has a cross section of 26 cm × 64 cm and is 32 cm deep, and axial arrays of Sm-Co permanent magnets (4.65 kG ±2%) spaced between the cooling channels which are lined up on the wall to make the cusp field around the inner wall of the chamber. An array of 32 tungsten filaments (1.2 mm diameter) are used as cathodes. Three kinds of different filament shapes are used in order to obtain plasma uniformity throughout the chamber. The filaments are mounted on the water cooled filament assembly, which contains one positive and one negative filament plate. Precisely aligned four sets of circular aperture grids extract the high energy and high current ion beams from the plasma generator. The schematic drawing of the assembled ion source including the four accelerating copper grid modules is shown in Fig. 2. There are 692 circular apertures (7.2 mm diameter) on every set of grids. For the long pulse operation cooling channels (1.8 mm diameter) are precisely aligned between the aperture layers.

3. BEAM LINE COMPONENTS

All of the beam line components including the neutralizer, bending magnet, ion dumps, calorimeter, and cryosorption pumps are installed in the large vacuum chamber, whose size is 3 m × 4 m × 5 m, and being tested with the beam load. The chamber has 81 ports for installing beam-line components, vacuum pumps, and beam-diagnostic tools. A pressure of 9×10^{-7} Torr is normally obtained with a 5500 l/s TMP. An ion source and an OMA chamber, which are isolated from the main chamber by 630 mm diameter gate valves, are installed to the source ports.

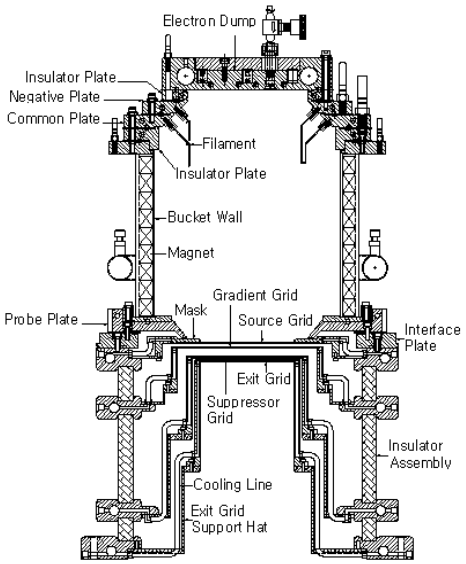

FIG. 2. Developed bucket ion source.

The bending magnet is designed to deflect the 120 keV deuterium beam 60° upward from the beam axis with a magnet current of 750 A. Low carbon steel (S10C) is used for the pole and yoke, and stainless steel is used for the case of the epoxy molded coil. Actively cooled pole-protection-plates, an electron dump and pre-magnet scrapers are prepared for the long pulse operation. The ion dump, located above the bending magnet, consists of three sets of plates which are made by swirl tubes as shown in Fig. 3. Pipes (inner diameter: 16 mm, thickness: 2 mm) made by 0.2 % Ag OFC (Oxygen Free Copper) and stainless steel swirl tape (thickness: 1 mm, twist ratio 2.0) are used in making the tube. The designed heat flux is 1 kW/cm^2. To measure the ratio of the ion species, each plate has its own calorimetric system in the cooling circuit. Hypervapotrons are used in calorimeter and neutralizer as a cooling unit. It is also designed to have sufficient thermal capability corresponding to the maximum heat load of 1 kW/cm^2 for the long pulse operation. The element is manufactured from a copper-chromium-zirconium alloy that is electron-beam welded. The calorimeter is made with a total of 32 beam stopping elements (hypervapotron unit; 112 mm × 1000 mm) arranged in two panels forming a *V* shape as shown in Fig. 4. The opening angle between the panels is 28°, and the effective aperture size is 430 mm × 1000 mm. It can handle 2-MW beam safely for the long pulse operation. 64 thermocouples are distributed on the calorimeter to measure the temperature of each element and the beam power profiles.

The cryopumping system consists of four cryosorption pumps, each of which is composed of a cryosorption pump body, a G-M helium refrigerator, and a 150 liter LN_2 bottle. The G-M refrigerator is installed upside down on the roof of the large vacuum chamber. The baffle and the lower thermal shield are put on the thermally insulated frame fixed to the chamber wall, and cooled by liquid nitrogen. The main components of the pump body of the cryosorption pump are an 80 K thermal shield and a 20 K cryosorption panel. The thermal shield is divided into upper/lower circular plates and a cylindrical baffle that allows gas molecules to pass through and to be adsorbed on the cryopanel. The baffle consists of 50 chevron blades of 120° bending angle. The blades are placed regularly at 7.2°, and form as a whole a cylinder of 550 mm O.D, 356 mm I.D, and 1000 mm L. The cryopanel consists of 4 identical AC (Activated Carbon)-coated rectangular plates of 145 mm×1000 mm, are brazed to a center rod along the long side at intervals of 90°.

The surface density of the AC layer is about 500 g/m^2. All the adsorbing surfaces of the cryopanel look directly at the baffle in contrast with the case of a commercial unit. Therefore, most gas molecules transmitted by the baffle can reach the surface of the cryopanel without additional reflections, and a maximum hydrogen pumping speed can be obtained. Figure 5 shows the temperature variation of the cryopanel when cooling the baffle, and operating the refrigerator. The ultimate temperature is about 18 K, which is attained about six hours after the start of cooling. Liquid nitrogen of 150 liter is consumed to cool down the baffle to 80 K in three hours and to keep the temperature for two hours, and another 150 liter is used to maintain the cooling stage for six hours. This means that it is possible to carry out the beam extraction experiment for at least five hours under the full pumping speed of the cryosorption pump with a consumption of liquid nitrogen of 300 liter. The pumping speed of the cryosorption pump is shown in Fig. 6 as a function of the cryopanel temperature. The cryosorption pump starts to show its pumping capability for hydrogen gas at a temperature around 60 K. The pumping speed is steeply increased at a temperature below 50 K and reaches the ultimate level of about 90,000 L/s at below 20 K. The sticking coefficient is calculated by comparing the measurement and Monte Carlo simulation to be about 0.6–5, when assuming T_{gas}=240 K.

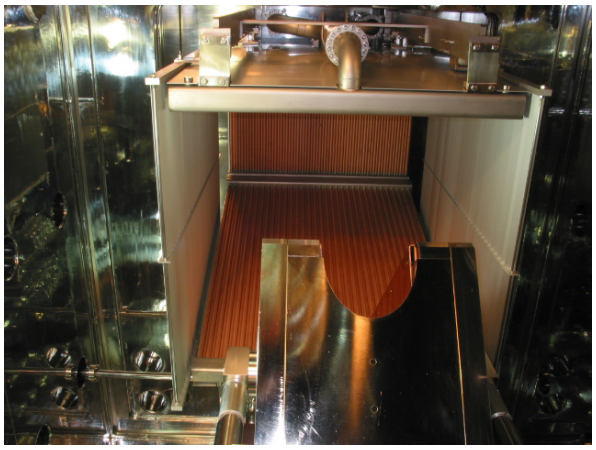

FIG. 3. Ion dumps made by swirl tubes.

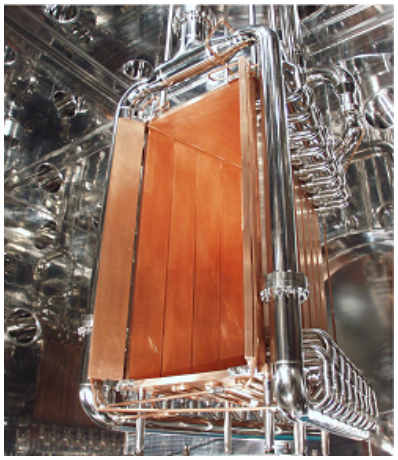

FIG. 4. Calorimeter target made by Hypervapotrons.

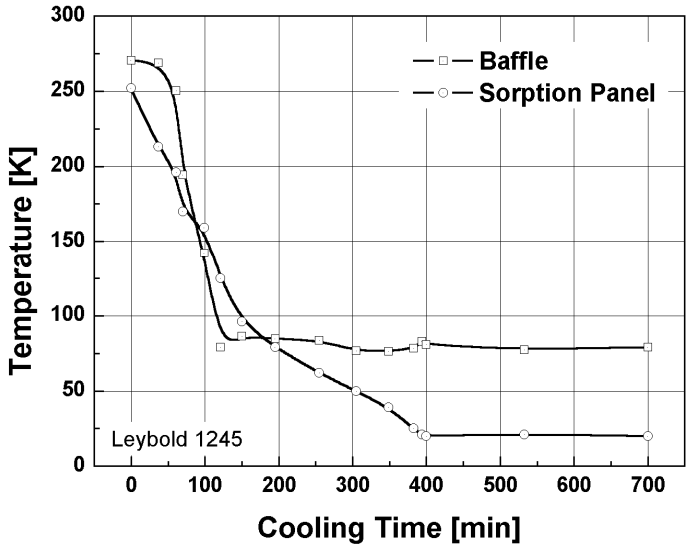

FIG. 5. Variations of panel temperatures with time.

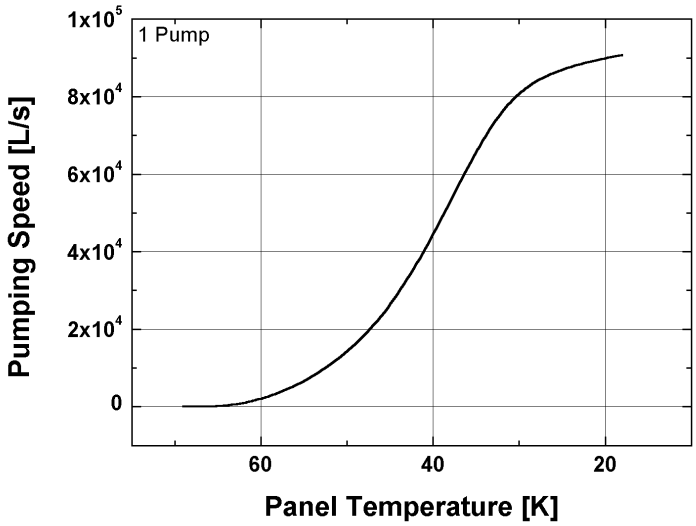

FIG. 6. Pumping speeds of the cryosorption pump for H_2 depending on panel temperature.

4. POWER SUPPLIES

The power system for the beam facility consists of an acceleration power supply, a deceleration power supply, a gradient grid potential divider, an arc power supply, a filament power supply, and a snubber bias power supply. Among these, arc, filament and snubber bias power supplies are on the high voltage deck floated at the accelerating potential, and powered via isolation transformer. Figure 7 shows the principal interconnections for the power supplies and how these are connected to the grids and the arc plasma chamber of the ion source. The ratings of the power supplies are summarized in Table 1.

The acceleration power supply powered from a 22.9 kV 3-phase AC line is made of six units of modular high voltage DC sources among which five units are of 22 kV fixed (HVTR) and last one is of variable from 0 to 32 kV with 40 differential steps of 800V each (LVTR),

and valve (HVS)/crowbar switches as shown in Fig. 8. The DC link high voltage is set by the active number of fixed high voltage unit of 22 kV and 40 switching power modules. The ions are extracted from the source by an accelerating structure where the electric field is very high (~10 kV/mm): an efficient design requires that the working voltage is near to the breakdown value. Therefore, breakdown can occur often during beam extraction and must be considered not as a fault but as part of the normal operation of the beam facility. To avoid the degradation of high voltage holding capability, it is very important to interrupt the power promptly and suppress the breakdown surge into the accelerating structure of the ion source for every breakdown. A high voltage valve switch made of MOSFET units is employed to meet the fast switching feature and turn the rated power off within 2μs. The impact of surge due to the energy stored in the stray capacitance between HVS and ion source is suppressed by a snubber circuit implemented by amorphous core. As a result, the breakdown surge is finally suppressed to a peak current of less than 1kA within 1μs at the rated accelerating voltage of 120 kV.

The oil cooled high power resistive divider of 24 kΩ and 5A at the rated voltage of 120 kV (600 kW) has 18 taps and provides a potential to the gradient grid of the ion source appropriate to beam optics in 18 steps at the range from 90% to 64% with a differential step of 1.5 % of the accelerating voltage. The deceleration power supply is equipped to the voltage of -5 kV and the current of up to 20 A for the decereration grid of the ion source to block the backstreaming electrons from the neutralizer and is synchronized with the accelerating voltage pulse. The operation sequence and timing of all the power supplies are managed by a central timing/interrupt controller so as to initiate the beam by arc discharge plasma with the correct synchronization.

TABLE 1. RATINGS OF THE POWER SUPPLIES FOR THE LARGE BEAM FACILITY

	Voltage	Current	Pulse length	Duty Factor
Acceleration P.S.				
• 1st Grid	0 ~ 120 kV	70A	300sec	1/6
• 2nd Grid	0 ~ 105 kV	5A	300sec	1/6
Deceleration Grid P.S.	- (0 ~ 5) kV	20A	300sec	1/6
Arc P.S.	0 ~160 V	1200A	300sec	1/6
Filament P.S.	0 ~ 15 V	3200A	320sec	1/6
Snubber Bias P.S.	0 ~ 100 V	100A	CW	1/1

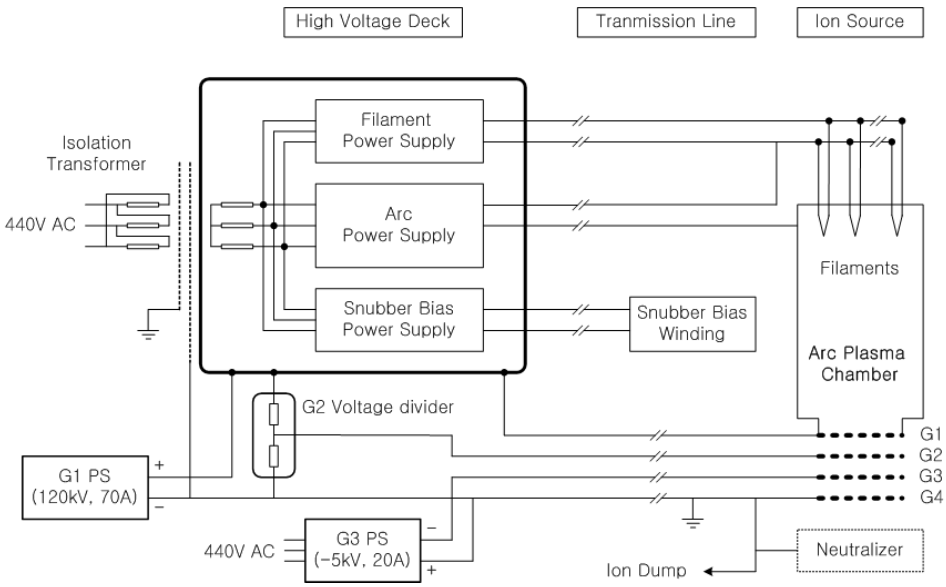

FIG. 7. Basic interconnection diagram for the power supplies.

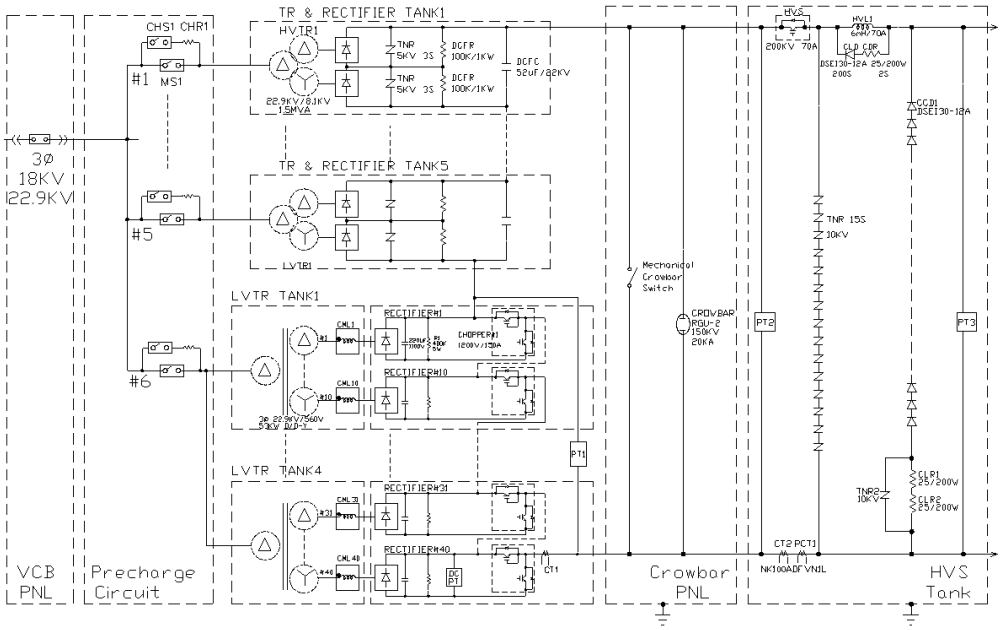

FIG. 8. Schematic circuit diagram of the acceleration power supply.

5. OTHER SYSTEMS

The machine control and DAS system consist of two PCs. One for a power supply control including a timing, and the other for a data acquisitions. Labview and PXI modules are used in the system, providing 20 channels with fast sampling (10 kHz), and 206 thermocouple channels with slow sampling (10 Hz). An optical multichannel analyzer system is employed to measure the divergence and the ion species present in the beam. The focal length of the Czerni-Turner type spectrometer is 75 cm with a 2400 gr/mm grating.

The calorimeter is used for measuring the beam profiles of the ion source on the target. IR cameras can also be used for measuring the beam profile on calorimeter or ion dumps.

Small water leakage into the vacuum chamber can be detected by using a residual gas analyzer system. A CW 2-MW cooling water system has been prepared for cooling the beam-line components. The cooling system has a water flow rate capability of 100 l/sec with a pressure of 5 kgf/cm^2. The water quality is controlled by chemical treatment to maintain the resistivity within 1 Mohm-cm.

6. EXPERIMENTAL RESULTS

The most critical component for the long pulse operation is the ion source. A JT-60 positive ion source and a KSTAR prototype ion source have been used in estimating long pulse effects. Figure 9 shows the longest beam results which had been made by the JT-60 ion source in the KSTAR NB test stand. An hydrogen beam of 1 MW was obtained during 200 seconds in the test. Two sets of cryosorption pumps were used in maintaining a constant pressure in the NB chamber. Most of the heat load is imparted to the calorimeter which is made by Hypervaportron plates. The water temperature of the calorimeter was saturated at 14° C after 6 seconds of the beam-on with the target temperature of 175 °C. During the long pulse operation the maximum heat load on the hypervapotron component, which are used in the most of the prototype beam line components, was estimated as 0.3 kW/cm^2. It should be tested more up to 1 kW/cm^2 to be used in the 8 MW long pulse KSTAR beam line system. The gradual increase of the current into the gradient grid of the ion source accelerator after 125 seconds, as shown in Fig. 4, is thought to be caused by a long pulse effects. The reasons for the beam-optics change with time should be identified with the help of calorimetric system of the grids of the ion source during a long pulse operation.

An experimental set up for a beam extraction with the KSTAR prototype ion source was built. Power supplies, passive snubbers to protect the ion source, Langmuir probes, filaments, electrodes for a plasma discharge, and beam extraction grids constitute an ion source circuit for plasma generation and beam extraction (see Fig. 10). The hydrogen gas is injected into the ion source by two gas feed lines at the top of the ion source. The maximum beam energy, which has been tested in the system, is 100 keV with a beam current of 24 A for a duration of three seconds. The time and current limits of the beam with the prototype ion source at present are from the ion source and power supply system. A hydrogen beam of 1.8 MW with an energy of 80 keV was created, and loaded onto the system during seven seconds. Beam power deposition in the prototype system along the beam lines has been measured by a water calorimetric system, which is composed of water flow meters, thermocouples, and noise filtered DAS modules. The power transmission rates of an accelerator and the beam line components are summarized in Table 2. 95.5 % of the total beam power was measured by the water calorimetric system. The cooling water temperatures of the beam line components were saturated within six seconds, but the temperature of the grids of the ion source were not saturated even after 20 sec because of a lower water pressure than the designed value. The water pressures will be increased in the next experiments.

The simulation results of a beam power transmission are also included in the table, where one degree divergence was assumed. Comparing measured and calculated results indicates that the beam divergence of the ion source is approximately 1°. Also the calorimetric data of the three ion dumps provided the ratio of the beam species of the beam. The maximum heat load on the swirl tubes, which are used in the ion dumps as a cooling unit, was estimated as 0.4 kW/cm^2 because of the focusing effects on the first beam dump. It should be tested more up to 1.5 kW/cm^2 to be used in the 8 MW long pulse KSTAR beam line system.

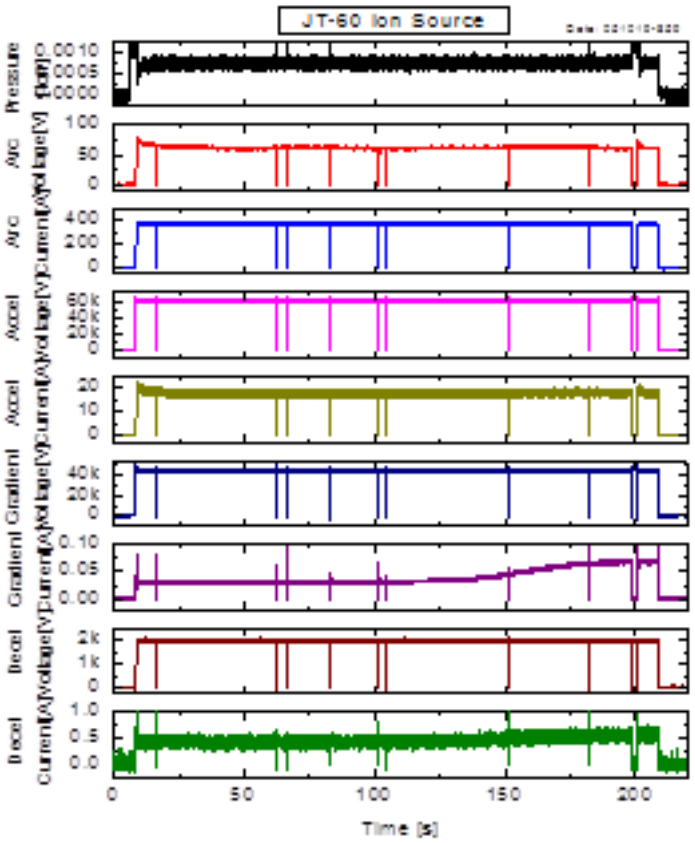

FIG. 9. Beam extraction results with JT-60 ion source (60 keV, 18 A, 200 sec) beam)

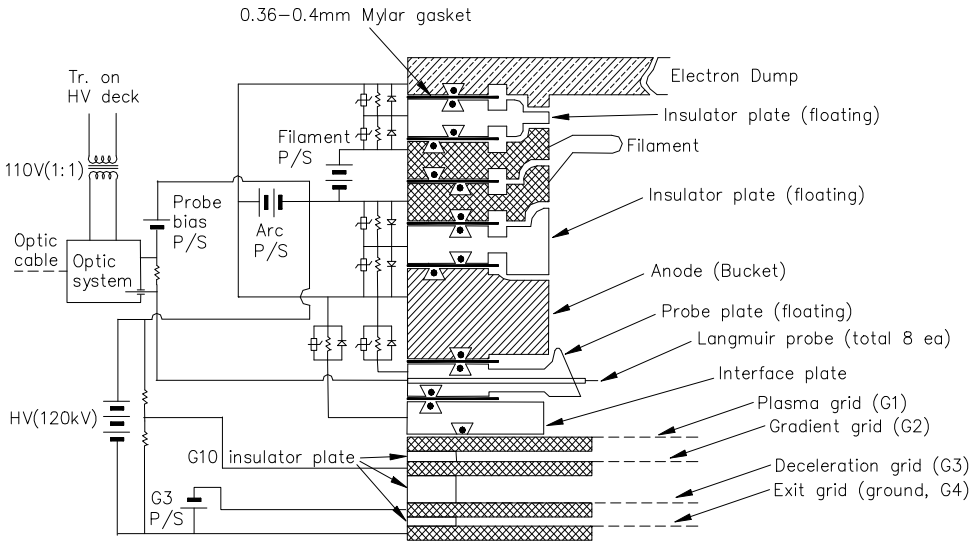

FIG. 10. Schematic circuit diagram for a beam extraction of the ion source

TABLE 2. BEAM POWER DEPOSITIONS ON THE BEAM LINE COMPONENTS

Test-Stand Component	Power Loading (%)	Calculated Loading (%)
Plasma Grid (Up, Down)	0.4, 0.35	
Gradient Grid (Up, Down)	0.2, 0.18	
Suppressor Grid (Up, Down)	0.01, 0.01	
Exit Grid (Up, Down)	0.09, 0.11	
OMA Duct 1(R-D), 2(L-U)	3.01, 3.18	7.4
Neutralizer	7.66	4.1
BM Scraper & wall	1.81	0.58
Ion Dump (full-energy)	40.28	50.5
Ion Dump (half-energy)	2.67	1.6
Ion Dump (third-energy)	5.25	2.4
Calorimeter	30.29	30.8
TOTAL	95.5	97.4

7. CONCLUSION

A large beam system has been developed and tested. Presently, the system has produced a 100 keV/24 A beam for three seconds, 95 keV/36 A beam for four seconds, and a 60 keV/18 A beam for 200 seconds. The test and upgrade with the developed prototype system will be continued for long pulse operation. In addition, high heat flux experiments and large beam applications could be conducted in the near future.

REFERENCES

[1] HEINER RYSSEL AND INGOLF RUGE, Ion Implantation (John Wiley & Sons, New York, 1977.

[2] The KSTAR Team "The KSTAR Project: Advanced Steady-State Superconducting Tokamak Experiment" in IAEA-F1-CN-69/FT1/1, 17th IAEA Fusion Energy Conference (1998), Yokohama, Japan.

[3] OH, B. H., KIM, K. R., and CHOI, B. H., Rev. Sci. Instrum. 71, (2000) 1140–1143.

[4] IN, S.R., and PARK, M.Y., J. Kor. Vac. Sci. Technol. 5, (2002) 25–32.

[5] WELCH, K.M., Capture Pumping Technology (Pergamon, 1991) 308.

[6] OH, B.H., LEE, K.W., JEONG, S.H., SONG, I.H., SHIN, H.S., CHOI, C.H., Development of an Acceleration Power Supply for the KSTAR Tokamak, 3rd IAEA Technical Committee Meeting on Steady-State Operation of Magnetic Fusion Devices (2002), Greifswald, Germany.

[7] KURIYAMA, M. et al, Fusion Science and Technology 42 (2002) 424–434.

INFLUENCE OF POWERFUL PULSE BEAMS PRODUCED BY DENSE PLASMA FOCUS DEVICES UPON CONDENSED MATERIALS FOR MODIFICATION OF THEIR PROPERTIES AND FOR DEVELOPMENT OF NEW TECHNOLOGIES OF PULSE TREATMENT OF MATERIALS

V. PIMENOV
Effect of Irradiation on Metals Laboratory
A.A. Baikov Institute of Metallurgy and Material Science RAS
Moscow, Russian Federation

Abstract

The plasma focus devices PF-1000, PF-60, and PF-6 with different gases and different irradiation modes were used to carry out experimental investigations of interactions between pulsed ion and high-temperature plasma beams and several materials to be applied in structural and functional components of thermonuclear fusion devices with magnetic and inertial plasma confinement, as well as for working chambers of plasma devices. On the basis of the investigations carried out, significant progress was achieved in understanding the mechanisms of the interaction of high-energy nano- and microsecond pulsed beams upon irradiated materials. Particularly under the different power densities typical of three regimes of the fluence of ion and plasma beam upon the target material disposed in the cathode part of PF device were found: (i) "implantation" ($q \approx 10^5$–10^7 W/cm^2); (ii) screening of the surface by a secondary plasma cloud ($q \approx 10^7$–10^8 W/cm^2); (iii) absence of implantation ("explosive rupture") ($q \approx 10^8$–10^{10} W/cm^2). It was found that the ion and plasma beams in the dense plasma focus devices can be separated temporary and make different energy contribution to the material damage. In this case, the redistribution of the elements in the surface layer of austenitic chromium-manganese steels was found. A remarkable increase of Mn content and a reduction of Fe content took place near the blister-like bubbles formed on the irradiated surface. The interaction of the pulsed deuterium plasmas and ion beams with the material of an axially oriented tube-like target of the PF-1000 device chamber was studied. Two cases were investigated: with the use of a special protective screen and without it. In both cases the phase transformation and structure change resulted in hardening and strengthening of the surface layers. These results demonstrated the application possibility of DPF devices to modify the surface layer in difficult to reach areas of treated parts, such as internal surfaces of elongated tubes. Important results were obtained on deuterium ions and dense plasma beams interaction with ferritic steels and tungsten, the latter was produced by the powder metallurgy method. It was found that damages of the surface layer of ferritic steels (10Cr9WV and Eurofer97 types) under realized conditions were markedly lower compared to those in austenitic steels. Phase compositions of ferritic steels remained steady under the pulsed action of high power density (up to 10^{10} W/cm^2) and pulse durations up to 1 μs. The surface layer of tungsten after a 10-fold action of pulsed irradiation under hard conditions ($q \approx 10^{10}$ W/cm^2, $\tau \approx 1$ μs) was strongly damaged. Elongated surface cracks and significant erosion of the material were observed: the mean thickness of the layer evaporated per single pulse was 2 μm. Taking into account the fact that ferritic-martensitic steels and tungsten are the basic structural materials for the first wall and the divertor plate in ITER, the results obtained are useful for preliminary estimation of the prospects for applying these materials in future thermonuclear fusion devices with magnetic and inertial plasma confinement. Prospects for using DPF devices to solve scientific and applied problems in material science such as material damage, ion implantation and modification of the surface layers were given. It was also shown that the DPF devices are capable of simulating conditions of material damage by high temperature plasma close to plasma disruption at ITER. We think that this approach, based on the DPF device application, is very promising to simulate the thermal influence under plasma disruption at ITER as well as the explosive action of pulsed high-energy beams upon the materials in reactors with inertial confinement of plasma. It is proposed that this approach may be useful for preliminary tests of materials for structural elements of ITER working under pulsed high-energy actions. DPF devices were found to be useful for preliminary treatments of materials with pulsed ion and plasma beams to improve mechanical properties and corrosion resistance of the surface layers and to enhance radiation resistance during their operation in thermonuclear and plasma facilities. The results obtained also point to the advisability of using DPF devices in developing new pulse technologies for material treatment with the use of power nanosecond and microsecond pulses.

PART 1. INTERACTION OF HIGH TEMPERATURE PLASMA AND FAST ION BEAMS WITH MATERIALS IN DENSE PLASMA FOCUS DEVICE

1.1. INTRODUCTION

Dense plasma focus (DPF) devices, by comparison with other thermonuclear devices, have a number of important advantages.

- They provide an opportunity to expose materials to pulsed beams of various types (ion, electron, plasma, X ray, neutron and shock wave) of high-power flux density (up to 10^{14} W/cm^2) with pulse duration in the range from 10^{-8} to 10^{-6} s.
- They provide the opportunity to vary the distribution of pulse energy between ion and plasma beams: energy flux density of ion and plasma beams may be significantly different depending on the mode of irradiation.
- These beams in DPF devices can be separated in time due to their different velocity (approximately one order of magnitude) of ion beam and plasma jet. The problem of plasma-surface interaction is especially amenable to the study of damage to materials under high-power energy pulses generated in different radiation devices including DPF devices, chambers for inertial (laser and heavy ion fusion) and magnetic (TOKAMAK and stellarator) confinement thermonuclear fusion.

During the last few years we have performed investigations on material damage under pulsed ion and high temperature plasma (HTP) beams in different PF devices in the frame of national and international scientific programmes. The obtained results show that the influence of pulsed high energy ($E_i \geq 100$keV) ion beams and HTP (particle velocity ~ 5×10^7 cm/s) on the target material results in a remarkable distinction in radiation and thermal effects in dependence of irradiation conditions. The features of physical and chemical processes, structure-phase transformations and elements distributions in irradiated materials are also different. These factors lead to different material damage and changes to their properties and chemical content.

The present paper deals with the most interesting results obtained within these investigations on the basis of international cooperation (particularly in the frame of INCO COPERNICUS research contract IC-15-CT98-0811 and the project of the International Atomic Energy Agency "Dense Magnetized Plasma"). Most of most significant results have been published previously in our papers [1–17]. In addition, the data of new experiments and investigations, which were carried out recently, are presented. On the basis of the analysis and generalization of obtained results, the estimation of the prospects of PF device application for scientific and applied problems of radiation material science is made.

1.2. Aims of the project

The main aims of the project were:

- Modes of the DPF operation with a low power flux density, which would be favourable for the implantation of deuterium ions into the material to form an implanted near surface layer, and to determine, in contrast, to find regimes that would make the above mentioned process difficult;
- To study some results of a simultaneous interaction of dense plasma streams and fast ion beams having a medium power flux density ("detachment regime") with special ferro-alloys;
- To investigate some characteristics of the specimen irradiated by high power flux density streams in the regimes of intensive surface melting and evaporation ("broken implantation regime", which has been found in the course of the experiments);
- To investigate the influence of powerful pulsed ion beams and HTP, generated in DPF, on physical and chemical processes, structure and phase transformations, damage of the surface layers, elemental distributions in irradiated materials;

- To estimate the possibilities of modifying the surface layers (SL) of irradiated materials (particularly in parts difficult for access), by pulsed beams of HTP to improve the properties of materials (mechanical, radiation, corrosion et al.);
- To estimate the prospects of applying plasma focus devices for simulating of heat load and damage of materials in the thermonuclear fusion reactor with magnetic and inertial confirmation of the plasma at extremal regimes of disruption type;
- To estimate the prospects using the plasma focus devices for solving scientific and applied problems of radiation material science.

Systematic investigations of the features influencing dense plasma streams, ion and electron beams and shockwave loads generated in DPF devices on a wide range of materials, applied for heat loaded parts in different devices was carried out for the first time.

1.3. Materials

The following materials were chosen for the experiments: austenitic chromium-manganese and ferritic steels, pure vanadium, tungsten, graphite, copper, aluminum and their alloys [7–14]. These metals have a great potential to be applied in structural and functional components of thermonuclear fusion devices with magnetic [18] and inertial [19] plasma confinement, as well as for working chambers of plasma devices [20]. As plasma facing elements, these materials have tested for its durability and various mechanical characteristics under pulsed power irradiation by plasma streams and fast ion beams. Various kinds of stainless steel steels were examined as construction materials for use in different radiation devices including high current pinch facilities, chambers for inertial (laser and heavy ion fusion) and magnetic (TOKAMAK and stellarator) confinement thermonuclear fusion. In this project low activation austenitic and ferritic steels were of major interest because they do not give long lived isotopes during neutron irradiation [6, 21–25]. All the above mentioned materials are corrosion resistant and exhibit good mechanical properties.

1.4. Experiment

The experiments were carried out by using two different types of DPF devices: PF-60, which has a Filippov-type (plane) electrode geometry [9, 20] with deuterium as working gas (initial pressure of about 40 Pa); PF-1000 (see Fig. 5) and PF-6, which have a Mather-type (cylindrical) electrode geometry [1–3, 7, 10–14, 26] with deuterium or hydrogen as working gases (~ 400 Pa). Samples of materials were positioned at the cathode part of the devices. In the experiments we used for the irradiation plasma jets and beams of fast ions in a broad range of power flux densities. Influence of other types of radiation was negligible in these experiments. Pulsed irradiation of specimens was performed in different regimes: by microsecond high temperature plasma pulses with power flux density $q = 10^7$–10^9 W/cm^2 (PF-1000, PF-6), and by 100-nanosecond deuterium plasma (DP) pulses with $q = 10^5$–10^{10} W/cm^2 (PF-60). In each shot in the PF-60 device a specimen was irradiated with a powerful high energy ion pulse ($E_i \geq 100$ keV) and then, about 1 microsecond later, with the plasma jet. The energies of these two streams were approximately the same. In the case of the PF-1000 device ion and plasma beams in some experiments were separated in time and made a different energy contribution to the target material damage [10–12]. As was shown in [12], the fast ion beam, having a very low energy content ($q < 1$ W/cm^2), hit the target about 6–8 μs earlier than the plasma jet, whereas the latter contributed the main part of the energy to the surface damage.

1.5. Analysis methods

The irradiated samples were investigated by optical and scanning electron microscopy (SEM), X ray diffraction analysis (XRD), X ray spectral analysis and atomic force microscopy (AFM). The recoil nuclei method (elastic recoil detection analysis — ERDA [22, 26]) was used to trace the deuterium atoms scattering profile within the irradiated specimens. In this method the He+ ion beam of the energy 1.9 MeV irradiated test sample at an angle of 15° to its surface. The recoil deuterons were registered at an angle of 30° to the incident beam direction. The method provides the integral characteristics of the deuterium concentration profile on the part of the surface investigated.

The thickness of the layer evaporated during the sample irradiation was determined by means of weighing specimens before and after irradiation taking into account the irradiated area and density of the material.

1.6. Ion implantation

Under different power densities, three typical regimes of the influence of ion and plasma beam upon the target material were found [5].

(1) It was shown, that in the absence of the fast ion beam and at an irradiation power flux density of about 10^5–10^7 W/cm^2, the ”implantation mode” was realised. High concentration (more than 12 at%) of deuterium in the target can be reached (see Fig. 1). The implanted ion concentration increases with the number of pulses. Concentration distribution is governed by the diffusion process. It was also shown, that in this regime of irradiation ($q \sim 10^6$ W/cm^2, pulse duration $\tau \sim 1\mu$s) surface layers of all tested materials were malting.

(2) If the irradiation power flux density was increased to 10^7–10^8 W/cm^2, the “detachment effect” rules the interaction process. The cloud of the plasma in front of the specimen’s surface is produced mainly by the beam of fast ions, which penetrates the material surface up to the order of the ion projective range (~ 0.5 μm) and evaporates it. The plasma of the jet and of its shock wave with low energy ions cannot reach the specimen’s surface resulting in the formation of a very thin surface implantation layer of deuterium. At the medium power flux density $q = 10^7$–10^8 W/cm^2 (Fig. 2), we have also rather a high concentration of deuterium, but at the surface of the specimen (to only 30 nm).

(3) It has been found that when the power flux density increases up to 10^9–10^{10} W/cm^2 the so-called broken implantation (“explosive rupture” implantation) is observed. At this regime, a surface layer implanted by one irradiation pulse of about 100 keV deuterons appears to be completely evaporated, while the concentration of the implanted low energy deuterons ($E_i \sim 1$ keV) in the specimen decreases with the number of irradiation pulses (Fig. 3). This last feature finds its explanation on the basis of the successive diffusion enhancement due to the evolution of the topographical structure of the irradiated surface and because of the influence of the shock wave, generated inside the bulk of the material due to its ablation [5].

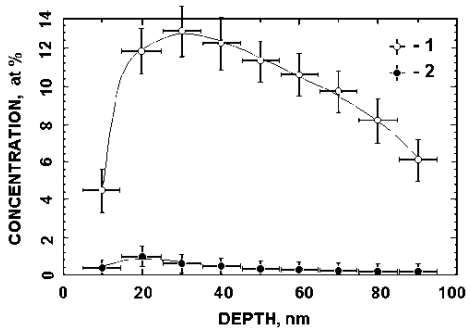

FIG. 1. Deuterium concentration distribution in the surface layer of austenitic chromium-manganese 25Cr12Mn20W steel after irradiation by 120 low power flux density plasma pulses:(1) in the centre of irradiated region, (2) point closed to the border of irradiated region (q = 105–107 W/cm2).

These results show the problem which exists in technological application of PF device for implantation of working gas ions into material. It is connected with the melting of the surface layer of most materials under heat load $q \geq 10^6$ W/cm^2 and pulse duration $\tau \approx 0.1–1$ μs. To avoid this effect the power density q should be in the range of $10^3–10^6$ W/cm^2 depending on the melt temperature of the material. However, in this case the time required for the formation of a uniformly implanted layer of sufficient thickness may be rather long. The solution to this problem may be connected with the use of high frequency (~10 Hz) PF devices with low energy (≤ 10 kJ).

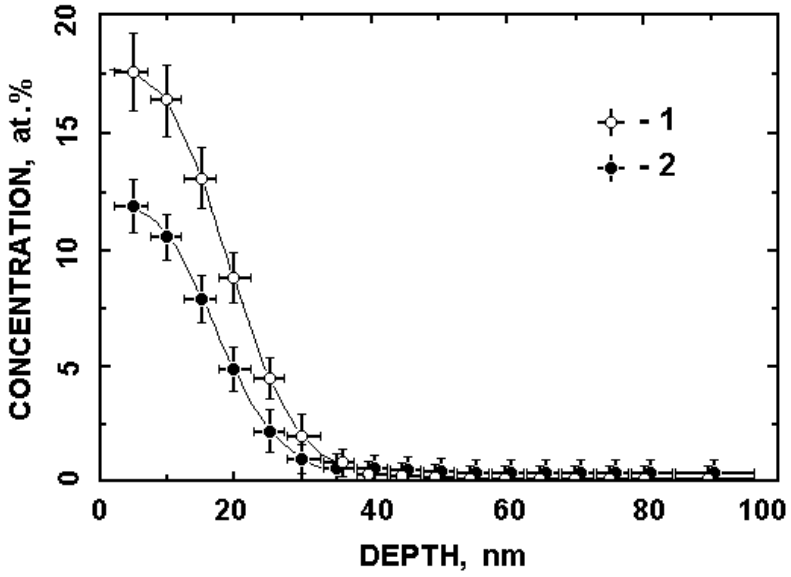

FIG. 2. Deuterium concentration distribution in the surface layer of ferritic 10Cr9W steel after irradiation with 5 medium power flux density pulses of plasma jet and beam of fast ions:(1) in the centre of irradiated region, (2) in the periphery of irradiated region ($q = 10^7–10^8$ W/cm^2).

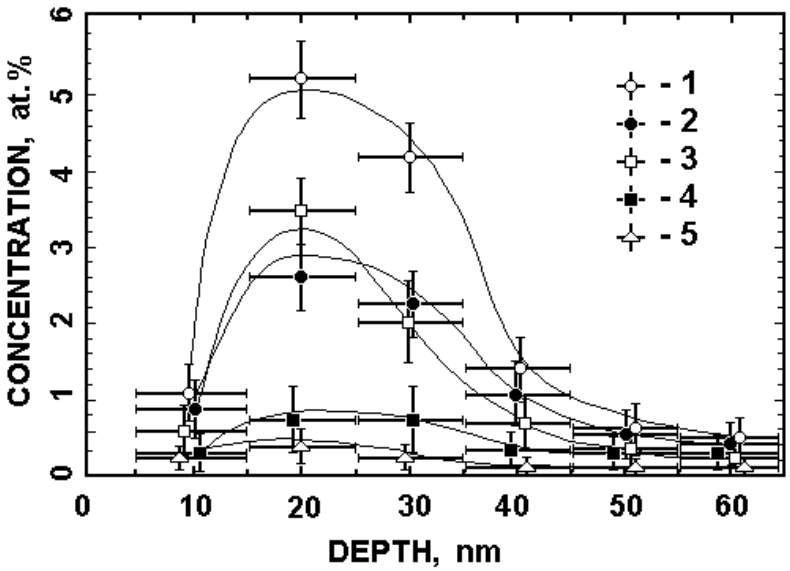

FIG. 3. Deuterium concentration distribution in the surface layer of austenitic chromium-manganese 25Cr12Mn20W steel after multi-fold irradiation with pulses of high power flux density plasma jet and fast ion beam: (1) 1 pulse, (2) 2 pulses, (3) 4 pulses, (4) 8 pulses, (5) 16 pulses ($q = 10^9 – 10^{10}$ W/cm^2).

1.7. Surface damage

The irradiated samples have revealed that the implantation of high-energy hydrogen ions to the sample material took place. The strongly displayed phenomena of melting, evaporation, and sputtering of the surface layer have been registered. The flowing surface of the irradiated materials had often a wavy nature and included craters, blisters, and micro-cracks. Nevertheless, some irradiated samples retained the appearance of a plane surface. On the whole, the damage character as well as the type of modification of topographic surface structure of the tested materials has some distinctive properties.

The micrographs taken by SEM of the primary and irradiated surfaces of the 25CrMn20W steel specimens are presented in Fig. 4. It is seen that the surface irradiated with 3 pulses contains an ample quantity of relatively deep craters of diameters d up to 10 μm, small bubbles ($d \leq 1$ μm), and also micro-craters. It should be emphasized that the majority of the craters is situated on the convex part (crests) of the surface. It is noticeable that the10Cr12Mn20W steel surface has different damage character than the other specimens. It shows a substantial number of relatively large bubbles ($d \leq 10$ μm) and a small number of craters (Fig. 5).

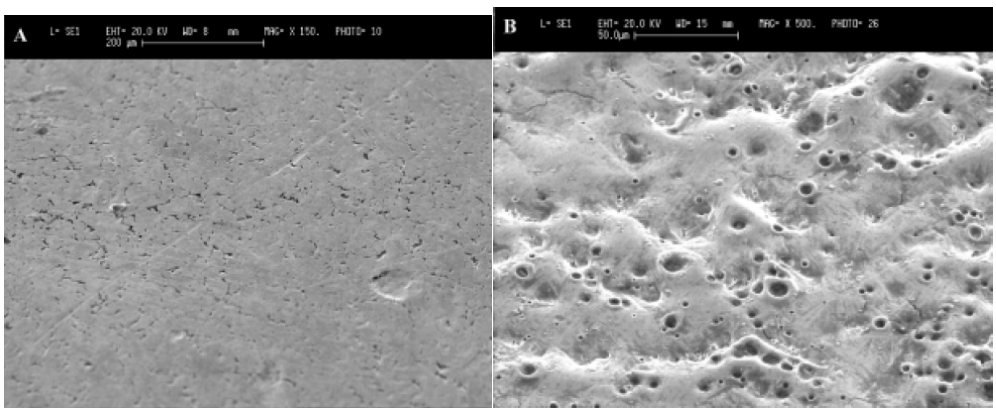

FIG. 4 SEM micrographs of the part of 25Cr12Mn20W steel sample surface. (A) initial state; (B) after 3 pulses of the hydrogen plasma. Wavy nature of the surface containing craters, small bubbles and micro-cracks is visible.

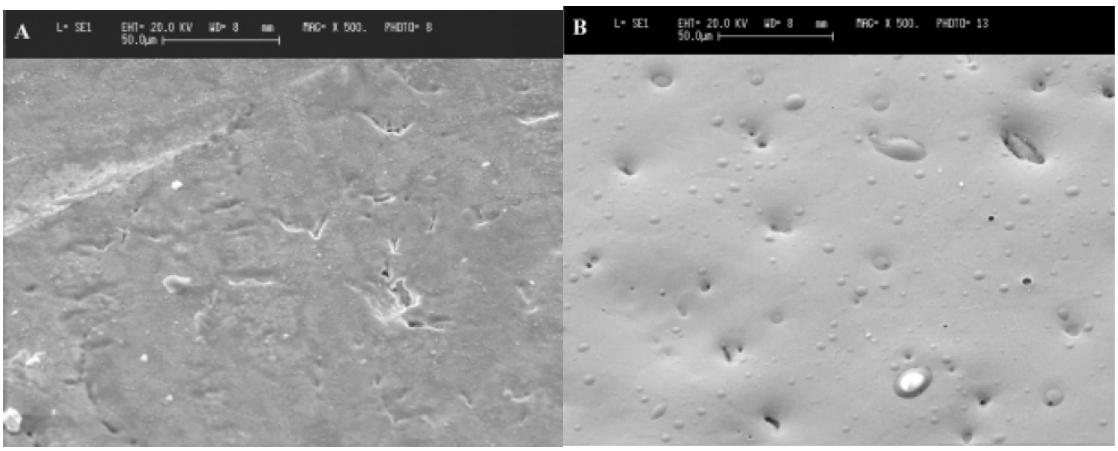

FIG. 5. The SEM micrographs of the part of 10Cr12Mn20W steel sample surface. (a) initial state; (b) after eight pulses of the hydrogen plasma actions. Wavy nature of the surface containing multitude bubbles and some craters are visible.

1.8. Redistribution of elements

As was noted above, the PF-1000 device allows realizing the special regime of irradiation: the ion and plasma components of the energy pulse are separated temporary and make different energy contribution to the material damage.

In the works [10–12], the austenitic chromium-manganese 25Cr12Mn20W and 10Cr12Mn20W steels were irradiated in the described regime. The distribution of the elements before and after irradiation was analyzed qualitatively. The distributions of Fe, Mn and Cr in the initial state of the steel specimens were uniform. But after three pulses of irradiation a redistribution of the components on the surface of 10Cr12Mn20W steel was observed (see Fig. 6). In areas where radiation defects blisters-type (bubbles) occurred, a remarkable increase of the Mn content and a reduction of the Fe content took place. After six pulses this effect remained but was less evident. Where radiation induced craters (in both types of austenitic steels), a significant increase (~ 3–5 times as much [10, 11]) of the carbon and the oxygen content was observed.

We hypothesize [10–12] that implanted hydrogen ions have created vacancy clusters [27, 28]. This cluster appears to act as a nucleus of gas phase (micropore) and hence a sink for atoms of the light elements. Under the subsequent (6–8 microseconds later) heating by the plasma jet Mn, as well as compounds of light elements (CH_4, CO, CO_2), may be collected in these micropores, with the formation and growth of gas bubbles. After crystallization and cooling these bubbles (blisters) burst with the formation of craters or are trapped in the solid state. Manganese from the retained gas phase, as well as compounds of carbon with hydrogen and oxygen condensed onto the inner surface of the bubbles. That is the reason for an increase of manganese, as well as carbon and oxygen content in the vicinity of blisters and craters was observed on the surface of the irradiated steels. These results show new possibilities of application of DPF devices for ion-plasma treatment of materials and creation of modified surface layers with new properties.

1.9. Simulation of material damage under plasma disruptions in thermonuclear fusion reactor

In the work we proposed a new experimental technique using DPF devices where irradiation conditions in cathode part of PF chamber would be similar to plasma disruption

regime in the thermonuclear fusion reactor with magnetic confinement of the plasma. In accordance with this technique the tested specimen is an elongated cylindrical tube (parameters of the tube presented in section "Test specimen"). Irradiation conditions for this case are presented in the Table 1. As can be seen from the Table the time of interaction between a DP pulse and the tube surface increased by a factor of two, while the value of q decreased approximately by a factor of 5 when the distance $L(A)$ increased from 20 to 36 cm. At the same time the thickness of the melted surface layer d decreased about 3.5 times. Besides, it is evident that application of a protective screen provided a decrease of q by approximately 2 to 3 orders of magnitude in comparison with the value of $q = 10^9$ W/cm^2 for the screen surface (no protection).The data concerning the plasma disruption in ITER reactor and interaction conditions of the pulsed deuterium plasma with the tube material in our experiment (Table 2) are presented. Damage factor $F = q\tau^{1/2}$ in the Table 2 is a parameter which allows comparing a surface damage under different irradiation conditions. From the table it is seen that the damage factor of the material in our experiments conformed to the one for plasma disruption conditions in ITER within one order of magnitude.

On the basis of experimental results and numerical estimation we propose that DPF devices may be applied to simulate the thermal conditions of material damage on the first wall and divertor plate of ITER in the plasma disruption regime. But approximation of simulation conditions to conditions of real plasma disruption requires broad experimental research using DPF (μs pulse duration) in comparison with devices of millisecond pulse duration.

1.10. Influence of pulsed beams with extreme energy upon the material of low activation austenitic steel tube

The influence of microsecond pulses of deuterium ions and plasma upon the low activation austenitic steel 25Cr12Mn20W tube was investigated in the PF-1000 device. Tubes of this type have hexagonal shape [14]. Unlike the experiments with a duralumin tube, the steel tube had no protective screen so ion and plasma beams irradiated both the external and the internal surface of the tube. The study of material damages, surface relief changes, as well as structure of the re-solidified layer along the external and internal surfaces of the tube was of special interest.

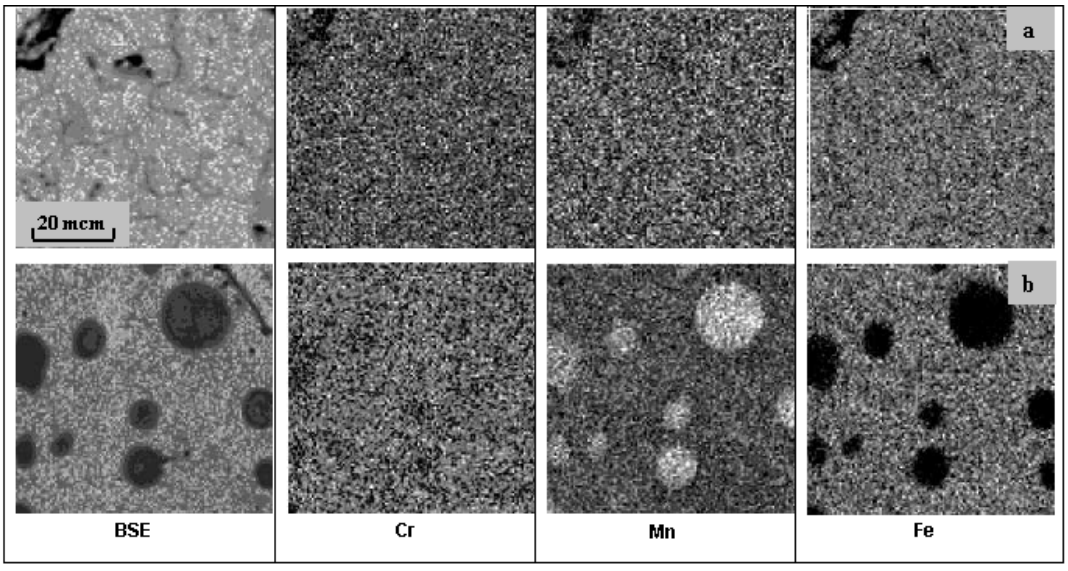

FIG. 6. Back scattered electron image (BSE) and distribution of characteristic X ray radiation for Fe, Cr and Mn on the surface of 10Cr12Mn20W steel: (a) original surface, (b) after three ion and hydrogen plasma pulses in the PF-1000 device.

TABLE 1. OBSERVED PARAMETERS OF IRRADIATION

№ of the tube specimen	1	2	3	4	5
Distance between the specimen and the anode *L(A)*, cm	20	24	28	32	36
Duration of interaction between the specimen and the plasma stream τ, μs	1.9	2.4	2.8	3.3	3.9
Thickness of the melted surface layer *d*, μm	23.8	17.9	12.6	11.2	7.1
Power density of the plasma stream q, 10^6 W/cm^2	5.0	2.5	1.6	1.2	0.8

TABLE 2. PARAMETERS NECESSARY TO SIMULATE PLASMA DISRUPTION IN THE ITER REACTOR

Damage factor $F = q\tau^{0.5}$ [W· cm^{-2}· s$^{0.5}$]			
Plasma disruption in reactor ITER [29, 30]		Influence of pulsed plasma upon the tube material in PF-1000 device	
The first wall	Divertor plate	The nearest to the anode part	The outermost from the anode part
~ (10^3–10^4)	~ (10^3–10^5)	~10^4	~ 10^3

1.11. TEST SPECIMEN

The steel tube was manufactured in the form of a regular hexahedral prism. Formerly similar hexahedral tubes manufactured of different stainless steels were investigated as covers of heat generating elements for fission reactors [31]. Tube #14 (25Cr12Mn20W) was selected for our experiments. The length of the tube was L = 30 cm, the width of each facet a = 2.2 cm and the thickness of the wall h = 0.1 cm. The tube was manufactured by rolling. After rolling the samples were annealed at 1150 °C for 10 min. The chemical composition of the steel is presented in the Table 3.

TABLE 3. CHEMICAL COMPOSITION OF THE STEEL TUBE

Steel	Elements, mass %								
	C	Cr	Mn	Si	W	V	Sc	P	S
25Cr12Mn20W	0.28	12.9	19.3	0.13	2.0	0.15	0.1	0.04	0.008
10Cr12Mn20W	0.09	13.0	20	0.12	1.0	0.10	-	-	-

1.12. Irradiation conditions

The tube was placed along the axis of the PF-1000 device (see Fig. 7). The tube was strongly fixed on two cathode bars by special copper holders. The shortest distance between anode and tube side was $L_1 \approx$11 cm. On the opposite cut of the tube the copper arc was fixed. Its dimensions were: arc radius $R \approx$ 25cm, arc length $L \approx$ 30 cm, arc width $a \approx$ 1.5 cm and arc thickness $h \approx$ 0.12 cm. The arc prevented the ion and plasma streams from leaving the tube (see Fig 7). The energy store in the device PF-1000 was ~ 600 kJ. Pure deuterium at the initial pressure of 470 Pa was used as working gas. Duration τ of the DP pulse moving over the plane of the front cut of the tube was 1 μs. The power density of the plasma beam q at this plane was 10^9 W/cm^2. Power density absorbed by the side surface of the tube was about

~10^6 W/cm^2. The total number of pulses in our experiments was $N = 4$ and the neutron yield in individual "shots" $n = (10^9–10^{11})$.

1.13. Surface relief, microstructure and micro-hardness

Visual analysis showed melting both at the inner and the outer surfaces of the tubes. The features of the surface layer damage and micro-relief of irradiated surface are presented in Figs 8 and 9. It is seen that both the inside and outside surfaces have wave like relief. There are many droplets and ridges; the size of such relief fragments on the inner surface is substantially larger than that on the outer one. With decreasing distance from the irradiation source the typical sizes of the elements of the surface relief get smaller, i.e. the topographic structure of the irradiated surface becomes more dispersed. In other words, the surface relief at the "cold" end of the tube ($q \sim 10^6–10^7$ W/cm^2) is smoother than at the "hot" end ($q \sim 10^8–10^9$ W/cm^2).

The micro-hardness was measured in the re-solidified surface layers, in the areas adjoining to them and in the depth of the samples (in the depth of the tube wall). Figures 10(a)–(c) show that the micro-hardness increases in the zones of outer and inner surface layers. Maximum values H, as a rule, are observed in the surface layers. Hardening of the surface layers is associated with the formation of a specific non-equilibrium microstructure of the steel (see Figs 11, 12) under ultra-fast quenching of liquid phase (with speed of cooling ~ $10^6–10^8$ K/s [9, 11]). These results show that conditions of solidification and structure formations were different in the external and internal surface layers of the tube, as well as in different parts of the tube. Observed re-solidified layer thickness ~15–40 μm requires detailed analysis and temperature estimations. X ray diffraction analysis showed that the dispersible inclusions of marten site and α-phase were present in the re-solidified surface layers along with the austenite (γ-phase). The volume content of the secondary phases was in the range of 1.5–3.0% in the external surface layer and 5.0–9.5% in the internal one. The dispersion of the secondary phase, as a rule, induces hardening and strengthening of the surface layer. It is obvious, that conditions of pulsed plasma irradiation were essentially different on external and internal surfaces of the steel tube: in the internal cavity of the tube ions and plasma streams had no opportunity to dissipate within the chamber. For this reason the internal re-crystallized surface layer of the tube has more uniform thickness than external one (see Fig. 12).

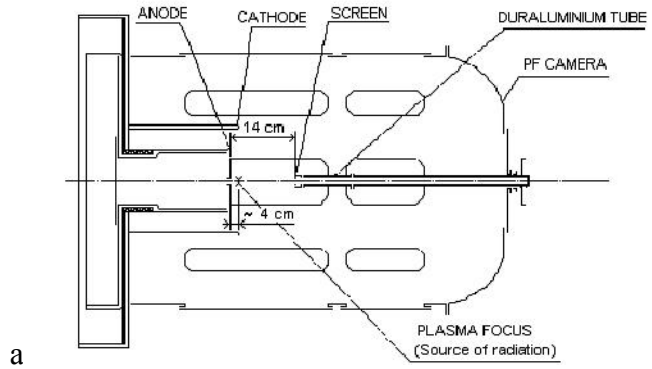

a

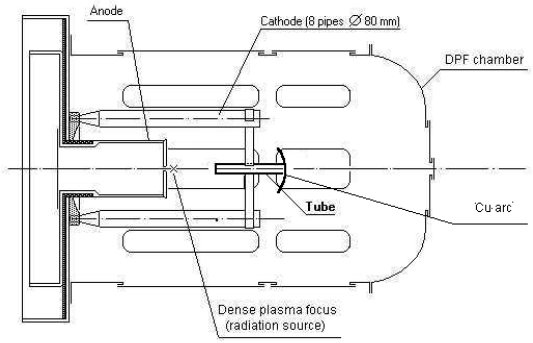

b

FIG. 7. Scheme of dense plasma focus device PF-1000: (a) experiment with duralumin tube and protective screen [2, 24], (b) experiment with hexahedral steel tube.

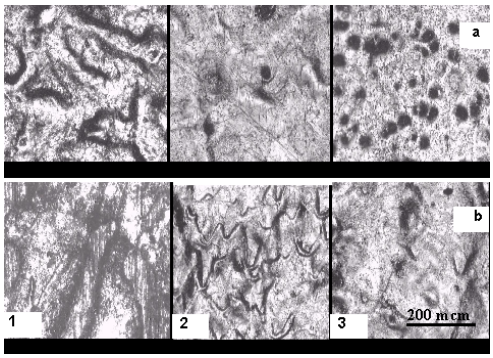

FIG. 8. Parts of the external (a) and internal (b) surfaces of the tube #14:(1) in the "hot" zone (specimen #2), (2) in the middle part (specimen #8), (3) in the "cold" zone (specimen #14).

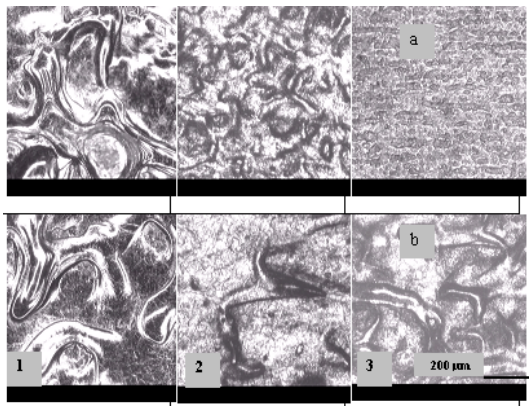

FIG. 9. Parts of the external (a) and internal (b) surfaces of the tube #41:(1) in the "hot" zone (specimen #1), (2) in the middle part (specimen #7), (3) in the "cold" zone (specimen #13).

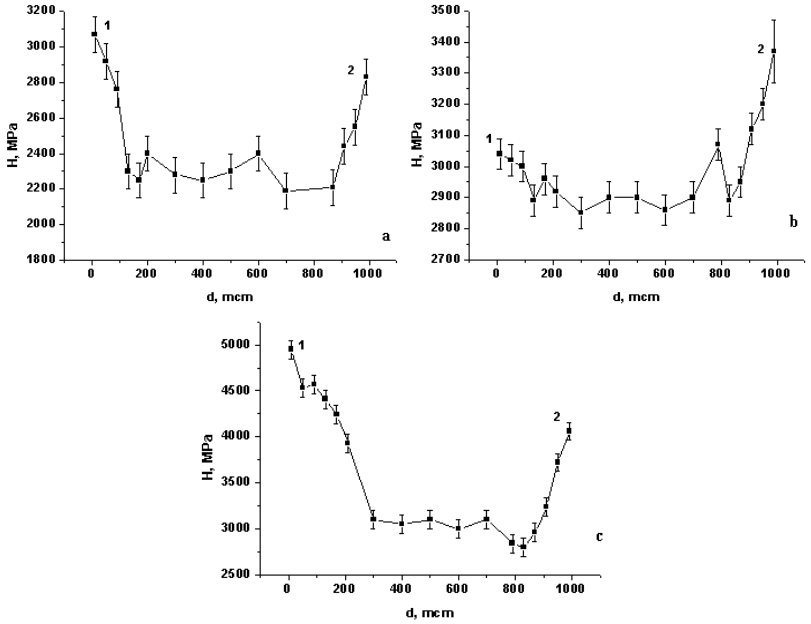

*FIG. 10. Distribution of the micro-hardness in the specimens of the irradiated tube #14 in the zone between the external surface layer (**1**) and the internal one (**2**): (a) sample #1 ("hot"), (b) #9 ("middle"), (c) #15 ("cold").*

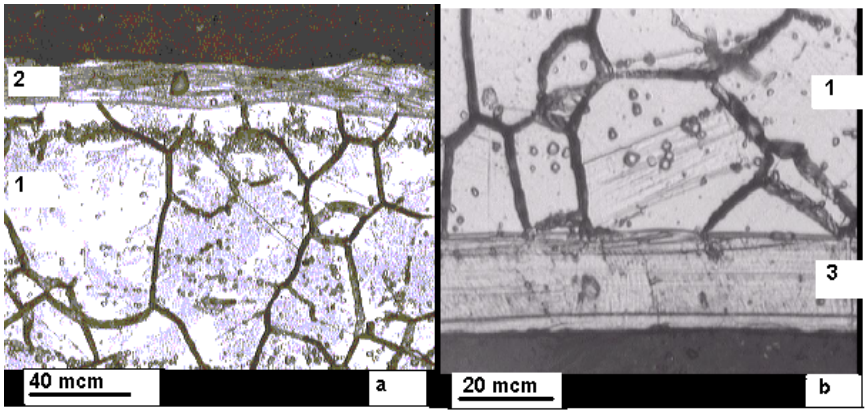

FIG. 11. Optical micrographs of the Cross-sections of the steel tube #14 at the central part after irradiation:(a) specimen #8, (b) specimen #9. (1) initial microstructure, (2) re-crystallized layer of the external surface, (3) re-crystallized layer of the internal surface.

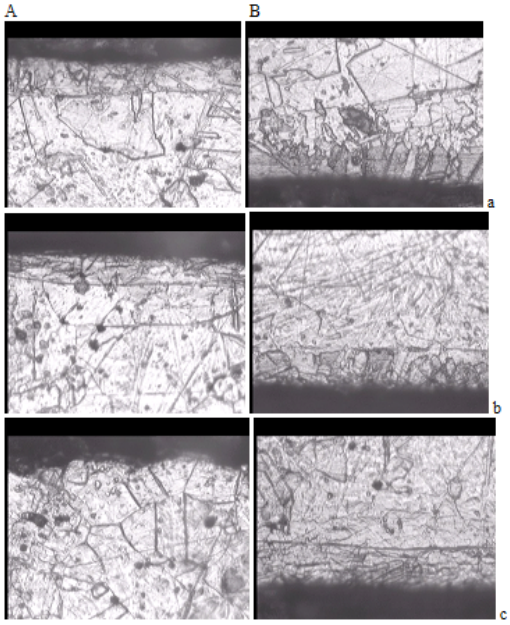

FIG. 12. Optical micrographs of the Cross-sections of the steel tube # 41 the after irradiation: (A) external surface, (B) internal surface; (a) specimen #1("hot"), (b) specimen #7 (central part), (c) specimen # 13 ("cold"). (1) initial micro-structure, (2) re-crystallized surface layer.

PART 2. THE MAIN FEATURES OF INTERACTION OF DENSE PLASMA AND FAST ION BEAMS WITH MATERIAL SURFACE

2.1. Introduction

One of the problems of the project for this year was to compare the character of damage and erosion of the surface layers (SL) of austenitic and ferritic steels with reduced activity of different compositions under pulsed deuterium ion and plasma beams under different irradiation conditions. The importance of the work is connected with the fact that ferritic-martensitic steel is one of the structural materials of ITER and may be convenient for using in the next generation of thermonuclear fusion reactors. Austenitic steels are widely applied in the working chambers of different plasma devices. Experiments were performed on devices PF-1000 and PF-6 (Institute of Plasma Physics and Laser Microfusion, Warsaw, Poland). The working gas PF-1000 was deuterium, in PF-6 deuterium and nitrogen were used.

Scanning electron microscopy and X ray diffraction analysis were carried out in collaboration with Tallinn University (Tallinn, Estonia) and Ferrara University (Ferrara, Italy). The results on the study of the influence of pulsed energy streams taking place in PF-1000 and PF-6 devices, upon damage, mass transfer, evolution of microstructure and properties of the steels and a number of other plasma facing materials are given below. On the basis of the results (see also Part 1) the prospects of applying plasma focus devices for solving scientific and applied problems of radiation material science are discussed.

2.2. Materials and radiation conditions

The samples of austenitic and ferritic steels were smelted in the form of ingots, rolled up to 0.1 cm thick and formed into plates of size of $1.5\times1.5\times0.1$ cm^3. The chemical compositions of the steels are given in Table 4. The power density q adsorbed by the target materials was in the range of 10^7–10^8 W/cm^2. Ferritic steel Eurofer97 was irradiated under

harder conditions at $q \sim 10^9$ W/cm^2. Pulse duration τ was about 1 μs and 100 ns in PF-1000 and PF-6 devices, respectively. The frequency of the pulses was one pulse per 15 minutes and one pulse per three minutes in PF-1000 and PF-6 devices, respectively.

TABLE 4. CHEMICAL COMPOSITION OF THE STEELS

	Content, mass%									
Steel	C	Cr	Mn	Si	W	V	Ta	N	P	S
10Cr12Mn20W	0.10	12.10	20.10	0.02	2.05	-	-	0.01	0.02	0.02
25Cr12Mn20W	0.25	11.57	20.75	0.02	2.01	0.1	-	0.003	0.04	0.008
10Cr12Mn20W +(0.05%La)	0.10	11.90	20.10	0.02	2.05	-	-	0.002	0.02	0.02
10Cr12Mn20W +(0.05%Sc)	0.10	11.90	20.10	0.02	2.05	-	-	0.002	0.02	0.02
30Cr10Mn33W	0.30	10.0	33.0	-	1.0	1.0	-	-	-	-
10Cr9WV	0.11	9.2	0.65	0.3	1.0	0.15	0.1	0.03	0.02	0.007
Eurofer97 Ni-0.021	0.11	9.0	0.48	-	1.1	0.20	0.07	0.03	0.005	-

2.3. Results and discussion

2.3.1. Radiation and thermal effects

As it was mentioned above, DPF devices provide an opportunity to expose materials to pulsed beams of various types (ion, electron, plasma, X ray, neutron and shock wave) of high-power flux density (up to 10^{14} W/cm^2) with pulse duration in the range from 10^{-9} to 10^{-6} s. The influence of these beams on the material results in different radiation and thermal phenomena. The experiments performed, where different types of facilities PF [5–14] were used, show that the influence of pulsed high-energy ion beam ($E_i > 100$ keV) and dense plasma (velocity of the particles is about 5×10^7 cm/s) on the target materials lead to a remarkable difference in radiation and thermal effects. This difference strongly depends on irradiation conditions in the PF chamber, which effects on the character of physical and chemical processes in the materials tested, the damage to its surface layer (SL) and changes in phase-structure.

Radiation effects under the conditions considered mainly are connected with the sputtering of the irradiated material and the formation of surface and bulk structural defects. Thermal effects induced by the high energy pulsed action on the material become apparent mainly in the processes of melting and re-crystallization, evaporation, boiling and heat and mass transfer. Under radiation conditions realized in DPF devices the thermal effects, as a rule, dominate over radiation phenomena. Jointly, radiation and thermal pulsed influences resulted in the damage and erosion of the surface layer of the target material as well as in changing its phase-structural state and properties.

2.3.2. Features of surface layer damage

Analysis showed that the character of the surface damage and the relief of the irradiated surface depend on both irradiation mode (working gas composition, power density and pulse duration) and thermal properties of the target material. Investigations of austenitic and ferritic steels (see Table 4) after irradiation showed that the irradiation resulted in melting, evaporation, sputtering and sometimes crack formation in the surface layer. The re-melted surface always had a wavelike relief with different defects: craters, influx, droplets, pores,

micro-cracks et al. The wavelike relief of the irradiated surface was observed for a number of materials irradiated in PF [9–12] (see also Figs 4, 5, 8, 9). Figures 13 and 14 present scanning electron photos of irradiated surfaces of the steels listed in Table 4.

These Figures show that the surfaces of ferritic steels and steel 10Cr12Mn20W are less damaged. They contain the least number of defects (mainly pores, droplets and spots of re-deposited copper). The surfaces of other specimens (in addition to the noted defects) have numerous craters, bubbles, open bubbles and micro-cracks (Fig. 13(d)). Analysis showed that irradiation resulted in erosion of the materials, mass loss and reduction of the specimen thickness compared to their initial state.

Table 5 presents the results of weighing the steel specimens before and after deuterium plasma irradiations and estimation of evaporated layer thickness d. These values of d are somewhat lower because the re-deposition of the copper from anode to irradiated surface as well as re-deposition of other elements from the parts of PF chamber is not taken into account. Re-deposition is, in particular, responsible for the mass increase of Eurofer-97 steel specimen after irradiation in PF-6 device (see Table 5). Nevertheless, we can conclude that under irradiation with q=10^8–10^9 W/cm^2 austenitic steel 10Cr12Mn20W doped by Lanthanum has the lowest resistance to erosion. At realized irradiation conditions this steel was liable to exhibit enhanced crack formation (see Fig. 13(d)) leading to a reduction of heat transfer from the surface to the bulk and an increase of surface erosion.

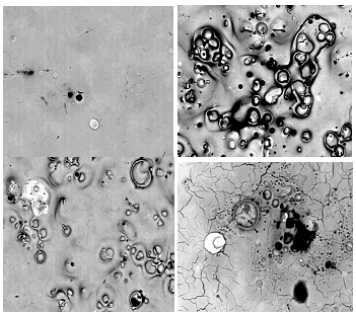

FIG. 13. SEM micrographs of the surfaces of austenitic steels irradiated in PF-1000 device by deuterium plasma: (a) 10Cr12Mn20W (eight pulses); (b) 25Cr12Mn20W (eight pulses); (c) 10Cr12Mn20W+0,05Sc (five pulses); (d) 10Cr12Mn20W+0,05La (five pulses).

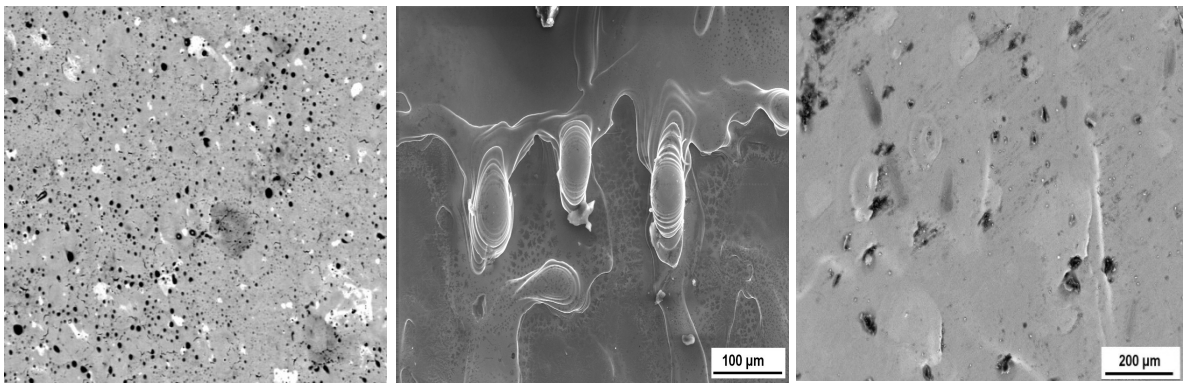

FIG. 14. SEM micrographs of irradiated surfaces of ferritic steels: (a) 10Cr9WV (PF-1000, eight pulses, DP), (b) Eurofer97 (PF-6, eight pulses, DP), (c) Eurofer97 (PF-1000, single pulse, DP).

For all the test specimens (except steel Eurofer-97, which were irradiated under more severe conditions) the thickness d and the mean projective path R_i of fast ions (with energy

$E_i \approx 100$ keV) are connected by the relation $d \leq R_i \approx 1$ μm [24]. It means that deuterium ions were implanted into the target material [5] (see part 1). Steel Eurofer-97 was irradiated under the condition of "explosive rupture implantation" and for this regime the irradiation condition was $d > R_i$ (see Table 5). In this case the implanted deuterium ions are removed from the material together with the evaporated layer.

TABLE 5. CHANGES OF MASS OF STEEL SPECIMENS UNDER IRRADIATION

Material	Number of pulses	Total mass loss Δm mg	Mass loss per pulse, mg	Mass loss per unit area , mg/cm^2	Evaporated layer thickness per one pulse μm
Steel 25Cr12Mn20W	8	0.30	0.0375	0.531	0.67
Steel 12Mn20W	8	0.25	0.03125	0.442	0. 56
Steel 10Cr12Mn20W doped with La	5	0.29	0.058	0.821	1.04
Steel 10Cr12Mn20W doped with Sc	5	0.10	0.0200	0.283	0.36
10Cr9WV	8	0.35	0.04375	0.619	0.78
Eurofer97	1	0.75	0.75	1.785	2.26
Eurofer97	8	+ 0. 35	+ 0.044	+ 0.044	–

Thus, comparing the tested steels and the results of irradiation of other materials [9–14] (see also Part 1) we can conclude that the main factors for damage of material under high energy pulses in PF devices are relief changes on irradiated surfaces, erosion of materials, formation of different types of surface defects (droplets, influxes, pores, craters, bubbles, open bubbles, micro-cracks et al). It should be noted that the outer surface of the tubes placed along the axis of the chamber of PF device was damaged remarkably less than the surfaces of the steel specimens disposed normally to the plasma stream (see Figs 4, 5, 8 and 9). The surface of the tubes had significantly fewer surface defects, mainly droplets and influxes. Similar results were observed for the irradiated surface of a duralumin tube [15, 16] (irradiation conditions and the scheme of the experiment are given in Part 1). Figure 15 shows the surface relief with droplets, influxes and ridges. Large ridges formed in the zone with high power density (Fig. 15(b)), are curved in the direction of the plasma stream. The extension of the ridges and the distance between them are of the order of hundreds of micrometers. The typical size of relief details (ridges, droplets and influxes) decreased with the distance from the anode.

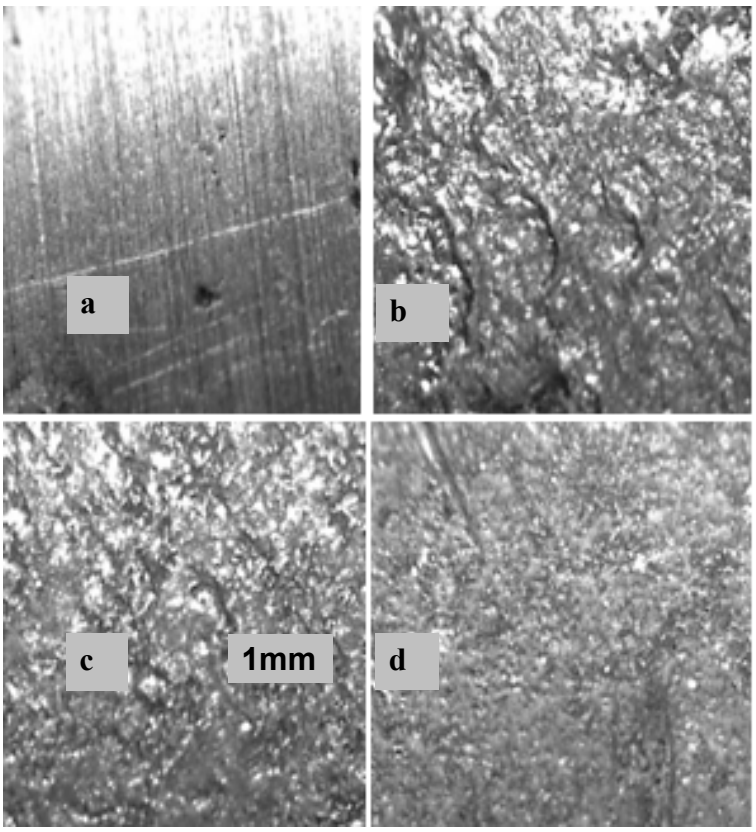

FIG. 15. Topographic structure of the surface of a duralumin tube in the original state (a) after 13-fold DP pulses, (b) the part nearest to the anode, (c) central part, (d) the part which was the farthest from the anode.

The reduction of the damage observed on the surfaces of the tubes compared to the specimens placed normally to plasma is connected with the decrease of intensity in the influence of plasma, fast ions and shock wave on the surface at "axial geometry" of the experiment. The formation of wavelike relief of the surface layer at the preliminary stage of treatment may be used to reduce the material erosion in the subsequent operations in a thermonuclear reactor.

2.3.3. Nature and state of structural defects

Above (see Figs 4–6, 8, 9, 13, 14) we described different structural defects observed on the irradiated surfaces after pulsed energy actions in PF devices (droplets, influxes, pores, craters, bubbles, cracks). From the results obtained in this project [10–14, 26] we can conclude that the character and state of the defects observed depend on the power density absorbed by the specimen, type of the working gas and properties of the material tested. The formation of the surface cracks is usually highly undesirable. The formation of cracks results in degradation of mechanical properties as well as of radiation and corrosion resistance of the material.

Under the irradiation conditions in PF devices we observed crack formations not only in austenitic steels (Fig. 13(d)) but in more refractory materials, such as vanadium and tungsten (Fig. 16). In the surface layers of vanadium specimens, which were irradiated in PF-1000 with hydrogen plasma under power density $q = 10^8$ W/cm^2 [11], the grain boundary cracks were observed. However, tungsten irradiated under more severe conditions ($q = 10^{10}$ W/cm^2, ten pulses) had a significantly rougher surface relief with highly elongated micro-cracks.

Surface melting of the tungsten specimens was also observed under less harsh irradiation conditions ($q = 10^9$ W/cm^2, ten pulses) in the absence of high energy ions (see Fig. 17).

The formation of micro-cracks shows that thermal stresses in the surface layer under high energy pulses exceed the breaking point of the tungsten. The estimation of the erosion of the irradiated tungsten specimen, which was prepared by a powder technique, showed that a single pulse irradiation with deuterium ions and plasma at power density $q = 10^{10}$ W/cm^2 resulted in the evaporation of the layer with thickness $d \approx 2$ μm.

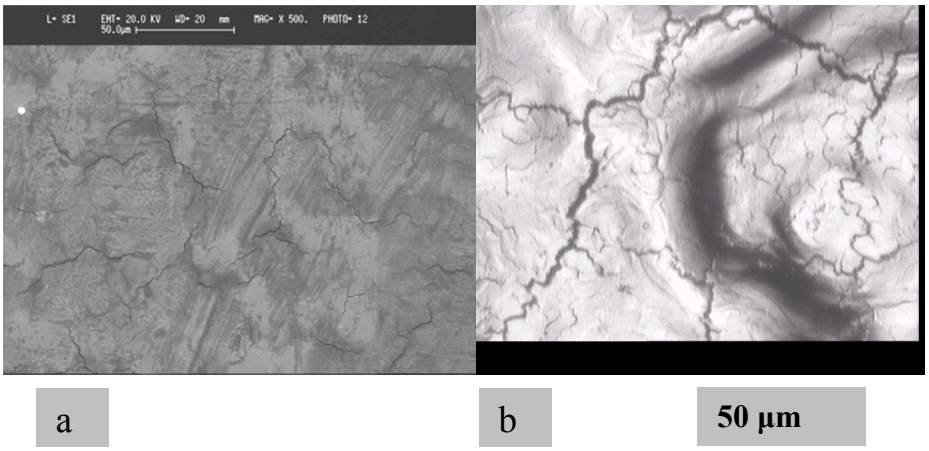

FIG. 16. SEM micrographs showing Micro-cracks on the surfaces of irradiated vanadium and tungsten. (a) the electron scanning of the part of the vanadium sample surface after three pulses of the hydrogen plasma beams ($q = 10^8$ W/cm^2). (b) optical microscopy of the part of the tungsten sample surface after 10 pulses of the deuterium plasma and ion beams ($q = 10^{10}$ W/cm^2).

Taking into account the fact that tungsten is intended to be applied as a structural material for divertor plates in ITER, the results obtained may be useful for preliminary prediction of the material behavior in extreme situations for plasma disruption in a thermonuclear fusion reactor

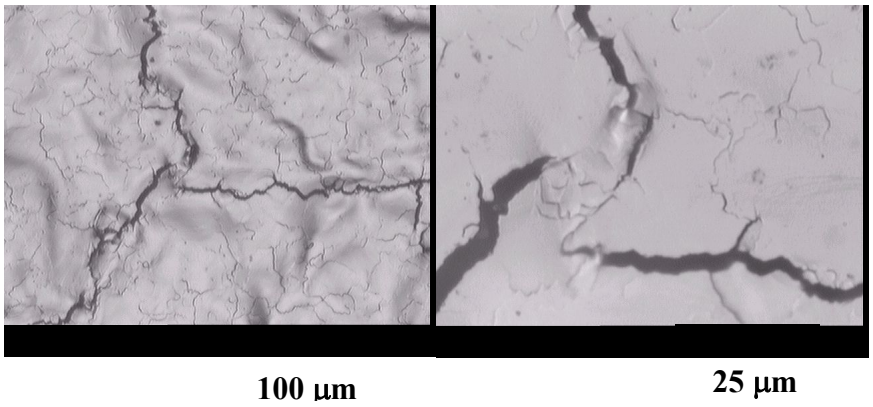

FIG. 17. Micro-cracks on the irradiated surface of tungsten after 10 pulses of the deuterium plasma ($q = 10^9$ W/cm^2 , optical microscopy).

Specific defects are formed on the irradiated surface of the test specimen because of the deposition of different materials placed in the PF chamber. If the material is deposited in the form of droplets (for example after the action of a power electron beam on the copper anode surface [32]) then it covers the surface with a great number of spots (see Fig. 18). Under

multifold irradiations the deposited material can mix up with the liquid phase; it can lead to alloying the surface layer. If the element is deposited in the form of an ion or atom stream then it is dissolved in the liquid phase as a dopant and alloys the surface layer too. It is clearly in Fig. 19. Copper rich layer uniformly covers the central part of irradiated specimen, which did not contain copper in the initial state.

Thus, in addition to possibility of the implanting the working gas ions [5] (see Part 1) the plasma focus devices allow us to alloy irradiated surfaces under the action of ion streams and dense plasma. It may improve mechanical properties and corrosion resistance of the material. On the whole, the results obtained show that plasma focus devices may be used as effective means for studying material damages of different types under power pulsed fast ion and dense plasma beams. It allows us not only to investigate radiation and thermal effects but also apply the results obtained for the development of new techniques of pulsed ion treatments of materials.

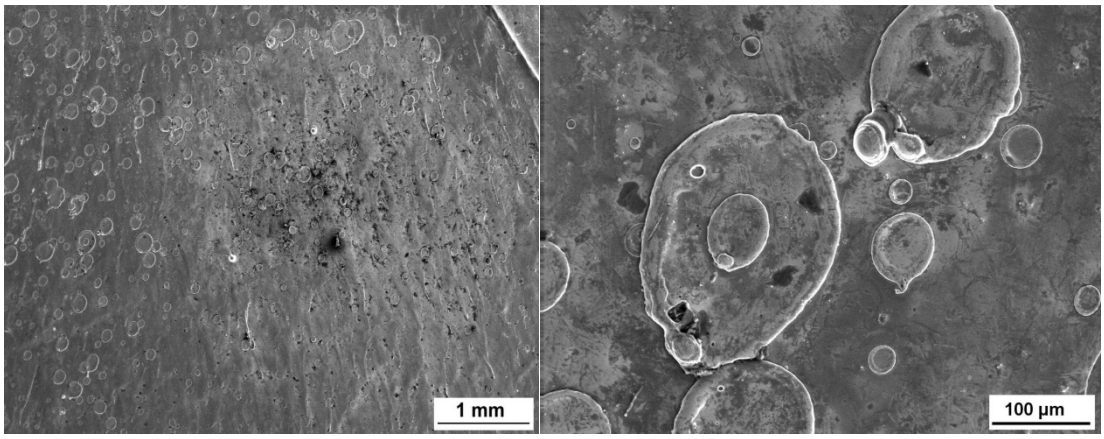

FIG. 18. Irradiated surface of pure iron after DP irradiation in PF-1000 device (single pulse, q = 10^9 W/cm^2). Copper spots are clearly seen.

2.3.4. Structural and phase stability

The investigations of structures of irradiated specimens in cross-section show that the influence of pulsed ion and dense plasma beams result in the change of microstructure and sometimes in the phase structure state of the surface layer. As a rule, the reduction of the grain size in the surface layer in comparison with the initial state and formation of microstructures with typical grain sizes in the range from tens nanometers to few micrometers were observed. The fact is connected with the high cooling rate of the liquid phase (~10^6 to 10^8 K/s) after pulsed action [9, 11]. Examples of disperse microstructures in re-crystallized surface layers for the steels tested and for pure Al and Al-alloy are given in Figs 11, 12 and Figs 20, 21, respectively [15, 24].

Grain size refinement, as a rule, results in improving the mechanical properties of the surface layer: hardening and strengthening (see part 1 Fig. 10). The changes of phase-structural states in of the materials after ion and plasma pulsed beams was studied for austenitic steels and Al-based alloy. In steels 10Cr12Mn20W and 25Cr12Mn20W under irradiation there appeared dispersive inclusions of α-phase in austenitic (γ-phase) matrix (see Fig. 22). It is seen that the irradiation results in structure-phase transformation in the surface layers. In irradiated specimens we observe the reduction of (111)γ peaks and amplification of (200)γ peaks and appearance of α-phase, having the marten site structure.

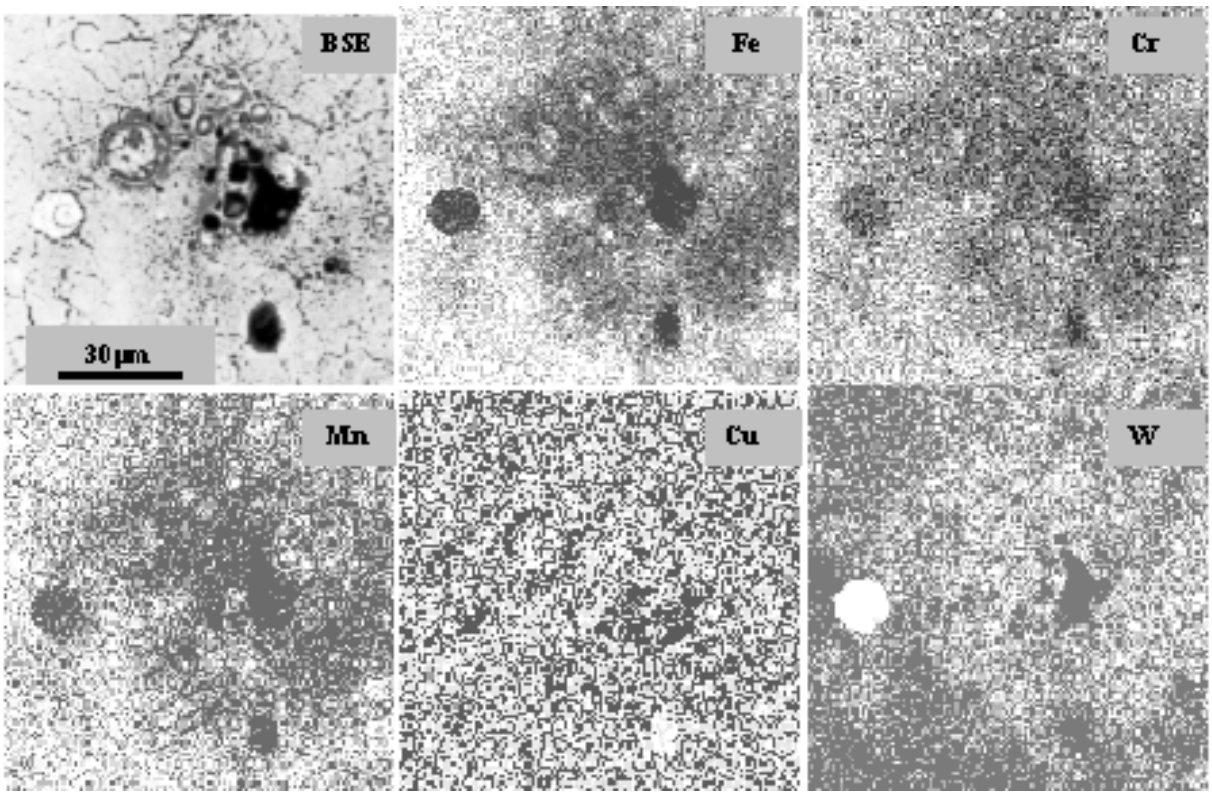

FIG. 19. Micro-cracks on the irradiated surface of tungsten after 10 pulses of the deuterium plasma (q = 109 W/cm2, optical microscopy).

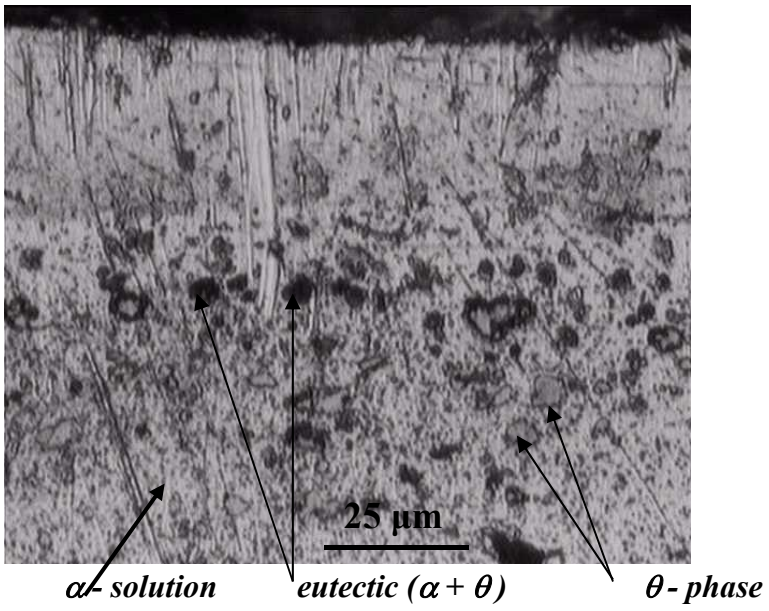

FIG. 20. The cross-section of the surface layer on a duralumin tube after 13-fold pulsed irradiation. (1) re-crystallized surface layer, (2) initial structure.

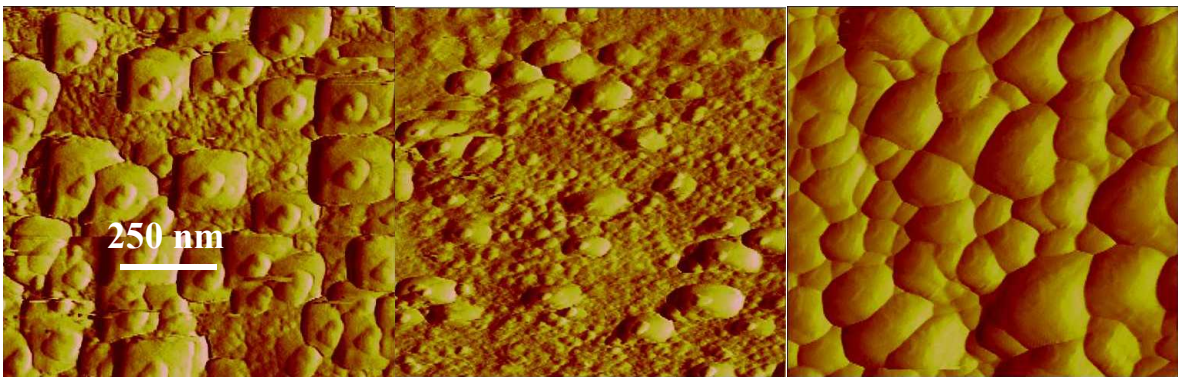

FIG. 21. AFM measurements of Surface topography of Al surface after irradiation with deuterium ion and plasma beams in PF-1000 device.

At the same time the tested ferritic steels 10Cr9WV and Eurofer97 (see Table 5) did not show any $\gamma \rightarrow \alpha$ phase transformation. The phase composition of these steels under multifold action of power deuterium plasma pulses did not change. This result is important for estimating the prospects of applying ferritic-martensitic steels in thermonuclear reactors with magnetic and inertial plasma confinement.

The Al-based alloy in the initial state had a double-phase structure [15] and consisted of α_{Al} — solid solution and inclusions of the second phase $CuAl_2$ (θ - phase). After plasma irradiation there appeared two zones (see Fig. 20): (i) re-crystallized α_{Al} layer where θ-phase inclusions were practically completely dissolved; (ii) adjacent (transition) zone with inclusions of θ-phase and eutectic (α_{Al} + θ-phase). The structural and phase transformations observed as well as the formation of the microcrystalline structure induced hardening and strengthening of the surface layers.

On the whole, we can conclude that the evolution observed in the phase-structural states of the surface layer as well as the effect of its hardening show the possibility of applying the material treatment with power pulses in PF devices to improve mechanical properties and corrosion resistance of materials. We can also expect that the resistance to the radiation influence of surface layers, treated with dense plasma streams, will be improved due to the reduction of erosion on the wavelike relief of the irradiated surface (Figs 8, 9 and 15). Besides the increase of the total grain boundary area with the formation of dispersive structures in the surface layer results in the increase of concentration of the crystal lattice defects (dislocation, lattice distortion et al.). That induces generation of sinks for radiation defects and positively reduces blistering under irradiation [22].

3. CONCLUSIONS

The plasma focus devices PF-1000, PF-60, and PF-6 with different gases and different irradiation modes were used to carry out experimental investigations of interactions between pulsed ion and high-temperature plasma beams and some materials to be applied in structural and functional components of thermonuclear fusion devices with magnetic and inertial plasma confinement, as well as for working chambers of plasma devices.

On the basis of the investigations carried out, a significant progress was achieved in understanding the mechanisms of the influence of high energy nano- and microsecond pulsed beams upon irradiated materials. Particularly under the different power densities three typical regimes of the influence of ion and plasma beam upon the target material disposed in the

cathode part of PF device were found: (i) “implantation” ($q \approx 10^5$–10^7 W/cm^2); (ii) screening of the surface by a secondary plasma cloud ($q \approx 10^7$–10^8 W/cm^2); and (iii) absence of implantation (“explosive rupture”) ($q \approx 10^8$–10^{10} W/cm^2).

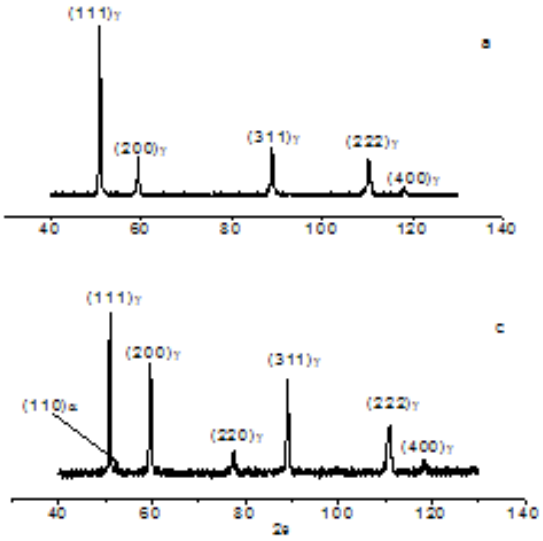

FIG. 22. X ray diffraction patterns for the irradiated steel 25Cr12Mn20W tube in initial state (a) and after 4 pulses of deuterium plasma actions (c).

It was shown that the ion and plasma beams in the dense plasma focus devices can be separated temporary and make different energy contributions to the material damage. In this case, the redistribution of the elements in the surface layer of austenitic chromium-manganese steels was particularly marked. A significant increase of Mn content and a reduction of Fe content took place near the blister-like bubbles formed on the irradiated surface.

The interaction of the pulsed deuterium plasmas and ion beams with the material of an axially oriented tube-like target of the PF-1000 device chamber was studied. Two cases were investigated: with the use of a special protective screen (results were described in [15, 16]) and without it (the low activated steel 25Cr12Mn20W and 10Cr12Mn20W hexahedral tube [18]). In both cases the phase transformation and structure change resulted in hardening and strengthening of the surface layers. These results demonstrated the possible application of DPF devices to modify the surface layer in hard to reach parts of the treated details, such as internal surfaces of elongated tubes.

Important results were obtained on deuterium ions and dense plasma beams interaction with ferritic steels and tungsten, the latter was produced by the powder metallurgy method. It was found that damages of the surface layer of ferritic steels (10Cr9WV and Eurofer97 types) under realized conditions were remarkably lower compared to those in austenitic steels. Phase compositions of ferritic steels remained steady under the pulsed action of high power density (up to 10^{10} W/cm^2) and pulse durations up to 1 μs.

The surface layer of tungsten after a 10-fold action of pulsed irradiation under hard conditions ($q \approx 10^{10}$ W/cm^2, $\tau \approx 1$ μs) was rather strongly damaged. Elongated surface cracks and significant erosion of the material were observed: the mean thickness of the layer evaporated per single pulse was 2 μm.

Taking into account the fact that ferritic-martensitic steels and tungsten are the basic structural materials for the first wall and the divertor plate in ITER, the results obtained are useful for preliminary estimation of the prospects for applying these materials in future thermonuclear fusion devices with magnetic and inertial plasma confinement.

Prospects for using DPF devices to solve scientific and applied problems in material science such as material damage, ion implantation and modification of the surface layers were given. It was also shown that the DPF devices allow realizing the conditions of material damage by high temperature plasma close to plasma disruption at ITER. We think that this approach, based on the DPF device application, is very promising to simulate the thermal influence under plasma disruption at ITER as well as the explosive action of pulsed high-energy beams upon the materials in reactors with inertial confinement of plasma. It is believed that this approach may be useful for preliminary tests of materials for structural elements of ITER working under pulsed high-energy actions.

(1) DPF devices were found to be useful for preliminary treatments of materials with pulsed ion and plasma beams to improve mechanical properties and corrosion resistance of the surface layers and to enhance radiation resistance during their operation in thermonuclear and plasma facilities. The results obtained also point to the advisability of using DPF devices in developing new pulse technologies for material treatment with the use of power nanosecond and microsecond pulses.

(2) During the course of this project the experimental and research potential of the laboratory "Effect of irradiation on metals" of A.A. Baikov Institute of Metallurgy and Material Science RAS was significantly raised due to the use of different plasma focus devices (PF-1000, PF-150, PF-6) and analytic equipment as well as peopleware of research Institutes and Universities of countries participants of the project of the International Atomic Energy Agency "Dense Magnetized Plasma". A.A. Baikov Institute of Metallurgy and Material Science RAS actively collaborated with Institute of Plasma Physics and Laser Microfusion (Warsaw, Poland), Institute of Plasma Physics (Prague, Czech Republic), Tallinn University (Tallinn, Estonia), University of Ferrara (Ferrara, Italy). Russian Federation Universities and Institutes of higher education (Institute for Theoretical and Experimental Physics, Moscow Research Institute of Nuclear Physics, M.V. Lomonosov Moscow State University, Moscow State Industrial University and Moscow State Institute of Electronics and Mathematics) and Moscow Physical Society took part in carrying out the Project.

(3) In cooperation with Moscow Physical Society with partial support of IAEA the plasma focus device "PF-5M" was manufactured in the laboratory "Effect of irradiation on metals" of A.A. Baikov Institute of Metallurgy and Material Science RAS. The device is aimed at solving scientific and applied problems of radiation physics of solid and radiation material science. Characteristics of the device are presented in the final report of Moscow Physical Society (Research Contract No 11942/R0-R4). In future, the device PF-5M will be modified for operation in repetition mode with high repetition frequency.

REFERENCES

[1] BOROWETSKI, M., DE CHIARA, P., GRIBKOV, V.A. et al. Experimental study of a powerful energy flow effect on materials in PF-1000 installation, Nukleonika **46** (2001) 117–122.

[2] PIMENOV, V.N., MASLYAEV, S.A., IVANOV, L.I. et al. Interaction of pulsed streams of deuterium plasma with aluminium alloy in a plasma focus device. I. A new methodology of the experiment. In: Proc. of the Tallinn University of Social and Educational Sciences. Tallinn (2003) 30–39.
[3] GRIBKOV, V.A., DUBROVSKY, A.V., MIKLASZEWSKI, R. et al. (2004) Experimental studies of the ion and plasma beams interaction with carbon-based targets located in the cathode part of Plasma Focus devic. In Proceedings of XVI International Conference on Physics of Radiation Phenomena and Radiation Material Science. Krym, Alushta, 297–298.
[4] GRIBKOV, V.A., IVANOV, L.I., MASLYAEV, S.A. et al. On the nature of changes in the optical characterization produced in sapphire on its irradiation with a pulsed powerful stream of hydrogen ions, Nukleonika **49** (2004) 43–49.
[5] GRIBKOV, V.A., PIMENOV, V.N., IVANOV, L.I. et al. Interaction of High Temperature Deuterium Plasma Streams and Fast Ion Beams with Condensed Materials in Dense Plasma Focus Device, Journal of Physics D: Applied Physics **36** (2003) 1817–1825.
[6] IVANOV, L.I., MASLYAEV, S.A., PIMENOV, V.N. The use of liquid metals in porous materials for diverter applications, J. Nucl. Mater. **271/272** (1999) 405–409.
[7] IVANOV, L.I., PIMENOV, V.N., MASLYAEV, S.A. et al. Influence of dense deuterium plasma pulses on materials in Plasma Focus device, Nukleonika 45(2000) 203–207
[8] IVANOV, L.I., UGASTE, YU.E., PIMENOV, V.N., GRIBKOV, V.A., MEZZETTI, F. Mass transport of hydrogen from iron based alloys to outside F environment. Perspektivnye Materialy **2** (2000) 18–25 (in Russian).
[9] MASLYAEV, S.A., PIMENOV, V.N., PLATOV, Yu.M. et al. Influence of deuterium plasma pulses generated in plasma focus device on the materials for thermonuclear fusion reactor. Perspektivnye Materialy **3** (1998) 39–46 (in Russian).
[10] PIMENOV, V.N., DYOMINA, E.V., IVANOV, L.I. et al. Damage of Structural materials for fusion devices under pulsed ion and high temperature plasma beams. J. Nucl. Mater. 307/311 (2002) 95–99.
[11] PIMENOV, V.N., GRIBKOV, V.A., DOUBROVSKY, A.V. et al. Influence of powerful pulses of hydrogen plasma upon materials in PF-1000 device. Nukleonika **47** (4) (2002) 155–162.
[12] PIMENOV, V.N., GRIBKOV, V.A., IVANOV, L.I. et al. New possibilities of the application of the Dense Plasma Focus devices to modify material surface layers. Perspektivnye Materialy 1 (2003) 13–23 (in Russian).
[13] PIMENOV, V.N., GRIBKOV, V.A., IVANOV, L.I. et al. (2004) The pulse influence of extreme energy beams upon low activated austenitic steels. In: Proc of the XVI th Int Conf on Physics of Radiation Phenomena and Radiation Material Science, Krym, Alushta, 17–18.
[14] PIMENOV, V.N., MASLYAEV, S.A., IVANOV, L.I. et al. Surface and bulk processes in materials Induced by pulsed ion and plasma beams at Dense Plasma Focus devices. Nukleonika 51 (1) (2006) 71–78.
[15] PIMENOV, V.N., MASLYAEV, S.A., IVANOV, L.I. et al. (2003) Interaction of pulsed streams of deuterium plasma with aluminium alloy in a plasma focus device. II. Investigation of irradiated material. In: Proc. of the Tallinn University of Social and Educational Sciences. Tallinn B2: 40–50.
[16] PIMENOV, V.N., MASLYAEV, S.A., DYOMINA, E.V. et al. Influence of pulsed energy beams on the surface of the Al alloy tube in dense plasma focus device. Perspektivnye Materialy 4 (2006): 43–52 (in Russian).

[17] UGASTE, YU.E., PIMENOV, V.N., IVANOV, L.I. et al. Diffusion-stochastic model of the mass transfer of interstitial elements. Calculation of the redistribution of deuterium, implanted in an iron-based alloy. J. Adv. Mater. **9** (2002) 398–405.
[18] GAUSTER, W.B., SPEARS, W.R. and ITER Joint Central Team Requirements and selection criteria for plasma-facing materials and components in the ITER EDA design. Nucl. Fusion **5** (1994) Suppl: 7–18.
[19] Lawrence Livermore National Laboratory (1992) Inertial confinement fusion. In: 1991 ICF Annual Report, 1–198.
[20] BURTSEV, V.A., GRIBKOV, V.A., FILIPPOVA, T.I. High-temperature pinch phenomena. Itogi nauki i tehniki. Fizika plazmy 2 (1981) 80–137 (in Russian).
[21] ABE, F., GARNER, F.A., KAYANO, H. Effect of carbon on irradiation hardening of reduced-activation 10Cr-30Mn austenitic steels. J. Nucl. Mater. 212–215 (1994) 760–765.
[22] IVANOV, L.I., PLATOV, Yu. M. Radiation physics of metals and applications. Moscow: Intercontact Nauka, (2002) 299 p (in Russian).
[23] LYAKISHEV, N.P., DYOMINA, E.V., IVANOV, L.I. et al. Prospect of development and manufacturing of low activation metallic materials for fusion reactor. J. Nucl. Mater. **233/237** (1996):1516–1522.
[24] PLESHIVTSEV, N.V., BAZHIN, A.I. (1998) Physics of interaction of ion beams with the materials. Vuzovskaya kniga, Moscow (in Russian).
[25] VERTKOV, A.V., EVTICHIN, V.A., LYUBLINSKI, I.E. et al. Mechanical properties of low activation Cr-Mn austenitic steel changes in liquid lithium. J. Nucl. Mat. 203 (1993) 158–163.
[26] KODENTSOV, A.A., UGASTE, YU.E., PIMENOV, V.N. et al. (2003) Influence of dense deuterium plasma pulses on Fe and Fe-Mn alloy specimens in a plasma focus device. In Proc. of the Tallinn Univ. of Social and Educational Sciences. Tallinn B2, 51–56.
[27] ZABOLOTNYI, V.T., LAZORENKO, V.M. (1993) Cascades, sub-cascades and peaks of displacement in the tungsten after the irradiation by own ions. 3:17–22 (in Russian)
[28] ZABOLOTNYI, V.T., IVANOV, L.I., SUVOROV, A.L. Field-ion microscopy and principal aspects of the radiation damage of the solid. Fizika i Khimiya Obrabotki Materialov 2 (1994) 5–10 (in Russian).
[29] HASSANEIN, A., KONKASHBAEV, I. Erosion of plasma-facing materials during a tokamak disruption. Nucl. Fusion **5** (1994) Suppl: 193–224.
[30] MARTYNENKO, YU.V., MOSKOVKIN, P.G., KOLBASOV, B.N., Accumulation and penetration of tritium in the firstwall of tokamak ITER in disruption regime.The questions of atomic science and technique. Nucl. Fusion **3** (2001) 65–72.
[31] SHAMARDIN, V.K., IVANOV, L.I., DYOMINA, E.V., BULANOVA, T.M., NEUSTROEV, V.S., PRUSAKOVA, M.D. The influence of neutron beem in the reactor BOR-60 upon the material of the cromium-manganese cover. PHIZHOM **6** (1989) 5–8 (in Russiann).
[32] GRIBKOV, V.A., DUBROVSKY, A.V., SCHOLZ, M. et. al. PF-6 — an effective plasma focus as a source of ionizing radiation and plasma streams for application in material technology, biology and medicine. Nukleonika 51 (2006) 55–62.

INVESTIGATION OF THE IONIZING RADIATION EFFICIENCY AND SPECTRA FROM 1.2 MJ PLASMA FOCUS DEVICE AND ITS APPLICATIONS

M. SCHOLZ
International Center for Dense Magnetized Plasmas
Warsaw, Poland

Abstract

This report presents a summary of experimental results obtained with the PF-1000 plasma-focus device, which was operated at energy 0.6 MJ. In the following sections a progress in studies of a different plasma-focus phases are given. Some theoretical models of the initial breakdown, which occurs at the insulator surface, are compared in Section 2. It is pointed out that modeling of the breakdown is sensitive to kinetics of ionization processes and transport coefficients. Particular attention has been paid to correlation between pinch evolution and the emission of pulsed X ray, fast electron beams, and fusion produced neutrons. Progress in experimental studies of the axial acceleration phase is unsatisfactory. Important experimental data have been collected, but new measurements are still needed. For the radial collapse phase it was shown that the MHD modeling is efficient until the maximum compression, but plasma instabilities require more sophisticated approaches. The pinch phase was investigated by means of different diagnostics. Fusion neutron yields were measured in different experiments, but some discrepancies in scaling must still be explained. The conclusions concern the main results obtained from different experiments performed with the PF-1000 device in the last few years.

1. INTRODUCTION

The plasma focus (PF) device belongs to the family of dynamic, non-cylindrical Z-pinches and is based on a pulsed high-current discharge between two coaxial electrodes placed in a working gas (Fig. 1). The development of the PF discharge can be divided into a number of phases. The first phase constitutes the initial breakdown of the working gas on the surface of the insulator separating the coaxial electrodes, and the formation of a dense ionized plasma layer (current sheath). During the second phase, the current sheath is driven off the insulator surface and is accelerated towards the open end of the electrodes. During the subsequent phases (i.e. radial compression, column creation and column disruption) the current sheath collapses rapidly toward the axis of the inner electrode where a dense pinch column is formed. The micro-instabilities and turbulences of dense magnetized plasma compressed inside the pinch leads to the generation of powerful electron and ion beams, large emission of electromagnetic radiation and of fusion neutrons when deuterium is used as the working gas. In general, the PF device can be considered as a power transformer in which the energy stored in the magnetic field is abruptly converted into the energy of the pinch plasma. The propagation time from the breakdown to the pinch formation usually takes a few microseconds. The final stages of PF phenomena are much shorter and they last from several tens to several hundreds of nanoseconds (depending on PF device scale).

During recent years the interest in PF devices has increased, because they are one of the most efficient sources of pulsed neutron emission. Moreover, in comparison to other pulsed neutron sources that are used worldwide, the scaling laws for the neutron yields, as formulated at the beginning of the PF studies, were very promising. Later investigations, however, which were performed with larger devices, suggested that there is a certain energy limit above which the scaling laws are not valid. Hence, the essential problem to be solved in PF research has always been to discover the physics which dominates the plasma formation. This question is closely related to neutron production mechanisms, plasma dynamics and physics of different phases of such plasma discharges [2, 3]. The experimental studies of high-current PF discharges have been continued in Warsaw with the PF-1000 facility [4, 5] which can be operated with bank energy up to 1 MJ.

The PF-1000 Plasma-Focus facility, constructed and operated at the Institute of Plasma Physics and Laser Microfusion (IPPLM), is equipped with a large condenser bank with a total capacitance of 1347 μF. This bank can be charged up to 40 kV, corresponding to 1.2 MJ of electrical energy. The problem is how to transmit this energy to plasma discharges effectively.

Recently, PF-1000 facility has been modernized, and new experiments (aimed at the optimization of PF discharges) have been carried out. The mega joule PF-1000 facility, is equipped with a 3.5 m long experimental chamber, as shown in Fig. 2.

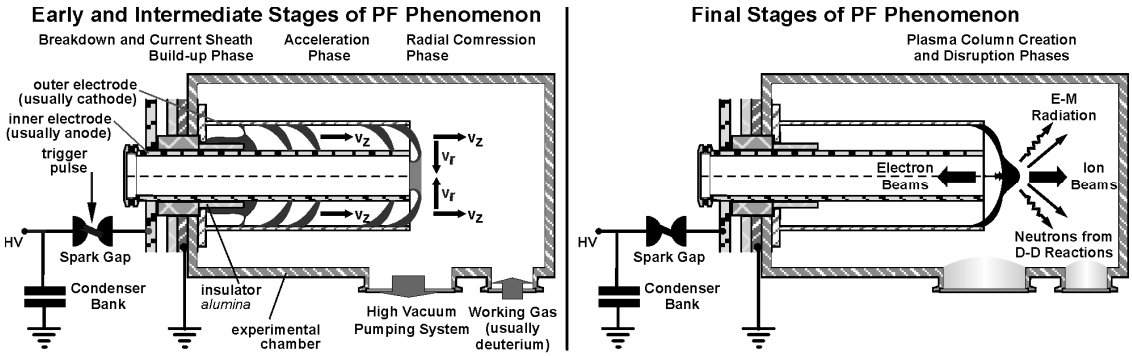

FIG. 1. Plasma-focus device (Mather type) — general layout and principle of operation.

This facility is equipped with various diagnostic tools: equipment for measurements of voltage- and current- waveforms, high-speed cameras recording VR and X ray images of plasma, X ray pinhole cameras and crystal spectrometers, ion pinhole cameras and sets of nuclear track detectors (NTDs) for measurements of fast primary ions (mostly deuterons), as well as scintillation- and activation- detectors for measurements of fusion produced neutrons, etc. All these tools have been used for numerous experimental studies, which have been performed by international teams within the frame of the International Center for Dense Magnetized Plasmas (ICDMP) operated at IPPLM in Warsaw.

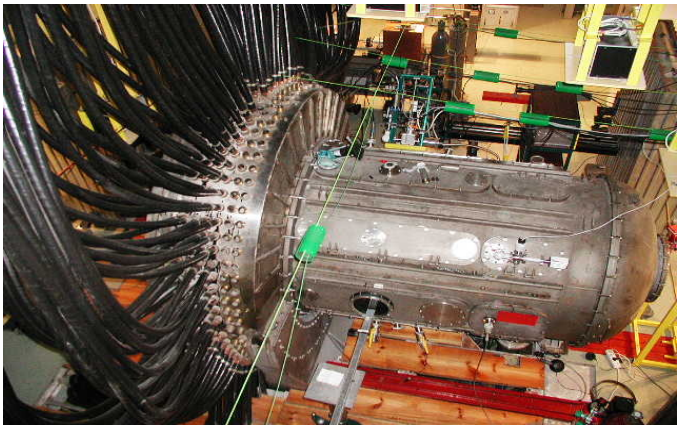

FIG. 2. Top view of the present experimental arrangement with the large PF-1000 chamber.

Stochastic character and complexity of PF phenomena require a detailed qualitative and quantitative analysis. For this purpose the data obtained with a given diagnostic technique should easily be related to those obtained with other methods (even after a long time). Therefore, all the PF discharge phases should still be studied in more detail and more systematically.

2. PROGRESS IN STUDIES OF BREAKDOWN

The initial breakdown occurs at the insulator surface, and the final PF pinch column is formed at the electrode outlet. These two stages, which are separated by the axial acceleration and radial collapse phases, can in fact be optimized in different ways. A current sheath layer, as formed at the insulator, cannot be accelerated within the inter-electrode gap effectively at a very low gas pressure. An appropriate amount of gas must be delivered to ensure an effective "snow-plough" process. Numerical simulation of the breakdown phase were performed by different researchers and the results of such computations agree relatively well with results of experimental observations, as shown in Fig. 3.

Other theoretical approaches to modeling the breakdown phase have been reported recently. Unfortunately, an accurate quantitative model, taking into account the complexity of the current sheath formation phase, is still missing. In particular, the influence of the insulator surface condition should be taken into consideration. Active experiments with planned modifications of the insulator surface have not been performed so far, although they were proposed during the IWDMP in 2002. A localized gas puffing has also been under consideration only.

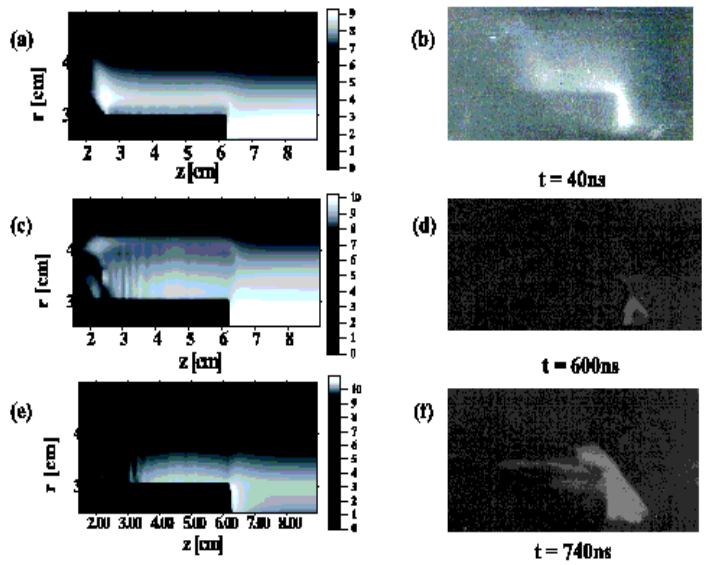

FIG. 3. Comparison of computed density distributions with high-speed camera pictures showing a relatively good agreement.

The well known difficulties in the operation of PF facilities at large energy are probably connected with a lack of the optimization of different parts and/or procedures. It should be remembered that in the POSEIDON facility the replacement of a glass insulator by a ceramic one shifted the so-called "neutron saturation limit" and made possible the operation at higher energies and with higher neutron yields. As regards the breakdown phase in the PF-1000 facility, it is a pity that no experimental optimization of the main insulator material and configuration has been made so far.

3. STATUS OF RESEARCH ON AXIAL ACCELERATION PHASE

To model the axial acceleration phase different approaches have been applied. The most popular and effective appeared to be the 2-fluid MHD model using plasma continuity, momentum and energy equations, Maxwell equations and the electrical circuit equation. In

general, the modeling is very sensitive to kinetics of the ionization and transport coefficients. The computer simulation must of course be include the chosen electrode configuration and gas conditions. The developed PF-1000 simulation employed Braginski transport coefficients. The ionization process was described by the known formula $dn_e/dt = n_e(n_o - n_e)\, S - \alpha_r n_e^2 - \beta_{3B}\, n_e^3$, where values of coefficients S, α_r and β_{3B} were assumed according to the Braginski theory. Anomalous resistivity of plasma was also taken into account. Some results of the performed computations are presented in Fig. 4. Unfortunately, there is no progress in experimental studies of the axial acceleration phase, although new probe and spectroscopy measurements are under preparation.

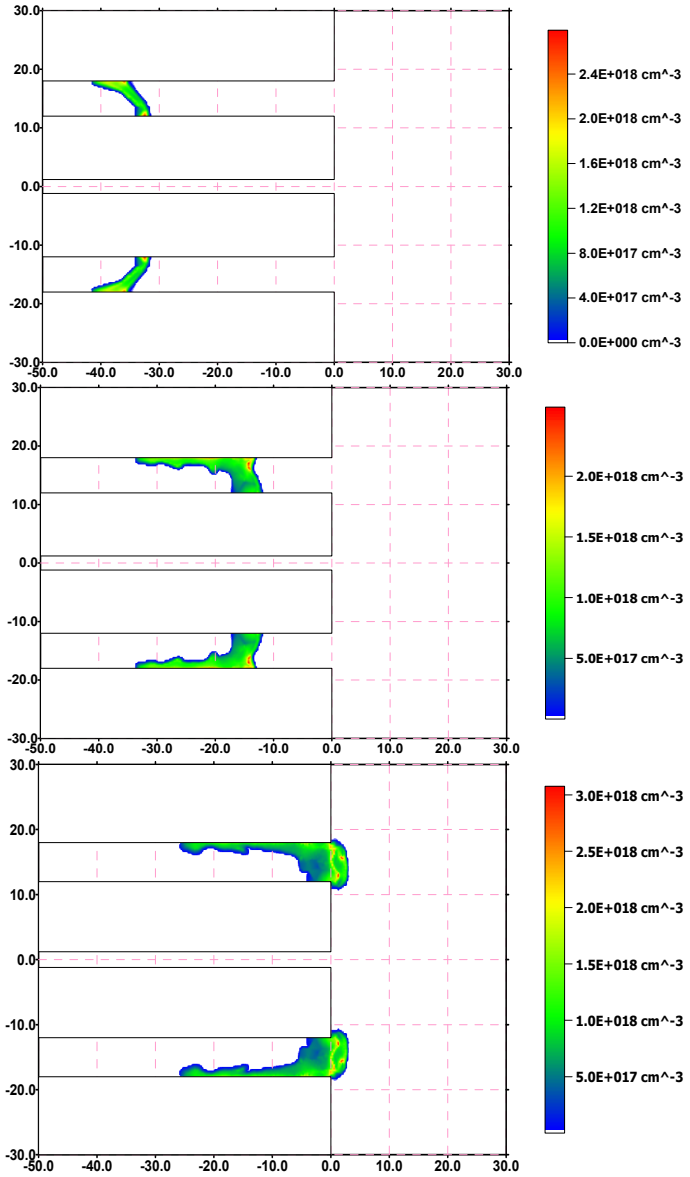

FIG. 4. Plasma density distribution in the accelerated current sheath, as computed for the PF-1000 device [9]at different instants: 3 μs, 5 μs and 7 μs after the start of the discharge.

4. STATUS OF RESEARCH ON RADIAL COLLAPSE PHASE

The performed computations have demonstrated that the MHD modeling of the collapse phase is reasonably accurate until the maximum compression occurs. After this point, the development of different plasma instabilities requires more sophisticated approaches. Nevertheless, using an extended MHD model described above, some valuable computer simulations of the collapse phase were carried out. Some examples are shown in Fig. 5.

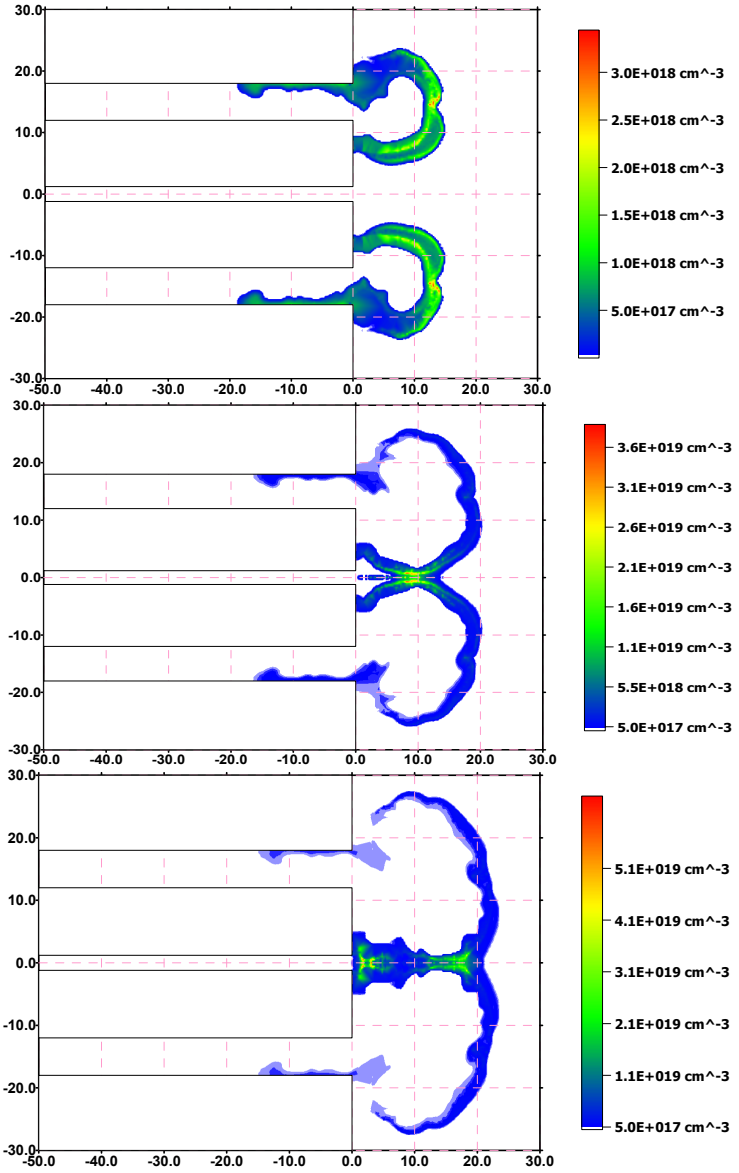

FIG. 5. Plasma density distribution during the radial collapse, as computed for the PF-1000 device at different instants: 9 μs, 9.7 μs and 10 μs after the start of the discharge.

The dynamics of the radial collapse phase have been extensively investigated with high-speed cameras. Numerous VR pictures were collected and analyzed by comparing them with model computations. These calculations were performed simultaneously on the basis of the extended MHD model described above. In general, the recorded VR pictures display good qualitative agreement with results of the performed simulations, as shown in Fig. 6.

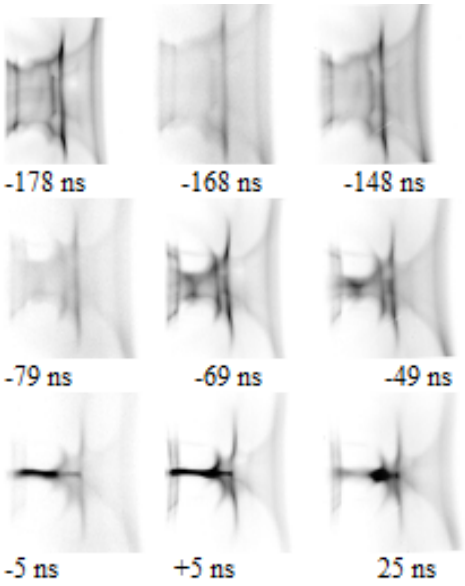

FIG. 6. High-speed frame camera pictures of the radial collapse phase, as taken in the PF-1000 experiment performed at p_o = 4 hPa, U_0 = 33 kV and I_{max} = 1.7 MA (2002). Time is expressed in relation to the maximum compression.

One can easily see that the development of local MHD instabilities can be simulated, but their location in the real experimental situation cannot be indicated synonymously, due to their stochastic character. Another problem is the disparity between the computed and recorded current waveforms, as shown in Fig. 7.

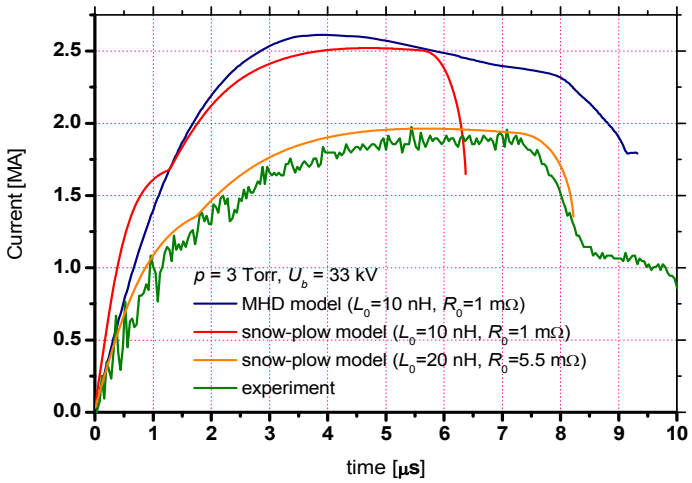

FIG. 7. Discrepancies between computed current-waveforms and experimental traces, as observed in the PF-1000 device.

These differences could be due to incorrect values for the circuit parameters used the modeling of the PF-1000 discharge. But one cannot exclude the possibility that the applied model does not work sufficiently well. This question must still be investigated experimentally and theoretically.

The acceleration phase is followed by the radial compression phase, formation of the pinch and its disintegration. Those processes can be seen on streak camera images made for

different pressures of deuterium in the experimental chamber. Experimental set up and the location of streak camera slit are presented in Fig. 8.

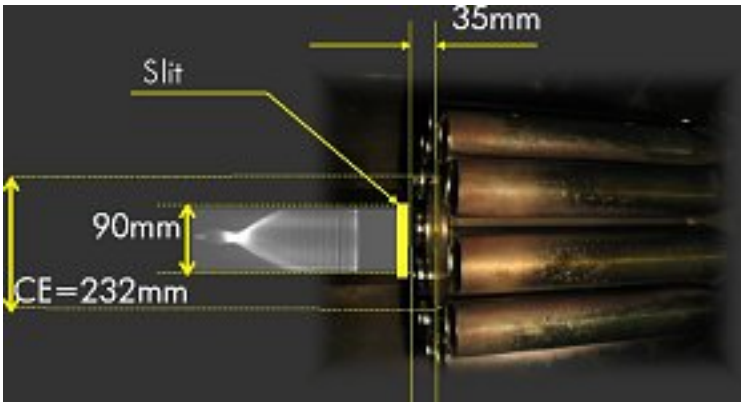

FIG. 8. Location of the streak camera slit in relation to the PF-1000 electrodes.

The final rundown phase (for d = 90 mm) and the creation of the pinch on PF-1000 axis have been registered in such a set up. These measurements have been performed for a wide range of deuterium filling gas pressures, as shown in Fig. 9.

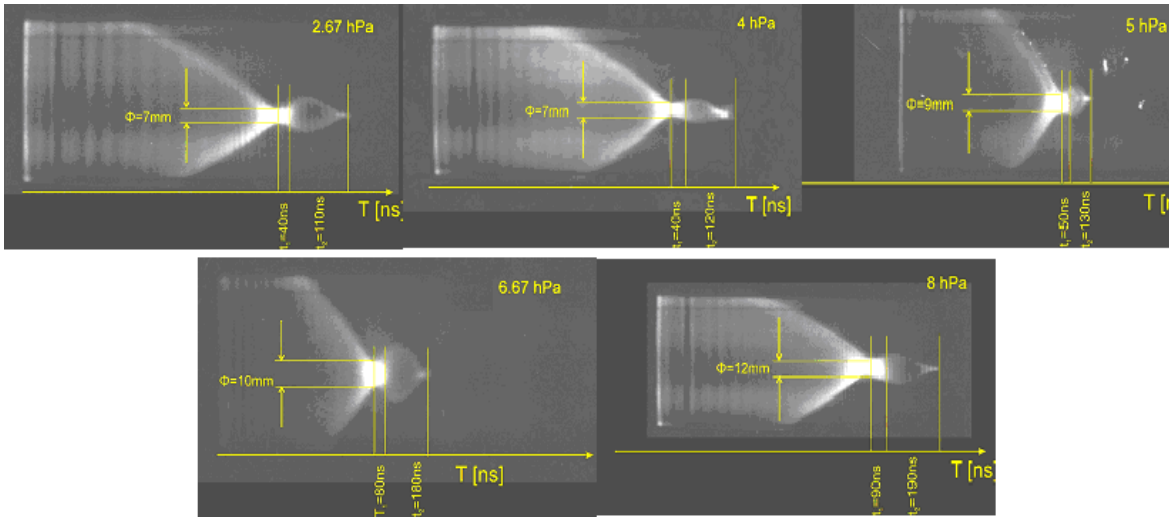

FIG. 9. Streak camera pictures taken at different initial deuterium pressures in the PF-1000 chamber.

The investigations of the process of creation and disruption of the pinch have demonstrated that two pinches are characteristic for this phase of the discharge (if one can interpret in that way two regions of the luminosity occurring on streak images). It has been found from streak camera images obtained for discharges with similar neutron yield that the time intervals, lifetime of the pinch and its dimensions strongly depend on the pressure of the deuterium filling gas. It has also been found that the time interval between pinches depends on the total neutron yield for the same pressure. For larger neutron yields the time interval decreases. As shown in Fig. 10, the second pinch is not observed when there is no significant neutron yield.

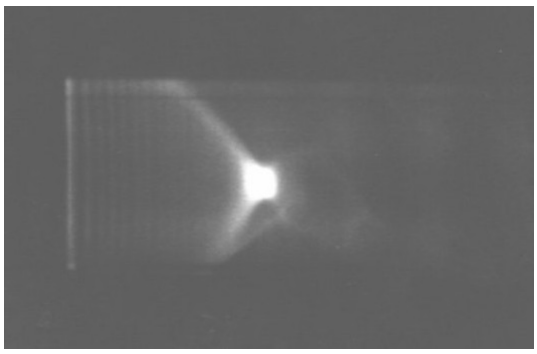

FIG. 10. Streak camera picture taken for a shot with no neutron yield.

One interpretation of this phenomenon could be based on the relationship between neutron production and the magnitude of the current flowing through the plasma (neglecting axial outflow of the current from the pinch). In the case of large current, the associated magnetic field exerts a large pressure on plasma and does not allow for long free expansion of the pinch, this results in a rapid second pinch. These two pinches are observed as two luminous points located close to each other on streak images. However, when the current and neutron yield are low the weak magnetic field does not balance gasokinetic plasma pressure until the plasma particle concentration decreases strongly (i.e. until the radial expansion of the pinch has continued for a sufficient length of time). And as a result the second pinch occurs after a much longer time.

The obtained streak images allowed us to estimate the acceleration of plasma sheath on the system axis during the final stage of compression. The acceleration of the plasma sheath on the radius of 45 mm for the pressure p = 5 hPa is presented on Fig. 9. Maximum velocity just before the pinch on the axis was estimated as 4.5×10^7 cm/s. Those values are 5×10^7 cm/s and 3×10^7 cm/s for pressures 2.67 hPa and 8 hPa, respectively. These streak camera images also enabled us to determine how the mean velocity of the plasma sheath (during the radial compression phase) varied with the pressure of the deuterium filling gas. The experimental results are presented in Fig. 11.

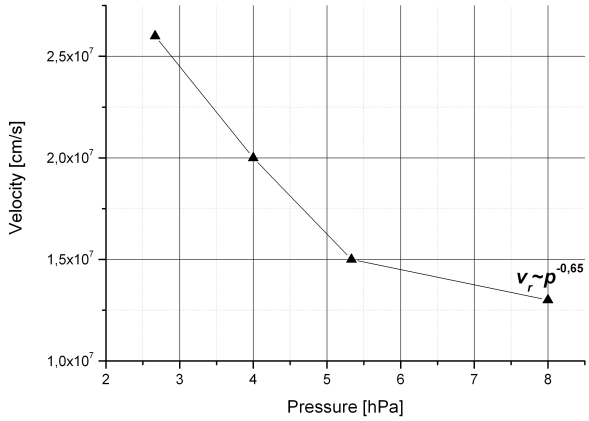

FIG. 11. Mean velocity of a plasma sheath during radial compression phase versus deuterium filling pressure.

The dependence of v_r on p is much lower than the theoretical prediction ($v_r \sim p^{-1}$) given by Trunk. No effective "sweeping of the gas" on the system axis during the radial compression phase can explain this result.

5. PROGRESS IN STUDIES OF THE PINCH PHASE

The pinch phase of PF discharges has also been investigated extensively. Use was made of high-speed smear- and frame- cameras and the other diagnostic tools, as described above. Some examples of the recorded traces and high-speed VR pictures are shown in Fig. 12.

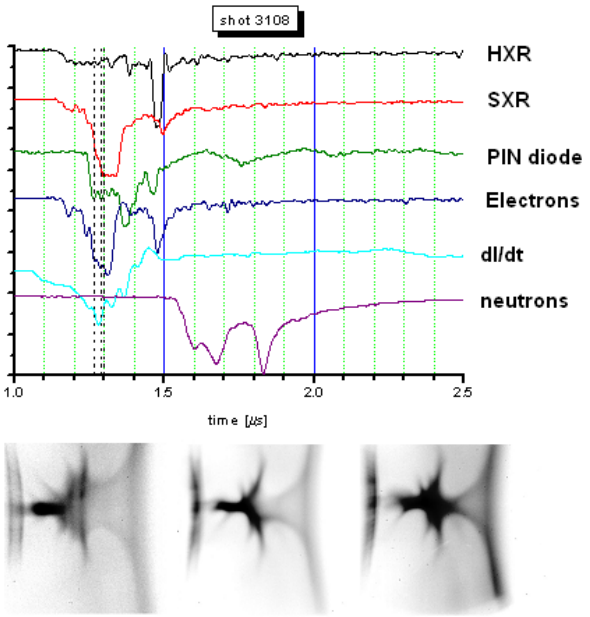

FIG. 12. Time resolved traces and high-speed pictures of the pinch phase in the PF-1000 experiment performed at po = 4 hPa, Wo = 734 kJ and Imax =1.66 MA. The images correspond to instants indicated by broken lines.

Typical sequence of the frame pictures taken in visual wavelength range with the operation of the device at the same initial condition and with similar neutron yield (by four frames during shot 4618 and 5055) is presented in Fig. 13.

A radiating pinch column of minimum diameter equal to ~ 5 mm and 5 cm in length is observed. This phase ended with the formation of a dense spherical structure of ~ 1 cm in diameter (Fig. 13(d)). The spherical structure is situated 6–8 cm from the anode end, in the top of the focus region and at the bottom of the dilated current sheath. The second pinch, i.e. the implosion of the weak radiating surface that surrounded dark regions (of low temperature and density) was recorded on Figs 13(d). During this phase, the pinch diameter decreased considerably, but the intensity of the radiation increased noticeably. The explosion of the second pinch was probably very fast and it was not recoded on frame images. Only a dense structure situated ~ 8 cm in front of the anode, at the bottom of the dilated current sheath, similar to the structure after the first pinch was recorded. The evolution of the pinch phase, as shown in these frames, was observed around the time of the neutron production. At t = 120–130 ns the hot and dense second pinch was formed in correlation with the second implosion, as recorded in the streak-camera image shown in Fig. 14 (shot 5055).

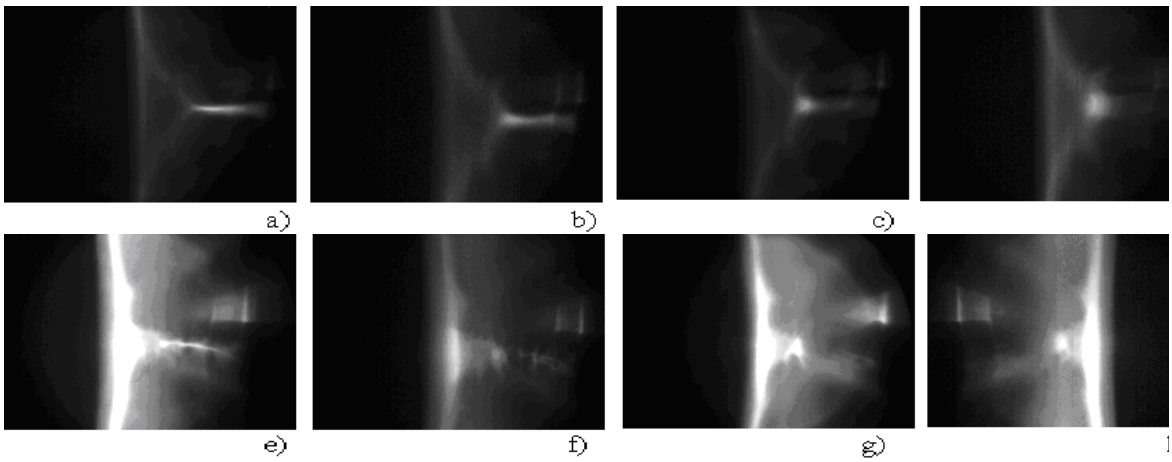

FIG. 13. Typical sequence of the frame pictures taken in visual wavelength range, at the operation of the PF-1000 device under the same initial conditions and with similar neutron yield (eight frames were taken during shots #4618 and 5055).

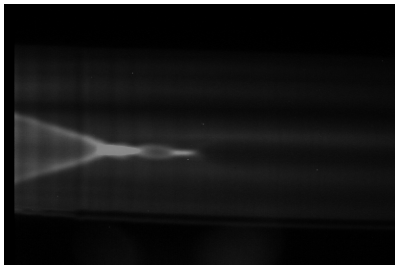

FIG. 14. Streak camera picture (taken during shot #5055) showing the double pinch effect.

6. PF EMISSION CHARACTERISTICS

The emission of X rays from PF discharges was investigated with different techniques: pinhole cameras, scintillation detectors and crystal spectrometers. Numerous data were collected and reported.

Comparing obtained streak images with other diagnostics it can be stated that hard X ray radiation impulse is generated from the first pinch in most discharges while soft X ray impulse is generated from the first and the second pinch Fig. 15.

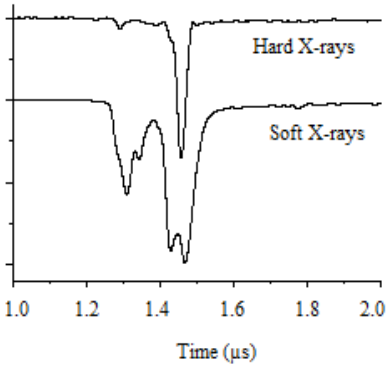

FIG. 15. Hard and soft X ray pulses obtained from PF-1000 shot #3128.

There have been also discharges, in which hard X ray impulse has been connected in time with second pinch especially when the neutron yield has been large.

The emission of accelerated primary ions (mainly deuterons) was investigated with different techniques, as described above. Angular distributions of the emitted ions have been measured by means of NTD samples placed at various angles and fixed upon the semi-circular support, as shown in Fig. 16.

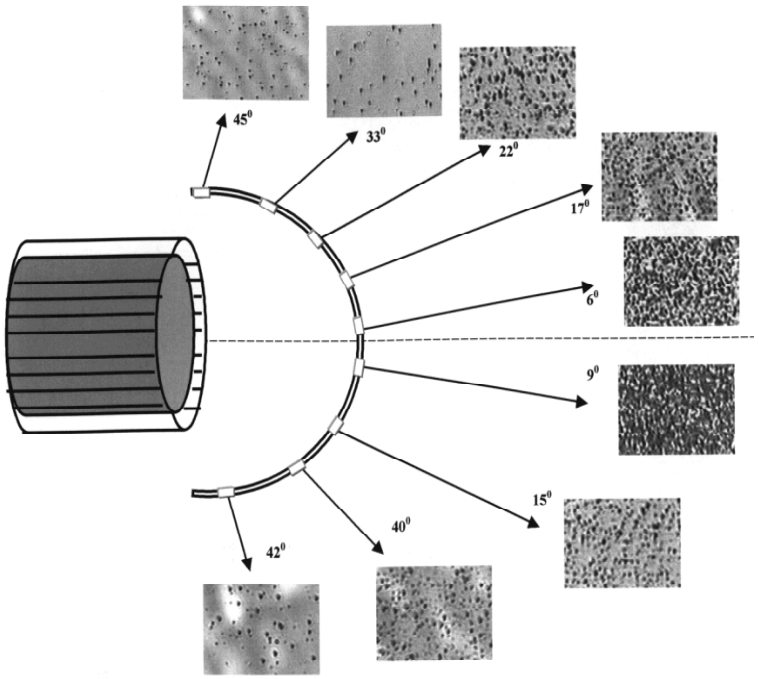

FIG. 16. Ion angular distribution in the PF-1000 facility, as measured by means of NTDs placed at different angles to the z-axis.

Energy spectra of these fast ions have also been investigated, but they are not of direct importance for the D-D fusion reactions occurring mostly within the dense magnetized plasma column. During recent PF experiments particular attention has been paid to the emission of fast neutrons produced by the D-D fusion reactions.

The fusion neutron yield was measured for the PF-1000 device for standard experimental conditions. The facility was operated at the same conditions during each shot, i.e. the deuterium filling pressure was p_o = 4.7 hPa, the charging voltage of condenser bank was U_0 = 27 kV, and energy stored in the condenser bank was W_0 = 480 kJ. The total discharge current achieved the maximum of 1.8–1.9 MA, and the rise time was equal to about 7.5 μs with a relatively good repeatability, as was measured with a Rogovski coil (see Fig. 17).

In order to measure the total neutron yield and neutron angular distributions at the PF-1000 facility, there were designed and manufactured five silver-activation counters. The neutron yield was measured at angles equal to 30º, 60º, 90º and 150º in relation to the z-axis. The activation counters were placed around the main PF-1000 experimental chamber, as shown in Fig. 18.

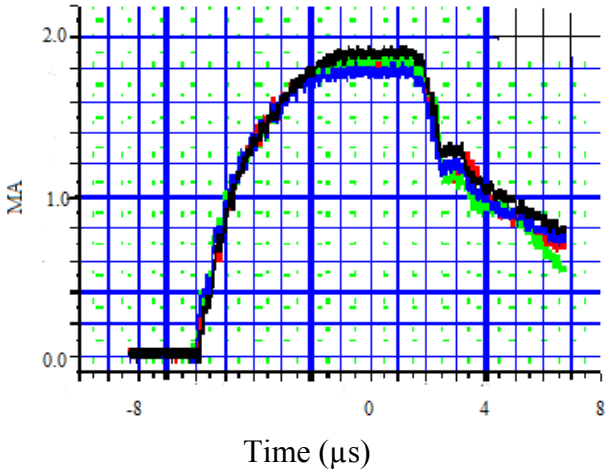

FIG. 17. The total discharge current from Rogovski coil for different shots with the same experimental conditions: pD = 4.67 hPa, U0 = 27 kV.

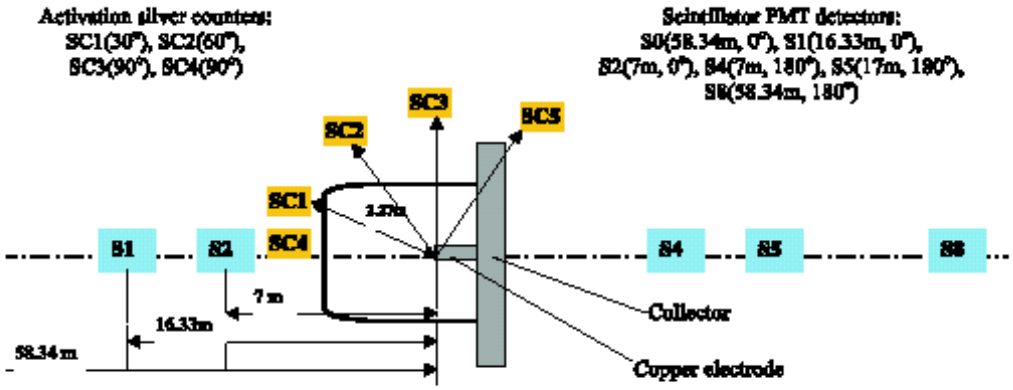

FIG. 18. The location on silver activation counters and PMT probes with reference to the electrodes.

To make appropriate corrections of the data because of the neutron scattering, use was made of an AmBe steady state neutron source which was placed inside the PF-1000 chamber. Most of the background scattering materials had high Z values. Nevertheless, small thicknesses of the metal walls (and other parts) require significant intensity corrections. The use of the steady state neutron source, characterized by a different energy spectrum (i.e. AmBe), rather than pulsed D-D neutron source, makes calibration by this method undesirable.

In order to perform the detailed TOF measurements of the neutron emission and the hard X rays (penetrating a 3 to 5 cm thick wall made of stainless steel or lead, which was used as a filter), use was made of six probes equipped with NE-102 scintillators and fast photo-multipliers (as shown in Fig. 18). They were located at different angles and at various distances: at 0° — at distances of 7.0 m, 16.3m and 58.3 m; and at 180° — at distances of 7.0 m, 16.3 m, and 58.3 m, respectively. At the PF-1000 device the angles $\theta = 0°$ and $\theta = 180°$ correspond to the downstream- and upstream- direction, respectively. Typical signals of X rays and neutrons emitted from the source at the instant of 150 ns, are presented in Fig. 19.

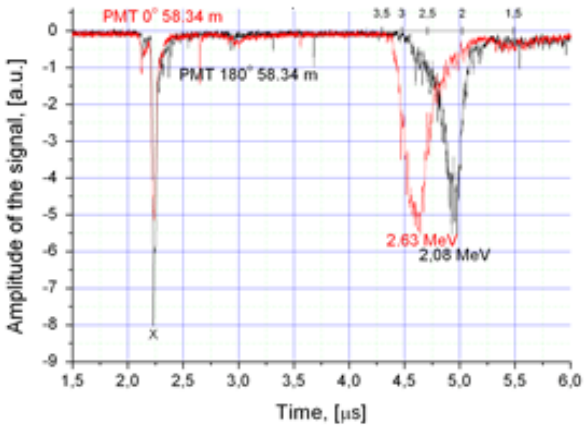

FIG. 19. Typical hard X ray and neutron signals from PMT located at the distance 58.34 m, at the angles 0° and 180°.

The energy resolution of the TOF method is given by the known formula:

$$\frac{\Delta E}{E} = 2\frac{\Delta t}{t_f}$$

where D_t is the neutron production period and t_f is the particle time of flight. In the described experiment those values were as follows: D_t = 150–180 ns and t_f = 2.69 μs, corresponding to the time of flight of 2.45 MeV neutrons over the distance of 58.3 m. Hence, the energy resolution was equal to 11 to 13 %.

The half-width and shape of the neutron energy spectrum can be used for comparison with predictions of the models mentioned above. However, both the half-width and the shape of the measured neutron energy spectrum are affected by neutron scattering. Thus, the overall energy resolution, including all the effects considered, has been estimated to be below 13%. Hence, only the energy values corresponding to the peak of the neutron induced TOF signal were evaluated.

The results obtained from a few recorded signals at distances of 58.3 m, at angles of 0° and 180° in relation to the pinch axis, have been shown in Table 1.

TABLE 1. SIGNALS AT DISTANCES OF 58.3 M, AT ANGLES OF 0° AND 180° IN RELATION TO THE PINCH AXIS

Shot No.	t_n 0°	t_n 180°	E(0°)	E(180°)	E(0°)-2.45	2.45-E(180°)
5544	4.734×10^{-6}	5.055×10^{-06}	2.69	2.14	0.24	0.31
5566	4.615×10^{-6}	5.035×10^{-06}	2.90	2.12	0.45	0.33
5569	4.643×10^{-6}	4.956×10^{-06}	2.63	2.08	0.18	0.37
5575	4.509×10^{-6}	4.789×10^{-06}	2.66	2.17	0.21	0.28
5592	4.623×10^{-6}	4.911×10^{-06}	2.66	2.15	0.21	0.30
5605	4.770×10^{-6}	5.158×10^{-06}	2.80	2.10	0.35	0.35
5620	4.860×10^{-6}	5.147×10^{-06}	2.58	2.06	0.13	0.39
5649	4.573×10^{-6}	4.874×10^{-06}	2.69	2.14	0.24	0.31

In Table 1 values E(0°) and E(180°) are the energy values corresponding to the peak of the neutron TOF signal in 0° and 180°, respectively. The average maximum energy of the neutrons was found to be at 0° equal to 2.70 MeV, and at 180° — to about 2.12 MeV, respectively.

The angular distribution of the neutron emission and the ratio of the neutron intensity measured at 30° to those determined at angles of 60°, 90° and 150° are shown in Table 2.

TABLE 2. ANGULAR DISTRIBUTION OF THE NEUTRON EMISSION AND THE RATIO OF THE NEUTRON INTENSITY MEASURED AT 30° TO THOSE DETERMINED AT ANGLES OF 60°, 90° AND 150°

	L1(30°)	L2(60°)	L3(90°)	L5(150°)	L_1 / L_2	L_1 / L_3	L_1 / L_5
544	1.87×10^{11}	1.48×10^{11}	2.03×10^{11}	1.70×10^{11}	1.26	9.21×10^{-1}	1.10
566	1.56×10^{11}	9.88×10^{10}	1.49×10^{11}	1.40×10^{11}	1.58	1.05	1.11
569	1.95×10^{11}	1.71×10^{11}	1.76×10^{11}	1.79×10^{11}	1.14	1.11	1.09
575	1.99×10^{11}	1.82×10^{11}	1.92×10^{11}	1.82×10^{11}	1.09	1.04	1.09
592	1.46×10^{11}	1.31×10^{11}	1.34×10^{11}	1.46×10^{11}	1.11	1.09	1.00
605	2.38×10^{11}	2.48×10^{11}	2.28×10^{11}	2.13×10^{11}	0.96	1.04	1.12
620	1.17×10^{11}	1.34×10^{11}	1.14×10^{11}	1.08×10^{11}	0.87	1.03	1.08
649	1.56×10^{11}	1.36×10^{11}	1.55×10^{11}	1.50×10^{11}	1.15	1.01	1.04

The average intensity ratios were found to be $(L_1/L_2) = 1.15$, $(L_1/L_3) = 1.03$ and $(L_1/L_5) = 1.08$, respectively. In general, it was observed that the intensity ratio changes slightly near the value of 1.00.

Since the neutron energy values measured in the downstream- and upstream- directions appeared to be different, one should consider plasma models, in which the use is made of motion of the center-of-mass. Motion of the center-of-mass (c.m.) is considered in the beam-target model or in a model in which a portion of plasma ions moves with a velocity v_{cm} along the z-axis (i.e. in an isotropic moving plasma model). In such a model a neutron emitted with velocity u_{cm} at angle of 0º and 180º in the c.m. in relation to the v-direction will have a laboratory energy given by:

$$E(0^0) = E_{ncm}\left(1+\frac{v}{u_{cm}}\right)^2, \qquad E(180^0) = E_{ncm}\left(1-\frac{v}{u_{cm}}\right)^2$$

where E_{ncm} is the neutron energy in the c.m. system.

These equations have been rewritten to give the neutron energy ratio at 0º in relation to that observed at an angle of 180º in the laboratory frame, and that center of mass ions velocity can be evaluated. The quantity $r = v/u_{cm}$, where $u_{cm} = 2.17\times10^9$ cm/s, gives a value for v of 1.32×10^8 cm/s.

Since our optical and neutron observations of the axial motion of plasma have indicated velocities of about 10^8 cm/s, the center-of-mass velocity equal to about 1.32×10^8 cm/s seems to be a realistic one. On the other hand, considering the formula for the angular distribution function in the general case, in which the deuterons impinge upon a cold stationary target at an angle θº, we can see that the angular distribution expected for the target-beam model for the considered incident angles shows the distinct maximum at 90º. In contrary, the experimental intensity distribution of neutrons (see Table 2) shows another character. It suggests that the moving plasma model agrees better with the experimental data. However, three or two peaks in the hard X ray signals and the subtle structure of the neutron induced signals (see Fig 20.) have been observed for many PF shots.

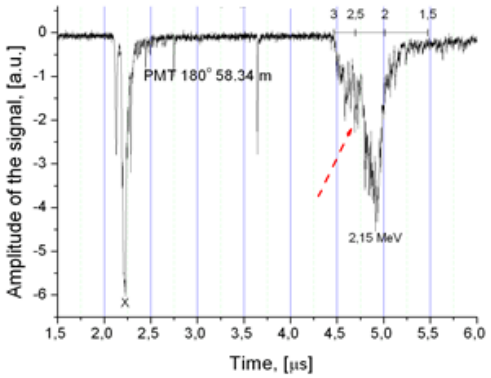

FIG. 20. The hard X ray and neutron signals from PMT located at the distance 58.34 m, at the angles 0^0 and 180^0.

It shows that two or three pulses of fast neutrons of different maximum energy values can be emitted from the PF pinch column.

In general, PF discharges with the highest neutron yields are not necessarily the ones with the strongest anisotropy. High neutron yields were observed in some large scale PF experiments, when the first predominant neutron pulse was characterized by a reduced anisotropy. In order to optimize the operation of the chosen PF facility and to estimate possibilities for an increase in the fusion neutron yield, one should analyze the whole circuit of the PF discharge. For this purpose one should consider energy (W_{in}) supplied to the system, energy cumulated within the pinch ($W_{\text{pinch-internal}}$) which can be divided into two components: thermal (W_{th}) and fast beam ($W_{\text{fast-ion}}$). The final neutron yield is in fact determined both by the thermo-nuclear processes and beam-target interactions, as shown in Fig. 21.

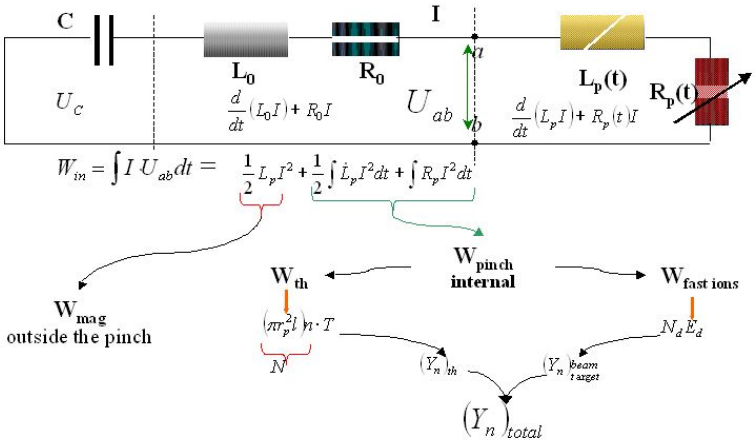

FIG. 21. Simplified PF-discharge circuit showing the parameters which determine the total neutron yield from D-D fusion reactions.

Such an analysis, which should be performed for realistic experimental parameters, may deliver valuable information how to increase the total neutron production.

7. SUMMARY AND CONCLUSIONS

The most important conclusions from this review can be formulated as follows:

(1) The PF-1000 facility has been operated at the energy level exceeding 1 MJ, with a regular and reproducible neutron emission of the order of 10^{10}–10^{11} neutron/shot, but

optimization of PF machine operation, analysis and optimization of the fusion yield is needed.

(2) The highest neutron yield registered so far has achieved about 3.5×10^{11}, but it is expected that higher emission will appear after appropriate conditioning of the insulator and electrode surfaces.

(3) A two dimensional approach describing the initial formation of the current sheath near the insulator (breakdown phase) has been proposed. This model is based on the continuity equations for electron and ions, Poisson's equation, and Townsend formula for ionization coefficient. The results of calculations from the model agree relatively well with results of experimental observations To study the breakdown phase an improved model should be developed and the dedicated experiments should be run with special preformed insulators or localized gas puffing.

(4) The soft X ray emission, as measured with PIN diode equipped with a pinhole covered with a 10-μm Be-foil, seems to be proportional to the neutron yield.

(5) In case of high neutron yields from PF-1000, the typical neutron signal usually shows a double structure with the second pulse more intense than the first one (Fig. 9).

(6) The first pulse correlates with soft X ray and the second pulse corresponds to the beam emission. This can be interpreted as the first pulse comprisingly mainly thermal neutrons and the second pulse — neutrons produced by the beam target mechanism.

(7) It has been shown, that the sheath structures of experimentally recorded plasma images are at least in qualitative agreement with the results taken by MHD numerical modeling. However, further improvements of numerical modeling are necessary. The role of current-sheath symmetry and uniformity must be investigated.

(8) Two phases of the pinch development are observed by frame camera.

(9) It was confirmed by streak camera.

(10) Stable plasma radiating structures situated on the end of pinch column is observed in each phase of the pinch development.

(11) A correlation between the two phases of pinch evolution and generation of soft and hard X ray radiation is observed.

(12) Total neutron yield to depend on the time intervals between pinches.

(13) The neutron measurements showed that the neutron energy value can be evaluated from the time delay between the maximum X ray and neutron peaks, as obtained from the signals measured with scintillation probes placed at distances of m 58.3 m. In fact, the neutron spectrum $f(E,t)$ is the convolution of two independent functions: the first function is the real energy spectrum and the second one is that determining the time of the neutron production. Therefore, it is difficult to separate these functions. In order to determine the time dependent neutron energy spectrum $f(E,t)$ during a single discharge, one would require to use about ten probes located at different distance and special mathematical deconvolution procedure.

(14) It has been shown that the long neutron path, observed for TOF detectors located upstream and downstream the PF system, can be used as a convenient tool for evaluations of the most probable and maximum neutron energy values. The results of these measurements as well as the neutron yield angular distribution have been used to compare the moving plasma model and the beam-target approach. In view of this, the real physical mechanisms leading to ion acceleration and forming the specific properties of the main (well localized) neutron source are still unknown. However, the summary of the results obtained in this experiment suggest that a more sophisticated model is needed, e.g. similar to that presented in [13].

ACKNOWLEDGEMENTS

Work was carried out in close cooperation with scientists from the following organizations:

- Institute of Plasma Physics and Laser Microfusion, 00-908 Warsaw, Poland;
- Czech Technical University, Technicka 2, 166 27 Prague 6, Czech Republic;
- Soltan Institute for Nuclear Studies (IPJ), 05-400 Otwock–Świerk, Poland;
- International Centre for Dense of Magnetised Plasmas, 00-908 Warsaw, Poland;
- National Inst. for Laser, Plasma and Radiation Physics, Magurele-Bucharest, Romania;
- ENEA, Centro Ricerche Brasimone, 40032 Camugnano, Bologna;
- Laboratorio di Montecuccolino; (DIENCA), University of Bologna, 40136 BO, Italy.

The most important scientific results of those investigations will be presented on following conferences:

- 13th International Summer School on Vacuum, Electron and Ion Technologies, 15–19 September 2003, Varna, Bulgaria;
- 21st Symposium on Plasma Physics and Technology, 14/06–17/06/2004, Prague, Czech Republic;
- 13th International Symposium On High Current Electronics, Tomsk, Russian Federation, July, 2004.

Besides, the scientific results there are the following human benefits of the experimental session:

- Meeting of known research who are working in dense magnetized plasma.
- Scientific discussion and training young research during the experimental session.

REFERENCES

[1] HEROLD, H., JERZYKIEWICZ, A., SADOWSKI, M., SCHMIDT , H., Nuclear Fusion 29 (1989) 1255.
[2] SADOWSKI, M. J. and SCHOLZ, M., Results of large scale Plasma-Focus experiments and prospects for neutron yield optimization, Nukleonika, 47(1) (2002) 115–155.
[3] KASPERCZUK, A., KUMAR, R., MIKLASZEWSKI, R., PADUCH, M., PISARCZYK, T., et al., Study of the plasma evolution in the PF-1000 device by means of optical diagnostics, Phys. Scripta, 65 (2002) 96–102.
[4] SCHOLZ, M., MIKLASZEWSKI, R., PADUCH, M., SADOWSKI, M. J., SZYDŁOWSKI, A., et al., IEEE Trans. Plasma Sci., 30(2) (2002) 476–481.
[5] SCHMIDT, H., KASPERCZUK, A., PADUCH, M., PISARCZYK, T., SCHOLZ, M., TOMASZEWSKI, K., AND SZYDŁOWSKI, A., Phys. Scripta, 66 (2002) 168–172.
[6] SCHOLZ, M., BIENKOWSKA, B., et al., Czech. J.Phys. 52 (2002) Suppl. D100.
[7] SADOWSKI, M.J., et al., Proc. Intern. Workshop DMP, Warsaw, Poland, 2003, p.I–1.
[8] J.W. MATHER in “Methods of experimental physics” ed by R.H. Lovberg, H.R. Griem, Vol. 9 Acad. Press, New York — London 1971,pp, 187–249.
[9] SADOWSKI, M.J., SCHOLZ, M., in Proc. 30th EPS Conf. on CFPP, St. Petersburg, Russian Federation; ECA 27A, 1.207 (2003).
[10] MATHER, J.W., Phys. Fluids Suppl. 7 (1964) 528.
[11] TRUNK, M., Plasma Phys. 17 (1975) 237–248.
[12] BERNSTEIN, M.J., COMISAR, G.G., Phys. Fluids, 13 (1972) 700.
[13] JAGER, U., HEROLD, H., Nuclear Fusion 27 (1987) 407.

[14] STĘPNIEWSKI, W., MHD numerical modelling of the plasma focus phenomena, Vacuum, 76 (2004) 51–55.

PLASMA FOCUS FUSION RESEARCH IN SINGAPORE

S.V. SPRINGHAM, M.V. ROSHAN, F. MALIK, T.H. SIM, S. MAHMOOD, S.M. HASSAN, P.M.E. SHUTLER, T.L. TAN, R.S. RAWAT, P. LEE
National Institute of Education
Nanayang Technological University
Singapore

Abstract

Protons from two fusion reactions — D(^{3}He,p)^{4}He and D(d,p)^{3}H — were measured for a small plasma focus device operated with a ^{3}He-D_2 gas mixture. A pinhole camera on the forward plasma focus axis imaged the emission zones of protons for both reactions. For the sake of comparison, analogous experiments were performed with a ^{4}He-D_2 gas mixture and pure D_2 gas. For the ^{3}He-D_2 and ^{4}He-D_2 gas mixtures the He to D_2 partial pressures were in the ratio of 2:1, corresponding to an atomic number ratio of 1:1. For the ^{3}He-D_2 gas mixture two groups of protons with energies of approximately 3 and 15 MeV were observed: products of the D(d,p)^{3}H and D(^{3}He,p)^{4}He reactions, respectively. These protons were recorded simultaneously using a double-layer arrangement of CR-39 polymer nuclear track detectors. For the ^{4}He-D_2 and D_2 gases, D(d,p)^{3}H protons were measured using a single layer of CR-39. For the ^{3}He-D_2 gas mixture it was found that the D(^{3}He,p)^{4}He and D(d,p)^{3}H proton yields were of similar magnitude, but their angular distributions were very different. Monte Carlo simulations were performed to interpret the measured angular distributions in terms of an isotropic pinch-source contribution and an anisotropic beam-target source over an extended conical volume. It was found that both the D(^{3}He,p)^{4}He and D(d,p)^{3}H fusion yields are produced predominantly by the beam-target mechanism: any contribution from thermonuclear fusion being less than 10% of the total yield. For the case of pure D_2 gas, a magnetic spectrometer was employed to measure the energy spectra of forward axially-directed deuterons emitted from the plasma focus pinch. Spectra for a large number of plasma focus shots were measured, enabling the correlation between the intensity of the deuteron beam and the associated neutron yield to be studied at each of three working gas pressures. A clear positive correlation was observed at each gas pressure, further supporting the conclusion that the beam-target fusion mechanism is dominant for this small plasma focus device.

1. INTRODUCTION

When operated with deuterium gas, the plasma focus (PF) device produces intense short duration bursts of fusion neutrons and protons: from the D(d,n)^{3}He and D(d,p)^{3}H reactions, respectively. However the details of the fusion mechanisms involved are still not well understood. The majority of previous experimental investigations have focussed on the characteristics of the neutron bursts, with both the neutron pulse duration (~100 ns) and the observed neutron anisotropy [7] providing clear evidence for the importance of non-thermal fusion processes. In addition, investigations of the deuteron-ion beam energy, spatial, and temporal distributions employing Faraday cups [8, 9] and magnetic spectrometers [10, 11] have underlined the importance of the beam-target mechanism in which energetic deuterons emitted from the plasma focus pinch interact with the cold deuterium gas. In contrast to the substantial amount of work related to fusion neutrons, experimental investigations of fusion protons have been comparatively rare. Notable exceptions to this trend are the proton measurement on the Poseidon plasma focus made during the 1980's [12, 13]. These experiments demonstrated that measurements of fusion protons can provide more precise energetic and spatial information than the corresponding neutron measurements.

In this paper we report measurements of plasma focus fusion protons from two nuclear reactions: D(d,p)^{3}H and D(^{3}He,p)^{4}He (henceforth abbreviated to DD and ^{3}HeD). DD protons are studied for pure D_2 gas, as well as mixtures of D_2 with ^{3}He or ^{4}He gas. Of course ^{3}HeD protons are measured only for a D_2 and ^{3}He gas mixture. Furthermore, a magnetic spectrometer is used to investigate the energy distribution of axially emitted deuterons for the case of pure D_2 gas only. All experiments are performed on a 3.1 kJ UNU/ICTP plasma focus device operated at 14 kV charging voltage.

With regard to DD and ^{3}HeD reactions, it is important to note that they have very different *Q*-values: being 4.03 MeV for DD and 18.35 MeV for ^{3}HeD. Hence the outgoing protons have very different energies: ~3 MeV for DD and ~16 MeV for ^{3}HeD. For the very few previously reported experiments performed with a ^{3}He-D_2 PF gas mixture the ~16 MeV ^{3}HeD protons were detected by nuclear emulsion [14] or the proton activation of copper [15]. In the present work, CR-39 polymer nuclear track detectors were employed to simultaneously image the spatial distributions of the DD and the ^{3}HeD fusion reactions by means of a pinhole camera located on the forward PF axis ($\theta = 0^o$).

2. PLASMA FOCUS DEVICE

The device used for these experiments is UNU/ICTP plasma focus [16] with a hollow copper anode of length 16 cm and 19 mm diameter, surrounded by six copper cathodes in a squirrel cage configuration at a radius of 3.2 cm. Hence this device is of the Mather-type geometry [17]. The chamber has a diameter 160 mm and the anode to top-plate distance is 170 mm. The system is energized by a 32 μF capacitor and has an overall inductance of 110 nH, giving a discharge quarter period time of 2.9 μs. The PF discharge is triggered by a simple parallel-plate spark gap with a swinging cascade configuration. A charging voltage of 14 kV is used throughout the experiments, giving a stored bank energy of 3.1 kJ.

For pure D_2 filling gas the neutron optimised regime corresponds to a gas pressure in the range 300 to 450 Pa. Under these conditions a peak focus current of about 170 kA and an approximate neutron yield of ~10^8 are obtained. When operated with ^{3}He-D_2 or ^{4}He-D_2 gas mixtures the average neutron yield is reduced to ~3×10^6 per shot. The electrical diagnostics employed are a Rogowski coil for the focus current, and a voltage probe comprising a high-voltage resistive divider. The neutron yield (into 4π sr) for each shot was determined by means of a paraffin moderated indium foil activation counter. The typical statistical uncertainty associated with the neutron yield measurement is ~6%.

3. PROTON PINHOLE CAMERA

The proton pinhole camera, shown schematically in Fig. 1, is fixed to the chamber top plate on the forward PF axis ($\theta = 0^o$). The diameter of the camera pinhole is 8 mm and the distance from entrance pupil to the tip of the anode is 120 mm. Within the camera the CR-39 detectors are positioned 34 mm from the entrance pupil, and the exposed area is a circle of diameter 20.4 mm. The relatively large pinhole diameter is necessitated by the observed low proton yields; consequently, the resulting pinhole image has only moderate angular resolution (approximately 7º half-angle).

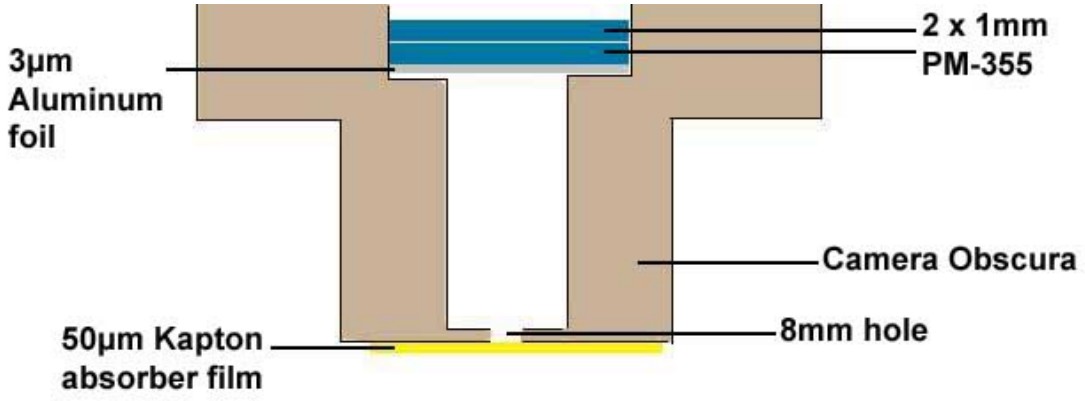

FIG. 1. Schematic diagram of the proton pinhole camera showing positions of CR-39 detectors, aluminium and kapton filters.

In order to record only protons from the fusion reactions, a 50 μm kapton filter was used to stop all other energetic charged particle. In addition, a 3 μm aluminium foil was placed between the kapton film and the front CR-39 detectors to eliminate any possible effect on the detectors from the visible and UV radiation emitted during the PF discharge.

3.1. ^{3}HeD and DD Protons: Energy and Range

SRIM simulations [18] show that normally incident 3.0 MeV protons (from DD fusion) pass through 50 μm of kapton, 3 μm of aluminium, and traverse 65 μm of CR-39 before being stopped. Taking 16.0MeV as the upper energy limit of the ^{3}HeD protons, the corresponding path length in CR-39 is 2,220 μm (after passage through the kapton and aluminium filters). It was therefore determined that the optimum detector arrangement was two CR-39 detectors each of 1000 μm thickness placed behind the kapton and aluminium filters. With this arrangement only DD protons are registered on the front-most CR-39 surface, and only ^{3}HeD protons are registered on back-most surface. The specific energy loss at the front CR-39 surface is much lower for the ^{3}HeD protons (5 keV/μm) than for the DD protons (20 keV/μm); this difference explains the insensitivity of CR-39 to full energy ^{3}HeD protons.

The double layer arrangement of CR-39 detectors was employed for all PF shots fired with a ^{3}He-D_2 gas mixture. Whereas a single CR-39 detector layer (1000 μm thick) was used when the PF was operated with a ^{4}He-D_2 gas mixture or pure D_2 gas, as only DD protons are produced.

4. PROCEDURE FOR GAS MIXTURE EXPERIMENTS

4.1. ^{3}He–D2 Gas Mixture

Deuterium and ^{3}He gases were mixed in the PF chamber with partial pressures in the ratio of 1:2 (corresponding to a 1:1 atomic number ratio) using pressure transducer with a precision ~ 1 Pa. Operation of the PF device was tested for a range of total pressures ranging from 420 to 600 Pa. A total gas pressure of 480 Pa was chosen for the ^{3}He–D_2 measurements on the basis that it gave a suitable plasma sheath rundown time (approximately ¼ of the discharge period) and sharp peaks in the *dI*/*dt* trace.

Two further series of experiments were performed in which the PF was operated with a ^{4}He–D_2 gas mixture and pure D_2 gas; the motivation being to compare the DD fusion distributions obtained for these gases with that found for the ^{3}He–D_2 mixture. Table 1, summarizes the exposures made with each of the three gases. All CR-39 detectors were etched for 24 hours in 6.25M NaOH solution at 70 ºC. The detectors were then scanned using an automated system [19]. Spurious tracks were eliminated from the analysis by applying shape, size and grey value criteria to the dark features recognized and measured by the image processing software. The scatter plot in Fig. 2 shows the *x*-*y* distribution of proton tracks recognized by the system on one front detector exposed to 24 PF shots (^{3}He–D_2 gas mixture).

4.2. ^{4}He–D_2 Gas Mixture

In order to obtain the best comparability of results, the mass density for the ^{4}He–D_2 gas mixture (1:1 atomic ratio) was chosen to be equal to that for the ^{3}He–D_2 mixture. This ensured that the dynamics of the plasma focus discharge were most nearly the same for the two cases. Therefore the total pressure used for the ^{4}He–D_2 mixture was 400 Pa, as shown in Table 1.

TABLE 1. EXPOSURES PERFORMED FOR EACH OF THE THREE GAS MIXTURE

Experimental Series		Gases & Pressures (Pa)	No. of Exposed Detectors	Total No. of PF Shots	Total No. of Proton Tracks (1000's)
(I)	$^3He–D_2$	^3He (320) + D_2 (160)	5 front (DD)	119	67.5
			5 back (^3HeD)		66.4
(II)	$^4He–D_2$	^4He (267) + D_2 (133)	12	384	258.2
(III)	D_2	D_2 (400)	12	12	160.1

4.3. Pure D_2 Gas

For the case of pure D_2 gas it is not possible to ensure that the PF dynamics are comparable to the $^3He–D_2$ case due to the dissimilar thermodynamic properties of these gases. Instead we chose to operate the PF with 400 Pa D_2 gas, corresponding to the neutron optimized regime for this device. For pure deuterium the DD yield is much higher than for the $^3He–D_2$ mixtures, and a single PF shot was sufficient to expose each CR-39 detector.

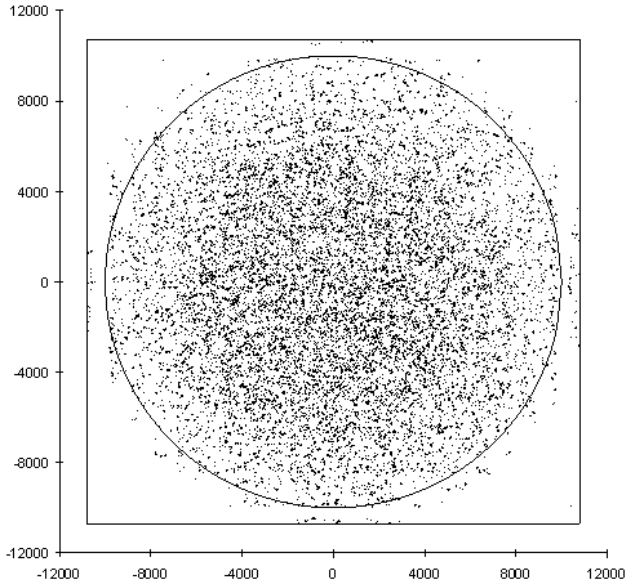

FIG. 2. Spatial distribution of DD proton tracks on front surface of one CR-39 detector. Units for axes are microns. ($^3He–D_2$ gas mixture).

5. RESULTS AND DISCUSSION FOR GAS MIXTURE EXPERIMENTS

The track information extracted from the CR-39 detectors by the scanning system was analyzed in a similar manner to that described in Ref. [20]. Radial track density distributions were obtained for each detector, with concentric 0.5 mm annular rings representing the bins for the distribution, resulting in 20 radial bins. For each gas, the individual detector distributions were summed and divided by the total number of PF shots to give a per shot average distribution.

5.1. ^{3}He-D_2 Gas Mixture

Figure 3 shows the radial distributions for both ^{3}HeD and DD protons obtained for the ^{3}He–D_2 gas mixture. A very pronounced central peak is apparent in the ^{3}HeD distribution. By contrast the DD distribution displays a significantly broader and shallower central peak. Also the number of proton tracks on the front and back detectors are found to be very similar (see Table 1). Therefore, despite the different spatial distributions associated with the ^{3}HeD and DD fusion, it is apparent that the total proton yields for the ^{3}HeD and DD reactions are similar.

With regard to thermonuclear fusion, the reaction rates $\langle \sigma v \rangle$ given in Ref. [21] show that the ^{3}HeD rate falls off very rapidly for plasma temperatures below ~20 keV. At 4 keV the ^{3}HeD rate is more than an order of magnitude lower than the DD rate. Time and space resolved X ray measurements [22] indicate that when neutron emission begins, the pinch temperature is ~1 keV. Assuming that the atomic number density of D and ^{3}He ions in the pinch column is 1:1 (as it is in the ambient gas) then the DD thermonuclear yield should be many times greater than the ^{3}HeD thermonuclear yield. However, the data presented in Fig. 3 shows the opposite: there are more ^{3}HeD protons than DD protons being emitted from the pinch region. It can therefore be concluded that the ^{3}HeD protons from the pinch region are not of thermonuclear origin.

A Monte Carlo code, PF-Moca, has been written which simulates fusion within the plasma focus and the resulting track density distributions [20]. This program assumes two contributions to the fusion yield: (i) a pinch source (PS) contribution, treated as an isotropic proton point source centered on the pinch column; and (ii) a beam-target (BT) source represented by a cone of half-angle φ on the forward PF axis emitting protons in accordance with the (lab frame) differential reaction cross-section. Small-angle scattering of protons in the kapton film at the front of the camera is included in the calculation of the expected track density distribution at the position of the detector surface. The solid curve in Fig. 3 show the fit obtained for the 3HeD distribution using the PF-Moca code. For this curve, 80% of the 3HeD proton yield is produce by beam-target fusion in a cone of half-angle φ = 60º, with 20% of the yield arising from the pinch-source.

By contrast, the DD distribution obtained for the ^{3}He–D_2 gas mixture cannot be satisfactorily fitted using PF-Moca. The dashed curve in Fig. 3, shows one attempt to perform such a fit to the DD distribution using a beam-target cone of φ = 60º, and zero PS contribution. The simulation curve is normalized to the r = 4 mm data point, but it is clearly a poor fit to the data. The experimental distribution is much shallower than any reasonable PF-Moca simulation curve. The inclusion of a non-zero PS contribution would give a more centrally peaked simulation curve, and therefore a still worse fit to the experimental DD data. In general terms the shallowness of the distribution indicates that the DD fusion is occurring relatively far from the pinch region. It also clearly means that thermonuclear fusion is not the dominant mechanism for the observed DD fusion yield.

In order to make a meaningful comparison between the ^{3}HeD and DD proton yields in terms of the beam-target model, we must consider the reaction cross sections shown in Fig. 4. The experimental data used for plotting these curves is taken from Ref. [23] (DD) and Ref. [24] (^{3}HeD). The cross sections are plotted in terms of a notional acceleration potential V_a. For example, for V_a = 50 kV, the D^+ and $^3He^{2+}$ ions would have lab kinetic energies of 50 keV and 100 keV, respectively.

It can be seen that, for all values of V_a, the cross section for D(^{3}He,p)^{4}He is significantly larger than that for ^{3}He(d,p)^{4}He. Assuming the ratio of D^+ and $^3He^{2+}$ beam ions is 1:1 then the bulk of ^{3}HeD beam-target fusion should result from the D(^{3}He,p)^{4}He reaction.

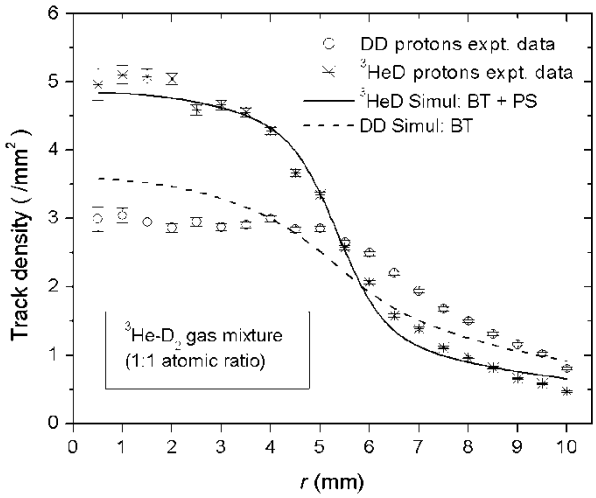

FIG. 3. Plots of radial track density distributions for the front and back CR-39 detectors: DD and ^{3}HeD protons, respectively. Distributions are per-shot averages from 5 front and 5 back detectors. The curves shown are discussed in the text. (^{3}He–D_2 gas mixture).

The energy spectra of fast primary ions have been measured for several plasma focus devices [25, 26] for pure deuterium filling gas, and these spectra are found to be of the form $f(E_d) \propto E_d^{-n}$, with values of n in the range of three to six. Then the distribution of acceleration potentials experienced by primary ions would be of essentially the same form: $f(V_a) \propto V_a^{-n}$. If we assume this to be true also for the energetic $^3He^{2+}$ and D^+ primary ions, then neglecting the slowing down of primary ions and differences in trajectory length, the beam-target fusion yield would be approximately proportional to $\int f(V_a)\sigma_r(V_a)dV_a \approx \int V_a^{-n}\sigma_r(V_a)dV_a$, where σ_r represents the cross section for the relevant reaction. Since the ^{3}HeD cross section is a more rapidly rising function of V_a than the DD cross section, the fusion yield contributed by $V_a^{-n}\sigma_r(V_a)$ will be skewed towards higher values of V_a. for the ^{3}HeD reaction. However, the very similar proton yields for ^{3}HeD and DD observed experimentally implies that the integrated values of $V_a^{-n}\sigma_r(V_a)$ are similar for the two reactions. Based on these considerations and the cross section plots shown in Fig. 4, the majority of DD fusion protons must then be associated with acceleration potentials V_a < 55 kV (i.e. deuterons with energies less than 55 keV).

5.2. ^{4}He–D_2 Gas Mixture

Figure 5 shows a comparison between the DD experimental distributions obtained for the ^{3}He–D_2 and ^{4}He–D_2 gas mixtures, and it can be seen that the heights and shapes of the two distributions are very similar. It should be remembered that the total gas pressures of 480 Pa (^{3}He–D_2) and 400 Pa (^{4}He–D_2) were selected so as to obtain the same mass density, and ensure similar operation of the plasma focus for these mixtures. Since the ^{4}He–D_2 distribution is derived from a significantly larger number of PF shots than the corresponding ^{3}He–D_2 distribution, it lends support to the conclusion drawn from the ^{3}He–D_2 data that the DD fusion occurs relatively far from the pinch region.

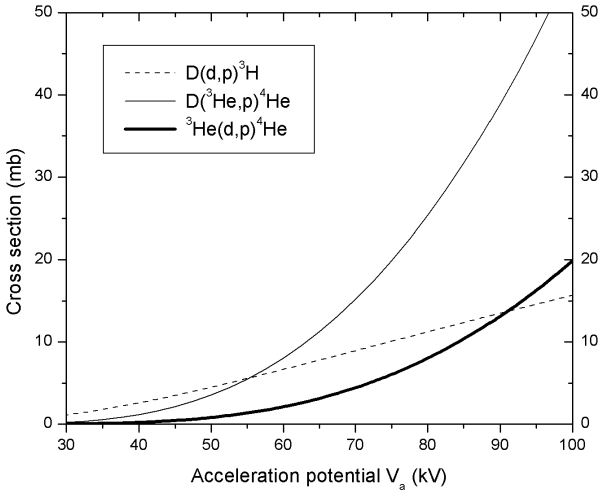

FIG. 4. Plots of cross section as a function of accelerating potential V_a for the fusion reactions: D(d,p)^{3}H, D(^{3}He,p)^{4}He and ^{3}He(d,p)^{4}He.

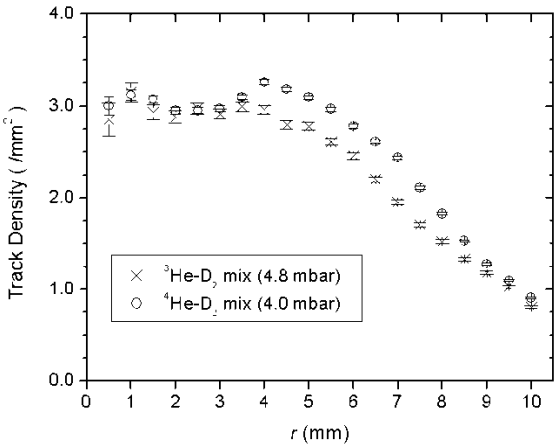

FIG. 5. Plots of radial track density distributions for DD protons obtained for two PF filling gas mixtures: ^{3}He–D_2 and ^{4}He–D_2. Distributions are per shot averages.

5.3. Pure D_2 Gas

It is interesting to compare the DD proton distribution for the ^{3}He–D_2 gas mixture (Fig. 3) with the corresponding distribution for pure D_2 gas (Fig. 6). Two points worth noting are: (i) the average yield of DD protons is much lower (about a factor of about 30) when the PF is operated with a ^{3}He–D_2 gas mixture than for pure D_2 gas, and (ii) the shape of the DD distribution is much shallower for the ^{3}He–D_2 gas mixture than the pure D_2 case. The solid curve plotted in Fig. 6 shows that the pure deuterium distribution can be well fitted by a linear combination of beam-target and pinch source contributions calculated from the simulation code PF-Moca. This fit corresponds to a 91% contribution from beam-target (BT) fusion (50 keV deuterons emitted from pinch in a cone of half-angle 60º), plus a 9% pinch-source (PS) contribution. The separate BT and PS contributions are plotted as the dotted and dashed curves, respectively, in Fig. 6.

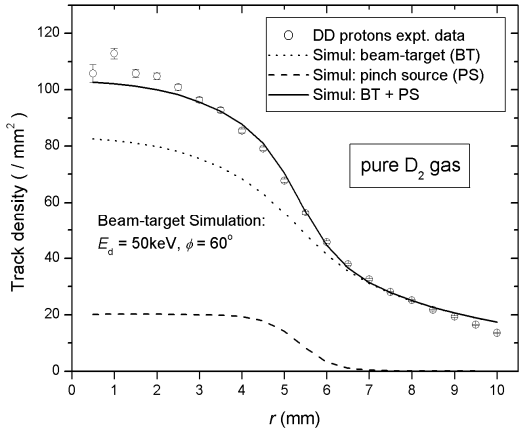

FIG. 6. Plot of radial track density distribution (per shot average) for the DD protons obtained for 12 PF shots. The curves shown are discussed in the text. (Pure D_2 gas).

6. CONCLUSIONS FOR GAS MIXTURE EXPERIMENTS

A 3.1 kJ plasma focus device is operated with a ^{3}He–D_2 gas mixture: 480 Pa total pressure and 1:1 atomic ratio. DD and ^{3}HeD proton tracks are measured simultaneously by a double-layer arrangement of CR-39 detectors, enabling the associated regions of fusion production to be imaged by means of a pinhole camera. The overall proton yields for the ^{3}HeD and DD reactions were found to be similar. The ^{3}HeD distribution was observed to be centrally peaked, and this distribution could be well fitted by PF-Moca simulations for which the pinch-source contribution is in the range of 20 to 30% of the total D(^{3}He,p)^{4}He yield. If the ^{3}HeD fusion occurring in the PF pinch were thermonuclear in origin then the necessary temperature, density and confinement time associated with the pinched plasma would result in a thermonuclear DD yield many times greater than the thermonuclear ^{3}HeD yield. However, the experimental data reveals the opposite: there are more ^{3}HeD protons than DD protons being emitted from the pinch region. Hence it does not seem possible to explain the substantial quantity of ^{3}HeD fusion from the pinch in terms of the thermonuclear model.

Comparing the experimental DD proton radial distributions obtained for the ^{3}He–D_2 and ^{4}He–D_2 gas mixtures (same mass density), it is apparent that the heights and shapes of the two distributions are very similar. This is evidence that the dynamics of the PF discharge were nearly the same for the two gas mixtures. Since a much larger number of PF shots were fired for the ^{4}He–D_2 gas mixture (384 shots) than for ^{3}He–D_2 (119 shots), the ^{4}He–D_2 distribution has better statistical accuracy. Therefore the similarity between the two distributions further supports the conclusion drawn from the ^{3}He–D_2 results that the DD fusion occurs relatively far from the pinch region.

Furthermore, a series of exposures performed with pure D_2 gas produced a DD distribution which is quite different from the DD distributions obtained for the ^{3}He–D_2 or ^{4}He–D_2 gas mixtures. The pure D_2 distribution can be well fitted with the PF-Moca simulation code using contributions from both a conical beam-target source and an isotropic pinch-source (PS) contribution: the beam-target contribution representing approximately 90% of the fusion yield. It should be remembered that the above DD distribution obtained for pure D_2 gas has only moderate angular resolution (~ 7º half-angle) as a relatively large pinhole (8 mm diameter) was used in order to obtain a sufficient number of tracks for the ^{3}He–D_2 and ^{4}He–D_2 gas mixture cases.

7. ENHANCED ANGULAR RESOLUTION PROTON IMAGING

Exactly the same pinhole camera arrangement was used as described in section 3, except that the diameter of the entrance pupil was reduced to 1.8 mm, giving an enhanced angular resolution of ~1.5º, and the approximate angular field of view is up to 20° from the camera axis. The pinhole is at the centre of a 75 μm thick brass disc. SRIM was used to check the performance of the camera. For deuterons of energy 50 keV, the DD protons emitted in the forward direction have an energy ≈ 3.3 MeV; after passing through 50 μm kapton and 3 μm aluminium foils these protons have a remaining energy ≈ 2.4 MeV and suffer an average angular deviation of ~1.2°, resulting in an overall angular resolution of ~2º.

With this smaller pinhole it is found that a satisfactory density of tracks on the CR-39 detectors is obtained for 5 to 7 PF shots. A total of 18 detectors were exposed (representing an accumulated 119 PF shots); all shots were fired with 400 Pa deuterium gas pressure and 14 kV charging voltage. The CR-39 detectors were etched in 6.25M NaOH solution at 90ºC for five hours. The detectors were then scanned as described in Ref. [19]. In total the positions of more than 80 000 tracks were measured and recorded by the scanning system.

8. RESULTS AND DISCUSSION FOR ENHANCED ANGULAR RESOLUTION PROTON IMAGING

The per shot average radial distribution obtained from experiment, together with best-fit simulation results are shown in Fig 7. The experimental data points represent the cumulative track density distribution for all 18 exposed detectors (divided by 119 shots). The statistical uncertainties in the experimental data points lie within in the range 1.5 to 2.3%.

It is found that the experimental data can be well fitted by the PF-Moca simulated distributions over a range of deuteron source energies and cone angles: E_d = 40–70 keV and ϕ_0 = 10°–50°. For a pair of E_d and ϕ_0 values in this range, the best-fit is obtained with a linear combination of the BT and PS distributions, but with BT fusion representing the predominant (~90% or more) contribution to the total neutron yield Y_n. For example, Table 2 shows the best fits at E_d = 50 keV, for a range of cone half-angles ϕ_0. These fits are shown as the first three curves (without point symbols) in Fig. 7, and they lie very nearly on top of one another. The last two curves (with open point symbols) represent the separate BT and PS distributions for the E_d = 50 keV, ϕ_0 = 30° case, for which *PS* fusion contributes a little less than 6% of the total neutron yield.

Table 2 also shows the calculated total neutron yield (Y_n) and neutron asymmetry (A_n) associated with the PF-Moca simulation results — the neutron asymmetry associated with PS fusion is assumed to be unity. The neutron yields shown in Table 2 are smaller than the per shot average yield determined from the indium activation counter (~10^8). This disparity may (at least partially) be due to a drift in sensitivity of our activation counter since its calibration several years ago.

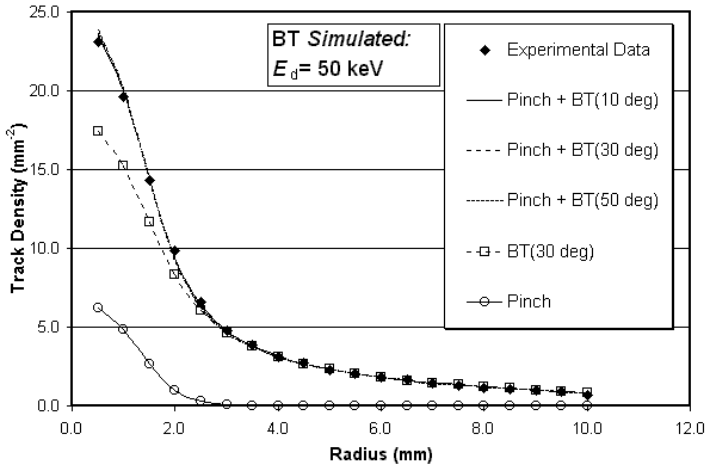

FIG. 7. Data points (♦) are per shot average radial track density data. Lines are results of PF-Moca simulations for deuteron source energy E_d = 50 keV, and cone half-angle ϕ_0 of 10, 30, and 50 degrees. Error bars have been omitted for clarity.

TABLE 2. BEST-FITS TO EXPERIMENTAL DATA FOR DEUTERONS OF ENERGY 50 KEV

ϕ_0	Beam-Target Source			Point Source		Total	
(deg)	N_d	Y_n^{BT}	A_n^{BT}	Y_n^{PS}	PS %	Y_n	A_n
10	1.49×10^{15}	1.54×10^{7}	1.77	2.10×10^{6}	12.0%	1.75×10^{7}	1.68
30	3.99×10^{15}	4.24×10^{7}	1.62	2.60×10^{6}	5.8%	4.50×10^{7}	1.58
50	6.69×10^{15}	6.08×10^{7}	1.42	2.80×10^{6}	4.4%	6.36×10^{7}	1.40

In conclusion, these proton pinhole camera measurements show that beam-target fusion is the dominant fusion mechanism for this plasma focus, and represents about 90 to 95% of the total neutron yield. It is also apparent that about 5 to 10% of the neutron yield is associated with fusion occurring in the vicinity of the pinch. This may, or may not, be the result of thermonuclear fusion.

9. PROCEDURE FOR MAGNETIC SPECTROMETER EXPERIMENTS

As shown in Fig. 8(a), the magnetic spectrometer is positioned to analyze ions emitted along the forward axis of the plasma focus. A 32 μm diameter pinhole placed 328 mm from the end of the anode images the deuteron source on a 200 μm wide spectrometer entrance slit. A fan-beam of deuterons passes between a pair of neodymium permanent magnets of 19 mm diameter producing a nearly uniform field of strength 0.65 T. A seal around the pinhole enables differential vacuum to be performed between the PF and spectrometer chambers maintaining a typical pressure of 4×10^{-4} mbar in the later, virtually eliminating all charge exchanging collisions. The energetic deuterons are analyzed onto the CR-39 plate whose front face is positioned 3.75 cm above the axis of the permanent magnets (L in Fig. 8(b)). A linear translator permits several exposures to be made on the same CR-39 detector plate.

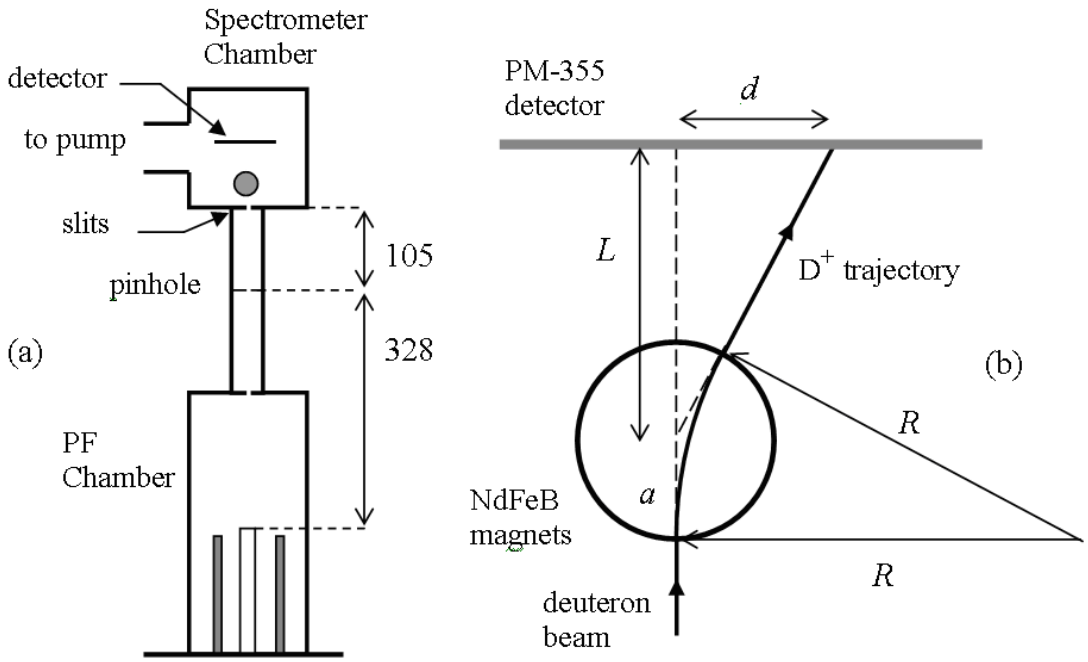

FIG. 8. (a) Schematic diagram of plasma focus and magnetic spectrometer. Dimensions are in mm. (b) Diagram of magnetic spectrometer and associated parameters used in text: a= radius of magnetic field region (9.5 mm), L=distance from centre of magnetic field region to detector surface (3.75 cm), d=displacement of ion track on detector, R=radius of curvature of ion trajectory in magnetic field.

Ion energy spectra were obtained for deuterium filling gas at three pressures, for a constant charging voltage of 14 kV. The pressures and average yields obtained were: 300 Pa (Y_n=1.1×10^8), 350 Pa (Y_n=1.3×10^8) and 400 Pa (Y_n=1.1×10^8). For improved statistical accuracy in track counting, 3 consecutive shots were fired for each energy spectrum, and 8 spectra were exposed on each CR-39 plate. Overall, eight CR-39 detectors were exposed for each working gas pressure. Hence for each gas pressure we obtained 64 spectra representing 192 plasma focus shots. Detector plates of dimensions 45×20 mm were cut from 500 μmthick sheets of CR-39. After exposure, the CR-39 detectors were etched in 6.25 molar NaOH solution at 70°C for eight hours. The resulting etched ion tracks are 6 to 7μm in diameter.

The CR-39 detectors were scanned at ×400 magnification, for which the CCD field-of-view is a 241×181μm rectangle. Each spectrum on the detector was scanned in a meander path comprising 44×14 images. The recognized and counted tracks were accumulated in a histogram of track displacement (d in Fig. 8(b)), in bins representing 100 μm wide 'equal energy' stripes on the detector. It is convenient that a very distinct neutrals band is clearly visible for each spectrum (resulting from uncharged deuterons passing through the spectrometer in straight line paths and producing a densely tracked strip slightly wider than the spectrometer slits). The midline of this neutrals band is used as the position of zero track displacement (d=0). Image processing and track recognition routines were applied to each 8 bit grey image from the CCD camera. The number and position of the recognized tracks were used to accumulate a histogram (i.e. track count vs. displacement d).

10. MAGNETIC SPECTROMETER DATA ANALYSIS

In deriving the source deuteron spectrum $d^2N/dE\,d\Omega$ from the track displacement histogram, it is necessary to take into consideration: (i) energy loss, (ii) small-angle scattering, and (iii) charge exchange of the deuterons over their 32 cm path through the working gas

before reaching the pinhole. Beyond the pinhole, in a vacuum of $\leq 10^{-3}$ mbar, the ions/neutral atoms travel in effectively straight line paths with negligible energy loss and charge exchange. The Monte Carlo program SRIM was used to simulate the stopping powers and small angle scattering suffered by the ions in the working gas. Figure 9(a) is a plot of the energy loss E_{loss} suffered by deuterons, as a function of their degraded energy E' on arrival at the pinhole (as measured by the magnetic spectrometer).

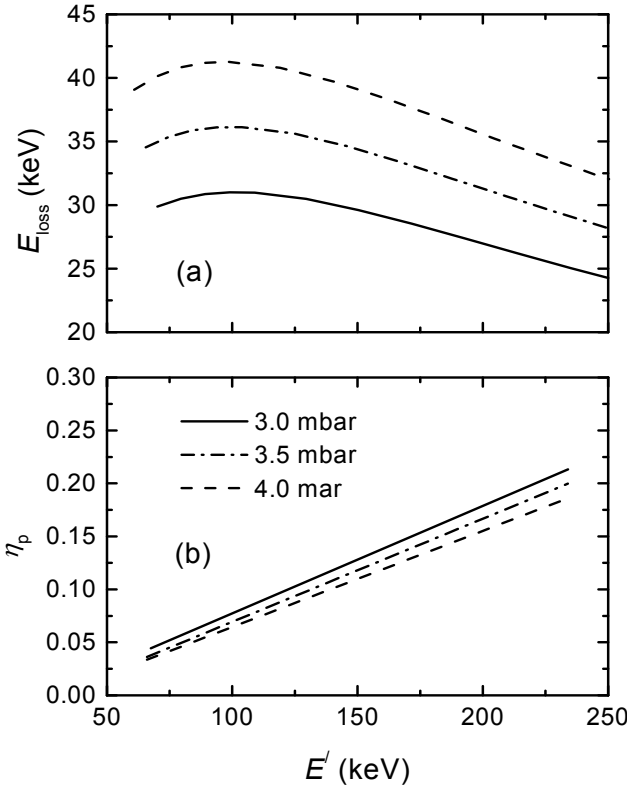

FIG. 9. (a) Plot of the energy loss E_{loss} suffered by deuterons, as a function of their degraded energy E' on arrival at the pinhole. (b) Plot of $\eta_{\text{p}}(E')$, the probability for a deuteron of energy E' at pinhole subsequently passing through spectrometer slit and arriving in the scanned region of the detector.

The original energy of the deuterons emitted from the pinch is simply $E = E' + E_{\text{loss}}$. The directional information for individual transmitted ions generated by SRIM simulation was used to calculate the probability $\eta_{\text{p}}(E')$, for the ions to pass through both the pinhole and spectrometer entrance slits and arrive within the scanned region of the detector. $\eta_{\text{p}}(E')$ is plotted in Fig. 9(b).

It is also necessary to correct for the fraction of neutral deuterons, which are not analyzed by the spectrometer, but contribute to the neutrals band observed on the CR-39 detector. Using an empirical formula $Z_{\text{eff}} = Z(1-\exp(-130\beta / Z^{2/3}))$ and $\beta = v/c$, given by [27], for the effective charge Z_{eff} on a low energy ion, then the probability of a deuteron being in an ionized state is to a reasonable approximation $\varepsilon = 1-\exp(-0.134\times\sqrt{E'})$ with E' in keV. The energy resolution of the spectrometer is mainly determined by the width of the entrance slit and is approximately ±2% for $E' = 100\,\text{keV}$ and ±3% for $E' = 250\,\text{keV}$.

Then for a given bin in the track position histogram with a mean transmitted energy E', width $\Delta E'$, and track count C, the intensity of energetic deuteron emission on the forward axis of the plasma focus is

$$\frac{d^2N}{dE\,d\Omega}(E) = \frac{C}{\Omega_{\rm ph}\ \varepsilon(E')\ \eta_p(E')\ \Delta E'} \Big/ dE\,.$$

Where $\Omega_{\rm ph} = 7.85\times10^{-9}\,\text{sr}$ is the solid angle subtended by the pinhole at the position of the energetic deuteron source at the end of the pinch column.

11. MAGNETIC SPECTROMETER RESULTS

All the resulting energy spectra display a rapidly decreasing intensity $d^2N/dE\,d\Omega$ with increasing energy, and apart from statistical variations appear to be smoothly varying. There are no obvious peaks or other sharp features in any of the obtained spectra. In order to investigate the relationship between neutron yield $(Y_{\rm n})$ and the associated deuteron energy spectra, we sorted the 64 spectra (for each pressure) with respect to $Y_{\rm n}$ and divided them into five groups, labeled I to V (I-IV containing 13 spectra each, and V with 12 spectra). For each group, per shot average deuteron spectrum and neutron yield $\overline{Y_{\rm n}}$ are obtained as in Fig. 10.

Figure 10(a)–(c) shows that for all three pressures (300, 350 and 400 Pa) the intensity of the deuteron beam decreases progressively from neutron yield group I to V, demonstrating a clear correlation between the neutron yield and deuteron beam energy. However, a comparison between the deuteron spectra and the averaged neutron yield per shot $\overline{Y_{\rm n}}$, as shown in Fig. 10(d), reveals that the relative variation in beam intensity is considerably larger than the associated relative variation in neutron yields. For example, the solid lines in 6(a)–(c) show fitted curves of the form $dN/dE \propto E^{-n}$, and Table 3 gives the ratios between the ordinate values of these curves at $E = 150\,\text{keV}$ for groups I and V, and the corresponding ratios of $\overline{Y_{\rm n}}$.

TABLE 3. RATIOS OF DEUTERONS BEAM INTENSITIES AND NEUTRON YIELDS

	Ratios	
Pressure (Pa)	$\frac{(d^2N/dEd\Omega)_{\rm I}}{(d^2N/dEd\Omega)_{\rm V}}(150\,\text{k}$	$\frac{\left(\overline{Y_{\rm n}}\right)_{\rm I}}{\left(\overline{Y_{\rm n}}\right)_{\rm V}}$
300	12.5	1.96 ± .07
350	39.4	2.42 ± .08
400	21.1	2.90 ± .11

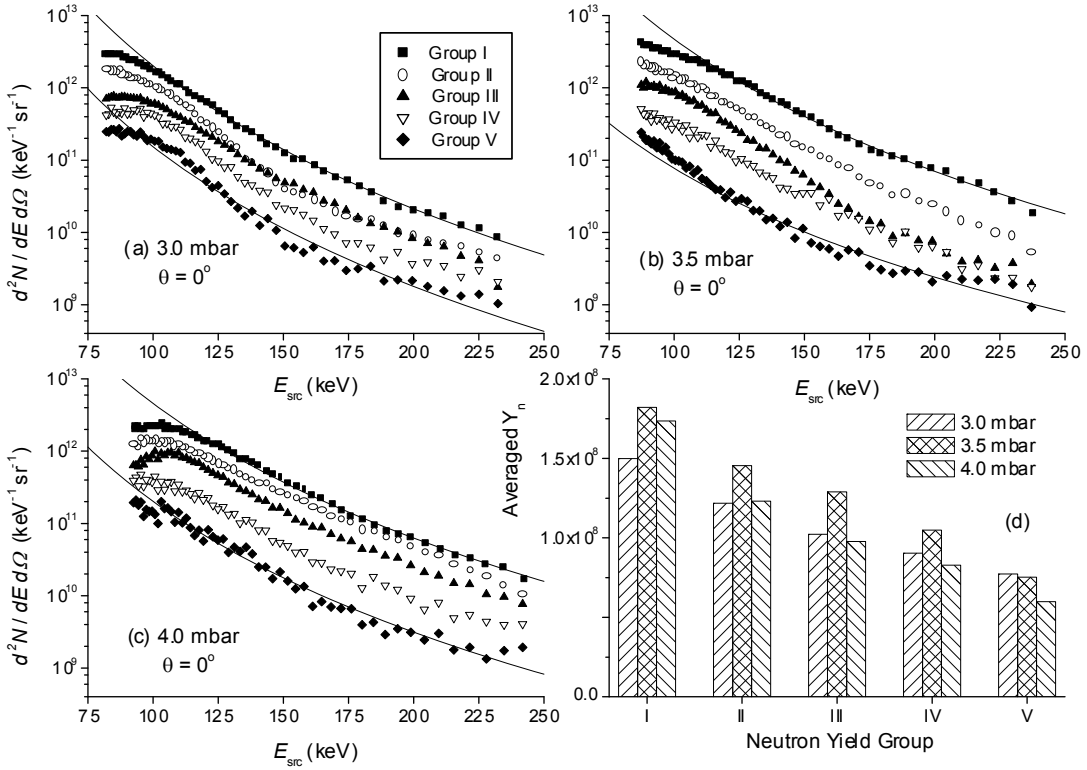

FIG. 10. (a–c) Plots of group averaged deuteron spectra $d^2N / dE\, d\Omega$ *emitted on the forward axis* $(\theta = 0^\circ)$ *from plasma focus pinch, for deuterium working gas pressures of (a) 300 Pa, (b) 350 Pa, (c) 400 Pa. Solid lines are fitted* E^{-n} *curves for yield groups I and V only. Error bars have been omitted for clarity. (d) Average neutron yield per shot* $\overline{Y_n}$ *(into* 4π *sr) for each pressure and neutron yield groups I to V. As an example of the statistical uncertainties in* $\overline{Y_n}$ *, at 350 Pa the uncertainties are 1.2% and 2.0% for yield groups I and V, respectively.*

The presence of such a clear correlation between the deuteron beam intensity and the observed neutron yield is further evidence for the importance of the beam-target mechanism for plasma focus fusion. That the proportional change in deuteron beam intensity is significantly larger than the associated change in neutron yield is perhaps explicable in terms of a shot-to-shot variation in the angular width of the deuteron emission cone. Another possible explanation is that the intensity variation in the deuteron energy spectra above 100 keV, as measured here, is not indicative of a similar variation in the lower energy part of the deuteron spectrum (~40 to 60 keV) which is responsible for the bulk of the fusion production [2, 14].

12. OVERALL CONCLUSIONS

In this paper we have presented a series of experimental investigations of fusion protons and ion beam emission for a small Mather-type plasma focus device. The polymer nuclear track detector material, CR-39, is used throughout these experiments for the detection of energetic protons (~3 to ~ 16 MeV) and deuterons (90 to 240 keV). The principal objective of these experiments has been to study the respective roles of thermonuclear fusion and beam-target fusion within the plasma focus.

Proton imaging experiments for the $^3He–D_2$ gas mixture (1:1 atomic ratio) show that: (i) the average yield of (~ 3 MeV) DD protons is much lower (approximately a factor of 30) than the DD yield for pure D_2 gas, and (ii) the shape of the DD distribution is much shallower for the $^3He–D_2$ and gas mixture than the pure D_2 case. This finding is confirmed for the $^4He–D_2$ mixture (1:1 atomic ratio) performed for the purpose of comparison with the $^3He–D_2$ mixture. It is very difficult to explain the shallowness of the DD distribution in terms of either the thermonuclear or beam-target model — as it indicates that the DD fusion is occurring relatively far from the pinch region. At present the authors do not have a satisfactory explanation for this finding. On the other hand, the (~ 15 MeV) ^{3}HeD angular distribution can be well fitted using the PF-Moca code, where 80% of the ^{3}HeD proton yield is produce by beam-target fusion in a cone of half-angle $\varphi = 60^\circ$, and 20% of the yield is emitted from the pinch. However there are strong arguments against the ^{3}HeD fusion occurring in the pinch being of thermonuclear origin.

Proton imaging was performed for pure D_2 gas at two different angular resolutions: ~7º and ~2º. The enhanced angular resolution is obtained at the cost of reducing the acceptance angle for protons entering the camera. Hence, for ~7º resolution a single PF shot was sufficient to expose each CR-39 detector, whereas for ~2º resolution the images were averaged over 5 to 7 shots. It was found that images from both resolutions could be well fitted using the PF-Moca simulation code, and that typically beam-target fusion occurring in a conical zone in front of the pinch accounted for about 90% of the proton yield, while about 10% of the proton yield was emitted from the pinch. Whether the fusion occurring in the pinch is thermonuclear or not is still an open question. Hence for pure D_2 gas it can be concluded that $\geq$ 90% of the fusion is beam-target in origin.

Furthermore, for pure D_2 gas a magnetic spectrometer was employed to measure the energy spectra of deuterons emitted on the forward axis of the plasma focus for a large number of shots. All the deuteron spectra obtained exhibit a smooth monotonic decrease in beam intensity with increasing deuteron energy. There is a clearly observed correlation between the intensity of the deuteron beam and the associated neutron yield, at each of three working gas pressures (300, 350 and 400 Pa). This result supports the conclusion that the beam-target fusion mechanism is dominant for the UNU/ICTP plasma focus device. It is found that the relative variation in the deuteron beam intensity is significantly larger than that associated with the neutron yield. The explanation for this disproportionate variation requires further investigation.

ACKNOWLEDGEMENTS

The authors are pleased to acknowledge the financial support for this work provided by grants from the National Institute of Education, Nanyang Technological University, Singapore (grant numbers: RI 2/04 SVS and RP 2/05 SVS), and by a Coordinated Research Programme contract with International Atomic Energy Agency (IAEA CRP contract number: 12412/R0).

REFERENCES

[1] BERNSTEIN, M.J., COMISAR, G.G., Phys. Fluids 15 (1972) 700.
[2] TISEANU, I., et al., Plasma Phys. Control. Fusion 36 (1994) 417.
[3] GERDIN, G., et al., J. Appl. Phys. 52 (1981) 3269.
[4] STYGAR, W., et al., Nucl. Fus. 22 (1982) 1161.
[5] HEROLD, H., et al., Rev. Sci. Instrum. 52 (1981) 24.

[6] KELLY, H., MARQUEZ, A., Plasma Phys. Control. Fusion 38 (1996) 1931.
[7] JAGER, U., et al., Rev. Sci. Instrum. 56 (1985) 77.
[8] JAGER, U., HEROLD, H., Nucl. Fus. 27 (1987) 407.
[9] FILIPPOV, N.V., et al., Sov. J. Plasma Phys. 4 (1978) 1364–1369 (In Russian).
[10] GULLICKSON, R.L., et al., J. Appl. Phys. 48 (1977) 3718–3722.
[11] LEE, S., et al., Am. J. Phys. 56 (1988) 62.
[12] MATHER, J.W. Phys. Fluids 8 (1965) 366–72.
[13] ZIEGLER, J.F., MANOYA, J.M., Nucl. Instr. And Meth. B35 (1988) 215.
[14] SPRINGHAM, S.V., et al., Plasma Phys. Control. Fusion 42 (2000) 1023.
[15] SPRINGHAM, S.V., et al., Braz. J. Phys. 32 (2002) 172–178.
[16] LILLEY, J.S., Nuclear Physics: Principles and Applications, New York, Wiley, 2001, pp. 303.
[17] ROUT, R.K., SHYAM, A., Phys. Contr. Fusion 31 (1989) 873–877.
[18] BROWN, R.E., JARMIE, N., Phys. Rev. C41 (1990) 1391.
[19] KRAUSS, A., et al, Nucl. Phys. A 465 (1987) 150–172.
[20] BERNARD, A., et al, Phys. Fluids 18 (1975) 180–194.
[21] STEINMETZ, K. et al, Nucl. Fusion 22 (1982) 25–29.
[22] HECKMAN, H.H., et al., Phys. Rev. 117 (1960) 544.

BEAM DIAGNOSTICS AND RADIOISOTOPE PRODUCTION IN LOW AND MEDIUM POWER PLASMA FOCUS DEVICES

A. TARTARI, E. ANGELI,
Department of Physics
University Of Ferrara
Ferrara

C. BONIFAZZI,
Department of Biomedical Sciences
University of Ferrara
Ferrara

S. MANNUCCIC, D. MOSTACCI, F. ROCCHI, M. SUMINI
Laboratory of Nuclear Engineering
DIENCA, University of Bologna,
Bologna

Italy

Abstract

The report deals with activity at two distinct plasma focus facilities. The first with 7 kJ bank energy represents the traditional apparatus used for more than ten years at the University of Ferrara. The other, just constructed, reaches 150 kJ bank energy and is exclusively dedicated to the production of sizeable quantities of medical radioisotopes. In regards to the first device, the energy spectra of X rays generated by the impact of electron beams on high- and medium- Z targets following the pinch implosion of plasma focus (PF) devices are discussed in terms of the possible mechanisms of X ray production following electron impact ionization. In addition, a temperature measurement of the PF inner electrode is reported and some results have been proved useful in order to optimize the device functionalities. An experimental campaign was conducted in order to assess the feasibility of short lived radioisotope (SLR) production within the pulsed discharges of a plasma focus (PF) device. This so-called ‘‘endogenous production’’ technique rests on the exploitation of nuclear reactions for the creation of SLR directly within the plasma, rather than on irradiating an external target. Following the results displayed in such campaign a second high energy PF machine was designed and its characteristics together with the first tests are presented too.

1. INTRODUCTION

Plasma focus (PF) may find potential applications in medicine and industry. It represents a solution at low cost of management, compact and reliable, and offers performances in terms of intensity and of the time of exposure (<100 ns). The main peculiarity of the PF radiation is represented by very intense beam of ion, electrons, X ray and short exposure time together with strong electromagnetic radio frequency production. So, the usual diagnostics based on large arrays of NaI and silicon PIN detectors are not suitable because of the high electromagnetic noise. Following a procedure similar to that utilized for X ray spectrometry from terawatt laser sources an X ray spectrometric measurement was carried out by means of a differential absorption technique based on calibrated LiF TLD dosimeters which allow a measurement of an attenuation curve at a given time. The energy distribution of the produced X rays is then calculated, from such attenuation data, using an iterative procedure based on spectral algebra formalism. A systematic comparison of different X ray beams observed at different PF exit windows is carried out and discussed in terms of the possible mechanisms of X ray production following electron impact ionization.

In addition, in order to have devices industrially competitive, plasma focus needs to be operated in repetitive mode. However at each pulse, or shot, part of the machine input energy is converted into thermal loads on the structural components of the machine itself, and this can be a major cause for the mechanical failure of a device operated in repetitive mode. The amount of energy converted into heat at each shot needs to be known in order to design an

efficient cooling system. Unfortunately no quantitative data about PF heating have been published to date. In this paper the results of an experimental campaign, aimed at estimating the heat generated in the inner electrode of a PF, are presented for the first time and compared with theoretical models. These results will be of help in the design of the cooling systems needed for the repetitive operation of PF.

In recent years, a research group in the USA [3–5] tried successfully to demonstrate the use of PF to produce several short lived radioisotopes (SLRs) with relatively high yields per discharge. In the present paper, some preliminary results are presented that were obtained from an ongoing, joint experimental collaboration between the University of Ferrara and the University of Bologna. The first experiments, discussed here, concentrated on the production of a few positron emitting radioisotopes through (d,n) reactions. While the present apparatus is similar in energy and geometry to that used by the US group, the measurement technique is different: the 511 keV annihilation photons were measured with gamma spectrometers located outside the filling gas atmosphere, whereas in the US experiments, GM detectors were used to measure beta emission directly inside the chamber. The results obtained so far are within the same order of magnitude as those obtained by the US group. Following the results displayed in such campaign a second high energy PF machine was designed and its characteristics together with the first electro mechanic tests results are presented too.

2. MATERIALS AND METHODS

2.1. The plasma focus device and X ray diagnostics in the 7kJ machine

The experimental setup of the implosion chamber is shown in Fig. 1. The general scheme of typical experimental setup is reported in Fig. 2. The plasma focus is a Mather type device with hollow inner anode that allows the piping of the backward directed electron beam. The energy of the capacitor bank is 7 kJ with a maximum peak current of 0.5 MA at the working voltage of 17.0 kV. In the present paper we consider only the X ray production due to the impact of: (a) electron beams turning back to the inner electrode after the implosion of the current sheet into the pinch, and (b) relativistic electron beams (REB) originated in the pinch zone and backward accelerated in a narrow cone along the axis of the electrodes. In the case of X ray characterization the PF was operated at a fixed atmosphere of 6.0 Torr of H_2.

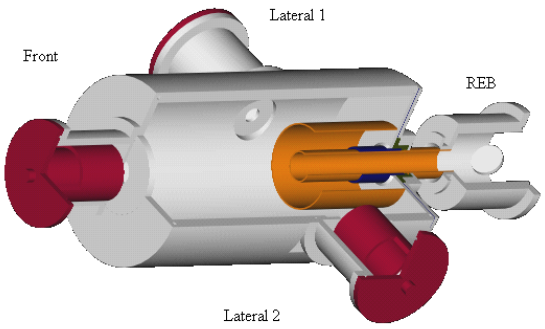

FIG. 1. Sketch of the experimental apparatus based on plasma focus discharge for REB exploitation as an X ray source. Dimensions not to scale.

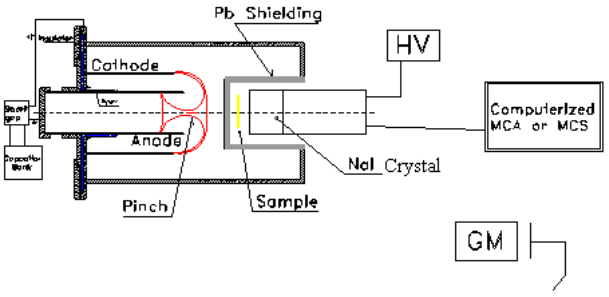

FIG. 2. Schematic diagram of the experimental setup with a section of the PF vacuum chamber. The plasma sheath is shown at its pinch phase. The lead sheath and the "sample" were removed in the present application.

The X ray characterization is performed by extracting the photon beams through four windows positioned around the pinch region. One of them, forward positioned and aligned with the electrode axis, looks at both the pinch and the region of electrode impacted by the backward emitted electron beam from the pinch. Other two windows are positioned laterally to the pinch region and look at the same region as the preceding one. All these windows are equipped with double-layered sheets composed of 24 μm thick aluminized Mylar plus 18 μm thick aluminium foils; these are used to suppress the soft X ray component directly produced in the pinch region, i.e. photons with energy $E < 3–4$ keV.

For the measurement of the REB based X ray source a special chamber is positioned on the reverse axis of the hollow inner electrode. A target holder, well collimated to the REB and to the spectrometer window, is positioned inside this chamber. The target is 45° tilted with respect to the electrodes axis and is placed at about 10 cm from the beginning of anode.

The spectrum of the X rays is evaluated using a differential absorption based technique [7]. The X ray spectrometer consists of a stack of LiF dosimeters which act both as detectors and filters to give curves of attenuated intensities. The energy distribution is calculated from such attenuation curves using an iterative procedure based on spectral algebra formalism. The LiF dosimeter nearest to the source acts at the same time as exposure meter.

2.2. Relationship between thermo-luminescent counts and photon intensity

The dosimeters are calibrated at the well established 59.54 keV X ray facility of the Department of Physics — University of Ferrara which utilizes a 500 mCi ^{241}Am sealed source emitting 2.8×10^{8} photons/count/sr. Taking into account that the number of thermo-luminescence counts is induced by the whole energy deposition into the dosimeter and, referring to a planar geometry in which the dosimeter surface is normal to the direction of the photon beam, we can define an absorbed energy rate per solid angle:

$$E_A = I(E)\left(\frac{\mu_{en}(E)}{\rho}\right)Et_D \tag{1}$$

where $I(E)$ is the number of photons per second and solid angle of the beam and t_D the crossed thickness of the dosimeter. $\mu_{en}(E)/\rho$ (with ρ the density of LiF material) is the energy

absorption coefficient of LiF as defined by Hubbell and Seltzer 1995 [8]. Bearing in mind that the thermo-luminescence is induced by the whole energy deposition E_A into the dosimeter, in the case of a monochromatic beam of photon energy E the resulting thermoluminescent counts will be given by means of response factor $K(E)$, i.e. $c = K(E)\, E_A$.

The essential independence of the LiF response over energy [9] allows the absorbed energy to produce a thermoluminescent count c which is the same regardless of the energy of the incident photon. This leads to the definition of a conversion factor F_C to compare thermoluminescent counts at different energy E of the photon beam and irradiation geometry (solid angle Ω) with the following relationship:

$$I(E) = c_M \frac{I(E_c)\left(\frac{\mu_{en}(E_c)}{\rho}\right)E_c\Omega_c}{c_c\left(\frac{\mu_{en}(E)}{\rho}\right)E\,\Omega_M} \qquad \text{i.e. } I(E) = c\ F_c(E) \tag{2}$$

In equation 2) the indices *"c"* and *"M"* refer to calibration with monochromatic photons and actual measurement with PF beams respectively.

Moreover, the assumption of the dosimeter energy response independence leads to the validation of the energy photon hardening evaluation by successive attenuation of stacked TLD dosimeters which form the basis of differential absorption spectrometry.

For a polychromatic beam the energy transmission $T_M(t)$ after passing a thickness t of material is:

$$T_M(t) = \frac{\int_0^{E_{max}} I(E)\mu_{en}(E)\ E\ e^{-\mu(E)t}\,dE}{\int_0^{E_{max}} I(E)\mu_{en}(E)EdE} \tag{3}$$

Being the denominator a constant (k) defined by the measurement of the first vicinal detectors, it follows that by choosing n measurements (with t_1,.. t_n thickness), and dividing the energy interval into n bins (with E_1,.., E_n energies) the relationship between the measured transmission series $T_M(t_i)$ and the energy spectrum of the incident beam can be expressed in terms of matrix formalism as:

$$\begin{bmatrix} T_M(t_1) \\ " \\ T_M(t_n) \end{bmatrix} = \frac{1}{k}\begin{bmatrix} A(E_1,t_1) & " & A(E_n,t_1) \\ " & " & " \\ A(E_1,t_n) & " & A(E_n,t_n) \end{bmatrix} \times \begin{bmatrix} I(E_1) \\ " \\ I(E_n) \end{bmatrix} \tag{4}$$

where:

$$A(E_i,t_i) = \mu_{en}(E_i)E_i e^{-\mu(E_i)t_i} q_i \tag{5}$$

In equation 4, T_M refers to the transmission measurement, i.e. the ratio between the actual reading of the i-th dosimeter and that of the first one which represents the un-attenuated measurement. μ_i is the attenuation coefficient at the energy E_i of the LiF material. As can be

seen in Equation 5 all terms are independent from the energy spectra and can be obtained from available databases [9].

2.3. Breeding of short life radioisotopes with the 7kJ machine

The experimental work presented here was performed on the Ferrara University PF1. A scheme of the experimental setup is shown in Fig. 1. Each discharge was monitored with a RIAL quadrupole mass spectrometer (QMS), a NaI(Tl) gamma spectrometer, a Geiger–Mueller–based silver activation neutron counter and a Rogowski coil. The NaI(Tl) crystal used is 3.22" in diameter and 3.28" in length, with a resolution of 7.5% at 511 keV; the phototube was coupled to an ORTEC digibase and digital MCA, connected to a remote PC via an USB port. The choice of the Digibase MCA was made to avoid electromagnetic noise induced by PF discharges. Although the grounded vacuum chamber partially screens electromagnetic waves, disturbances due to fast spark-gap switching cannot be avoided. Different bases and/or unshielded MCAs cannot be used to measure spectra because of intense electromagnetic pulses.

The NaI crystal and phototube plus Digibase were placed in a cavity, designed to position the detector as near as possible to the pinch region in order to maximize the geometrical factor. Calibration of the gamma spectrometer in terms of detected activity is discussed in detail in the next paragraph. In addition to the NaI spectrometer, an ORTEC LO-AX coaxial HPGe detector was used separately to verify the presence of spurious peaks near 511 keV; the crystal thickness: 22.5 mm; crystal diameter: 51 mm; and crystal resolution: 0.35% @ 511 keV. Both Ge and NaI spectrometers were controlled with Maestro-32 software that can be programmed through Job Files, as needed. In no instances were flux thresholds for radiation damage to crystals by fast neutrons ever reached. High-purity gases were used for all experiments. The QMS was used to monitor gas mixtures and to control their purities inside the vacuum chamber and from shot to shot. Neutron counting was performed with a silver activation detector of the ''Los Alamos type'' composed of four LND 72527 GM tubes wrapped in a thin silver foil; the tubes are placed inside a paraffin block covered with a thin cadmium foil. The array was placed 80 cm from the pinch region and 45° forward with respect to the direction of the electrode axis. The activation produced in the silver foil by the fast neutrons and slowed down by the paraffin was recorded with a standard counting chain for 60 s. The cadmium around the paraffin block prevents ambient backscattered thermal neutrons from reaching the silver foil.

In case of high counting-rates, present for very efficient neutron producing discharges, discharges were separated in time by more than 60 s to allow for decay of the activated silver. In all cases, the counter saturation limit was never reached. The neutron counting device was adopted because the neutron burst emitted by the PF has a very narrow time-spread (tens of nanoseconds, depending also upon the detector-to-source distance), too small for the time-resolution of available electronics. The calibration of the neutron counting device was made using a set of eight bubble detectors (high-sensitivity superheated emulsions) of type BD-100R, manufactured by BTI, Inc. The neutron emission was assumed to be isotropic. Then, the total neutron yield calculations had an accuracy of about ±25% (2 sigma), taking into account accuracy of the detector calibrated with high-sensitivity superheated emulsions, small deviations from isotropic emission and all possible measurement errors. A Rogowski coil was used to register the total current time-derivative on a 1GHz oscilloscope; the traces were recorded and then numerically integrated to obtain the total current waveforms. To obtain quantitative estimates of activities from the NaI spectra, the system was calibrated with a 10 mCi 137Cs sealed reference source, chosen for its single line at 661.65 keV, very close

to that for the 511 keV energy annihilation photons. The source was placed on the outer walls of the vacuum chamber, directly above the detector. To assess the relative geometrical efficiency of the detector with the ^{137}Cs source and with the positron emitting source to be measured, Monte-Carlo simulations were performed.

The following hypotheses were adopted for the simulations:

- The ^{137}Cs is an isotropic and monochromatic point source;
- The positron source is uniformly distributed in the volume of the whole vacuum chamber (this is justified by the ionic bursts created by the post-pinch MHD instabilities which spreads the reaction products around the chamber);
- The positron range in the vacuum chamber gases is short enough so that annihilation gamma emission coincides geometrically with the β^+ emission;
- Each element of the volume source emits isotropically distributed, monochromatic gamma rays;
- Structural elements are neglected.

The simulation was performed with MCNP-5. The results for the geometrical efficiencies were:

$\varepsilon_X \cong 0.040$ and $\varepsilon_{Cs} \cong 0.045$

where ε_X is the geometrical efficiency of the detector with respect to the positron source and ε_{Cs} is the same quantity but with respect to the ^{137}Cs source. Using these results, the following equation can be written:

$$\frac{A_X}{P_X}\varepsilon_X = \frac{A_{Cs}}{P_{Cs}}\varepsilon_{Cs} \tag{6}$$

where A_X and A_{Cs} are the activities of the positron volume and ^{137}Cs sources, respectively, in Becquerel and P_X and P_{Cs} are the peak areas recorded by the gamma spectrometer in equal time intervals for both sources. Within limits of experimental errors, Eq. (6) can be simplified to

$$A_X \cong A_{Cs}\frac{P_X}{P_{Cs}}$$

To evaluate the activities of the sources at time $t = 0$ (initial activities), just after the end of a PF discharge, the following equations were used:

$$P_X(\tau) = P_X(0)\int_0^{\tau} e^{-\lambda t}\,dt \tag{7}$$

where $\lambda = \ln 2/T_{1/2}$ Eq. (6) holds in this simple form because the time interval of the measurement t is much less than the ^{137}Cs half-life ($T_{1/2}$=30 years).

2.4. Temperature measurement in the 7 kJ machine

Temperature measurements were performed with a type K thermocouple which was kept fixed in position and in direct contact with the inner surface of the inner electrode by a very small aluminium ring spring. The thermocouple tip was positioned at about 4.5 cm from the end of the electrode. The data readout was made with a data-logger which could send data to a PC via RS232 connection. The uncertainty in temperature measurement was ± 0.5 °C, so

that only values differing by 1 °C could be obtained. The sampling frequency was 0.2 Hz; higher frequencies resulted in a data redundancy which proved to be, once tried, an obstacle in the analyses of data. In this experimentation the plasma focus was operated at 6, 8, 10 or 12 Torr of D_2. For each shot the total current and the total neutron yield were measured with a Rogowski coil and a silver activation counter respectively [10]. The temperature decay modelling is performed by means of the well known Newton law:

$$T(t) = T_A + \Delta T e^{-kt} \tag{8}$$

with T_A the initial environment temperature before PF firing and ΔT the temperature increase after a given shot. "k" is a positive parameter which describes altogether all the possible different cooling mechanisms (conduction, convection and radiative transfer) which are very difficult to separate and distinguish via theoretical simulation.

The heat loading is consequently determined by:

$$Q = m_f c_p \Delta T \tag{9}$$

with m_f the fraction of the mass actually heated and c_p the specific heat of the material composing the observed part.

2.5. New medium energy and repetitive PF machine

Scaling laws for neutron yield in PF neutron generators are experimentally well established up to 1MJ of bank energy. If similar laws are supposed to hold also for nuclear reactions that produce SLRs, then, from the results obtained by Brzosko et al 2001 [6] and by the present authors [see present report], it could be expected that a PF with a bank energy of 150 kJ working at 1 Hz repetition frequency could produce (order of) 1 Ci of ^{18}F in 2 hours, from the neutron-free reaction (1). This radioisotope will be produced in gaseous form, $^{18}F_2$, and could be utilized for the radiochemical production of positron-emission tracers employed in medical examinations such as PET. The availability of an alternative, reliable source of molecular $^{18}F_2$ may constitute a further advantage in comparison with current cyclotron-based technologies, which are not yet able to provide an efficient route for the production of $^{18}F_2$. The chemical reactivity of electrophilic F_2 could be advantageous for the labelling of bio-molecules and drugs. Therefore the production of $^{18}F_2$ in PF devices may lead to the development of novel categories of PET diagnostic agents. Two other major advantages in this use of a PF to breed short lived radioisotopes are: (1) the prompt production (isotopes can be prepared ''on demand''); (2) many radioisotopes can be produced without neutron emission depending on the gases that are used in the process. The following sections present the preliminary design of a Mather-type PF constructed by our research group, capable of breeding one Ci of ^{18}F in two hours of operation.

3. X RAY

3.1. X ray production in the 7 kJ machine

The quantities in the second member of 1) and their energy dependence will affect the conversion factor when different photon energy is concerned. The conversion factor F_c results 4.87×10^9 photons/count/sr and a fluence at the pinch source of 9.7×10^{14} photons/shot/sr if the window attenuation isn't accounted. With the attenuation accounted and hypothesizing a photon energy of 25 keV, the fluence at the pinch position will be 5.0×10^{15} photons/shot/sr.

In Table 1, a comparison with other photon sources is made on the basis of data taken from HPA 1979 Catalogue [11] in the case of X ray tubes. Such data, together with those of REB PF source, are scaled to the geometrical condition of the ^{241}Am facility geometry. At a first sight, the PF source looks very similar to that given by ordinary diagnostic X ray tubes. However, such intensity is not referred to 1 s unit time, as for X ray tubes or sealed radioisotopes, but is delivered in about 30 to 50 ns.

An example of the energy spectrum calculated by means of the above mentioned formalism from the measured attenuation curves is shown in Fig. 3 for the two modalities of X rays production by electron impact, i.e. the brass target material for the lateral exit window and a tungsten target in case of the REB.

TABLE 1. COMPARISON WITH OTHER SOURCES

Source	Energy (keV)	Fluence/sr (at source position)
500 mCi ^{241}Am	59.54	2.8×10^8 Ph/sr/s
X ray tube	56.5	6.1×10^{14} Ph/sr/s
X ray tube	17.9	5.6×10^{13} Ph/sr/s
PF-REB single shots	25.0	5.0×10^{15} Ph/sr/shot

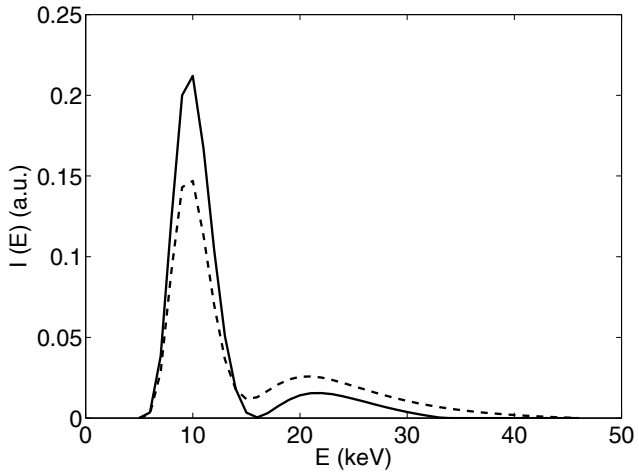

FIG. 3. Comparison of EGS4 Monte Carlo simulation, dotted line, and the experimental measured spectra, continuous line.

The results show that the energy spectra of the photons consist mainly of characteristic L-shell X rays in the case of high-Z materials (i.e. tungsten) and K-shell X rays for low or medium-Z materials such as the zinc and copper in the brass alloy. This characteristic radiation is superimposed to a continuous low intensity Bremsstrahlung whose photon energy extends up to several tens of keV. As can be noted, the REB component seems to exhibit an

electron energy higher than those impinging on the inner anode. This conclusion partially supports the results of Bostik and Nardi et al. about the presence in the REB of high energy components by using a device very similar to the present one [12].

Using the well known EGS4 Monte Carlo code modified to include the characteristic X rays production by electron impact [13, 14] the spectra of the emitted photons from an energetic electron beam against a high-Z target may be simulated and the results compared with those given by the spectrometer assessment. An example of these spectra is shown in Fig. 4 for tungsten target REB impact with energy of 50 keV. In these simulated spectra two components, the characteristic radiation and the continuous Bremsstrahlung can be seen.

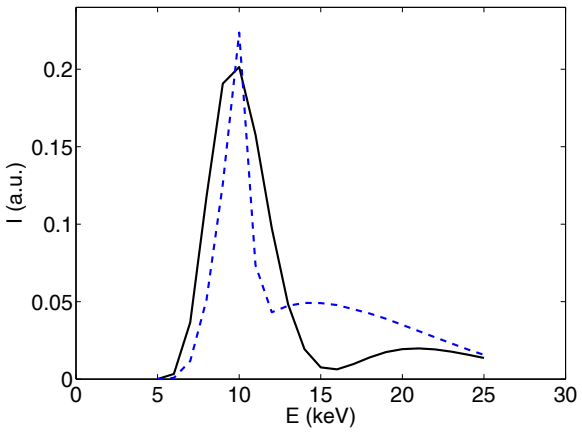

FIG. 4. Calculated energy spectra of the X rays measured in the REB window (dotted line) and in the lateral window (continuous line).

The Monte Carlo results are found to be in a good agreement with experimental data, especially with regard to the experimentally observed enhancement of the characteristic L-shell X ray line group. This enhancement is well beyond the estimated spectrometer resolution which is conservatively included in the EGS4 results presented in Fig. 5. One hypothesis is to consider phenomena induced by multiple ionization followed by satellite line in the K and L lines spectra [15]. This possibility together with the inclusion of a failure in the inversion algorithm of Equation 4, forms part of the actual work in progress.

3.2. Breeding of short radioisotopes in the 7 kJ machine

As an example of results, Fig. 5 shows a gamma spectrum (background not subtracted) recorded for a typical discharge. The live counting time was 244 s, which corresponds to about two half-lives of ^{15}O. The filling gas was a mixture of about 7 Torr of D_2 and 0.5 Torr of N_2. The gamma peak is exactly at 511 keV. The initial activity of ^{15}O, obtained from this discharge, was 0.7±0.15 μCi, within the model described in the previous paragraph, corresponding roughly to breeding of approximately $N = 4.7\times10^{-6}$ nuclei of this radioisotope. A neutron yield, $Y_n = 6\times10^8$, was measured in the same discharge, giving a ratio $Y_n/N = 127.7$. The ^{15}O breeding in this discharge was one order of magnitude less than the average values published by Brzosko et al (2001) [5].

However, considering that the Ferrara machine is not optimized for the production of SLRs, the results obtained are in quite good agreement with those of Brzosko and co-workers. Two experimental proofs that detected gamma peaks are to be solely ascribed to positron annihilation 511 keV photons are available: (1) when the PF is operated only with deuterium,

no peaks are seen on the spectrometer; and the HPGe spectrometry reveals a single line at 511 keV within detector resolution, i.e. within less than 200 eV. Finally a few extraction tests were performed with the PF pumping system. Figure 6 shows decay of the peak produced in a discharge of 6 Torr D_2+0.5 Torr of air accompanied by a total neutron yield, $Y_n = 4.5\times10^8$.

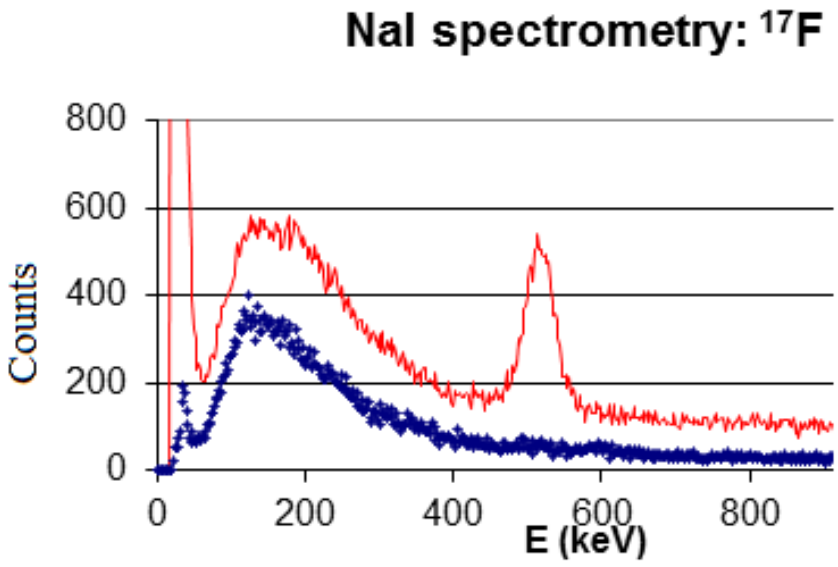

FIG. 5. Photon spectrum (background not subtracted) for a typical discharge producing ^{17}F. The upper curve was taken 10 s following the shots. The lower ones was registered 20 minutes after ($T_{½}$=1.05 min).

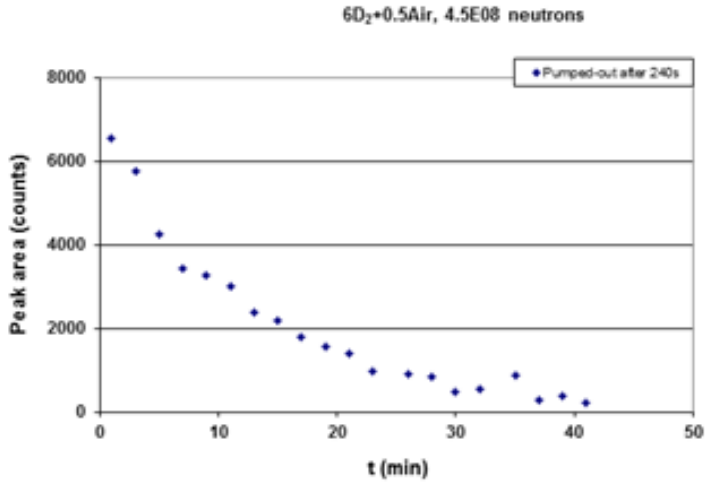

FIG. 6. Time decay of 511 keV peak of 15O: to be noticed discontinuity of the curve due to the gas extraction at t=4min.

Four minutes after the discharge, the vacuum chamber was evacuated from the original 6.5 Torr total pressure level to 1×10^{-2} to 1×10^{-3} Torr, in approximately two minutes. As the figure shows, a sudden drop of the multi-exponential decay at about t = four minutes occurs; however, not all the activity could be extracted from the vacuum chamber, as can be seen from the curve after the end of the pumping process, circa t=six minutes. This could be due both to the poor extraction efficiency of the pumping system or to other phenomena connected with the quality of the materials used. This finding will form the objective for further investigations. In conclusion, activities of the order of 1 mCi of ^{15}O, ^{17}F and ^{13}N were produced in a single 7 kJ PF discharge in the endogenous production scheme. These data

seem to agree with those in literature; the fact that a different measurement technique was used further validates the results. More research is needed and issues related to gas extraction from the vacuum chamber as far are presently being addressed.

3.3. Heat load measurements in the 7 kJ machine

An example of the inner electrode temperature time decay after a shot at 19 kV is given in Fig. 7. The evaluated ΔT for this series was 17.19 °C and the coefficient k was found to be 0.003803 s^{-1}. It has been found that there is a rather strong dependence of ΔT on the bank energy, as might be expected. Therefore for each integer value of the voltage in kilovolts from 12 to 19 kV at least 10 series of either 5 or 10 shots were performed and the relative ΔTs were evaluated. Figure 7 shows the variation against bank charge voltage of the inner electrode thermal deposition per shot. The dependence is found to follow a power law estimated as Q=0.00245(V)^2 with Q in kJ and V in kV. This leads to conclude that a linear dependence with the bank energy (E=½CV^2 with C the total bank capacitors) may be accepted. It must be said that all the points shown were obtained from series of shots performed at the same pressure of 8 Torr (the present PF neutron production is optimized at this pressure for 7 kJ bank energy); nonetheless no sensible variation of these results with pressure has been found.

Operation at different values of pressure (6, 8, 10 or 12 Torr) gave the same results. Moreover the formation of a good pinch does not imply higher heating; discharges in which no pinch at all was seen provided the electrode with the same amount of heat as those in which a very good pinch was obtained. These two observations are in agreement with the fact that the total neutron yield does not influence (nor is somehow correlated with) the heating of the electrode. Moreover, series of discharges with good neutron yield heated the electrode to the same degree as a series with low neutron yield. The unique requisite for a consistent heating is simply the formation of the plasma sheath. The decision to have a massive inner electrode (so to have higher heat capacity) or a thin hollow electrode with a heat removal system must be taken therefore with great care.

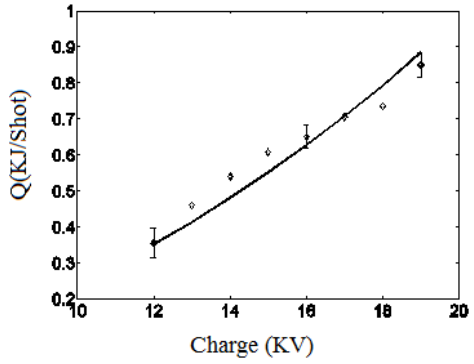

FIG. 7. Charge voltage dependence of the heat load at 8 torr of D2 filling atmosphere. , ◊ experimental;— Q=0.00245(V) 2interpolation curve.

3.4. New medium energy and repetitive PF machine: Electrode optimization and first single shot trials

The condition for device optimization is the time coincidence between pinch and maximum current. The problem is highly non-linear, since the external RLC circuit discharge influences the Lorentz force acting on the plasma sheath; on the other hand, the position and

shape of the plasma sheath determine the circuit inductance L, which increases in time; furthermore, the plasma dynamics are affected by the inertia of the gas, which is ionized and swept by the sheath in a sort of snowplow effect. An iterative, 2D code was developed and used to model the problem and obtain the optimum configuration of the electrodes. The sheath is modelled by a chain of conical finite elements linked together. The circuit equations are solved globally, while the equations of motion and mass continuity allow to obtain the shape of the plasma sheath driven by magnetic pressure; at each iteration the inductance due to the coaxial gun, short-circuited by the current sheath, is recomputed and substituted into the circuit equation closing the time loop. Moreover, the sheath shape needs a constant remeshing since some segments move faster than others leading to a non-uniform discretization. From the type of gases in the mixture and the partial pressures, the code computes the total mass density inside the chamber; feeding in the external circuit parameters, the code iterates until the optimum configuration is reached, giving as output the inner electrode radius r_{in}, the external electrode radius r_{ex} and the length l. Circuit current I, voltage V on the capacitors and total inductance L are automatically plotted as functions of time. The code also gives information about plasma dynamics, in particular the sheath profiles and the axial and radial average velocities; moreover transition time instants between the three phases of the PF discharge (detachment from the insulator sleeve—axial rundown—collapse) are output. It was chosen to work at a total pressure of about 10 mbar; the external RLC circuit parameters are known from the design of the components: bank capacitance C of 350 mF charged at 30 kV, resistance R of about 5 mΩ and inductance L_0 of 26.2 nH excluding electrodes contribution.

The resulting optimized configuration consists of an inner electrode radius of 5 cm, outer electrode radius of 8.5 cm and total length of 16 cm. It is also found that the rundown phase lasts about 1.2 μs, and the pinch occurs at 3.18 μs. Although maximum current is about 1.5 MA, the increasing inductance during the collapse phase leads to total current of 800 kA.

In Fig. 8 a partial view of the capacitor bank, discharge cables and cooling pipes are given. Figure 9 reports the first experimental current discharge plot for 25 kV. The maximum current can be estimated around 1.3 MA.

4. CONCLUSION

As illustrated by the list of publications which may be found in the appendix, both the results of the numerous experimental campaigns performed with the 7 kJ machine and the successful construction a new 150 kJ facility for SLR production, are evidence that plasma focus (PF) may find potential for innovative applications. It represents a compact and reliable solution at low cost of management, and offers good performances in terms of intensity and exposure time.

FIG. 8. Partial view of the new 150 kJ, 1 Hz repetition rate plasma focus machine.

Interesting results have been obtained in the area of SLR production. Many technological issues must be tackled in order to make this application practical. If successful, great benefits will result from this type of mechanism used to breed SLRs: while in conventional techniques, targets are irradiated with charged particle beams generated from outside, in endogenous production both projectile and target are confined in the same region where they react. Even more importantly, the radioisotopes of interest (^{18}F and ^{15}O) are produced without neutron emission. This considerably reduces the (undesirable) activation of structural elements, and also makes the shielding required for radiation protection far less demanding than for other devices.

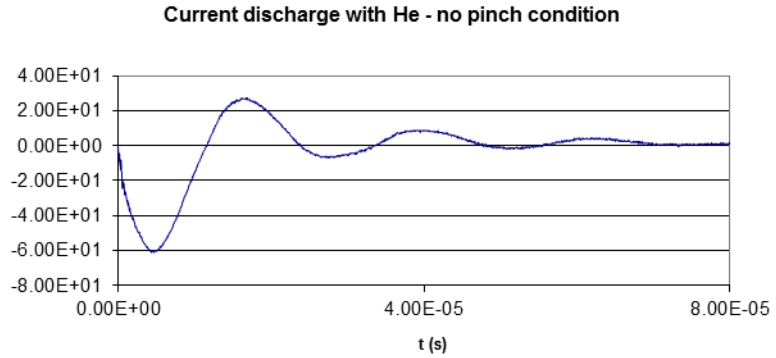

FIG. 9. Current discharge plot for 25 kV: the first trial on the new 150 kJ machine.

ACKNOWLEDGEMENTS

Work performed at the Department of Physics, University of Ferrara, I-44100 Ferrara, Italy. Regarding the new 150 kJ facility, the contract within the Frame Agreement between the Alma Mater s.r.l. of the University of Bologna, and ULSS 12 "Veneziana" is acknowledged. The authors would like to thank A. Padoan, Director General of ULSS 12 "Veneziana", for the supervision of the project, L. Karpinski of the Institute of Plasma Physics and Laser Microfusion of Warsaw for his precious technical suggestions, A. Duatti, of the Dipartimento di Scienze Chirurgiche, Anestesiologiche e Radiologiche—Sezione di Medicina Nucleare—University of Ferrara, for valuable discussions about the radiochemistry of fluorine, and G. Venturi for his valuable assistance in the mechanical design.

REFERENCES

[1] GRIBKOV, V.A., On possible formulation of problems of a dense Plasma Focus used in material science, Nukleonika, 43 (2000) 149–153.

[2] TARTARI, A., Da, Re, A., BONIFAZZI, C. and MARZIANI, M., Energy spectra measurements of X ray emission from electron interaction in a dense Plasma Focus device, Nucl Instrum. Meth. in Phys. Res., B213 (2004) 206–209.

[3] BRZOSKO, J.S., NARDI, V., BRZOSKO, J.R., GOLDSTEIN, D., Observation of plasma domains with fast ions and enhanced fusion in plasma-focus discharges, Phys. Lett. A 192 (1994) 250–257.

[4] BRZOSKO, J.S., MELZACKI, K., POWELL, C., GAI, M., FRANCE III, R.H., McDONALD, J.E., ALTON, G.D., BERTRAND, F.E., BEENE, J.R., BREEDING 1010/s radioactive nuclei in a compact plasma focus device, In: DUGGAN, J.L., MORGAN, I.L. (Eds.), Application of Accelerators in Research and Industry, 16th Inter. Conference, AIP (2001) 277–280.

[5] BRZOSKO, J.S., MELZACKI, K., POWELL, C., GAI, M., FRANCE III, R.H., MCDONALD, J.E., ALTON, G.D., BERTRAND, F.E., BEENE, J.R., Breeding 1010/s radioactive nuclei in a compact plasma focus device, In: Duggan, J.L., Morgan, I.L. (Eds.), Application of Accelerators in Research and Industry, 16th Inter. Conference, AIP (2001) 277–280.
[6] HUBBELL, J.H., SELTZER, S.M. Tables of X ray mass attenuation coefficients and Mass Energy Absorption coef. 1 keV to 20 MeV for elements Z=1 to 92 and 48 additional substances of dosimetric interest, NSTIR 5632, Gaithersburg MD, USA (1995).
[7] HOROWITZ, Y.S/, KALEF_EZRA, J., Relative thermoluminescent response of LiF TLD, Nucl. Instrum. Meth., 188 (1981) 603–607.
[8] TARTARI, A., VERRI, G., DA RE, A., MEZZETTI, F., BONIFAZZI, C., RAPEZZI, L., Improvement of calibration assessment for gold fast neutron activation analysis using Plasma Focus devices, Meas. Sci. Technol., 13 (2002) 939–945.
[9] BIRCH, R., MARSHALL, B., ARDRAN, G.M., Catalogue of Spectral Data for Diagnostic X rays, HPA, London, SRS 30 (1979).
[10] BOSTIK, W.H., NARDI, V., PRIOR, W.,FEUGEAS, J., BORTOLOTTI, A., CORTESE, C., MEZZETTI, F., PEDRIELLI, P., Production of GW electron and ion beams by focused discharges, In: Nardi, V., Salin, H., Bostik, W.H. (eds) Energy storage, compression and switching, Plenum Press, New York (1983) 267–287.
[11] CASNATI, E., TARTARI, A., BARALDI, C., An empirical approach to K-shell ionization cross section by electrons, Phys. B: At. Mol. Phys., 15 (1982) 155–167.
[12] MARZIANI, M., GAMBACCINI, M., TAVORA, L. and TAIBI, A., Advances in Monte Carlo for Radiation Physics, Khing, A., Barão, F., Nakagawa, N., Tavora, L. and Vaz, P.p (Eds.). Springer, Berlin (2001) 351–356.
[13] JACOBS, V.L., DAVIS, J., BALAZS, S.F., COOPER, J.W., Multiple ionization and X ray emission accompanying the cascade decay of inner shell vacancies in Fe, Phys. Rev., A21 (1980) 1917–1926.
[14] BRZOSKO, J.S., NARDI, V., High yield of 12C(d,n)13N and 14N(d,n)15O reactions in the plasma focus pinch, Phys. Lett. A 155 (2–3) (1991) 162–168.

CREATION OF A NEW TYPE OF CAESIUM NEGATIVE ION VOLUME SOURCE

E.I. TOADER, E.S. BARNA, V.N. COVLEA
Department of Plasma Physics
University of Bucharest
Bucharest, Romania

Abstract

In this project attention is focused on the possibility of obtaining a high production of negative hydrogen ions H^- within the volume of a new type of caesium-hydrogen negative ion volume source by addition of small quantities of caesium for gas pressure levels from 0.1 to 10 Pa. Langmuir probe, H^- ion photodetachment, visible and VUV spectroscopy, and surface work function measurements have been made. To obtain the best values for both the negative ion density $n\_$ and the negative ion fraction $n\_ / n_e$, the operating conditions are optimized as a function of pressure, discharge power, and magnetic field. When operating in pure hydrogen and pure deuterium the electron density, electron temperature and plasma potential measurements have been shown to be extremely reproducible. The experiment shows that the reflex discharge steady-state plasma is uniform for a dissipated power of 400W and has the best efficiency within the pressure range from 0.5 to 2.0 Pa, where the negative ion density is as high as 10^{17} m^{-3}, and the negative ion fraction can achieve values of 2.5%. When caesium was added to the ion source an increase in the H^- ion percentage was observed. However the most surprising result with caesium seeding was the observed decrease in the electron density while the plasma potential increased compared to the pure hydrogen case. Investigation of the inner surface of the walls of the chamber by using a work function measurement technique resulted in the conclusion that caesium was present on the surface. Correlation with H^- percentage proved that caesium coverage of the surface was the main factor in H^- ion enhancement due to caesium seeding. Also as part of the project, a new type of negative ion has been investigated, and a semiclassical–quantum mechanic model was used to show that the new type of negative ion is produced through a potential barrier interaction. A new diagnostic method, based on a combination of probe technique and dye laser technique, was developed to measure the negative ion density.

1. INTRODUCTION

Low-temperature plasma sources are directly involved in fusion research in connection with the production of intense beams of negative ions (Bacal et a1 1984), since one of the most powerful and effective methods for the additional heating of a fusion plasma is Neutral Beam Injection (NBI). Neutral beam injectors, with beam energies in excess of 150 keV, are essential for the next generation of fusion reactors. For this purpose, it requires a plasma source capable of generating high density plasma and low electron temperature over a large volume in order to obtain high negative ion densities. The plasma source developed should provide a dense quiescent and uniform (over several hundred square centimetres of extraction surface) plasma for producing tens of amperes of hydrogen or deuterium ion current in the energy range of tens to hundreds of kilo-electron-volt. Therefore, such negative ion volume sources require an understanding of atomic and molecular physics, plasma chemistry, and plasma physics. Many fundamental low-temperature plasma phenomena are poorly understood. Yet modern techniques are available to address a range of problems of fundamental importance that have important practical applications. Examples include the physics and chemistry of plasmas at material boundaries (i.e. plasma sheaths), the creation of plasmas by electrodeless discharges, and the stability and reproducibility of plasma discharges.

Fusion reactions in which two light nuclei combine to form a single heavier nucleus is a very promising energy source where plasma plays a crucial role. The tribute paid to the apparent simple method is given by the Lawson criterion, which involves plasma densities of the order of 10^{20} m^{-3}, plasma lifetime greater than two seconds and plasma temperatures of the order of 10^9 K. The crucial problem is how to heat the plasma to achieve such high temperature. Several methods are being investigated, i.e. Current Drive Heating (CDH), Neutral Beam Injection Heating (NBIH), Ion Cyclotron Resonance Heating (ICRH), Electron Cyclotron Resonance Heating (ECRH), and Lower Hybrid Current Drive (LHCD).

Our project is connected directly with NBI heating. More exactly, our goal is to obtain a negative ion plasma source where the enhancement effect of cesium can produce a high quantity of hydrogen and deuterium negative ions within a volume of plasma. The new type of negative ion plasma source belongs to the category of double diode glow-discharge sources working in an abnormal regime, and relies on a direct-current reflex discharge [1–4] obtained as a hybrid between a Penning discharge and a hollow cathode discharge. Its advantage, over other types of non-equilibrium direct current plasma sources, emerges from the enhanced hollow-cathode effect (HCE), produced by the presence of the magnetic field. The reflex discharge plasma source is characterized by an increased ionization rate (plasma density as high as 10^{18} m^{-3}) for a relatively low power density dissipated within the discharge, high uniformity, and technical simplicity. The bulk plasma is free of an electric field. A diagnostic method based on laser beam photodetachment of negative ions and detection of detached electrons by an electrostatic probe [7–10] is used to measure the density $n\_$ of the hydrogen negative ions. The positive ion density n_i, the electron density n_e, and the electron temperature T_e are measured using the Langmuir probe method and the Druyvesteyn procedure, along with suitable numerical analysis [11–13]. The operating conditions are optimized for all these internal parameters within the pressure range 0.1–10 Pa, discharge power 40–400 W, and magnetic field 0-150 G.

2. OPERATION PRINCIPLE AND EXPERIMENTAL PROCEDURE

A schematic diagram of the plasma source along with the other major auxiliary systems, are shown in Fig. 1. The discharge chamber is similar to one described in detail elsewhere [14]. Briefly, it is a 300 mm long, 200 mm diameter, non-magnetic stainless steel cylindrical vessel with two laterals ports and enclosed at each end by detachable, non-magnetic stainless steel flanges. The two 100 mm diameter, plane-parallel, stainless steel cathodes are on extensions, which penetrate but are insulated from the end flanges, via O-ring gaskets. The grounded, non-magnetic stainless steel anode, in the form of a ring with a 102 mm inside diameter, 10 mm width and 2.0 mm thickness, is placed symmetrically with respect to the two plane-parallel flanges. An oil sealed mechanical pump, backing a turbo-molecular pump, evacuates the discharge chamber to an ultimate vacuum less than or equal to 10^{-7} Pa. The discharge is produced within the pressure range of 0.1–10 Pa, buffering the pump and flowing hydrogen at a flow rate of 1 to 4 sccm, for an inter-cathode distance d = 20 to 100 mm, and a magnetic field (provided by two Helmholtz coils) within the range of 0–150 G. The power is provided by a 600-V, 1.5-A direct current power supply. A schematic representation of the discharge cavity is given in Fig. 2. The geometric parameters were varied to obtain a bulk plasma volume as large as possible. Consequently the experiment was carried out up to the maximum inter-cathode distance d = 100 mm.

The experiment shows that for d > 60 mm the two negative glow regions do not overlap, and the HC effect disappears. To obtain the optimum discharge conditions, the experiment must be run for the inter-cathode distance of the resonance cavity d = 50 mm, at a gas flow rate of 4 sccm. Since the inter-cathode distance d is much larger than the cathode fall distance dc, we may consider that the whole volume of the bulk plasma appears as a cage for the electrons. All the discharge voltage current characteristics show that the enhanced magnetic ionization is more effective at higher discharge currents and magnetic fields. When the potential difference of a few hundred volts is applied between the two plane-parallel cathodes and the ring anode, the reflex discharge plasma develops in the presence of a longitudinal magnetic field. The discharge consists of two distinct regions, i.e., the bulk plasma region, which is essentially electric field free, and the cathode fall regions near the cathode surfaces having the length dc << d, where all the applied voltage is concentrated. Electrons ejected

from the cathode surfaces by ion bombardment (primary electrons/fast electrons) are accelerated by the cathode fall electric field and enter the discharge volume.

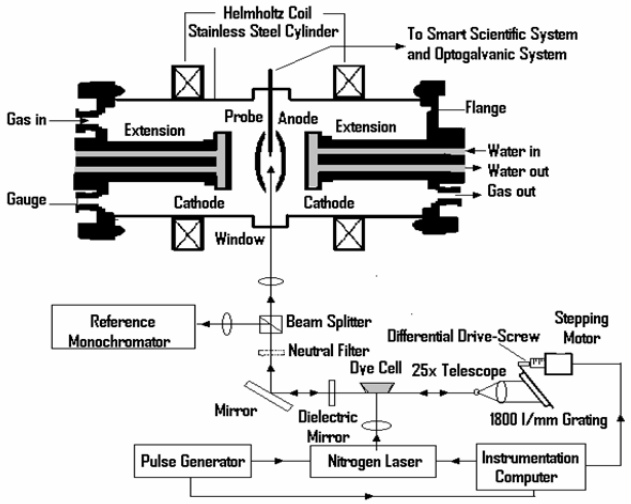

FIG. 1. Schematic representation of the experimental setup.

These fast electrons ionize and excite the gas particles. Any fast initial electron oscillates in the cavity between the two plane-parallel cathodes until it loses all of its energy (pendulum effect). Since the ionization within the cathode fall regions is negligible, the fast electron produces eU/w_0 ionizations within the bulk plasma region (w_0 is the energy cost of the electron-ion pair production). Low energy secondary electrons (slow electrons) are generated during the ionization of the gas particles. Their kinetics plays an important role in the plasma processes. Consequently, to analyze the discharge mechanism we must distinguish between the two electron energy ranges, i.e., the inelastic energy range $W^* < w < eU$, and the elastic energy range $0 < w < W^*$ (W^* is the threshold of inelastic processes, w is the electron kinetic energy, and U is the discharge voltage). In the inelastic energy range the electrons lose their energy through electron-molecule/atom inelastic collisions (excitation and ionization) while in the elastic energy range they lose energy essentially through electron-electron and electron-molecule/atom elastic collisions, and the processes of stepwise excitation and ionization. Since $eU_0/w_0 >> 1$, almost all electrons are concentrated in the elastic energy range (bulk electrons).

The bulk electrons ensure quasi neutrality of the plasma and carry no current. The electron current to the anode is due to the electrons with energies above several electron temperatures (intermediate/hot electrons), which can escape to the anode. The discharge mechanism described above, specific to the reflex discharge, resembles the mechanism that is characteristic of the driver region of the tandem multi-cusp negative ion sources [7–22], studied intensely since Bacal et al [13] reported the first results of significant ion production in the plasma volume. In both types of discharges there are two groups of electrons, that is, a group of high energy electrons ($E > 20$ eV) for generating the plasma and the ro-vibrationally excited molecules, and another group of cold electrons ($E \leq 1$ eV) for producing H^- ions by dissociative electron attachment [14–20]. To avoid confusion, we will henceforth adopt the terminology of hot electrons and cold electrons to categorize the electrons in these two energy ranges.

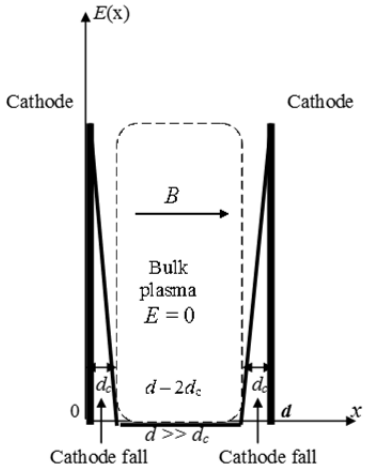

FIG. 2. Schematic representation of the cathode cavity, and pendulum effect.

A movable cylindrical Langmuir probe is inserted into the discharge region from the lateral port and can be positioned at any point in the discharge region, and at any angle with respect to the magnetic field. The thin wire probe tip is made of tungsten and is 8 mm long, and 100 μm in diameter. Often a linear extrapolation of the ion current at high negative bias is used to estimate the ion saturation current and from this the positive ion density n_i, but this method has been found to be highly inaccurate. A more accurate method involving the numerical solution to the equations which govern ion collection was found by Laframboise [14] and from these a set of ion current expansion curves have been deduced [15]. These curves are a function of the probe radius r_p to the Debye length λ_D and were used by Hopkins and Graham [11] in construction of a computer controlled Langmuir probe system. The probe voltage-current characteristics are recorded and analyzed for our experiments using such probe system that allows fast measurement of the plasma parameters. The electron density n_e and the electron temperature T_e of the cold electrons and hot electrons are obtained directly from the electron energy distribution function $f(\varepsilon)$, that is,

$$n_e = \int_0^\infty f(\varepsilon)d\varepsilon \tag{1}$$

and

$$T_e = \frac{2\langle\varepsilon\rangle}{3} = \frac{2}{3n_e}\int_0^\infty \varepsilon f(\varepsilon)d\varepsilon \tag{2}$$

where, according to Druyvesteyn procedure

$$f(\varepsilon) = 2(2m_e)^{1/2}(e^3A)^{-1}\varepsilon^{1/2}d^2I_p/dV^2 \tag{3}$$

and where ε is electron energy, m_e is the electron mass, e is the electron charge, A is the probe surface area, I_p is the probe current and V is the probe voltage.

To measure the density $n\_$ of the hydrogen negative ions in the plasma volume we use the method developed by Bacal et al, and reviewed recently in Ref. The electron affinity for hydrogen is 0.745 eV, hence for photo detachment of H^- ions to occur photons with energy greater than 0.745 eV are required. The principle of this method is to destroy all the negative ions in a region of the plasma illuminated by a laser beam of the appropriate energy by pumping the electron from the ground state into the continuum, that is $H^- + h\nu \rightarrow H + e^-$. Photo detachment produces an increase in the electron density without an immediate increase

of the positive ion density. Thus by simply collecting these extra electrons with a positively biased Langmuir probe, the fraction of negative ions which are destroyed during the laser pulse, $\Delta n_- / n_-$ has been shown by Bacal and Hamilton to be:

$$\frac{\Delta n_-}{n_-} = 1 - \exp\left[-\frac{\mathrm{E}}{\mathrm{A}_L} \times \frac{\sigma}{h\nu} \right] \tag{4}$$

where E is the laser pulse energy, A_L is the laser beam area, σ is the cross section for photodetachment of H^- ions, and $h\upsilon$ is the laser photon energy. At high pulse energy the photodetachment fraction $\Delta n_- / n_-$ is essentially 100% and the relative H^- ion density n_- / n_e can be determined from the change in the probe electron current.

$$\frac{n_-}{n_e} = \frac{\Delta n_e}{n_e} = \frac{\Delta i^-}{i_{dc}^-} \tag{5}$$

where Δi^- is the amplitude of the photo detachment pulse current, i^-_{dc} is the dc probe current, n_e is the electron density measured separately using the computerized Langmuir probe technique described above, and Δn_e is the increase in the electron density directly after the laser pulse, this is equivalent to the negative ion density.

To check the accuracy of the photo detachment optogalvanic measurements as a function of the laser energy and wavelength we use a tunable dye-laser within the wavelength range 450–500, as shown schematically in Fig. 1. The cross-section for the photo detachment of the electrons from H^- is almost half of its maximum of 4×10^{-17} cm^2. A pulsed nitrogen laser (wavelength of 337.1 nm and pulse width of 6 nsec), delivering about 200 kWatts peak power, can pump coumarin 1 in a dye-laser cavity, at a maximum repetition rate of 2 kHz internally and externally pulsed. Used with a $25\times$ beam-expanding telescope in the optical cavity, an 1800-lines/mm diffraction grating gives a line width of almost 0.019 nm within the wavelength range 430–520 nm. The wavelength drive consists of a differential screw, which rotates the grating. A stepping motor interfaced with a computer serves to advance the wavelength in 0.003 nm steps. The dye laser beam with a diameter of ≈ 2.5 mm, repetition rate of 10 Hz, and maximum output energy per unit area of ≈ 0.20 J/cm^2, is aligned coaxially with the cylindrical probe which is biased at an appropriate positive potential (electron saturation branch of the V-I probe characteristic) to collect the electrons liberated by photo detachment of the negative ions. A suitable electronics arrangement allows detection of only the liberated electrons and not the continuous current to the probe from the free electrons in the plasma. Neutral filters are used to check that the experiment is run in the conditions where the photo detachment fraction is independent by the dye laser pulse energy (Figs I, 6 and Refs [17]).

Finally, it is worth noting that there are different statistical errors associated with the measured plasma parameters. These have been estimated by comparing measurements made at different times under the same conditions (pressure, gas flow rate, magnetic field intensity, laser energy, laser wavelength and total input power). The relative standard uncertainty is less than 12% for electron temperature, 17% for electron density and positive ion density, and 22% for negative ion density. Taking into account the uncertainty of the probe surface area of about 5%, the total relative standard uncertainty for negative ion density is estimated to be 27%.

3. RESULTS OBTAINED IN PURE HYDROGEN

The ion density n_i is obtained directly from the ion branch of the probe characteristic. Dependence on power of the ion density measured at the center of the discharge chamber for p = 1.0 Pa and B = 100 G is presented in Fig 3.

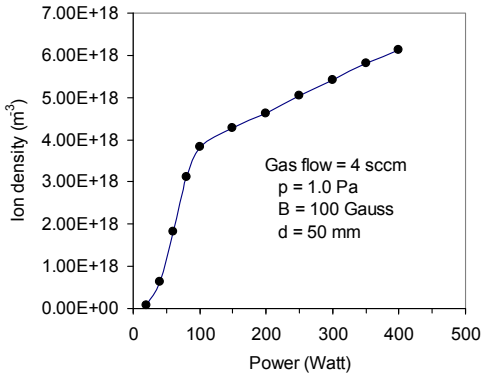

FIG. 3. Variation of the positive ion density versus dissipated power.

The enhanced magnetic ionization is evidenced clearly within the power level range from 40 to 100 Watt where the ion density increases almost one order of magnitude for only a factor of 2.5 increase in power; this phenomena is discussed in Ref. [1]. From 100 to 400 Watt the ion density n_i increases two times and seems to scale with the power. The magnetically enhanced hollow cathode effect leads to values of n_i as high as 6×10^{18} m^{-3} for P = 400 Watt.

Based on the results reported by other authors [11–13, 26] for low pressure hydrogen discharges we considered that H_3^+ is the dominant ion species in these plasmas. Indeed, the production of H_2^+ and H^+ ions is due to ionization in collision of energetic primary electrons (fast electrons e_f) with hydrogen molecules and hydrogen atoms, respectively. The reactions involved are $e_{fast} + H_2\ (v = 0) \rightarrow H_2^+(v) + 2e$; $H_2^+(v) + H_2(v = 0) \rightarrow H_3^+(v') + H$, and $e_{fast} + H \rightarrow H^+ + 2e$. The interaction cross section that leads to the appearance of H_3^+ can be as high as 10^{-14} cm^2 (Ref. [20]). Mullan and Graham [19] reported values of the positive ion fraction as high as 97% for H_3^+.

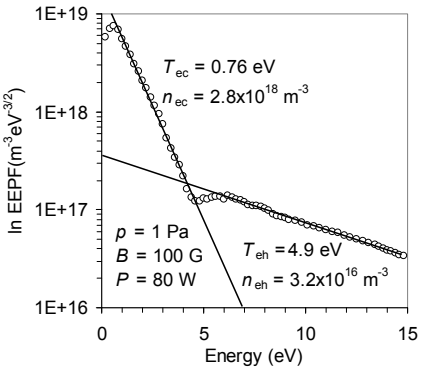

FIG. 4. Typical form of the electron energy distribution function.

The experimental electron energy distribution functions invariably show two electron temperatures (see Fig. 4). Here we are interested both in the group of cold electrons ($E \leq 1$ eV) responsible for producing H^- ions by dissociative electron attachment, DA, and the high energy electrons (hot electrons) responsible for generating the plasma and the ro-vibrationally excited molecules.

The dependence of the electron density n_{ec} and the electron temperature T_{ec} of the cold electrons on the gas pressure p for P = 400 Watts and B = 100 Gaus is presented in Fig. 5; the same parameters but for the hot group of electrons are presented in Fig. 6.

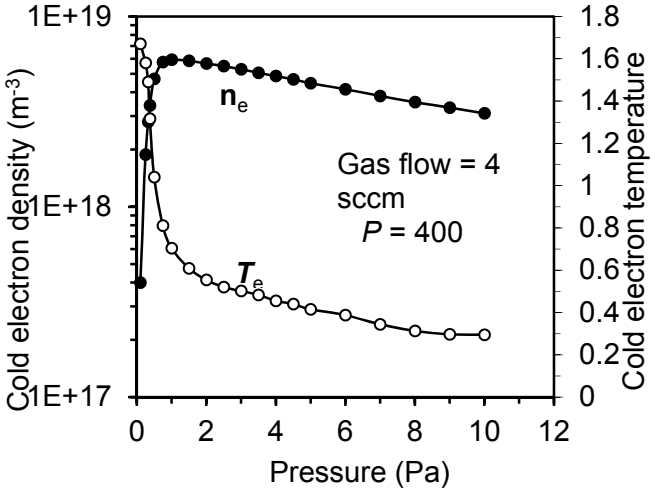

FIG. 5. Cold electron density and cold electron temperature versus pressure.

These data show that the cold group of electrons is dominant (densities n_{ec} of the order of 10^{18} m^{-3}), comparing to the hot group of electrons (densities n_{eh} of the order of 10^{16} m^{-3}).

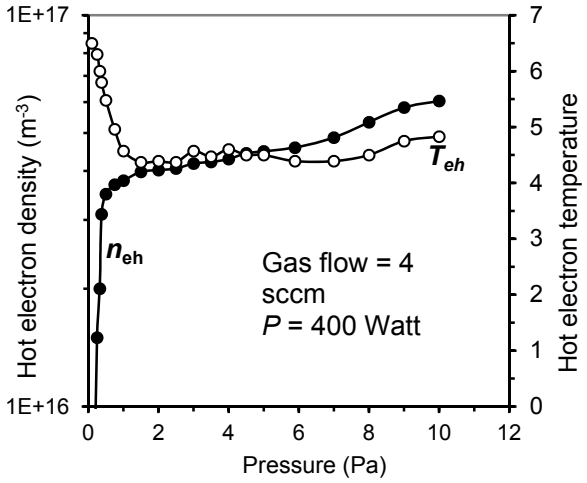

FIG. 6. Hot electron density and hot electron temperature versus pressure.

From inspection of the data in Fig. 5 it is clear that the pressure range centered on $p \approx$ 1.0 Pa is the most favorable one for the production of the hydrogen negative ions. For example, when p = 0.5 eV the cold electron density n_{ec} is 4.7×10^{18} m^{-3} and the cold electron temperature T_{ec} is 1.04 eV. A maximum value of 5.9×10^{18} m^{-3} is achieved for $p \approx$ 1.0 Pa

where $T_{ec} \cong 0.70$ eV. In the pressure range from 2.0 Pa to 10 Pa the cold electron density decreases smoothly to 3.1×10^{18} m^{-3} and $T_{ec} \cong 0.28$ eV. Since n_{eh} and T_{eh} remain almost constant in that pressure range, the conclusion is that the cold electron group controls the production of the negative ions and the pressure range where $p > 2.0$ Pa is not suitable for producing H^- using the reflex discharge plasma.

Figure 7 shows both the dependence of the negative hydrogen ion density $n\_$ and the negative hydrogen ion percentage $n\_ / n_e$ on the pressure p. The values of the external discharge parameters are the same as in Figs 5 and 6. Within the limit of the experimental errors of 27%, the data obtained for $n\_$ are independent of the tunable dye laser wavelength, when the dye laser is tuned within the wavelength range 450–500 nm. The variation of the optogalvanic signal Δi^- is no more than 24% and is due to the variation of the fluorescence efficiency of the coumarin 1 when pumped by nitrogen laser and the photodetachment cross section.

The negative hydrogen ion density increases with increasing pressure within pressure range 0.1–1.0 Pa up to almost 1.8×10^{17} m^{-3}, remains almost constant from 1.0 to 2.0 Pa, and then decreases to 0.5×10^{17} m^{-3} within pressure range 2.0–10 Pa. The two curves in Fig. 6 show that indeed the reflex discharge plasma is the most efficient within the pressure range from 0.5 to 2.0 Pa. Though $n\_ / n_e \approx 0.025$, the fact that the plasma density is higher than 10^{18} m^{-3} implies values of the negative ion density of the same order of magnitude as those obtained using tandem plasma sources [7–13, 19–22] but at higher power.

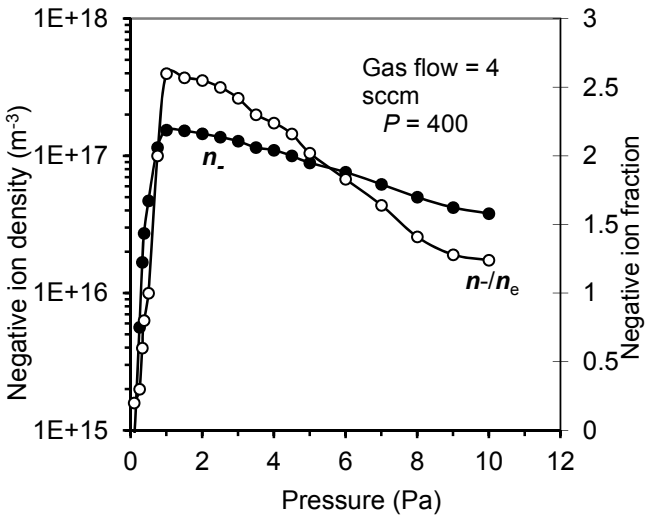

FIG. 7. Variation of the negative ion density and negative ion fraction with pressure.

The reason for an optimum pressure of around 1.0 Pa in the reflex discharge negative ion source can be explained considering first the mechanisms involved in producing negative hydrogen ions. Dissociative attachment from vibrationally excited H_2 molecules in their ground electronic state is the main accepted mechanism for $H\_$ negative-ion production in volume plasmas [20]. The first step is the formation of vibrationally excited molecules $H_2(v)$ via the radiative decay of the B and C excited molecule state

$$e_{fast} + H_2(X^1\Sigma_g^+, v=0) \rightarrow H_2^*(B^1\Sigma_u^1; C^1\Pi_u) \rightarrow H_2(X^1\Sigma_g^+, v) + e_{fast} \qquad (6)$$

The electron energy threshold for this process is around 13 eV and the cross-section is maximal at about 25 eV. Once the vibrational molecular state is formed it is long lived unless

a second fast electron collision occurs leading usually to dissociation or if it collides with the wall and jumps to a lower vibrational quantum level. If a slow electron collides with this vibrational molecule, dissociative attachment occurs forming an H^- ion via the short lived H_2^- state:

$$e_{slow} + H_2(v) \rightarrow H_2^- \rightarrow H^- + H \tag{7}$$

The cross-section for this process increases from about 10^{-22} cm^2 to 10^{-16} cm^2 as v changes from 0 to 6. It then saturates at 4×10^{-16} cm^2 for H_2 up to the highest vibrational level. The electron energy for a maximum rate coefficient is 0.6–0.8 eV for all vibrational levels. Detailed analyses of the volume sources shows that up to 85% of the H^- production from processes (6) and (7) is obtained via $H_2(X^1\Sigma_g^+, v > 5)$ states [21]. Another channel of enhancing the concentration of negative ions H^- relies on dissociative attachment from Rydberg states [30–32]. This process can be described as:

$$e_{slow} + H_2^* \rightarrow H + H^- \tag{8}$$

where H^*_2 represents a hydrogen molecule in a high lying excited Rydberg state.

The reflex discharge mechanism has also to be considered to discuss the data of Fig. 7. For $p < 1.0$ Pa the discharge voltage is higher than that one corresponding to the gas pressure range from 1.0 to 2.0 Pa. To maintain the dissipated power P constant, the discharge current must be lowered. But at lower current levels the hollow cathode effect and the magnetic enhancement ionization are less effective. This implies that the cold electron density decreases and the cold electron temperature increases. Fewer hot and cold electrons and higher temperatures for cold electrons within the plasma region means, according to the reactions (6) and (7), less vibrationally excited molecules, and lower values for the negative ion density. On the other hand, for $p > 2.0$ Pa the increase of the discharge voltage is small, so the variation of the discharge current is smooth and this fact is evidenced by the smooth variation of the electron density in Fig. 4. However, since $T_e < 0.5$ eV, the attachment process is less favorable, so the negative ion density decreases. The most favorable pressure range is from 0.5 to 2.0 Pa. where, according with the data of Fig. 3, the plasma density scales with the power.

It is worth mentioning that for $P < 200$ Watt the optogalvanic signal is very noisy for the whole pressure range analyzed, so the data for negative ion density is not reliable. If this is connected with a possible instability of the reflex plasma in this range of power then it is a problem which has still to be resolved. Fortunately, for power levels from almost 280 to 400 Watt the optogalvanic signal is stable and reproducible, so the experimental data of Fig. 6 are completely reliable.

4. RESULTS OF CESIUM SEEDING

Cesium was added to the source using a commercially available product from SAES getters (this company produces alkali metal dispensers which give a very pure alkali metal which can be delivered at a controlled rate). We used dispensers which were given to us by Queen's University Belfast, UK. The release of caesium is dependent on time and on temperature, the latter of which is controlled by the electric current passed through the dispenser, hence very accurate control of the quantity of caesium evaporated is achieved simply by controlling the current supply. From the current passed through the dispensers and

the manufacturer specification it was estimated that the total caesium input was 20.8 mg. If all this amount of caesium stays in the volume of the ion source the caesium density would be 1.1×10^{22} m^{-3}. This implies a ratio of neutral hydrogen to caesium between 50 and 300 for hydrogen pressure within the pressure range we used. If all of the cesium went to the wall this would give wall coverage of about 50 monolayers. The same fitting routine developed at Queens Univ. Belfast to fit Bi-Maxwellian energy distributions to EEPF/EEDF's was used to obtain values for the electron density and temperature. Typical examples are in Table 1.

TABLE 1. TYPICAL RESULTS OBTAINED FROM EEDF'S (P = 2 PA; P = 300 W; B = 100 G)

Population	Max Distribution 1		Max Distribution 2	
Parameter	n_{ec} (m^{-3})	T_{ec} (eV)	n_{eh} (m^{-3})	T_{eh} (eV)
Hydrogen	5.6×10^{18}	0.47	4.1×10^{16}	4.6
Hydrogen & Cs	3.8×10^{18}	0.59	3.6×10^{16}	4.2

The observed decrease in the electron density as seen in the plasma parameter values and EEPF's was not expected. If caesium was present in the volume of the source then the electron cooling by cesium can be regarded as very important if there are significant quantities of caesium. The cross sections for electron collisions at low energy are considerably larger for cesium than for hydrogen, and thus caesium would be expected to have a cooling effect on the electron population. Since the ionization potential of caesium (3.89 eV) is much lower than for hydrogen (13.56 eV) then the lower energy electrons are capable of causing ionization and producing positive Cs ions and more electrons. We can conclude at this point that there is no significant quantity of Cs in the volume of the source.

To detect if Cs is, or is not, present in the volume of the plasma source we made visible emission spectroscopy measurements. Light emission from the centre of the source was collected using a GDM-2 double monochromator. The most intense hydrogen lines H_α at 656.3 nm, H_β at 486.1 nm and H_γ at 434.0 nm, caesium lines at 455.53 nm and 459.32 nm, and Cs+ line at 535.85 nm were recorded. Both spectra, with and without caesium, are very similar and this implies that there are no cesium atoms or ions in the volume of the source.

The electron density and positive ion density were found to have no obvious dependence on the wall temperature. In contrast, the negative ion percentage changes with changing wall temperature. As the wall temperature increased the negative ion percentage decreased and as soon as the water cooling of the wall was turned on and the wall temperature started to decrease the negative ion percentage increased significantly. This would imply that H^- ion enhancement is a surface effect resulting from the caesium coverage of the inner walls of the ion source.

The work function measurements show that the cesium absorption/adsorption on the stainless steel surface leads to a reduction of the work function of the internal wall of the ion source. We based our measurements on the fact that the quantum efficiency Y is related to the photon energy $h\nu$ and the surface work function $e\varphi$ by $Y^{1/2} \propto (h\nu - e\varphi)$. From this it is easily seen that a straight line graph will mean that the x-axis intercept will be the work function of the surface. In pure hydrogen a value of about 4.3 eV was obtained for the work function of the inner wall (comparing with 4 eV for stainless steel) and it decreased for a cesium seeded hydrogen plasma. The experimental data proved that as the work function of the surface

decreased, the H^- ion percentage increased. This is very strong evidence indicating that the H^- ion enhancement mechanism in a cesium seeded ion source is due to a surface effect.

Combining all experimental conditions used in our research, i.e. presence of the magnetic field, no cesium lines within the volume of plasma source and variation of the wall work function, we conclude that the negative ion percentage enhancement effect is due to the magnetic field and to the cesium coverage on the inner walls of the chamber.

5. TRANSIENT INDUCED MOLECULAR NEGATIVE IONS

Further we present theoretical arrangments that a new type of particle may appear in hydrogen reflex discharge plasma as result of potential barrier interaction between a very cold electron and a hydrogen polarized molecule. Here we are particularly interested in seeing if the existence of short lived molecular negative ions can explain and/or predict absorption and stimulated emission of radio frequency radiation in both laboratory and space plasmas.

Classically the adiabatic interaction of the cold electron (charge *e* and mass *m*) with the polarizable molecule (polarisability *a*) can be considered in terms of the interaction potential $V(r) = \frac{-\alpha e}{8\pi\varepsilon_0 r^4}$, and the total energy of the system $E_0 = \frac{1}{2}mv_0^2$, where v_0 is the initial velocity of the electron, and the impact parameter *b*. Considering the momentum and energy conservation equations, the total energy of the system can be written as:

$$E_0 = \frac{mv_r^2}{2} + \frac{L^2}{2mr^2} - \frac{\alpha e^2}{8\pi\varepsilon_0 r^4} \tag{9}$$

where *r* is the distance of the electron from the molecule, assumed here to be a point, and $\vec{L}\ (= m\vec{r} \times \vec{r})$ is the electron's angular moment. The first term on the right side is the radial energy E_r where $v_r(r)$ is the radial velocity, the second term is the centrifugal potential energy $U_c(r)$, and the last term is the potential interaction energy $U_p(r)$. In equation (9), the last two terms are collectively the effective potential $U_{eff}(r)$, i.e.:

$$U_{eff}(r) = \frac{L^2}{2mr^2} - \frac{\alpha e^2}{8\pi\varepsilon_0 r^4} = E_0\frac{b^2}{r^2} - \frac{\alpha e^2}{8\pi\varepsilon_0 r^4} = \frac{A}{r^2} - \frac{B}{r^4} \tag{10}$$

The electron is moving in an inverse-square-repulsive potential $V_c(r) \propto r^{-2}$, and in an inverse-fourth-power-attractive potential $V(r) \propto r^{-4}$. The first term in equation (10) dominates at larger distances, while the second term (the attractive polarization potential) is dominant at smaller distances, producing a maximum in $U_{eff}(r)$. In general, a potential barrier will exist for any attractive potential $V(r)$ that is a steeper than an inverse square function of *r*.

The form of the electron trajectory upon approaching the molecule depends on the value of both E_0 and *L*. The variation of the different terms in equation (9) with the distance *r* between the incoming electron and the molecule is shown in Fig. 8. The axis values refer to a specific calculation for hydrogen, as discussed later. Consider, with reference to Fig. 8, the sequence of trajectories for electrons with initial kinetic energies E_0, but with a range of impact parameters corresponding to different values of *L*. With increasing *L* the corresponding curve $U_{eff}(r)$ moves upward. At some values of *L* the maximum in this curve

becomes equal to E_0, i.e., $U_{eff,}$ max = $U_{eff}(r_M)$ = E_0, where r_M is the attachment boundary radius. Electrons with energies lower than E_0 and with the same L will evidently be reflected by the potential barrier, while those with the total energy greater than E_0, pass over the potential barrier and pass through the point-like molecule.

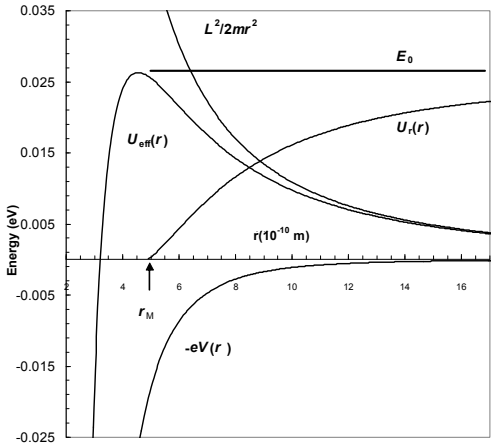

FIG. 8. Example of spatial variation of the terms in equation (9), for E0 ≈ Ueff,max = 0.026 eV.

The situation that particularly interests us here is when the initial kinetic energy of the electron E_0 is almost equal to the value of $U_{eff}(r_M)$ at the peak of the potential curve. In this case the electron will spend a considerable time at a radial distance close to r_M. The electron can then be said to "orbit" about the centre of force (the polarized molecule). The angular motion speeds up as r decreases in order to conserve angular momentum, and a large number of revolutions may be made. It is important to note that these are unstable orbits, unlike those when the r dependence of the interaction potential is shallower than an inverse square. Such sticky collisions [26, 27] where both the energy and the angular momentum are always conserved although the form of the energy may change, lead to the formation of Transient Induced Molecular Negative Ions (TIMNIs).

Referring to the data of Fig. 8, and considering the radius of the attachment boundary r_M, the classical value of the cross section $\sigma = \pi r^2_M$ is estimated to be of the order 10^{-15} cm^2. A better quantity to describe the interaction process is the two-body rate coefficient [28] $\beta = \sigma v_0$. For the specific case discussed here, its value is as high as 2×10^{-8} cm^3/s, evidencing a very probable process that can occur within a high density and low electron temperature reflex discharge plasma. Then, according to the classical analysis the free electron moves toward the polarized diatomic molecule up to a minimum distance, remains attached for a short time, forming a TIMNI, and then leaves the molecule on a symmetric trajectory. Both the total energy and the angular momentum of the electron are conserved at all times, though forms of energy can change. Consequently, the polarized molecules are under the influence of the magnetic field generated by the attached electrons. The attached electron makes tens of thousands of revolutions and the lifetime of a TIMNI can be of the order of 10^{-7} s. It is connected with the magnetic field generated by the attached electron, and is different by the lifetime of the resonance states involved in r_f transitions which is an intrinsic characteristic of the polarized molecules.

The hydrogen TIMNIs. As shown above, there is possibility for cold electrons in cold plasmas to move in circular orbits about the polarized molecules. Since the molecule feels only the influence of the magnetic field but not its origin, we can analyse the possible magnetic resonances following the methods used in the radiofrequency spectroscopy in the

presence of the external magnetic fields [29]. The orbiting electron is considered as a current loop in the form of a circle of radius r that carries a current I. For example, for $r = 5\times10^{-10}$ m, and $v = 5\times10^{6}$ m/s, the magnetic field at the centre of the loop is as high as 0.3 T. A more convenient way is to analyse the radiofrequency magnetic resonances in polarized molecular plasmas using a quantum mechanics vector model.

The angular momentum of the orbiting electron can be quantified as $L = \sqrt{2mE_0}b = \sqrt{l(l+1)}\,\hbar$, where l is the orbital momentum quantum number. The electron energy and the impact parameters must satisfy the condition:

$$b_l = \sqrt{\frac{l(l+1)}{2mE_0}}\hbar\,. \tag{11}$$

This means that there is an energy range and an impact parameter range for which the electron can form a TIMNI. The upper limit of the electron energy, E_0, max , is determined by the condition that a solution exists for equation (9) and the lower limit of the impact parameter $b_{\min}$ is determined by the condition $b > r_b$, where r_b is the bond length of the molecule.

The radius of the orbit, obtained as the largest real root of the equation (9), is:

$$r_l = \left\{\frac{l(l+1)\hbar^2}{4mE_0} + \left[\frac{l^2(l+1)^2\hbar^4}{16m^2E_0^2} - \frac{\alpha e^2}{8\pi\varepsilon_0 E_0}\right]^{1/2}\right\}^{1/2} \tag{12}$$

According to formula (12), the electron energy must satisfy the condition $E_0 \le \dfrac{\pi\varepsilon_0 l^2(l+1)^2\hbar^4}{2\alpha m^2 e^2}$, and for the hydrogen plasma ($\alpha_{H2} = 1.571\times10^{-30}\,m^{-3}$) the electron temperature must be lower than 1.5 eV. This is an encouraging result since in the reflex discharge plasmas, with bulk electron density as high as 10^{18} m^{-3}, the number of electrons within the energy range from 0 to 1.5 eV represents more than 60% of all electrons [1–4].

We coin this system formed from polarized diatomic molecule and attached electron Transient Molecular Negative Ion, TMNI; it is completely different by stable negative ion both from the viewpoint of the mechanism of formation and structure and stability. Therefore, the next analysis is concerned with the study of the TMNI from quantum mechanical point of view. The vector model for TIMNI is presented schematic in Fig. 9, where the notation corresponds to that used in quantum theory.

As part of TIMNI, the polarized molecule is characterized by the electron spin angular momentum, the rotational momentum $\vec{K}$, the total angular momentum, $\vec{J} = \vec{S} + \vec{K}$ (the corresponding quantum numbers are S, K, and J) and by the spin magnetic moment $\vec{\mu}_S$ due to $\vec{S}$. The projections of $\vec{\mu}_S$ along the axis $\vec{J}$ are $\mu J_1 = K+1$, $\mu J_2 = K$, and $\mu J_3 = K-1$. On the other hand, the orbiting electron is considered as an effective current loop that creates a magnetic field in the center of the loop.

Therefore to the orbital angular moment $\vec{l}$ corresponds an orbital magnetic moment $\vec{\mu}_l$ and to the spin angular momentum $\vec{s}$ corresponds a spin magnetic moment. Consequently, the electron has a total magnetic moment $\vec{\mu}_j$. We consider, a priori, $l = 1$ and the two values of the magnetic moment μ_j are $\mu_{3/2}$ and $\mu_{1/2}$, respectively.

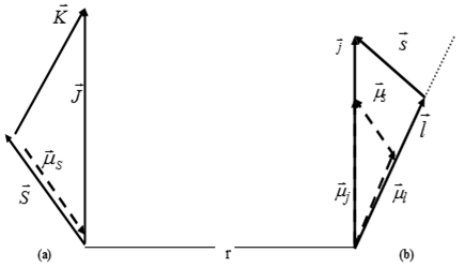

FIG. 9. Vector model of TIMNI; (a) molecule, (b) electron.

The magnetic field in the center of an orbit of radius r is:

$$B = \mu_0 \mu_j / r^3 \tag{13}$$

where μ_0 is the vacuum permeability. Since $\vec{B} // \vec{J}$, then the magnetic energy corresponding to a molecular quantum state will be $\mu_0 \mu_{J_{1,2,3}} \mu_j / r^3$, where $\mu_{J_{1,2,3}}$ is a function of *K*. There are two possible electron spin magnetic resonance transitions of the oxygen molecule within the magnetic field created by the attached electron, given by the expressions:

$$h\nu_{K+1\to K} = \frac{\mu_0 \mu_j}{r^3}(\mu_{K+1} - \mu_K) \quad ;$$

$$h\nu_{K\to K-1} = \frac{\mu_0 \mu_j}{r^3}(\mu_K - \mu_{K-1}) \tag{14}$$

The values of the frequencies corresponding to such a spin magnetic resonant transition can be obtained from (14) by replacing *r* by expression (12) and $\mu_{K+1}, \mu_K, \mu_{K-1}$ by the expressions given by molecular spectroscopy, that is:

$$\mu_{K+1} = 2\sqrt{\frac{K+2}{K+1}} \times \mu_B ; \qquad \mu_K = \frac{2}{\sqrt{K(K+1)}} \times \mu_B ; \qquad \mu_{K-1} = -2\sqrt{\frac{K-1}{K}} \times \mu_B$$

where μ_B is the Bohr magnetron.

For $j = 3/2$ state ($\mu_{3/2}$=2.582 μ_B) the corresponding magnetic resonant transitions are:

$$\nu_{K+1\to K} = 6.2\left(\sqrt{\frac{K+2}{K+1}} - \sqrt{\frac{1}{K(K+1)}}\right) \text{ MHz};$$

$$\nu_{K\to K-1} = 6.2\left(\sqrt{\frac{1}{K(K+1)}} + \sqrt{\frac{K-1}{K}}\right) \text{ MHz} \tag{15}$$

In this manner, doublets both in emission and absorption are to be observed. The transitions correspond to a variation of the magnetic energy that comes out of the change in projection of $\vec{\mu}_J$ onto the magnetic field of the attached electron.

The formula (15) predicts magnetic resonance transitions within the frequency range from 3.21 MHz ($K + 1 \rightarrow K$ transition and $K = 1$) to almost 6.2 MHz for higher values of *K*. This semiclassical model suggests that the interaction of cold electrons to form transient induced molecular negative ions could lead to observable resonant transitions. This potentially opens up a new area of spectroscopy in low temperature plasmas making it worthy of further experimental and theoretical study.

6. CONCLUSION

A new type of caesium-hydrogen negative ion volume source was designed, constructed and analyzed as a potential negative ion source to be used in next generation of fusion devices; it is complementary to other volume plasma sources. The new type of negative ion plasma source belongs to the category of double diode glow discharge sources working in an abnormal regime, and relies on a direct current reflex discharge obtained as a hybrid between a Penning discharge and a hollow cathode discharge. Its advantage, over other types of non-equilibrium direct current plasma sources, emerges from the enhanced hollow cathode effect (HCE), produced by the presence of the magnetic field. The reflex discharge plasma source is characterized by an increased ionization rate (with plasma density high as $10^{18}m^{-3}$) for a relatively low power density dissipated within the discharge, high uniformity, and technical simplicity. The bulk plasma is free of an electric field.

A diagnostic method based on laser beam photo detachment of negative ions and detection of detached electrons by an electrostatic probe is used to measure the density n_ of the hydrogen negative ions. The positive ion density n_i, the electron density n_e, and the electron temperature T_e are measured using the Langmuir probe method and the Druyvesteyn procedure, along with suitable software. The operating conditions are optimized for n_i, n_e, T_e , n_- and n_- / n_i within the pressure range 0.1–10 Pa, discharge power 40–400W, and magnetic field 0–150 G.

Caesium was added to the source. Visible and VUV spectroscopy measurements have been made, as have surface work function measurements of the internal wall of the ion source. Combining all experimental conditions used in our research, i.e. presence of the magnetic field, no caesium lines within the volume of plasma source and variation of the wall work function, we conclude that the negative ion percentage enhancement effect is due to the magnetic field and to the caesium coverage on the inner walls of the chamber.

We present theoretical arguments that a new type of particle, TIMNI, may appears in hydrogen reflex discharge plasma as result of potential barrier interaction between a very cold electron and a hydrogen polarized molecule. We were particularly interested in seeing if the existence of short lived molecular negative ions can explain and/or predict absorption and stimulated emission of radio frequency radiation in both laboratory and space plasmas. Doublets both in emission and absorption are to be observed. The transitions correspond to a variation of the magnetic energy that comes out of the change in projection of $\vec{\mu}_J$ onto the magnetic field of the attached electron. The expression of the transition frequency predicts magnetic resonance transitions within the frequency range from few MHz to almost one hundred MHz. The theoretical model suggests that the interaction of cold electrons to form transient induced molecular negative ions TIMNIs could lead to observable resonant transitions. This potentially opens up a new area of spectroscopy in low temperature plasmas making it worthy of further experimental and theoretical study.

ACKNOWLEDGEMENTS

The work is supported by the Romanian CNCSIS, Grant No. 33379/04, and the International Atomic Energy Agency, IAEA, Grant No. 12411/RO.

REFERENCES

[1] TOADER, E.I., AND COVLEA, V., Rev. Sci. Instrum., 76 (2005) 033502.
[2] TOADER, E.I., Plasma Sources Sci. Technol., 13 (2004) 646.

[3] TOADER, E.I., COVLEA,V., GRAHAM,W.G., AND STEEN, P.G., Rev. Sci. Instrum.,75 (2004) 382.
[4] TOADER, E.I., GRAHAM, W.G., MAHONY, C.M.O., and Steen, P.G., Rev. Sci. Instrum., 73 (2002) 2974.
[5] PHILLIPS, C.S., Proc. R. Soc. London, Ser., A64 (1898) 172 .
[6] PASCHEN, F., Ann. Phys. (Leipzig), 50 (1916) 901.
[7] BACAL, M., Plasma Sources Sci. Technol., 2 (1993) 451.
[8] BACAL, M., and HAMILTON, G.W., Phys. Rev. Lett., 42 (1979) 190.
[9] BACAL, M., HAMILTON, G.W., BRUNETEAU, A.M., DOUCET, H.J., and TAILLET, J., Rev. Sci. Instrum., 50 (1979) 719.
[10] BACAL, M., Rev. Sci. Instrum., 71 (2000) 3981.
[11] HOPKINS, M.B., and GRAHAM, W.G., Rev. Sci. Instrum., 57 (1986) 2210.
[12] HOPKINS, M.B., and GRAHAM, W.G., J. Phys. D: Appl. Phys., 20 (1987) 838.
[13] HOPKINS, M.B., and GRAHAM, W.G., J. Appl. Phys., 69 (1991) 3461.
[14] BARDSLEY, J.N., HERZENBERG, A., and MANDL, F., Proc. Phys. Soc., 89 (1966) 305 & 321.
[15] BOTTCHER, C., and BUCKLEY, B.D., J. Phys. B: At. Mol. Phys., 12 (1979) L497.
[16] ALLAN, M., and WONG, S.F., Phys. Rev. Lett., 41 (1978) 1791.
[17] WADEHRA, J.M., and BARDSLEY, J.M., Phys. Rev. Lett., 41 (1978) 1795.
[18] WADEHRA, J.M., and BARDSLEY, J.M., Phys. Rev., A20 (1979) 1298.
[19] BACAL, M., BRUNETEAU, J., and DEVYNCK, P., Rev. Sci. Instrum., 59 (1986).
[20] EL BALGHITI-SUBE, F., BACSHT, F.G., and BACAL, M., Rev. Sci. Instrum., 67 (1996) 2221.
[21] HOPKINS, M.B., and GRAHAM, W.G., Vacuum, 36 (1986) 873.
[22] HOPKINS, M.B., and GRAHAM, W.G., Rev. Sci. Instrum., 61 (1989) 451.
[23] BACAL, M., BRUNETEAU, A.M., DOUCHET, H.J., and MARECHAL, A.M., Bull. Am. Phys. Soc., 23 (1978) 846.
[24] LAFRAMBOISE, J.G., 1966 Univ. of Toronto, Inst. for Aerospace Studies, Report no. 100.
[25] HOPKINS, M.B., 1987 Doctor of Philosophy Thesis, University of Ulster.
[26] BACAL, M., BRUNETEAU A.M., GRAHAM W.G., HAMILTON G.W., and NACHMAN M., J. Appl. Phys., 53 (1981) 1247.
[27] MULLAN, A.A., and GRAHAM, W.G., J. Phys. D: Appl. Phys., 24 (1991) 1533.
[28] HOLMES, A.J.T., Plasma Physics and Controlled Fusion, 34 (1992) 653.
[29] BERLEMONT, P., SKINNER, D.A., and BACAL, M., Rev. Sci. Instrum., 64 (1993) 2721.
[30] PINNADUWAGE, L.A., and CHRISTOPHOROU, L.G., Phys. Rev. Lett., 70 (1993) 754.
[31] HASSOUNI, K., GICQUEL, A., and CAPITELLI, M., Chem. Phys. Lett., 290 (1998) 502.
[32] CELIBERTO, R., LARICCHIUTA, A., LAMANNA, U.T., Janev, R.K., and Capitelli, M., Phys. Rev., A60 (1999) 2091.
[33] LANGEVIN, P., ANNALES De Chimies et al., physique, 28 (1903) 317.
[34] MCDANIEL, E.W., 1964 Collision phenomena in ionized gases, (Wiley, New York) p.70.
[35] CHANIN, L.M., PHELPS, A.V., and BIONDI, M.A., Phys. Rev., 128 (1962) 219.
[36] AGARBICEANU, I.I., and POPESCU, I.M., 1975 Optical methods of radiofrequency spectroscopy, (Adam Hilger Ltd, London).
[37] NISHIURA, M., SASAO, M., and BACAL M., J. Appl. Phys., 83 (1988) 2944.
[38] BRUNETEAU, A.M., and BACAL, M., J. Appl. Phys., 57 (1985) 4342.
[39] HISKES, J.R., Rev. Sci. Instrum., 65 (1994) 1219.

STOCHASTIC PROCESSES AT DENSE PLASMA BEAMS INTERACTION WITH CONSTRUCTION MATERIALS

Ü. UGASTE
Department of Natural Sciences
Tallinn University
Tallinn, Estonia

Abstract

The processes of interaction between dense plasma beams and construction materials in a radiation device have been studied. As a result of theoretical investigation it was shown that some interesting phenomena take place in simple one dimensional systems, arising as a consequence of interplay between a non-equilibrium noise, thermal noise, and deterministic force. On the basis of an exact expression for the flux there have been found a number of collective effects displayed when periodic pulses of ions are injected into the bulk of material during a period that is short compared to the characteristic diffusion time. It was established that in certain parameter regions an increase in noise parameters (noise flatness, correlation time, temperature) can facilitate the conversion of noise energy into mechanical work — i.e. the dependence of the efficiency of energy transformation on noise parameters exhibits a bell shaped (resonance) form. Some possible applications to fluctuation induced separation of particles as well as to the amplifying of small signals also discussed. The redistribution of deuterium implanted into iron based alloys at plasma beam interaction with the alloy surface was investigated analytically. It was shown that deuterium implanted into a surface layer may redistribute very quickly even at low temperatures, and most of the implanted particles diffuse into the body of the specimen. In cooperation with the Moscow Institute of Metallurgy and Material Science and the Warsaw Institute of Plasma Physics and Laser Microfusion regular joint experiments on the plasma focus devices (DPF) PF-1000 and PF-6 available at the Warsaw Institute of Plasma Physics and Laser Microfusion were carried out in order to obtain information about hot plasma beam interaction with several materials placed in different distances and angles relative to DPF anode.

1. INTRODUCTION

Among innovative technologies those ones, which exploits extreme densities of power flux of ionizing radiation, are of a special interest particularly in the field of material sciences. In this case the dose of the radiation is compressed initially in time (at radiation device) and later (at its absorption within specimen) in space to very high extent. And recent high energy density technologies gave a possibility to ensure these two types of power compression up to the breakthrough extent. Namely it is such an extent, that every high-energy particle (or X ray photons) of the beam will interact with the material under treatment not in a sequence (one by one), but simultaneously. And if the effective spheres of each radiation particle action within the material (e.g. spheres filled by photoelectrons at X ray photon absorption) will overlap during the time period less than the relaxation time of interaction process, the interaction is likely to possess new qualitative aspects. In some cases various synergetic effects also may be foreseen. They might lead in its turn to new effects and/or result in technology changes.

The processes of interaction between dense plasma beams and construction materials in a radiation device have an essentially stochastic character. These stochastic processes of interaction may be conditionally divided into three stages: (1) interaction between plasma components and material surface — an essentially non-equilibrium and non-deterministic stochastic process, (2) possible redistribution of surface components heated by plasma — an non-equilibrium but deterministic stochastic process (atom diffusion) and (3) redistribution of light elements (e.g. gas atoms implanted into surface layers during irradiation) after interaction. All these stages have to be investigated separately as they have very specific character and therefore need different methods and tools for experimental and theoretical investigation. First of these stages may be investigated at the moment only in theory, the other two stages — both theoretically and experimentally. In our work the most detailed attention were paid to the investigation of the first and third stages of interaction due to our opportunities, at least during the first years of the CRP.

At the same time theoretical investigation of this very complicated phenomenon, as interaction between dense plasma beams and materials is, without experimental evidence seems to be not very effective. Thanks to CRP "Dense magnetized plasmas", our research group had opportunities to participate in experiments on plasma focus devices PF-6, PF-150 and PF-1000 at the Warsaw Institute of Plasma Physics and Laser Microfusion. Analytical procedures (optical measurements, scanning electron microscopy, X ray spectral analysis, X ray diffractometry, mass measurements etc.) were made in cooperation with the Warsaw Institute of Plasma Physics and Laser Microfusion, the Moscow Physical Society, the Institute of Nuclear Physics of the Moscow State University, the Moscow Institute of Metallurgy and Material Science, the Prague Institute of Plasma Physics.

2. SPECIFIC TOPICS UNDER RESEARCH

The main specific topics of our research during the CRP were as follows:

(1) Studies of the influence of colour noise on anomalous transport phenomena of nanoparticles and of noise flatness on the mobility of over damped particles in materials with a periodic structure driven by non-equilibrium three-level noise and an additive thermal noise.
(2) Irradiation of new sample sets using different regimes of the Plasma Focus PF-150 and PF-1000 and analysis of specimens using X ray diffraction, X ray spectral analysis, electron scanning and optical microscopy etc., in cooperation with the Institute of Plasma Physics and Laser Microfusion, the Moscow Physical Society, the Institute of Nuclear Physics of the Moscow State University, the Moscow Institute of Metallurgy and Material Science and the Prague Institute of Plasma Physics.
(3) Refinement of the phenomenological model describing dense plasma beams interaction with wall materials taking into account experimental results elaborated recently (in collaboration with the Institute of Metallurgy and Material Science RAS (Moscow, Russian Federation) and with the Institute of Plasma Physics and Laser Microfusion (Warsaw, Poland).

3. DETAILED RESEARCH METHODS

Besides theoretical methods (stochastic differential equation, master equation for the probability density, stationary solutions and methods of analysis of the solutions) many experimental methods were used. Among them: optical methods of surface analysis, scanning electron microscopy, qualitative and quantitative X ray microanalysis and atomic structure measurements by X ray diffraction.

4. NEW EQUIPMENT CONSTRUCTED

During the CRP several new equipment items were built and the research capabilities of the lab were improved. Particularly, in cooperation with the Warsaw Institute of Plasma Physics and Laser Microfusion and the firm Telab sp. z.o.o. (Poland) a new dense plasma device (DPD) was constructed and installed in our plasma physics laboratory.

5. RESULTS

5.1. Studies of possible phase transitions induced by non-equilibrium fluctuations in different systems by using a three-level coloured noise model.

5.1.1. Introduction

Experiments with plasma focus devices represent a special interest for investigation of the interaction of pulsed plasma streams with materials. Among the various tasks of scientific activity in this field there is one of a particular interest, namely, the elaboration of a phenomenological model of interaction between dense plasma beams and construction materials. Two sweeping generalization can be made about processes between plasma and materials: they are intrinsically nonlinear and operate in noisy environment far from thermodynamic equilibrium.

Within the past two decades the behavior of non-equilibrium systems depending on fluctuations (noise) has attracted considerable attention. Some phenomena recently discovered have brought about the idea that noise can induce order in nonlinear non-equilibrium systems. Stochastic resonance, noise induced phase transitions in spatially extended systems stochastic transport in ratchets, noise induced spatial patterns, noise supported traveling structures in excitable media, absolute negative mobility, hypersensitive response, and giant amplification of diffusion are among the new phenomena encountered in this field. Active analytical and numerical investigations of various models in this field were stimulated by their possible applications in chemical physics, molecular biology, nano-technology and for separation techniques of nano-objects.

The most productive abstraction of noise-like influence from the environment is the case of Gaussian white noise. There the problem is considerably simplified as the corresponding transition probability densities satisfy the Fokker-Planck equation, which in certain specific cases can be solved exactly. However, various physical effects are induced only by colored noise, which has a nonzero correlation time, and in these cases the white noise approximation represents an oversimplification. Theoretical investigations indicate that coloured noise induced non-equilibrium effects are sensitive to noise flatness, which is defined as the ratio of the fourth moment to the square of the second moment of the noise process. Although its significance is clear, the role of the flatness of fluctuations has not received due attention. The latter circumstance inspired us to model the non-equilibrium fluctuations as a three-level telegraph process that may be called trichotomous noise. Notably, the flatness of a trichotomous noise can have any value from 1 to ∞.

In our work we consider, as a toy model for the elaboration of the abovementioned phenomenological model, the dynamics of over-damped particles in a periodic, one dimensional potential landscape subjected to a static (or adiabatic) external force and to both thermal noise and a non-equilibrium three-level coloured noise.

The purpose of the present report is twofold: first, to provide a compact review of a series of our recently published papers [8–14] in which coloured noise induced non-equilibrium transport phenomena of Brownian particles were considered, and second, to discuss — on the basis of the proposed model system — some novel phenomena in stochastic systems where the role of noise flatness as a control parameter is crucial. Here we report, for the first time, the following results: (i) The phenomenon of four current reversals versus noise correlation time, i.e. a change in the sign of the particle flow while the correlation time of noise is varied, found in [10–12] at the large flatness limit, is also present in the case of moderate flatness of noise. The necessary condition for the existence of this effect is that the

flatness $\varphi > 2$; (ii) In the region of current reversals, the dependence of efficiency (with which the system converts fluctuations to useful work) on noise flatness as well as on temperature exhibits a bell shaped resonance form; i.e. the efficiency can be optimized if we vary either the noise flatness or the temperature; (iii) The possibility exists of a new interpretation of these results in terms of the cross-correlation between two dichotomous noises.

In particular, we show that the proposed simple toy model exhibits a rich variety of anomalous transport phenomena, namely, four current reversals, hypersensitive transport, negative differential resistance, hypersensitive differential response, the phenomenon of disjunct "windows" for an external force, and absolute negative mobility. We emphasize that to our knowledge such a rich variety of anomalous transport effects have never been reported before for over-damped Brownian particles in a one dimensional periodic structure with a simple periodic potential (i.e. with one minimum per period).

5.1.2. A model with a three-level noise

We consider over-damped motion of Brownian particles in a one dimensional spatially periodic potential of the form $V(x,t) = V(x)Z_1(t)$, where $Z_1(t)$ is a trichotomous process and *V(x)* is a piecewise linear function, which has one maximum per period. There is an additional force that consists of thermal noise $\xi(t)$ of temperature *D*, an external static force *F*, and a three-level colored noise $Z_2(t)$. The system is described by the following dimensionless Langevin equation:

$$\frac{dX}{dt} = [\alpha + \beta Z_1(t)]h(t) + F + aZ_2(t) + \xi(t) \tag{1}$$

where $h(x) \equiv -dV(x)/dx$, $V(x) = \widetilde{V}(\widetilde{x})/\widetilde{V}_0$ ($\widetilde{V}(\widetilde{x})$ is a spatially periodic function of a period $\widetilde{L}$, $\widetilde{V}_0 = \widetilde{V}_{\max} - \widetilde{V}_{\min}$), and α, β and *a* are constants. The usual dimensionalized physical variables are indicated by tildes and the space and time coordinates read as $X = \widetilde{X}/\widetilde{L}$ and $t = \widetilde{t}\,\widetilde{V}_o/\gamma\widetilde{L}^2$ with γ being the friction coefficient; $\widetilde{F} = F\widetilde{V}_0/\widetilde{L}$ is a constant external force. The thermal noise $\xi(t)$ with the correlator $\langle \xi(t_1), \xi(t_2) \rangle = 2D\delta(t_1 - t_2)$ satisfies $\langle \xi(t) \rangle = 0$.

As to the random function *Z(t)*, we assume it to be a zero-mean trichotomous Markovian stochastic process which consists of jumps among three values $z_1 = 1$, $z_2 = 0$, $z_3 = -1$. The jumps follow in time according to a Poisson process, while the values occur with the stationary probabilities $p_s(z_1) = p_s(z_3) = q$ and $p_s(z_2) = 1 - 2q$. In a stationary state, the fluctuation process satisfies $\langle Z(t) \rangle = 0$ and the correlator is $\langle Z(t_1), Z(t_2) \rangle = 2q \exp[-\nu\,|\,t_1 - t_2\,|]$, where the switching rate *v* is the reciprocal of the noise correlation time $\tau_c = 1/\nu$. It is remarkable that for trichotomous noises the flatness parameter $\varphi = \langle Z^4(t) \rangle / \langle Z^2(t) \rangle^2 = 1/2q$, contrary to the cases of the Gaussian colored noise ($\varphi = 3$) and the symmetric dichotomous noise ($\varphi = 1$), can be anything from 1 to ∞. This extra degree of freedom can prove useful in modelling actual fluctuations. Moreover, it is interesting that the results of the present paper can be interpreted in terms of the cross-correlation intensity between two noises. Namely, the trichotomous noise *Z(t)* can be presented as the sum of two cross-correlated zero-mean symmetric dichotomous noises $\widetilde{Z}_1(t)$ and $\widetilde{Z}_2(t)$, i.e., $Z(t) = \widetilde{Z}_1(t) + \widetilde{Z}_2(t)$. The dichotomous noises $\widetilde{Z}_1(t)$ and $\widetilde{Z}_2(t)$ are characterized as follows:

$\widetilde{Z}_1, \widetilde{Z}_2 \in \{1/2; -1/2\}$, $\nu_1 = \nu_2 = \nu$ and their correlation function is $\left\langle \widetilde{Z}_i(t'), \widetilde{Z}_j(t) \right\rangle = (\rho_{ij}/4)\exp[-\nu|t-t'|]$, $i, j = 1, 2$, where $\rho_{ii} = 1$, and $\rho_{ij} = \rho \in (-1,1)$ with $i \neq j$ is the cross-correlation intensity of the noises $\widetilde{Z}_1$ and $\widetilde{Z}_2$. In this case the probability $q = (1+\rho)/4$, from which it follows that $\rho = (2-\varphi)/\varphi$. Let us note that such a cross-correlation between dichotomous noises may be a result of the following two reasons: the two noises are either partly of the same origin or influenced by the same factors.

For a stationary state we can solve the master equation corresponding to Eq. (1), assuming that the potential *V(x) = V(x-1)* in Eq. (1) is piecewise linear (saw toothlike) and its asymmetry is determined by a parameter $d \in (0,1)$, with *V(x)* being symmetric when $d = 1/2$. The effective calculation scheme, appropriate to solving of the Eq. (1) with saw toothlike potential, is presented in Refs. [9, 13–14].

5.1.3. Multiple current reversals

In Refs [9–12] we have examined model (1) with $F = \beta = 0$, $\alpha = 1$. Considering the case when the trichotomous noise is very flat, it is shown that the transport direction of Brownian particles can be controlled by thermal noise also in the case it is induced by symmetric trichotomous noise. It is also established that on the basis of a large flatness limit a number of new cooperation effects occur, namely, for certain system parameters there appear more than two current reversals (CRs) versus temperature and the switching rate of noise, while at large spatial asymmetries of potential the current exhibits characteristic disjunct "windows" of temperature and switching rate, where the direction of the current is opposite to that in the ambient medium. The advantage of such multinoise models involving thermal noise is that temperature as a control parameter can be easily varied both in experiments and in potential technological applications. Unfortunately, within the framework of the calculation scheme of Refs. [9–11], the absolute value of the net current is very small. So, the results of Refs. [10–11] are mainly of theoretical interest while applications are possible at not too large values of flatness. A more fundamental question is, both from theoretical and practical viewpoints, whether the phenomenon of multiple CRs versus switching rate of noise also occur in the case of moderate values of the flatness parameter.

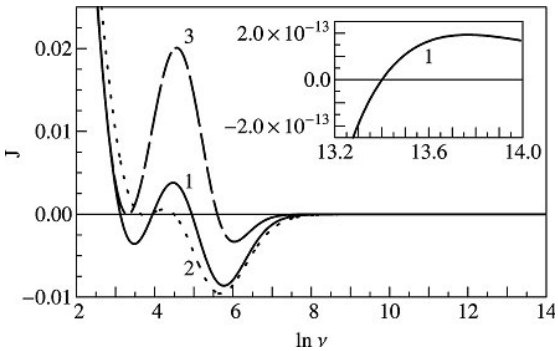

FIG. 1. Four current reversals vs switching rate ν . For all curves d = 0.1, q = 0.16, a=13.11, F= 0. Solid line (1): D =0.090. Dotted line (2): D=0.133. Dashed line (3): D=0.055. Note the phenomenon of 4 CRs in the case of the curve (1). The inset depicts the curve (1) in the region of the fourth current reversal.

Our major result is the establishing of the effects of both four CRs and disjunct "windows" at moderate values of noise flatness. Notably, as a rule, for moderate values of flatness ($50>\varphi>2$) the phenomenon of four current reversals is related with the effect of disjunct "windows". In Fig. 1, curve (2) demonstrates the phenomenon of four CRs at the

noise flatness φ = 3.125. It can be seen that the effect of four CRs occurs only in a narrow range of the temperature, $D \in (0.055, 0.133)$ i.e. the effect of disjunct "windows". If the temperature is lower than 0.055 or greater than 0.133, then there occur either two CRs or none. We emphasize that the phenomenon of four CRs occurs only at the flatness parameters φ>2; an important observation here is that a growth of the potential asymmetry will increase the region of the phase space (q, a), where four CRs with the disjunct "windows" effect appear. It is interesting that in terms of cross-correlation intensity between two dichotomous noises (see Section 2) the necessary condition for the existence of 4 CRs is that the correlation intensity ρ is negative. Thus, in the case of one symmetric dichotomous noise (φ = 1) the effect of four CRs is not possible. Moreover, if the tilting force is absent and φ = 1, no current reversals occur.

We now concentrate on another aspect in ratchet systems, namely, the efficiency with which the ratchet converts fluctuations to useful work. To calculate the efficiency, a load F is applied against the direction of the current. The current flows against the load as long as the load is less than the stopping force F_s, beyond which the current takes the same direction as the load. Thus in the operating range of the load $0 < F < F_s$, the Brownian particles move in the direction opposite to that of the load, thereby storing energy. The input power from non-equilibrium fluctuations $Z(t)$ and the output power done against the load F are given by

$$W_{in} = \left\langle \frac{dX}{dt} Z(t) \right\rangle, \quad W_{out} = -JF$$

and the efficiency of energy transduction is $\eta = -JF/W_{in}$. In the context of the present model (1) with α = 1, β = 0, a large efficiency $\eta \approx 1$ can be achieved at low values of the temperature D and the switching rate v. In this case, it is easy to ascertain that the optimal amplitude of the noise am and the optimal load force F_m, maximizing the efficiency, are: $a_m = 1/[2d(1-d)]$, $F_m = -(1-2d)/[2d(1-d)]$. The corresponding η takes the form $\eta_{\max} = 1-2d$. Hence, it follows that as the potential asymmetry increases, the maximal efficiency of the Brownian motor tends to the ideal limit of unity, i.e. $d \to 0$. The reason is that for a low diffusive Brownian motion the asymmetry of the potential profile ensures suppression of backward motion and hence reduction in the accompanying dissipation.

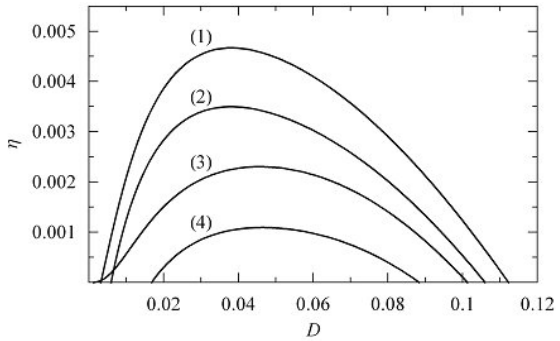

FIG. 2. The efficiency η vs temperature D in the region of the disjunct "windows" at the system parameteters: q=0.002, F=0.45, d=0.03 and a=34.4. The curves (1)–(4) correspond to the following switching rates: (1) v=164, (2) v=78, (3) v=430, (4) v=33. The nonmonotonic sequence of the values of v stems from the bell-shaped dependence η=η(v). Note that the maximum of the efficiency lies at $D_m \approx 0.038$ and $v_m \approx 164$.

We now discuss the effect of multiple CRs on the efficiency of energy transformation. Figure 2 shows the efficiency η as a function of the temperature D for four different values of the switching rate v. The nonmonotonic sequence of the values of v stems from the bell-shaped dependence $\eta = \eta(v)$. The efficiency η exhibits a bell-shaped (resonance) form as D or

v is varied. The optimal temperature D_m and the optimal switching rate v_m maximizing the efficiency are: $D_m \approx 0.038$, $v \approx 164$. The fact that the efficiency can be maximized as a function of the temperature shows that thermal fluctuations can facilitate the efficiency of energy transformation. Unfortunately, the efficiency in the region of CRs is very small. In the corresponding parameter regime, particles can move in both directions and hence the variance of particle velocity is large. The latter circumstance causes an increase of dissipation and thus a decrease of efficiency. Moreover, it is remarkable that the dependence of the efficiency on the flatness φ, as well as on the amplitude a, also reveals a broad resonance-like peak.

This result indicates that an increase in the flatness of nonequilibrium noise can sometimes facilitate energy conversion. Finally, it is suggested that the ratchet mechanism with CRs can be used for obtaining efficient separation methods of nanoscale objects, e.g. DNA molecules, viruses, etc. In this context, the CR phenomenon is one of the most interesting aspects of the theory of Brownian ratchets. To date, the feasibility of particle transport by human-made devices has been experimentally demonstrated for several ratchet types [5].

In one of our previous papers model (1) with $a = \alpha = 0$ and $\beta = 1$ was considered. It was established that at low temperatures the phenomenon of hypersensitive transport exists, i.e. a macroscopic flow (current) of matter appears under the influence of an ultrasmall dc driving, and the corresponding mobility, $m = J/F$ at $F = 0$, depends nonmonotonically on the flatness of the multiplicative noise. In the case of dichotomous noise (φ=1), which is the case addressed in Refs., the effect, for a piecewisely linear share potential, disappears.

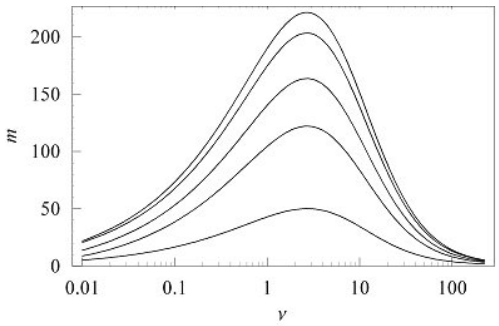

FIG. 3.The mobility m vs the switching rate v at d=1/2, D = 4·10^{-8}, and F=10^{-5}. The curves correspond, from top to bottom, to the following values of the flatness parameter: φ =3, φ =2, φ =10, φ =20, φ =1.1.

The dependence of the mobility m on the parameters v and φ for the fixed force value F=10^{-5} and for the fixed temperature D=4×10^{-8} is shown in Fig. 3. It can be seen that the functional dependence of the mobility on the correlation time $\tau_c = 1/v$ and on the flatness $\varphi = 1/2q$ is of a bell-shaped form. A major novel virtue of the model is that the noise flatness can induce the phenomenon of hypersensitive transport. Notably, for fixed low values of temperature the optimal system parameters at which the mobility is maximized, are determined as follows: the flatness parameter $\varphi \approx 3$, the correlation time $\tau_c \approx 3/8$, and asymmetry parameter d=1/2, i.e., the potential $V(x)$ is symmetric. For sufficiently low values of temperature, $D << \min\{2qv, 8q/v\}$, the mobility m is given by

$$m \approx \frac{8(1-2q)}{(v+8)^2}\sqrt{\frac{2qv}{D}}, F < \sqrt{2qvD} \qquad (2)$$

The condition $F < \sqrt{2q\nu D}$ has a distinct physical meaning: the characteristic distance of thermal diffusion $\sqrt{D/\nu}$ is larger than the typical distance F/ν for the particle driven by a deterministic force F in the state z=0. Let us note that the formula (2) for hypersensitive response is qualitatively valid, i.e. $m \sim 1/\sqrt{D}$, also in the case of systems where trichotomous noise is replaced by a multiplicative deterministic periodic stimulus. The physical mechanism which generates the result (2) has been considered in Ref. The phenomenon of hypersensitive transport is robust enough to survive a modification of the multiplicative noise (or deterministic periodic stimulus) as well as of the shape of the potential (i.e. asymmetric potentials and potentials with several extrema per period). In a general case, if the potential is smooth and the flatness of multiplicative noise is greater than 1, another mechanism desribed in Ref. plays an important role and should be taken into account when calculating the mobility.

However, in the adiabatic case, $\nu << 1$, the reported mechanism of generating hypersensitive transport by noise flatness induces hypersensitive transport more effectively than the one proposed by Ginzburg and Pustovoit in Ref. Consequently, for sufficiently small switching rates the leading order term of the mobility is generated by the mechanism described in the present paper (cf. [13]). It is remarkable that the phenomenon of noise-flatness-induced hypersensitive transport seems to be applicable for amplifying adiabatic time dependent signals $F(t)$, i.e. signals of much longer periods than the characteristic time for reaching a stationary distribution, even in the case of a small input signal-to-noise ratio $|F(t)|/\sqrt{D} << 1$ (cf. [13]).

5.1.4. Absolute negative mobility and hypersensitive differential response

A characteristic feature of models with absolute negative mobility (ANM) is that upon the application of an external static force F, these models respond with a current that always runs in the direction opposite to that of the force (if the force is small enough) [5]. Notably, for $F = 0$ no current appears due to the spatial symmetry of the system. The effect of ANM is distinct from the phenomenon of negative differential mobility (or resistance) which is, for a sufficiently large F, characterized by a decrease of the current as the driving force F increases, but the system does not exhibit ANM. Devices that display both ANM and negative differential resistance exist and they have important biophysical and technological applications, e.g. semiconductor devices [6], biological ion channels [7], tunnel junction in superconductor devices [8], etc.

We consider over-damped motion of Brownian particles described by Eq. (1) with $\alpha = 1$, $\beta = 0$. The term $Z_2(t)$ in Eq. (1) represents spatially nonhomogeneous fluctuations assumed to be a three-level Markovian stochastic process taking the values z_1=-1, z_2=0, z_3=1. That is, the three-level noise $Z_2(t)$ is assumed to be spatially non-homogenous, so that transitions between the states $z_3 = 1$, $z_2 = 0$ and between the states $z_2 = 0$, $z_1 = -1$ can take place only in the left half-period and in the right half-period of the potential, respectively (for more details see [14]). For brevity's sake, from now on we will confine ourselves to the case of a symmetric potential $V(x)$, i.e., $d = 1/2$. Regarding the symmetry of the dynamical system (1), we notice that $J(-F) = -J(F)$. Obviously, for $F = 0$ the system is effectively isotropic and no current can occur. For the stationary case, the dependence of the current J on the tilting force F enables us to establish a number of effects characterizing anomalous behavior of the resistance (or mobility).

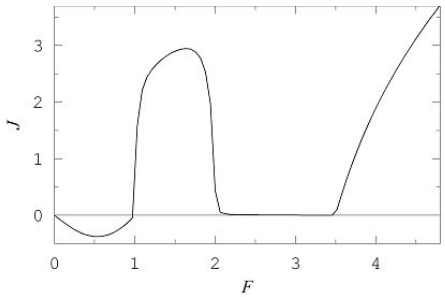

FIG. 4. The current J vs applied force F in the region of anomalous mobility. D = 10^{-7}, a = 3. The phenomenon of absolute negative mobility occurs.

Figure 4 illustrates the behavior of the current J as a function of the tilting force F in the region of anomalous resistance. It appears that the curve is highly nonlinear and the phenomenon of ANM occurs: the particles move in the direction opposite to a small external force F. Moreover, the curve exhibits intervals of F where particle speed decreases as the applied drive is increased — an effect that is termed negative differential resistance. Let us note that two additional effects occur. First, one can see a hypersensitive differential response (HDR) in jumps of the current at F=1 and $F \approx 2$. Second, at a low temperature and a large switching rate ν the current exhibits characteristic "disjunct windows" of the tilting force $2<F<3.5$, where the value of the current is very small.

For both slow and fast fluctuating forces, and for low temperatures, we have presented analytical approximations that agree with the exact numerical results (Ref.[14]). One of our major results is a resonant-like enhancement of absolute negative mobility at intermediate values of the switching rate of a non-equilibrium noise (see [14]). Two circumstances should be pointed out. (i) A resonant-like behaviour of ANM can occur in a system parameters domain where the characteristic distance of thermal diffusion $\sqrt{D/\nu}$ is comparable with typical deterministic distances for the driven particles during the noise correlation time. (ii) There is an upper limit temperature D_c beyond which the phenomenon of ANM disappears. Notably, at increasing the noise amplitude a the critical temperature D_c grows as $D_c \sim \sqrt{a}$. It is clear that the presence and intensity of ANM can be controlled by thermal noise or by the non-equilibrium noise amplitude a. The advantage of this model is that the control parameter is temperature, which can easily be varied in experiments. Moreover, as in Eq. (1) the friction coefficient γ is absorbed into the time scale, so, in the original (unscaled) setup, the particles of different friction coefficients are controlled by different switching rates. This can lead to an efficient mechanism for the separation of different types of particles.

Our other major result is the establishing of the effects of both HDR and a disjunct "window" at large values of the switching rate ν and low values of the temperature D. We emphasize that here the mechanism of HDR is of a qualitatively different nature from the mechanism of hypersensitive response considered in Section 5.1.4. It should be pointed out that in the present model the effect of HDR is pronounced in the case of a fast switching of the non-equilibrium noise, while in the models of Section 5.1.4 hypersensitive transport is generated by low or moderate values of the switching rate. Note, that the results of HDR also seem to be applicable for amplifying adiabatic time dependent signals (cf. Section 5.1.4). Surprisingly enough, at a low temperature and a large switching rate, $D\nu << 1$, the current is very small in the finite interval of the tilting force $2+(a/2) > F > \max\{2, a-2\}$. It seems that the behavior mentioned last is a new anomalous transport phenomenon for Brownian particles.

5.2. Irradiation of new samples sets and analysis of tested specimens

The joint experiments on PF-1000, PF-150 and PF-6 devices in the Warsaw Institute of Plasma Physics and Laser Microfusion were carried out during the CRP in several sessions. The aim of these experiments was on the one hand, to investigate the influence of powerful pulsed ion beams and high temperature plasma, generated in DPF, on physical-chemical processes in materials. The following specimen properties were investigated: features of surface layers damage; character of thermal and radiation effects; structural and phase stability, and composition changes in surface layers. On the other hand the results of these experiments have been used for the elaboration of a phenomenological model of dense plasma beams generated in dense plasma focus devices interacting with construction materials.

The irradiated specimens were analyzed by optical and scanning electron microscopy (SEM), X ray diffraction analysis and X ray electron probe microanalysis. The qualitative analysis of the carbon and oxygen distribution was carried out by means of a special X ray electron probe microanalysis device in the Moscow Institute of Metallurgy and Material Science and in the Prague Institute of Plasma Physics.

One of these experiments initiated by our research group was carried out to investigate the influence of alloy composition on material surface damage at irradiation. The following materials were chosen for the experiments: iron-manganese alloys with 3 wt.% Mn (Fe+3wt.%Mn) and with 18 wt.% Mn (Fe+18wt.%Mn), and pure iron. The alloys were melted and rolled to get specimens with a thickness of ~ 2 mm and ~ 8 mm in diameter. The iron specimens were prepared as plates of $10 \times 10 \times 1$ mm^3.

The experiments were carried out using a dense plasma focus device PF-1000, having Mather-type (cylindrical) electrodes (Fig. 5), with deuterium as working gas (initial pressure ~ 465 Pa). Pulsed irradiation of specimens was performed at the cathode part of the PF-1000. The position of specimens in the plasma focus device (PFD) are shown in Fig. 5.

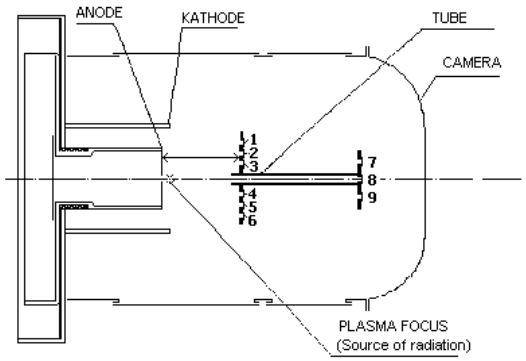

FIG. 5. A scheme of the plasma focus device (PF-1000) where the positions 1,2,3,...,8,9 of specimens are shown.

Some details of experimental conditions are given in Table 1. These conditions may be presented as three particular experiments (No. 1, 2 and 3), which differ by the number of shots and the distance between the specimens' position and the anode (see Table 1 and Fig. 5). It is necessary to note that in the cases of the experiments No. 1 and 2 the tube in PFD was made of chromium-manganese steel with scandium (10Cr12Mn20W+0.05Sc), while in the case of the experiment No. 3 it was of pure copper.

TABLE 1. EXPERIMENTAL CONDITIONS

No. of the experiment	Number of shots	Neutron output	Position of specimens in PFD (Fig. 5)	Distance from anode, cm
1	4	$(1.09 — 2.48)\times10^{11}$	1,2,3	15
2	4	$(1.09 — 2.48)\times10^{11}$	7,8,9	70
3	3	$(0.038—3.03)\times10^{11}$	2,3,4	15

In Table 2 the values of the mass of the specimens before and after irradiation are given. As follows from Table 2, no significant mass changes took place. The maximum change (0.0007 g) was observed for the Fe specimen in the experiment No 2. Note that in this case the Fe specimen was placed on the end of the steel tube, where the propagation of the plasma stream had a very specific character.

TABLE 2. MASS OF THE SPECIMENS BEFORE AND AFTER IRRADIATION

No. of the experiment	Specimen	Position (Fig. 5)	Mass of the specimen, g	
			before irradiation	after irradiation
1	Fe	3	0.9624	0.9627
	Fe+3wt.%Mn	2	1.1021	1.1021
	Fe+18wt%Mn	1	1.0392	1.0396
2	Fe	8	1.2209	1.2216
	Fe+3wt.%Mn	7	0.8334	0.8336
	Fe+18wt%Mn	9	0.9825	0.9828
3	Fe	4	1.2961	1.2965
	Fe+3wt.%Mn	3	1.0813	1.0813
	Fe+18wt%Mn	2	1.0555	1.0557

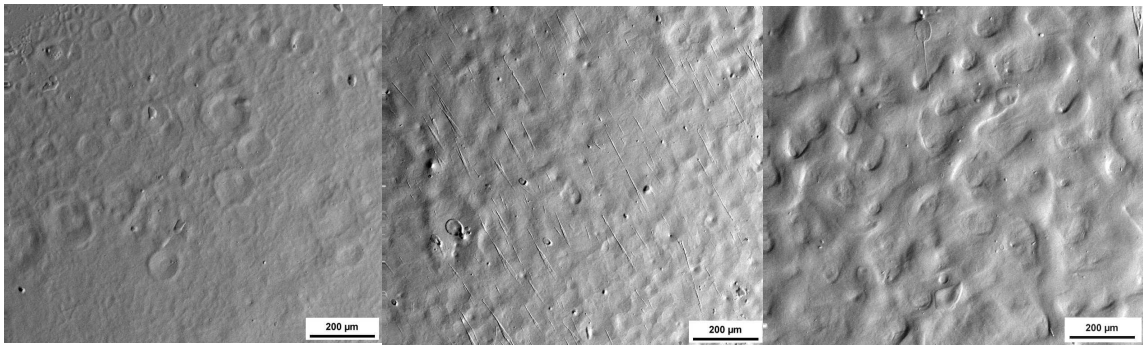

a b c

FIG. 6. (a) Surface of the Fe (experiment No 1; (b) Surface of the Fe + 3wt. %Mn (experiment No 1) and (c) Surface of the Fe + 18wt. %Mn (experiment No 1).

SEM pictures of the topography of specimens' surface after irradiation are presented in Figs. 6–14 for all samples. As can be seen from Fig. 6, where the results of the experiment No.1 are presented, the surface of the Fe + 18wt.%Mn specimen has been damaged more than that of the Fe + 3wt.%Mn and Fe specimens. Small craters, as well as blisters and microcracks can be observed.

In principle, the same picture can be observed also in the cases of the experiments No. 2 and 3, where the damage of specimens' surface is also indicated the more the more the content of Mn in the alloy is (Fig. 7). A remarkable exception is presented by the Fe specimen in the experiment No. 2 (see Fig. 7(a)). In this case, as it was already mentioned above, the

specimen was placed on the end of steel tube (position 8, Fig. 5), where irradiation conditions were principally different. Figure 7(a) in comparison with Fig. 6(a) and Fig. 8(a) demonstrates how huge may be the difference between dense plasma influence on the same material depending on the precise position of the specimen and the real conditions of irradiation.

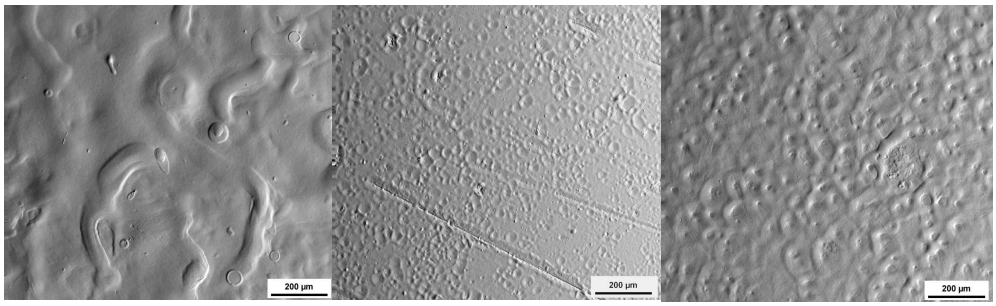

a b c

FIG. 7. (a) Surface of the Fe (experiment No.2; (b) Surface of the Fe + 3wt. %Mn (experiment No.2); (c) Surface of the Fe + 18wt. %Mn (experiment No.2).

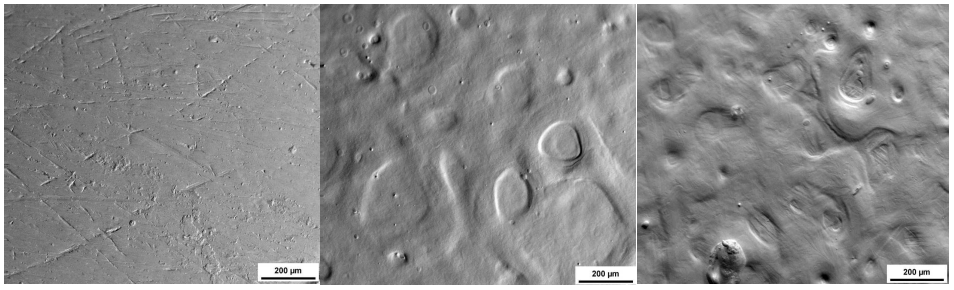

a b c

FIG. 8. (a) Surface of the Fe (experiment No.3); (b) Surface of the Fe + 3wt.%Mn (experiment No.3); (c) Surface of the Fe + 18wt.%Mn (experiment No.3).

X ray microanalysis of the irradiated specimens showed that all of them are covered by very small inclusions of steel (containing Cr, Ni, W etc.) and copper in the case of the experiments No. 1 and 2, and of copper in the case of the experiment No.3. Obviously, this is due to the presence of a steel tube and a specimen holder made of copper in the case of the experiments No. 1 and 2, and of a copper tube and a specimen holder in the case of the experiment No.3. It can be concluded that particles of tube and holder material were caught by hot plasma and implanted into the specimens' surface during the plasma propagation in the PFD camera.

X ray spectral microanalysis made in the regime of line scanning through the objects like that shown in Fig. 9 by Mn K_α and Fe K_α spectral lines indicated no compositional changes in any of the three experiments. Composition "changes", i.e. changes in the "darkness" distribution in Fig. 9(b), which normally have to be related to changes in the mean atomic number of the alloy components, in this case are rather due to surface roughness (see Fig. 9(a)), and are not at variance with the results of X ray spectral microanalysis.

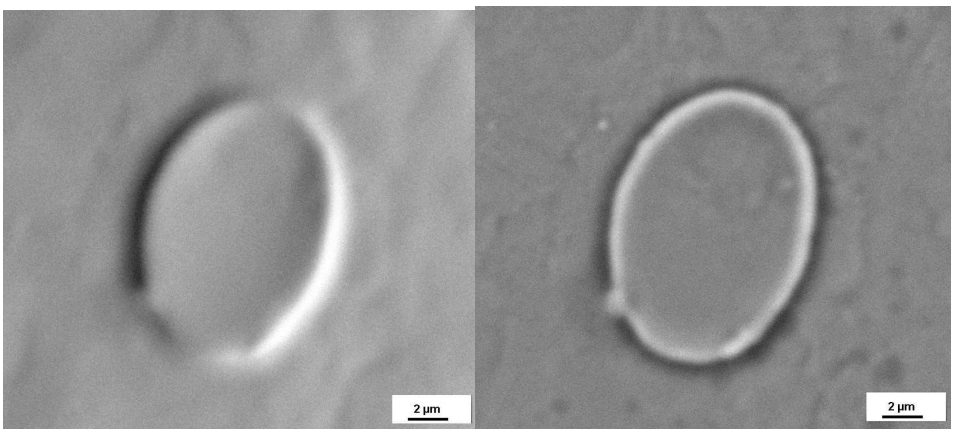

a b

FIG. 9. Surface of Fe+18wt.%Mn, exp. No.1, (a) SEM picture, backscattered electrons, topography; (b) SEM picture, backscattered electrons, composition regime.

Two remarkable conclusions can be made on the basis of the results just described. They are as follows: 1) in the case of model Fe-Mn alloys no significant redistribution of manganese under irradiation of deuterium plasma pulses occurred; and 2) the damage of Fe-Mn alloy specimens' surface depends essentially on the specimen composition — the more manganese the alloy specimen contains the more damage occurs on the surface. These results are published in [12]. During the last sessions several specimens of Eurofer 97, steel 25 and pure iron were irradiated at different regimes in deuterium and nitrogen plasmas using plasma device PF-6. One of these sessions was devoted to irradiation of iron alloys (including Eurofer) and CFC-specimen in deuterium plasmas in different regimes.

In the Table 3 several most characteristic samples of the specimens irradiated during previous period and the preliminary results of their analysis are presented. In the Table 3 are listed the specimens under consideration and given the regimes of irradiation (the power density of irradiation reached a value of $\sim 10^{14}$ W/cm^2, the duration of the pulses being in the interval of $\sim 10^{-8}$–10^{-6} s).

In the Table 3 are shown the results of mass measurements before and after irradiation. As one can see from the table, mass changes were not remarkable almost in all cases where these measurements were made.

In Fig. 10 the most characteristic SEM-pictures from surface layers of irradiated specimens are shown. As one can see from the Fig. 10, in all cases material damage and structure change can be observed. The line scanning by X ray charasteristic spectral line demonstrated the redistribution of elements in surface layers of the specimens, which take place as the result of local melting, evaporation and sputtering of the surface material during irradiation.

TABLE 3. SAMPLES OF THE ANALYSIS OF ONE SET OF SPECIMENS IRRADIATED IN DIFFERENT REGIMES

Specimen	Working gas	Number of shots	Mass of the specimen before irradiation, g	Mass of the specimen after irradiation, g	Designation
Eurofer 97	deuterium	1	0.9133	0.9117	1-700
Eurofer 97	deuterium	8	0.9382	0.9394	2-200
Steel 25 (25Cr12Mn20W)	nitrogen	15	-	-	22-400
Steel (03X10G33W1V1)	nitrogen	10	1.42453	1.4228	3-500
Steel 03X10G33W1V1	nitrogen	1	1.47875	1.4800	2-12
Steel 03X10G33W1V1	nitrogen	5	1.22833	1.2386	5-500
Fe (with additions)	deuterium	1	-	-	7-1000
Fe (with additions)	deuterium	1	-	-	8-500

According to the international cooperation agenda, the irradiated specimens are in process of the analytical investigation in the Moscow Institute of Metallurgy and Material Science and the results will be discussed and published later. More detailed description of these joint experiments will be presented elsewhere (Final Report of the contract No.11943/RBF).

The experimental results obtained in the frame of the CRP in cooperation with the Moscow Institute of Metallurgy and Material Science, the Warsaw Institute of Plasma Physics and Laser Microfusion and the Prague Institute of Plasma Physics are published in Ref.[1, 20–25].

5.3. Elaboration of a phenomenological model of dense plasma beams generated in dense plasma focus devices interacting with wall materials.

The results of the analysis of the irradiated specimens as well as similar observations made earlier allowed us to start the elaboration of a phenomenological model of interaction between dense plasma beams and construction materials under several specific conditions of irradiation. So far it has led to some generalizations of plasma beam behavior near the contact with material as well as implanted into material particles after pulse interaction.

First the redistribution of deuterium implanted into iron based alloys by plasma beam interaction with the alloy surface was analytically investigated (the results are published in [18]). The hitherto available solutions of the diffusion equation have been found analytically only for very simple and regular initial and boundary conditions even in the case of one dimensional diffusion with a constant diffusion coefficient D. So, it was impossible to use any known diffusion model for description of redistribution of elements in irradiated materials where the initial distribution of implanted plasma components may be generally quite arbitrary. At the same time the process of redistribution of elements is of great interest, particularly, in the case of relaxation processes in the wall materials specimens after irradiation where the initial distributions of light elements (hydrogen, deuterium etc.) are usually after shots essentially non-regular. Some features of this problem were discussed by us recently [18].

The idea of our model is based on the superposition of stochastic dissipation of thin layers of diffusing elements. The solution of the one dimensional diffusion equation in this case for a finite space, e.g. for a sheet with a thickness L, was found. This solution was then used for modeling the diffusion of the light elements (supposing the diffusion coefficient was a constant) in a sheet with an arbitrary initial distribution of the diffusing element by summarizing particular solutions for each thin layer at a given coordinate. The method was applied for the estimation of deuterium redistribution in thin surface layers of a steel sheet with an initially non-monotonous distribution of the element. It was found that deuterium diffuses not only in the direction of the surface but also into the bulk of the steel specimen.

For instance, if the diffusion coefficient D is taken 10^{-11} m^2/s, the diffusion processes practically vanish after 1 millisecond and about a half of the deuterium remains in the sheet. Further results on the investigation of diffusion-stochastic redistribution of light elements implanted into materials under plasma pulses are being prepared for publication.

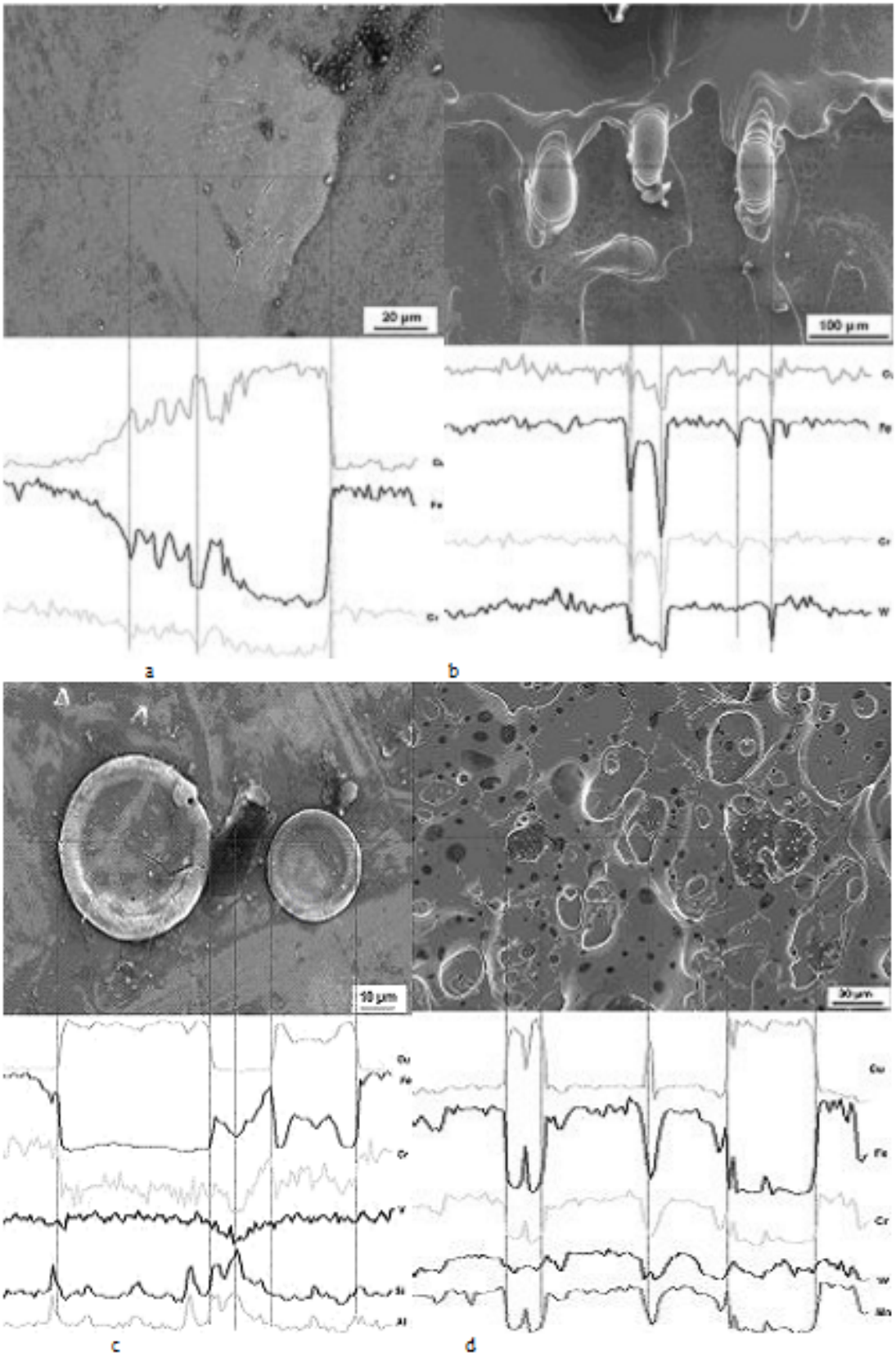

FIG. 10. SEM-pictures and line scanning by X ray spectra of elements for several specimens, listed in the table: a) specimen Eurofer 97 (D-plasma, 1 shot); b) specimen Eurofer 97 (D-plasma, 8 shots); c) specimen Steel 25 (N-plasma, 15 shots);d) specimen Fe (with additions) (D-plasma, 1 shot).

The problem of redistribution of alloy components at high temperatures was also analyzed. Particularly, it was found that the "diffusion path" in ternary alloy systems deviates from linearity mainly due to non-ideal thermodynamic properties of alloys [19, 20]. It was shown that thermodynamic properties of alloys play an important role in interdiffusion processes in a ternary system, which was confirmed by calculation of thermodynamic factors and by analysis of their role in the relationship between interdiffusion coefficients and physical properties of the system.

A more complicated problem is to understand how the interaction between powerful pulses of dense plasma and materials under every specific condition takes place. Nevertheless, on the basis of the experimental results obtained it is possible to draw some generalizations. For instance, it has been found that the surface density of surface structure defects (blisters and craters) is related to the influence of fast (E ~ 100 keV) ions implanted into the specimen. It has been found that when power flux density increases up to 10^9 –10^{10} W/cm^2, the so-called "broken implantation" can be observed. At this regime a surface layer implanted by 1 irradiation pulse of about 100 keV deuterons appears to be completely evaporated while the concentration of low energy deuterons (E_i = 1 keV) in the surface layer of the specimen decreases with the growth of the number of irradiation pulses.

This feature finds its explanation in a successive diffusion enhancement due to the surface structure modification. It was found that irradiation of steels with deuterium ion and plasma pulses with power density q = 10^9– 10^{11} W/cm^2 and the pulse duration τ = 100 ns results in mainly thermal influence: evaporation, melting and crystallization of the target material, formation of a specific droplet-ridge surface relief, $\gamma \rightarrow \alpha$ phase transformation in austenitic steels. The phase composition of ferritic steel remains stable. On the example of specimens of austenitic steels the correlation between the density of macroscopic surface defects in the irradiated material (blisters and craters) and the density of the high energy hydrogen ions implanted into the specimen per one pulse was studied: in both cases the considered density was about 10^5 cm^{-2}.

The experimental results obtained in the frame of the CRP in cooperation with the Institute of Plasma Physics and Laser Microfusion, the Moscow Institute of Metallurgy and Material Science, the Moscow Physical Society, the Institute of Nuclear Physics of the Moscow State University and the Prague Institute of Plasma Physics allowed to continue refinement of the phenomenological model of interaction between dense plasma beams and construction materials under several specific conditions of irradiation. Under these regimes the ion and plasma components of the energy pulse are separated by both time and energy contribution to the material damage. So far it has led to some generalizations of plasma beam behavior near the contact with material as well as implanted into material particles after pulse interaction.

5.4. Discussion

Above, we have presented some results for the dynamics of over-damped particles in a periodic, one dimensional potential landscape subjected to a static tilting force and to both thermal noise and a non-equilibrium three-level colored noise. A major virtue of the proposed model is that an interplay of three-level colored and thermal noises in tilted ratchets with simple periodic potentials can generate a rich variety of non-equilibrium cooperation effects.

An amazing noise-induced non-equilibrium phenomenon is a giant enhancement of free diffusion by the use of tilted periodic potentials [7]. The corresponding calculations for model

(1) are in progress. Furthermore, earlier results [29, 31] about the influence of colored noise in *N*-species stochastic Lotka-Volterra systems show that mutual interplay of interaction intensities of species (particles of plasma, atoms, photons, molecules, predators and preys, infected individuals, etc.) and colored noise can induce bi-stability and cause discontinuous non-equilibrium phase-transitions, even if the system is mono-stable in the absence of noise.

As the non-equilibrium phenomena considered above are robust enough to survive a modification of the colored noise (or deterministic periodic stimulus) as well as the potential landscape (i.e. potentials with several extreme per period) the results of the investigations of the basic model (1), belonging to a highly topical interdisciplinary realm of studies, can be applied for a variety of purposes, starting from a description of Josephson connections [11] and ending with a possible explanation of the catastrophic shifts sometimes occurring in ecosystems [9]. Possible applications range from superconductors to intracellular protein transport in biology, or to methods of particle separation in nanotechnology [4, 16].

We believe that the described model may shed some light on the stochastic interaction processes of plasma with wall materials in plasma focus devices, and it could be used for the elaboration of more realistic physical models for non-equilibrium transport and diffusion of particles as well as the non-equilibrium phase transitions, which take place at interactions between hot dense plasma beams and wall materials. Such a realistic model would be of utmost importance for experiments planned with small scale dense plasma focus devices, working in a short periodic pulse regime. Note that in such devices the role of non-equilibrium noise is played by periodic pulses of plasma.

As the behaviour of current in the phase space of the parameters proved unexpectedly complicated and yet the possible applications of current reversals are of great importance, it is essential to continue this research, focusing on the necessary and sufficient conditions of current reversals. The methodology should be generalized to cover multidimensional (two and three dimensional at least) cases in order to find out the role of non-equilibrium fluctuations in the formation of spatial patterns.

The reported mechanism of generating hypersensitive transport by the flatness of multiplicative noise is of general relevance for many physical, biological an chemical systems. As in cases of additive three-level noise, our mechanism can describe the diffusion of Brownian particles in materials with a periodic structure.

Of course, further experiments on a PF device and a detailed analytical investigation of irradiated specimens are needed to improve the developed phenomenological model of interaction in order to allow a theoretical approach to the stochastic problems taking place in these situations.

6. CONCLUSIONS

The obtained experimental results show that the special regime of the irradiation of the material may be realized in the PF device for specimens situated in the cathode part of a discharge chamber. Under this regime the ion and plasma components of the energy pulse are separated by both time and energy contribution to the material damage. This situation provides new perspectives of the application of PF-devices in the ion-plasma treatment of materials for the modification of their surface layers as well as to support the elaboration of the model of interaction between plasma beams and construction materials.

The results of experiments on the influence of high-energy pulses on materials carried out by using the dense plasma focus device PF-1000 with hydrogen and deuterium as working gas are of great use for the elaboration of a phenomenological model on interaction between dense plasma pulses and construction materials. Particularly, the results obtained have enabled us to work out some fundamental aspects of this model. We assume that hydrogen ions implanted into steel create vacancy clusters which form nuclei of gas phase (micro pores), as well as that powerful thermal influence of the plasma which results in an evaporation of Mn and probably some compounds of carbon and oxygen into the volume of micro pores, with the subsequent formation of blisters and craters on the surface layer of irradiated steel.

Theoretical investigations indicate that noise induced non-equilibrium effects are sensitive to noise flatness, viz., the ratio of the fourth moment to the square of the second moment. Although its significance is clear, the role of the flatness of fluctuations has not been much investigated. The purpose of our research was to discuss — on the basis of exact results — some novel phenomena in stochastic systems where colored noises are modelled as trichotomous fluctuations and where the noise flatness as a control parameter is crucial.

ACKNOWLEDGEMENTS

The work was carried out in close cooperation with the scientists representing the following institutions:

- The A.A.Baikov Institute of Metallurgy and Material Science, Leninsky pr. 49, 119991 Moscow, Russian Federation (IAEA Research Contract No 11943).
- The Institute of Plasma Physics and Laser Microfusion, Hery str.23, 00-908 Warsaw, Poland (IAEA Research Contract No 11940).
- The Moscow Physical Society, Leninsky pr. 53, 117333 Moscow, Russian Federation (IAEA Research Contract No 11942).
- Tallinn University of Technology, Ehitajate tee 5, 19086 Tallinn, Estonia.

REFERENCES

[1] PIMENOV, V.N., GRIBKOV, V.A., DUBROVSKY, A.V., MEZZETTI, F., SCHOLZ, M., UGASTE, Y.E., DYOMINA, E.V., IVANOV, L.I., MASLYAEV, S.A., MIKLASZEWSKI, R., BOROWETSKI, M., DE CHIARA, P., PIZZO, L., SZYDLOWSKI, A., VOLOBUEV, I.V., Influence of powerful pulses of hydrogen plasma upon materials in PF-1000 device, Nukleonika, 47 (4) (2002) 155–162.

[2] GAMMAITONI, L., HÄNGGI, P., JUNG, P., MARCHESONI, F., Stochastic resonance, Rev. Mod. Phys., 70 (1998) 223–2.87.

[3] GARCÍA-OJALVO, J., SANCHO, J.M., Noise in Spatially Extended Systems: Springer Verlag, New York (1999).

[4] REIMANN, P., Brownian motors: noisy transport far from equilibrium, Phys Rep, 361 (2002) 57–265.

[5] EICHHORN, R., REIMANN, P., HÄNGGI, P., Paradoxial motion of a single Brownian particle: Absolute negative mobility, Phys. Rev., E 66 (2002) 066132.

[6] GINZBURG, S.L., PUSTOVOIT, M.A., Hypersensitive transport in a phase model with multiplicative stimulus, Phys. Lett., A 291 (2001) 77–81.

[7] REIMANN, P., VAN DER BROECK, C., LINKE, H., HÄNGGI, P., RUBI, J.M., Pérez-Madrid. Giant Acceleration of Free Diffusion by Use of Tilted Periodic Potentials, Phys. Rev. Lett, 87 (2001) 010602.

[8] MANKIN, R., AINSAAR, A., REITER, E., Current reversals in ratchets driven by trichotomous noise, Phys. Rev., E 61 (2000) 6359–6367.
[9] MANKIN, R., AINSAAR, A., HALJAS, A., REITER, E., Constructive role of temperature in ratchets driven by trichotomous noise, Phys. Rev., E 63 (2001) 041110.
[10] MANKIN, R., TAMMELO, R., MARTILA, D., Correlation ratchets: four current reversals and disjunct "windows", Phys. Rev., E 64 (2001) 051114.
[11] TAMMELO, R., MANKIN, R., MARTILA, D., Three and four current reversals versus temperature in correlation ratchets with a simple sawtooth potential, Phys. Rev., E 66 (2002) 051101.
[12] MANKIN, R., AINSAAR, A., TAMMELO, R., Trichotomous noise: applications to stochastic transport, Proc. Estonian Acad. Sci. Phys. Math., 53 (2004) 64–72.
[13] MANKIN, R., HALJAS, A., TAMMELO, R., MARTILA, D., Mechanism of hypersensitive transport in tilted sharp ratchets, Phys. Rev., E 68 (2003) 011105.
[14] HALJAS, A., MANKIN, R., SAUGA, A., REITER, E., Anomalous mobility of Brownian particles in a tilted symmetric sawtooth potential, Phys. Rev., E 70 (2004) 041107.
[15] KAMEGAWA, H., HONDOU, T., TAKAGI, F., Energetics of a Forced Thermal Ratchet, Phys. Rev. Lett., 80 (1998) 5251–5254.
[16] LINKE, H., (ed) Special issue on "Ratchets and Brownian motors: Basics, experiments and applications", Appl. Phys., A75 (2002) 167–352.
[17] KEAY, B.J., ZEUNER, S., ALLEN, S.J., MARANOWSKI, K.D., GOSSARD, A.C., BHATTACHARYA, U., RODWELL, M.J.W., Dynamic Localization, Absolute Negative Conductance, and Stimulated, Multiphoton Emission in Sequential Resonant Tunneling Semiconductor Superlattices, Phys. Rev. Lett., 75 (1995) 4102–4105.
[18] HAGIWARA, S., MIYAZAKI, S., ROSENTHAL, N.P., Pottassium Current and the Effect on this Current during Anomalous Rectification of the Egg Cell Membrane of a Starfish, J. Gen. Physiol., 67 (1976) 621–638.
[19] GERSHENZON, M.E., FALEY, M.I., Absolute negative resistance in tunnel junctions of nonequilibrium superconductors, Zh. Eksp. Teor. Fiz., 94 (1988) 303–341.
[20] KODENTSOV, A.A., UGASTE, Y.E., PIMENOV, V.N., GRIBKOV, V.A., DOUBROVSKY, A.V., SCHOLZ, M., MIKLASZEWSKI, R., Influence of dense deuterium plasma pulses on Fe and Fe-Mn alloy specimens in a plasma focus device, — Acta Universitatis Tallinnensis, 2003, Realia B2: 51–56. (Proceedings of the International seminar, Estonia, Tallinn, 9–11 October, 2003).
[21] GRIBKOV, V.A., PIMENOV, V.N., IVANOV, L.I., DYOMINA, E.V., MASLYAEV, S.A., MIKLASZEWSKI, R., SCHOLZ, M., UGASTE, Y.E., DOUBROVSKY, A.V., MEZZETTI, F., KULIKAUSKAS, V.C., ZATEKIN, V.V., Interaction of High Temperature Deuterium Plasma Streams and Fast Ion Beams with Condensed Materials in Dense Plasma Focus Device, Journal of Physics D: Applied Physics, 36 (2003) 1817–1825.
[22] PIMENOV, V.N., MASLYAEV, S.A., IVANOV, L.I., PANIN, O.V., DYOMINA, E.V., GRIBKOV, V.A., DOUBROVSKY, A.V., UGASTE, Y.E., SCHOLZ, M., MIKLASZEWSKI, R., GRUNWALD, YA., Interaction of pulsed streams of deuterium plasma with aluminium alloy in a plasma focus device. I. A new methodology of the experiment, — Acta Universitatis Tallinnensis, 2003, Realia B2: 30–39. (Proceedings of the International seminar, Estonia, Tallinn, 9–11 October, 2003).

[23] PIMENOV, V.N., MASLYAEV, S.A., IVANOV, L.I., PANIN, O.V., DYOMINA, E.V., GRIBKOV, V.A., DOUBROVSKY, A.V., UGASTE, Y.E., SCHOLZ, M., MIKLASZEWSKI, R., GRUNWALD, YA., Interaction of pulsed streams of deuterium plasma with aluminium alloy in a plasma focus device. II. Investigation of irradiated material, — Acta Universitatis Tallinnensis, 2003, Realia B2: 40–50. (Proceedings of the International seminar, Estonia, Tallinn, 9–11 October, 2003).
[24] PIMENOV, V.N., MASLYAEV, S.A., IVANOV, L.I., DYOMINA, E.V., GRIBKOV, V.A., DUBROVSKY, A.V., SCHOLZ, M., MIKLASZEWSKI, R., UGASTE, Ü., KOLMAN, B., Surface and bulk processes in materials induced by pulsed ion and plasma beams at Dense Plasma Focus devices, Nukleonika, 51 (2006) 71–78.
[25] PIMENOV, V.N., MASLYAEV, S.A., DYOMINA, E.V., IVANOV, L.I., KOVTUN, A.V., GRIBKOV, V.A., DUBROVSKY, A.V., UGASTE, Ü.E., Influence of pulsed energy beams on the aluminium tube surface at Dense Plasma Focus device, J. of Advanced Materials, 4 (2006) 43–53 (in Russian).
[26] UGASTE, Y.E.,PIMENOV, V.N.,IVANOV, L.I. MYAGI, A.,MANKIN, R.,GRIBKOV, V.A., MEZZETTI, F., Diffusion stochastic model of the mass transfer of interstitial elements. Redistribution of deuterium implanted into a iron based alloy, J. of Advanced Materials, 4 (2002) 58–64 (in Russian).
[27] UGASTE, Ü., LAAS, T., Škled-Gorbatšova, T., The influence of thermodynamic properties of alloys on effective interdiffusion coefficients in ternary systems, Defect & Diffusion Forum, 263 (2007) 141–146.
[28] LAAS, T., UGASTE, Ü., PRIIMETS, J., Thermodynamic aspects of diffusion paths in ternary systems, Defect & Diffusion Forum, 263 (2007) 135–140.
[29] MANKIN, R., AINSAAR, A., HALJAS, A., REITER E. Trichotomous-noise-induced catastrophic shifts in symbiotic ecosystems, Phys. Rev., E 65 (2002) 051108.
[30] MANKIN, R., SAUGA, A., AINSAAR, A., HALJAS, A., PAUNEL, K., Colored-noise-induced discontinuous transitions in symbiotic ecosystems, Phys. Rev., E 69 (2004) 061106.
[31] MAJER, J.B., PEGUIRON, J., GRIFONI, M., TUSVELD, M., MOOIJ, J.E., Quantum Ratchet Effect for Vortices, Phys. Rev. Lett., 90 (2003) 056802.

DENSE PLASMA JET SOURCE DEVELOPMENT AND JET INJECTION IN GLOBUS-M

A.V. VORONIN, K.B. ABRAMOVA, V.K. GUSEV, E.E. MUKHIN, YU.V. PETROV,
N.V. SAKHAROV, S.YU. TOLSTYAKOV
A.F. Ioffe Physico-Technical Institute
St. Petersburg

A.V. DUBROVSKY
Moscow Physical Society NFO
Moscow

V.A.GRIBKOV
A.A. Baikov Institute of Metallurgy and Material Science RAS
Moscow

Russian Federation

Abstract

Theoretical and experimental development of the plasma jet source and injection of hydrogen plasma into the Globus-M spherical tokamak were performed. The new gas generating and improved plasma accelerating stages of the jet source were developed. Hydrogen plasma jet with a density up to 2×10^{22} m^{-3}, total number of accelerated particles $(1\text{-}5)\times10^{19}$ and a flow velocity up to 200 km/s was used as instrument for the density control in the Globus-M spherical tokamak. Fast density increase in all spatial points of the plasma column including the plasma central region was registered. Data suggest that 0.5 ms after a plasma gun shot, the density increases at all spatial points up to a radius $r \approx 0.3a$, thus evidencing deep plasma jet penetration. Such injection permitted a twofold increase of the plasma density in tokamak. Plasma startup in tokamak with the help of the plasma jet demonstrated faster heating of the discharge as compared to gas puffing with RF pre-ionization. The model for gas jet penetration into the tokamak was applied for the high-velocity jet accelerated by plasma gun. Numerical simulations showed that due to the large initial velocity such jet should penetrate deep (20cm) in the Globus-M plasma. The model predictions are consistent with experimental observations of the density rise recorded by interferometer and Thomson scattering diagnostics.

1. INTRODUCTION

A fundamental problem is the interaction of dense plasmas with magnetic field and high temperature magnetized plasma. Understanding the behaviour of the dense magnetized plasma (DMP) may give a key for arrangement of stable confinement extreme plasma pressure in the magnetic trap. Efficient work of setup, utilizing magnetized plasma, depends strongly on its confining properties and capability of a flexible plasma fuelling. DMP sources are of high interest in nuclear fusion energy research as a potential means for fusion power reactors. They are compact, inexpensive and technologically simpler than devices used in modern fusion programs. Development of operative and efficient fuelling method for a future thermonuclear reactor are of special importance. Controlling the ignition, burning and mitigation of the discharge in magnetic plasma confining system are also important tasks. In tokamak during current plateau phase jet injection into plasma core led to fast density increase. Local enhancement of plasma density can cause transport barrier improving plasma confinement in this region. Also such jets can initiate weak instabilities at the plasma edge (Edge Localized Mode) and avoid plasma degradation in the core region. Plasma startup in tokamak with the help of the plasma jet demonstrated faster heating of the discharge as compared to gas puffing with RF pre-ionization. Furthemore, intensive gas jet injection before disruption can mitigate the discharge and avoid uncontrollable energy release at the first wall of the reactor.

At the present time, solid matter, gas and plasma acceleration devices are studied and widely used for filling the plasma installations. The fuel must have a high enough directed

energy to pass through the magnetic field, dense and hot plasma border prior to reaching the central plasma region of the reactor. The total number of accelerated particles should to be 10^{19}–10^{23} for densities $>10^{21}$ m^{-3} and flow velocities of up to 800 km/s. In spite of definite demands for fuel supply of plasma core region in fusion reactor the absolute method of fuel injection into magnetic traps do not yet exist. For example, cheap and reliable fuelling of the tokamaks plasma with a gas puffing system has an efficiency of only about 10%. Significant progress has been made in pellet injection technology since the initial experiments [1–3].

Pellet injection systems, in spite of their high cost have essentially become necessary components for several research devices using magnetically confined plasmas. But due to principal limitation of the pellet velocity, pellet injection is not considered adequate to fuel the centre of reactor tokamak plasmas. Conventional injectors, based on light gas single-stage pneumatic guns or centrifuges, can provide frozen pellets (1–6 mm diameter sizes) at speeds up to 1 km/s. Injectors based on two-stage pneumatic guns can achieve velocities about 3 km/s. Neutral beam injection has been successful in producing high temperature and high fusion performance plasma. Nevertheless this expensive method requires further increase of beam energy up to MeV range value to be utilized for reactor fuelling. A collective acceleration of magnetically confined plasma rings (compact toroids) was proposed for central fuelling of tokamak plasmas. It can be formed in a magnetized Marshall gun. The plasma density reached 7×10^{21} m^{-3} and the average velocity of flow exceeds 100 km/s with the total number of particles about 10^{19}. Since the plasma is confined by a magnetic field the density is limited, therefore an increase of the total number of particles requires an increase of the plasma ring volume. The velocity of condensed matter ~7 km/s was achieved with sources based on electromagnetic rail gun [6]. The highest density of plasma (5×10^{26} m^{-3}) was achieved in capillary-explosion experiment [7]. Unfortunately, this plasma contained a very large amount of impurities. Dense plasma (~10^{23} m^{-3}) has been concentrated near the source edge in plasma-focus experiments [8]. But this high density region has no high directed motion. Study of plasma source (modified Bostic type) with titanium hydride electrodes has been carried out by the authors [9]. The total number of released hydrogen atoms ranged between 10^{16}–10^{18} and the maximum plasma flow velocity was 250 km/s. The ion density near the gun edge reached ~ 10^{20} m^{-3}. However, utilization of such plasma source is impossible in a fusion reactor because there is a strong deflection of the cluster by confining magnetic field 5–10 T. Further increasing the plasma density increases impurity flux coming from the electrodes. So, the conventional erosion type source cannot meet requirements of plasma density and purity.

Thus, there are accelerators of condensed substances with relatively low velocity of flow motion. And there are sources of low-density plasma with high velocity of flow. But none of these plasma sources generates simultaneously dense highly ionized and pure plasma cluster with high directed velocity.

Before the CRP initial development of double-stage plasma sources utilizing granules has been successfully tested. In frame of the CRP further development of the source has been performed for fusion confinement and other plasma experiments as a fuel or plasma source. Investigation, optimization and further employment of the source at Globus-M permitted us to confirm its efficiency as flexible tool for plasma fuelling and parameters profiles control.

One of the most attractive fusion relevant scenarios is a high plasma density regime as the fusion power depends on the square of the density [11]. Some of the declared program goals for the spherical tokamak Globus-M is the development of density control methods, as

well as the achievement of ultimately high densities due to unique technical characteristics of the machine [12].

An attractive direction is the development of effective plasma gun accelerators of DMP, which could be used for different applications in fusion and in particular as fusion device fuelling sources, as the traditional methods have exhibited numerous shortcomings. Plasma accelerators, producing clean, high density, high speed plasma and gas jets could be used for this purpose.

Earlier research carried out at the Ioffe Physico-Technical Institute has culminated in development of a fuelling method and a pulsed accelerator producing an intense, dense hydrogen plasma jet. The developed plasma source has several attractive characteristics, such as: strong gas release and/or strong plasma release on the 0.1 ms timescale; possibility to choose different gases that can be absorbed in grains. With the titanium-hydride grain sources the mockup model was able to demonstrate plasma density approaching 10^{22} m^{-3} and a total number of released particle about 10^{20}, an efficiency of ionization of 90 % and a velocity of flow motion ≥10 km/s. Preliminary experiments showed how to increase directed velocity. The generated plasma was mainly hydrogen as shown by spectral and gas analyses.

Parameters of the source, developed in the frame of the current program, could be acceptable for fusion devices and other plasma experiments as a fuel or plasma source. Investigation, optimization and further employment of the source at Globus-M may confirm its efficiency as a flexible tool for plasma fuelling and parameters profiles control. Current research is devoted to the development of double stage dense plasma coaxial source of novel type and its first application as the fuelling source for tokamak. The present communication reports on a theoretical and experimental study of such plasma sources and of injection of plasma and gas jets from a modified source into Globus-M. The report consists of two main parts. The first part is devoted to the results of plasma jet source optimization by means of calculations and special experiment performed at the test bench facility. In the second part experimental results obtained in tokamak experiments are described. Analysis of plasma jet penetration into high magnetic field region and plasma core is performed. Finally conclusions are drawn and future plans are discussed.

Detail plan of the CRP work plan included: (1) design and manufacturing of the modified double-stage sources with granules; (2) creation of test bed facility with number of new diagnostics; (3) testing and determination of plasma sources with improved parameters; (4) determination of optimal source characteristics and plasma parameters appropriate for injection into the tokamak Globus-M; (5) investigation of principal possibility to control the processes in tokamak plasma with external source generating dense plasma flux; (6) experimental investigation of improved plasma interaction with magnetised high temperature plasma in tokamak; (7) injection of high-density neutral gas jets in tokamak with a directed energy of several eV, comparison of super fast dense gas stream injection with the injection of DMP jet into tokamak; (8) plasma startup in tokamak with the help of the plasma gun in conditions of double and single swing regime; (9) possibilities of plasma gun operation utilising plasma focus technique.

2. DEVELOPMENT OF GAS GENERATING AND PLASMA ACCELERATING STAGES

We designed, constructed and investigated novel double stage source of dense plasma with high-directed velocity, utilizing titanium-hydride grains. The principals of operation are

basically described in [10]. The source was modified, upgraded to improve the kinetic energy of the DMP jet (Fig. 1). Gas production, ionization and plasma-acceleration are performed by intense electric discharges interacting with the condensed substance to produce a gas cloud and a DMP cluster in a succession. The source consists basically of two stages. The first (gas generating) stage contains titanium grains loaded with hydrogen. An electric discharge passing through the grains releases high-pressure hydrogen. Neutral hydrogen passing through a specially designed grid fills the accelerator electrode gap to a high pressure in a few tens of microseconds. The second (plasma generating) stage is actually a system of coaxial electrodes. Electric discharge fired through the gas between the coaxial electrodes provides gas ionization and plasma acceleration in the classical "Marshall gun scenario"[13]. Both stages of the source are connected to low inductance capacitor power supplies. Care was taken to minimize inductance of the discharge circuit and the highest power input into the source.

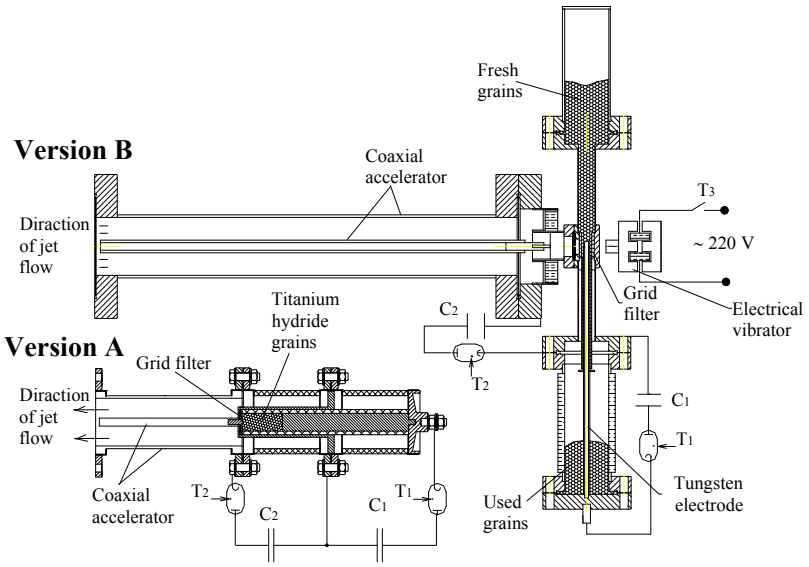

FIG. 1. Two versions of the source with different gas generating stages; (A) fresh grains loaded before series; (B) fresh grains loaded before each shot.

An experimental test bed, based on a 2 m^3 vacuum chamber, was developed for the investigation of the plasma jet parameters (Fig. 2).

The plasma source was installed on the vacuum chamber beyond the vacuum shutter. Both stages of the source were connected to low inductance capacitor power supplies. The stand was equipped with diagnostics and data acquisition system. Original 3-mirror He-Ne laser interferometer measured the plasma density Two movable newly designed piezoceramic probes measured the pressure profile and flow velocity. As well the flow velocity was measured with two collimated PM tubes recording the light near the gun edge and at the opposite wall of the vacuum chamber. AvaSpec 3648 spectrometer allowed investigations of spectral contamination of the plasma jet. A number of phtodiodes, connected with specially designed current shunts to the different parts of the outer electrode of the accelerator, observed discharge current distribution along the muzzle. CCD and streak camera registered time integrated and time resolved radiation from the jet accordingly. A permanent movable C-magnet (gap 5 cm) was placed inside the vacuum chamber for the separation of neutrals from charged particle.

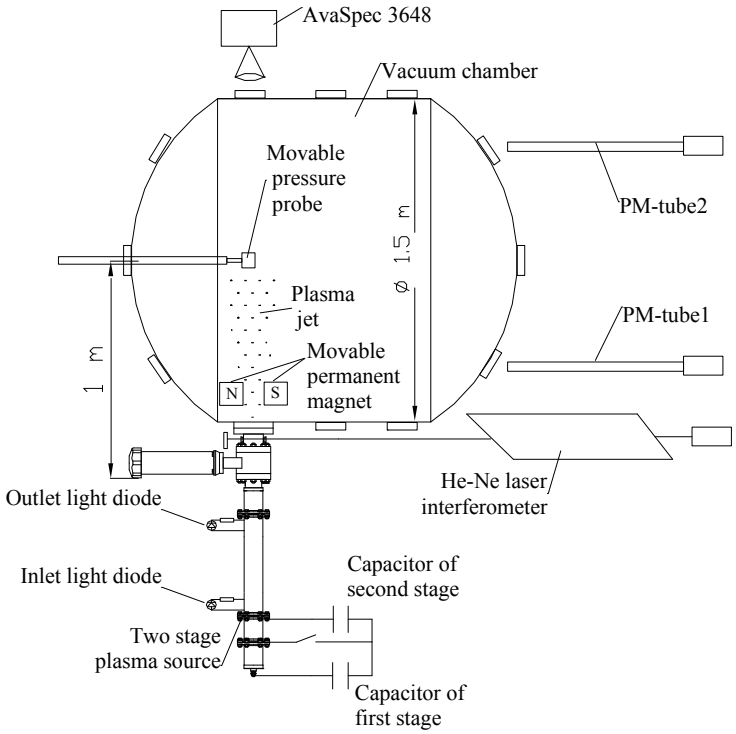

FIG. 2. Test bed for investigation of the plasma source.

Optimization of pulsed coaxial accelerator parameters by means of numerical calculations was performed. The goal of the present plasma source development is to generate a substance with high kinetic energy and with minimal impurity content, because it is very important to inject clean fuel into the fusion reactor. This is an essential difference of such a source from conventional plasma guns used in other applications. So, the substance with the highest kinetic energy (or plasma velocity) has to be generated with the lowest possible discharge current in coaxial accelerator. By numerical simulations we analyzed the acceleration process in a coaxial source with a variable capacity battery at a condition of fixed energy conservation (2 kJ) without losses. The process of electrodynamics plasma acceleration along *z*-axis can be described (in the simplest case) by coupled equations by Artsimovich [6]:

$$\begin{aligned} m_0 \frac{d^2 z}{dt^2} &= \frac{I^2}{2}\frac{dL}{dz}, \\ I &= -C_0 \frac{dU}{dt}, \\ \frac{d(LI)}{dt} &= U, \\ L &= L_0 + bz. \end{aligned} \tag{1}$$

Here t is time, m_0 is the mass undergoing acceleration which we assume constant, I is the current in the circuit, C_0 is the battery capacitance, U is the voltage between the electrodes, L_0 is the initial circuit inductance, and b is distributed inductance per unit length of the path traversed by the accelerating mass. The ohmic resistance of the electrodes and of the

plasma is neglected. The general parameters behaviour in dimensionless form is analyzed in Ref. [7]. For the particular case of finite coaxial electrode lengths and unipolar current waveform the system was solved numerically by the fourth order Runge-Kutta method.

The evolution of the plasma velocity and discharge current along the muzzle for different capacitances and muzzle lengths were calculated (Fig. 3).

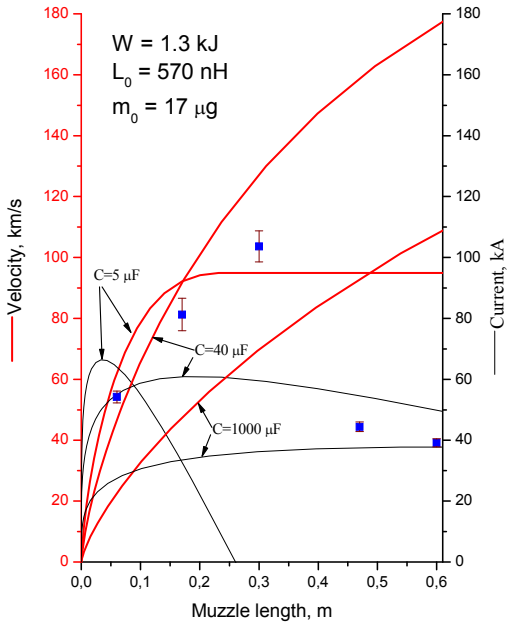

FIG. 3. Evolution of plasma velocity and discharge current distribution along the muzzle length of coaxial electrode accelerator. Squares with the error bars represent experimental velocity values for the gun with C=40 μF power supply.

Simulation reveals the highest velocity can be attained with the largest capacitance and a long enough muzzle. But the length of the electrodes is practically limited to ~1 m. It is seen that for a limited length the highest current can be localized near either the inlet (C_p=1 μF) or the outlet (C_p=1000 μF) of the muzzle, or it can be distributed (C_p=100 μF) along the muzzle length. At maximum current layer amplitude and maximum power deposited near the inlet or outlet of the muzzle the plasma jet velocity is low and the expected impurity contents is high. So, the highest velocity of the plasma jet at a given stored energy, limited muzzle length and lowest impurity content can be achieved when the current layer amplitude is high enough and the layer is running along the whole length of the muzzle. Peaked power deposition along the path of the accelerating mass may also bring about high impurity content. So, in order to achieve the maximum plasma jet velocity for a given energy and limited muzzle length intermediate capacitance e.g., C_p=40 μF was selected. Experimental measurements of the plasma jet velocity were carried out on the test bed for different muzzle lengths. The experimental points follow correctly the pattern of the theoretical curve up to muzzle lengths of 0.3 m. The experiments were conducted with close to optimum parameters of accelerator length and power supply.

The evolution of plasma source parameters measured at the test bed is presented in Fig. 4. Velocities of the gas, plasma and energy flows were measured by recording corresponding time delays between signals. These velocities varied with discharge current and measured plasma velocity was ~30–50% lower than predicted by the calculations. Radiation near the opposite wall indicated two enhancements apparently corresponding to fast and relatively slow velocity components of the jet. Observation of the discharge current

distribution along the muzzle confirmed the calculations (Fig. 3). The outlet current is delayed with respect to the inlet current. This indicates that current layer reaches the gun outlet. The amplitude and time duration of the outlet current are 2–3 times less than those of the inlet current.

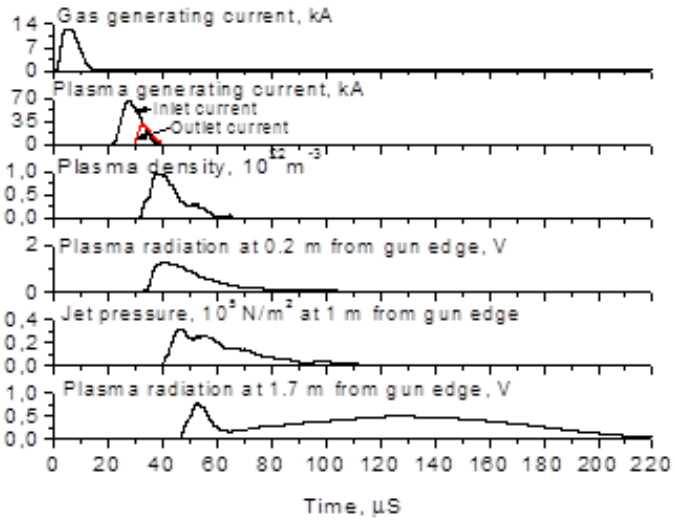

FIG. 4. Time dependence of jet parameters.

Velocities of the gas, plasma and energy flows were measured by recording corresponding time delays between signals. These velocities varied with discharge current and measured plasma velocity was ~30–50% lower than predicted by the calculations. Radiation near the opposite wall indicated two enhancements apparently corresponding to fast and relatively slow velocity components of the jet. Observation of the discharge current distribution along the muzzle confirmed the calculations (Fig. 3). The outlet current is delayed with respect to the inlet current. This indicates that current layer reaches the gun outlet. The amplitude and time duration of the outlet current are 2–3 times less than those of the inlet current.

Time integrated jet radiation picked up with the camera showed a regular, directed and sharp boundary jet, with a cross-section diameter of 10 cm at a distance of 1 m from the source edge (Fig. 5).

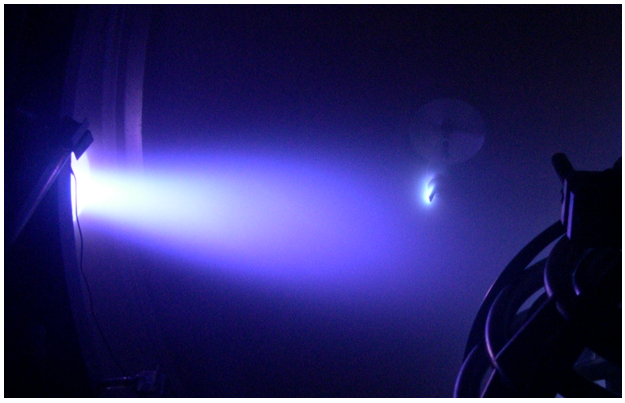

FIG. 5. Plasma jet radiation.

The plasma temperature reached ~1 eV. It was derived from measured line intensity ratio of H_α/H_β and assumption of Boltzmann energy distribution. The pressure profile of the jet shows that the energy flow was concentrated near the jet axis with diameter 10 cm (Fig. 6).

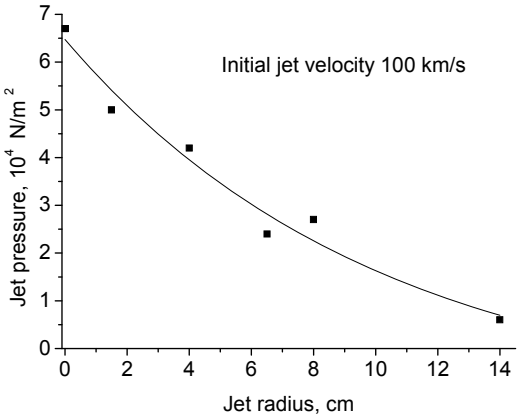

FIG. 6. Dependence of jet pressure on jet radius at 1 m from the source edge.

The kinetic energy of the jet reached a few hundreds Joules (stored capacitor energy 0.65–2 kJ). An optimized source generated, during ≤50 μs clean, highly ionised hydrogen plasma with density 2×10^{22}m^{-3}, total number of the accelerated particles (1–5) $\times10^{19}$ and flow velocity 30–200 km/s.

Jet penetration through the transverse magnetic field created with a movable magnet placed near the gun edge was investigated (Fig. 7).

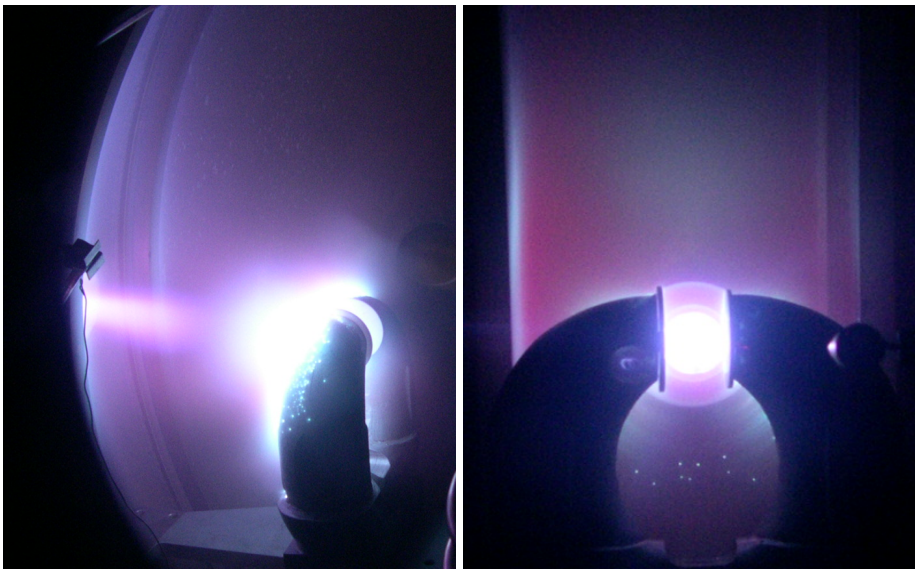

B = 0.3 T, view perpendicular source axis. *B = 0.3 T, view along source axis.*

FIG. 7. Radiation of the jet passing the transverse magnetic field

No visible radiation of the jet crossing magnetic field of 0.3 T (with a velocity of 50 km/s and density ≤10^{22} m^{-3}) was observed beyond the magnet.

Keeping the magnet position unchanged the magnetic field was varied in the range of 0–0.3 T. Jet pressure was registered with a piezoceramic detector located beyond the magnet (Fig. 8). The pressure decreases with increasing magnetic field strength.

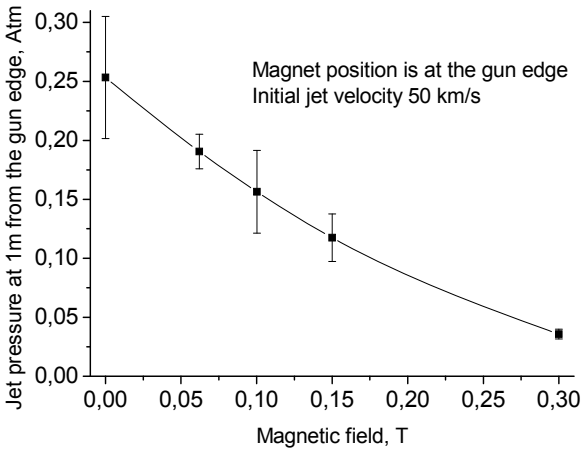

FIG. 8. Dependence of jet pressure from magnetic field.

The dependence of the jet pressure on the distance between the constant field strength magnet (B_{stop}=0.3 T) and the plasma source outlet was registered (Fig. 9).

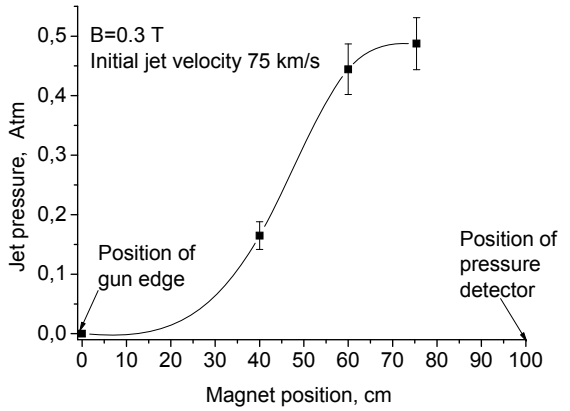

FIG. 9. Dependence of jet pressure on the distance between the magnet and the plasma source edge.

The jet pressure increases with increasing distance. The magnetic field does not stop the jet if the distance ≥70 cm. It was found that the highly ionized plasma jet recombines during time of flight into the fast neutral flow at this distance and can penetrate through magnetic field. The estimated recombination time and path based on measurements for plasma jet with velocity 50 km/s, density 10^{22} m^{-3} and temperature 1 eV are approximately 20 μs and ~1 m respectively.

The experiments with two colliding jets confirmed that the plasma recombined into the jet of neutrals at a distance from source edge (Fig. 10). The distance between two head on plasma sources was 2 m. It is seen that the plasma jet recombines into a gas jet at a distance of ~ 0.8 m from source edge. Near the center the jets are collided and ionized again. So, the jets of neutrals have kinetic energy higher than hydrogen ionization potential.

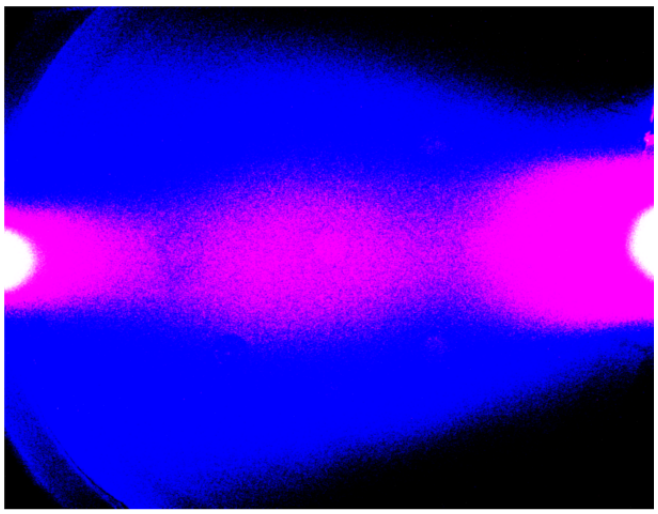

FIG. 10. Radiation of two colliding jets.

Latest experiments of time resolved plasma flow radiation with streak camera were carried out (Fig. 11). Observations showed that the flow consist of jets with a discrete number of the velocities. Velocity variation can be explained by current changing during discharge. Probably in this experiment the discharge passes along muzzle many times during acceleration at varying current.

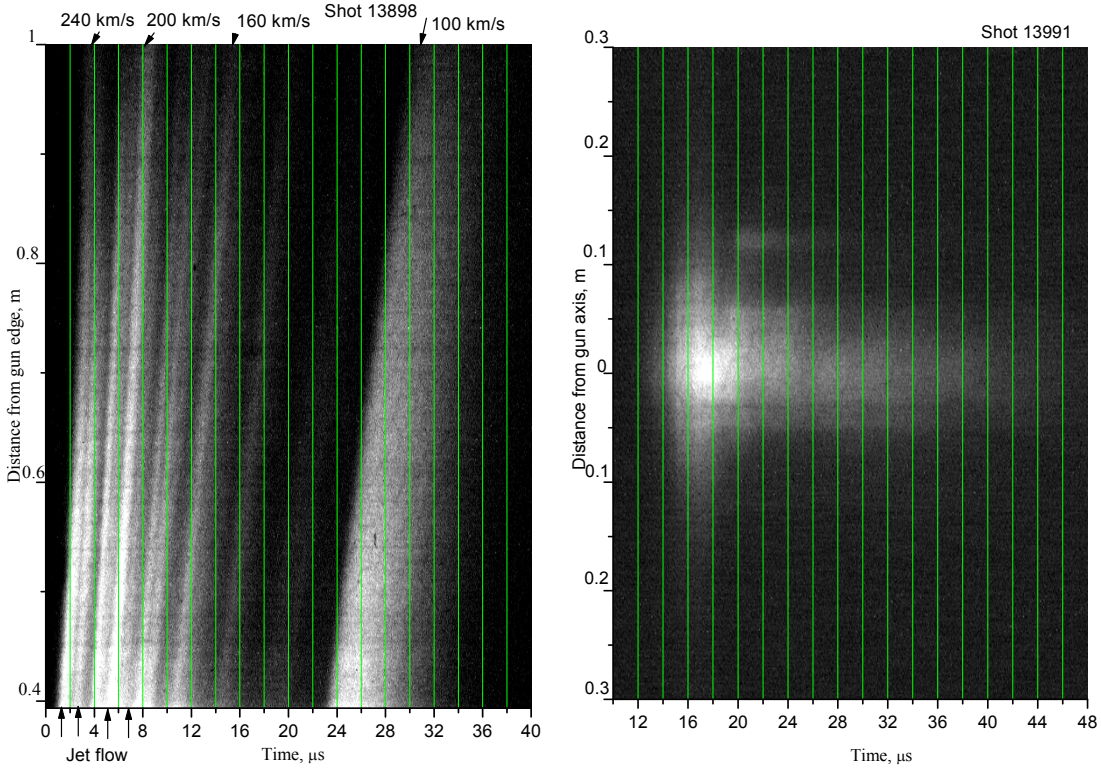

FIG. 11. Jet radiation observed through narrow slit with streak camera; shot 13898 — perpendicular view; shot 13991- view along gun axis.

Several successful modifications of the plasma gun were tested to get higher plasma jet parameters (velocity and/or density), namely:

Gas generating and plasma accelerating stages were equipped with separate switches to increase the specific kinetic energy of the jet. Time delay between the switching was optimized which allowed increasing the plasma density (from 1×10^{22} to 2×10^{22} m^{-3}).

To diminish some disregarded factors related to minor design flaws we conducted an experiment with two accelerating stages. A double accelerating stage connected in series allowed increasing plasma flow velocity on ~25% as comparison with acceleration by one stage alone.

Additional efforts were made for reproducible initiation of the discharge in the second stage of the plasma source. Similar to the plasma focus technique the discharge was initiated along ceramic surface at the inlet of coaxial electrodes (muzzle) and accelerated along whole muzzle length to the electrode outlet. This development enabled us to increase the plasma flow velocity from 100 to 200 km/s for the same muzzle length (~0.35 m).

Efforts to search for an alternative method of forming a compact gas cloud from the grains were explored by irradiation of the titanium hydride grains by a Ruby laser. The laser with the output beam energy of 100 J and 1.2 ms duration was used. The titanium hydride grain layer was placed between stainless steel grids discs spaced at few millimetres. This target was positioned in the gap of coaxial accelerator. Laser beam irradiated grains and produced gas cloud (number of particles ~10^{19}), which were ionized and accelerated. The plasma jet with similar characteristics was produced to the jet created by conventional (electrical) activation of the grains.

First experiments were conducted with fresh titanium hydride grains loaded before the series of 50 shots. An electric discharge passing through the whole package of grains releases quantities of hydrogen decreasing with shot number. The most recently developed construction allows loading the fresh grains before each shot (Fig. 1(b)). It consists of two chambers for fresh and used grains, and thin channel between where electrical discharge releases the hydrogen. An electric discharge passing through fresh grains releases constant quantity of hydrogen during each discharge. The source was able to generate stable gas release for many shots (Fig. 12).

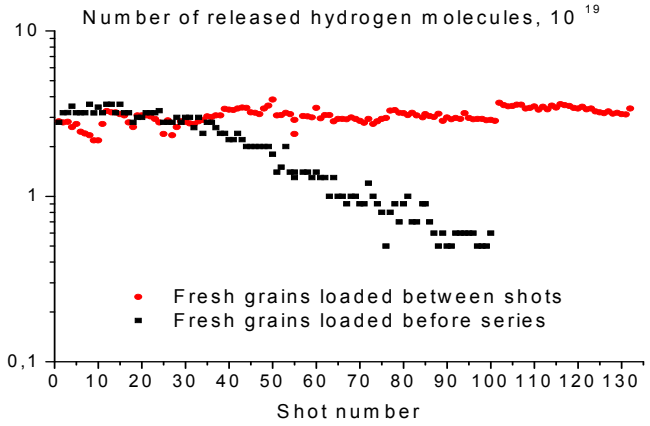

FIG. 12. Dependences of number hydrogen molecules on shot number.

Improvements of the jet source were made in order to decrease jet pollution (Fig. 13). Before loading into source the titanium hydride grains were cleaned with compressed air inside of volume surrounded by thin grid. Additionally the cell size of the grid filter was

reduced from 150 μm to 40 μm. These modifications considerably reduced impurities in the plasma jet. The impurity radiation was suppressed more than 100 times after cleaning the grains and thin filtering the gas cloud.

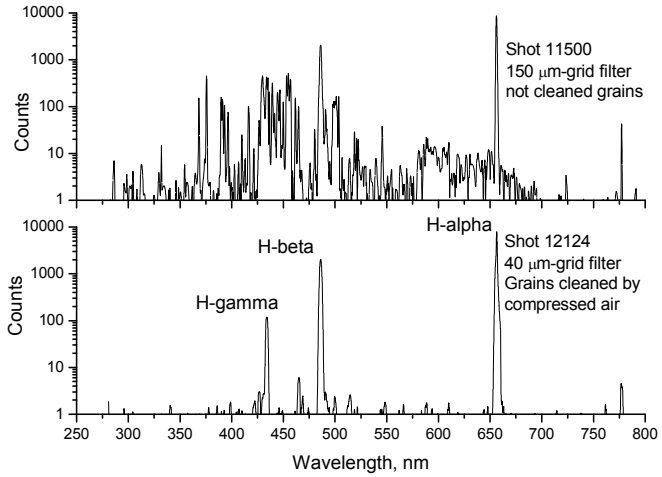

FIG. 13. Spectral radiations of plasma jet; sight along the source axis into the muzzle.

3. JET INJECTION IN THE TOKAMAK GLOBUS-M

The design description, operational principles and experimental program of the Globus-M are described in[12]. General and interior views of the tokamak are presented in Fig. 14. The basic design characteristics are as follows: aspect ratio $A=R/a$=1.5, major plasma radius R=0.36 m, minor plasma radius a=0.24 m, toroidal magnetic field at the vessel axis B_T = 0.2–0.5 T, plasma current I_p =0.1–0.35 MA, average plasma density $n_e = (1–7) \times 10^{19}$ m^{-3}, pulse duration with inductive current drive $\tau_{pulse} \leq 0.12$ s. Plasma current amplitude was in range 150–350 kA at the quasi stationary discharge phase. The toroidal magnetic field was changed in the range 0.3–0.4 T. The hydrogen jet was injected into Globus-M in OH deuterium plasma both at a small angle (15º) to the vertical axis and at the equatorial plane along the major radius from the low field side (Fig. 15).

Two applications of plasma jet injection have been studied. The first one is the plasma discharge initiation. The jet used during the breakdown phase instead of RF pre-ionization and vacuum vessel prefilling with working gas. The second application is the plasma density regulation. The hydrogen jet was injected in deuterium plasma during current plateau.

During injection of DMP jet into the tokamak plasma parameters of the main plasma were measured. Line integrated plasma density was measured by 1 mm interferometer along three vertical chords (at R=24, 42 and 50 cm). Video camera observed time integrated radiation of the injected plasma inside the vacuum vessel. The time evolution of hydrogen contents in the deuterium plasma and the ion temperature were measured by neutral particle analyser ACORD-12 [8]. The plasma density profile evolution was measured by multichannel radar-reflectometer in the frequency range 19.6–60.5 MHz. A bolometer registered radiation losses and a spectrometer detected line radiation of H_α and carbon.

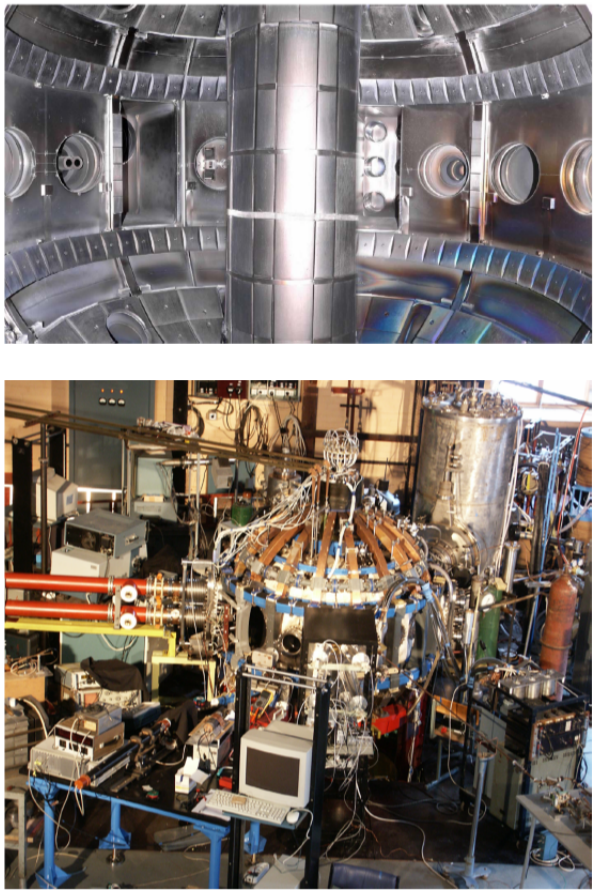

FIG. 14. General view of the Globus-M installation.

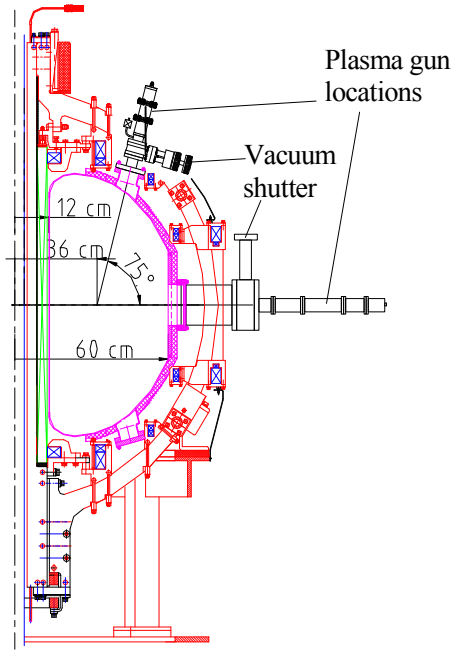

FIG. 15. Two stage plasma gun placed at the spherical tokamak Globus-M (two positions).

4. PLASMA STARTUP IN TOKAMAK WITH PLASMA GUN

The plasma source was placed in the equatorial plane and at a distance of 0.5 m from tokamak. The number of injected particles was comparable with total number of the particles in tokamak (5×10^{18}–10^{19}). The discharge was initiated by means of plasma jet injection into 0.4 T toroidal field. Experiments were performed in conditions both of single (at zero current in the central solenoid) and double (at the maximum current in the central solenoid) swing central solenoid operation regime. The injection of plasma at zero current in the central solenoid created better conditions for breakdown and buildup of the plasma current at lower MHD activity as compared with ECR pre-ionization and neutral gas prefill. The plasma parameter traces in the discharge, initiated by means of plasma jet are shown in Fig. 16 (left waveforms).

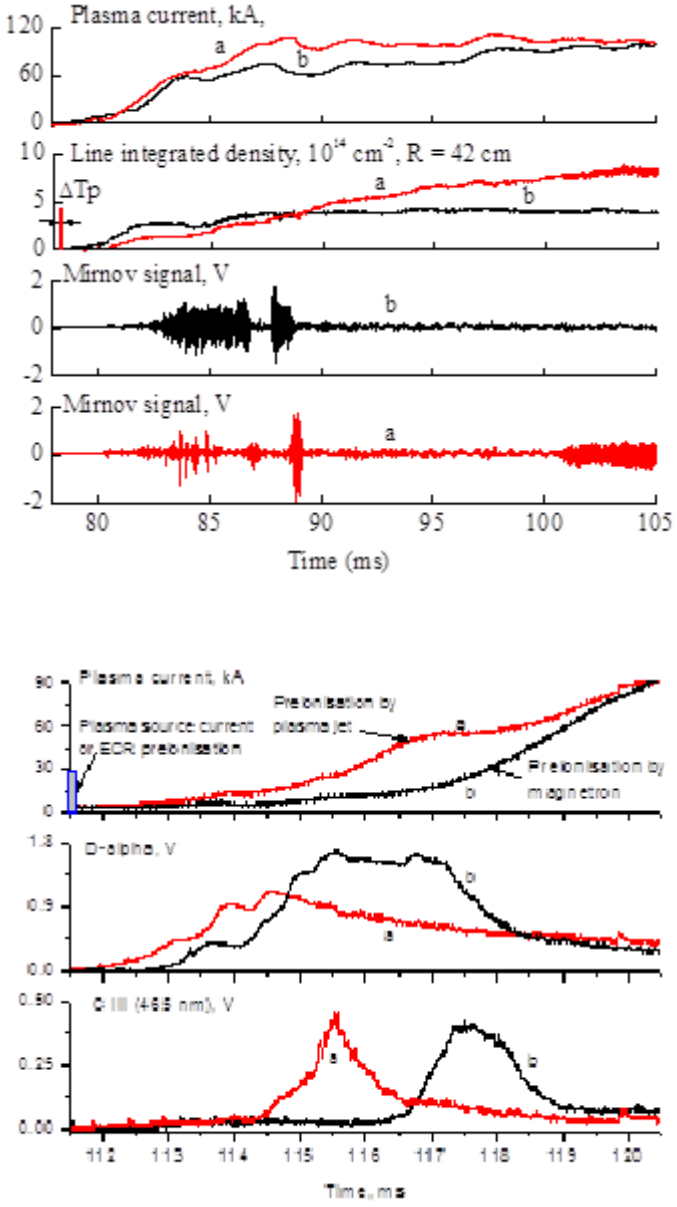

FIG. 16. Time dependence of some plasma parameters in Globus-M at different discharge initiation conditions; (a) with plasma gun; (b)with gas prefill and UHF pre-ionization; shots 3386, 3397-with single swing solenoid operation; shots15064, 15065- with double swing solenoid.

It can be seen that plasma current ramped up faster and to the higher value at the same loop voltage waveform than with traditional method. It is also seen that magnetic turbulence during current ramp-up is lower in the case of injection. Plasma density reached higher value; background radiation of Hα line was lower than with gas-puffing and pre-ionization system. In conditions at the maximum current in the central solenoid operation regime as well the maximum of the spectral line intensities (D_α and CIII) were shifted to the beginning of the discharge (Fig. 16 right waveforms). Higher plasma current and earlier spectral lines excitation may confirm more intense plasma heating at the initial stage of the discharge.

5. JET PENETRATION INTO TOROIDAL MAGNETIC FIELD

The hydrogen jet was injected into vacuum magnetic field of the Globus-M at a small angle (15 degrees) to the vertical axis. Plasma source located at 0.3 m distance from the chamber wall. The observation of the injected plasma radiation into the vacuum magnetic field helped to estimate the possible penetration depth of plasma jet into the main plasma (Fig. 17). The speed of the jet was 30 km/s. One could see the deeper penetration of plasma jet with equal velocities into lower magnetic field. It is seen that plasma jet is seems to be stopped by the magnetic field value below 0.25 T in the vessel centre (the field at the gun nozzle position is about 0.2 T).

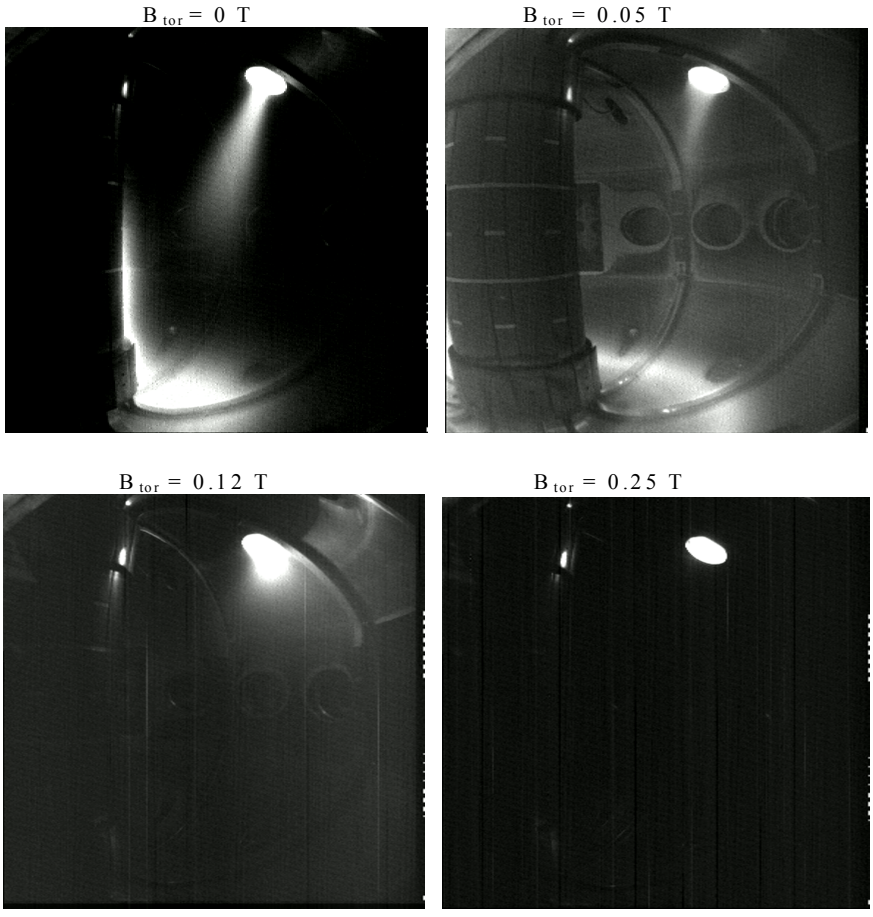

FIG. 17. Radiation of the injected plasma inside the vacuum chamber with toroidal magnetic field.

6. PLASMA DENSITY CONTROL DURING CURRENT PLATEAU PHASE

Plasma current amplitude ranged 120–300 kA at the quasi stationary discharge phase. The toroidal magnetic field was changed in the range 0.3–0.4 T. In earlier campaigns injection was performed at plasma jet velocity and density near the gun edge did not exceeding 100 km/s and 10^{22} m^{-3} accordingly [9, 10]. The hydrogen jet was injected into Globus-M in OH deuterium plasma at a small angle (15º) to the vertical axis from the low field side (Fig. 15). Jet injection led to the increase of the plasma average density (Fig. 18). The density rose up during 1 ms following the gun shot. Injection of the plasma jet led to a faster increase of the plasma density compared with gas puffing (more than 15 ms).

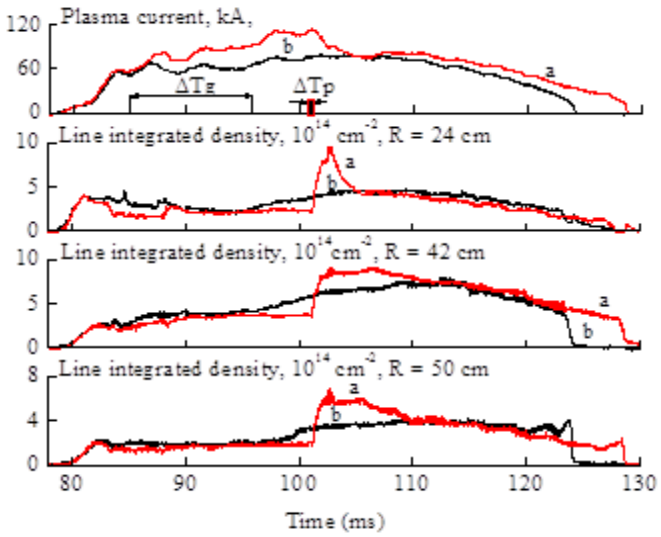

FIG. 18. Plasma injection at the maximum discharge current; (a)-with plasma gun; (b)with gas puffing.

Measurements of plasma density profile by means of multichannel radar-reflectometer revealed the increase of density gradient not only near the plasma periphery but inside the plasma volume (Fig. 19). The profile is steeper after plasma injection.

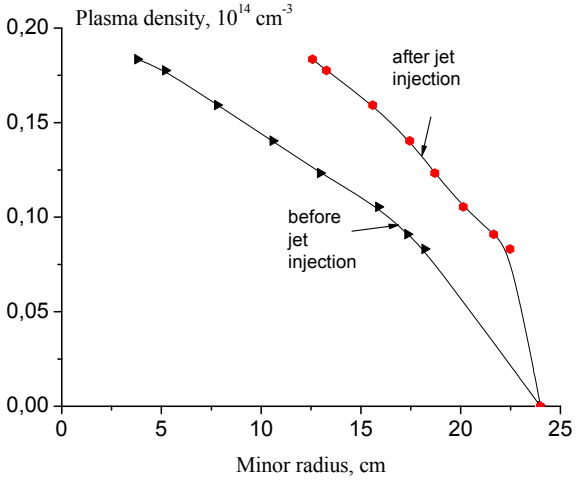

FIG. 19. Evolution of plasma density profile during jet injection; shot 5276.

The time evolution of the hydrogen charge-exchange flux in deuterium plasma was recorded by neural particle analyser (Fig. 20). The flux rose up with increasing plasma density during 1–2 ms after jet injection. Maximum flux of hydrogen was at the energy 470 eV. Percentage of the hydrogen increased in deuterium plasma up to 25 %. It means that injected plasma penetrated into the hot plasma body.

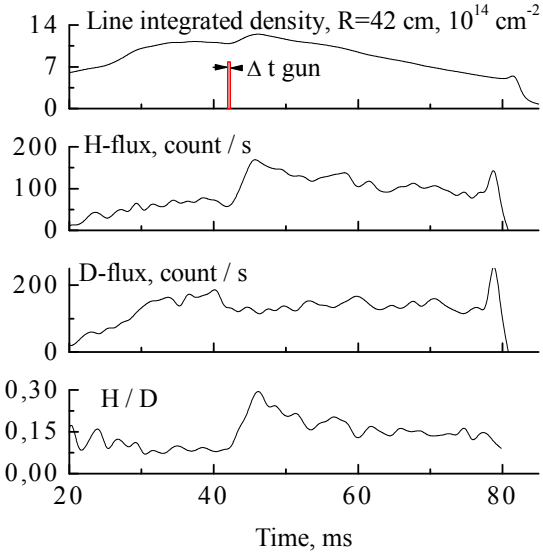

FIG. 20. Evolution of hydrogen in deuterium plasma; flux energy 470 eV; shot 6068.

At present time the hydrogen jet was injected into Globus-M in OH deuterium plasma at the equatorial plane along the major radius from the low field side (Fig. 15). Data demonstrates a fast density rise (<0.5 ms) recorded by the interferometer along the peripheral (R = 24 cm and 50 cm) and central (42 cm) chords (Fig. 21).

In this case, the density rise time was shorter than the diffusion time, and it could roughly be identified with the time necessary for injected particles to equilibrate along the field lines. While the plasma particle inventory increased by 50% (from 0.65×10^{19} to 1×10^{19}), it did not result in plasma degradation (as, e.g., a drop in plasma current, contamination by impurities, MHD activity enhancement). Initial short peaks recorded by D_α, OIII, CIII detectors are due to strong blackbody radiation of the jet illuminating the vessel interior. After time interval of 2–3 ms all the signals, including bolometer and Mirnov signals returned to the initial (pre-injection) level.

During recent experiments the jet speed was increased up to 200 km/s and density up to 2×10^{22} m^{-3} [11, 12]. After second RCM the injection of such jet in tokamak has been investigated. Waveforms of plasma discharge parameters in Globus-M under such plasma jet injection are presented in Fig. 22.

It is also seen that it led to an enhancement (<0.5 ms) of the plasma average density and local plasma density across the plasma core. The density is approximately doubled at all radii of the plasma column. AvaSpec 3648 spectrometer registered spectral radiation of plasma in Glonus-M viewing along the source axis outlet muzzle edge. Spectral radiation of the Globus-M plasma under jet injection is presented in Fig. 23.

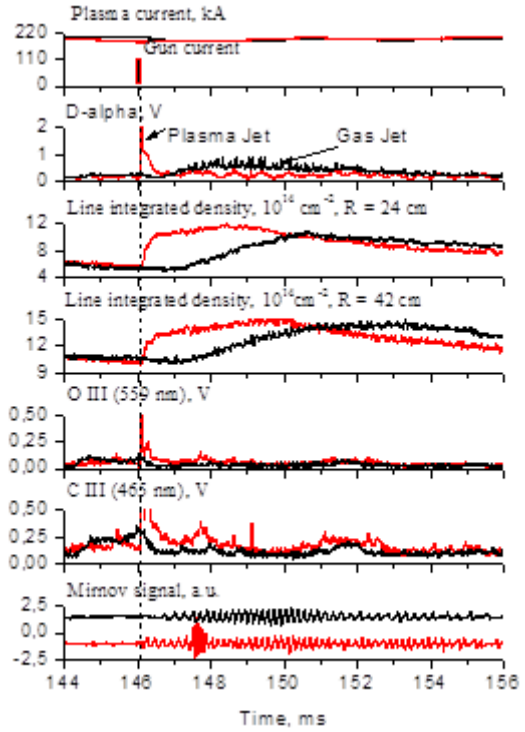

FIG. 21. Waveforms of plasma discharge parameters in Globus-M under gas jet (black lines) and plasma jet (red lines) injection.

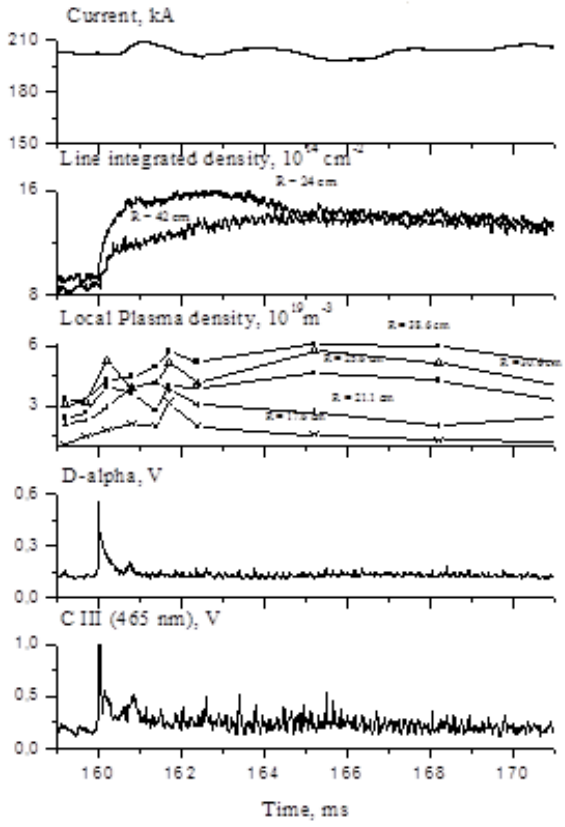

FIG. 22. Waveforms of plasma discharge parameters in Globus-M under improved.

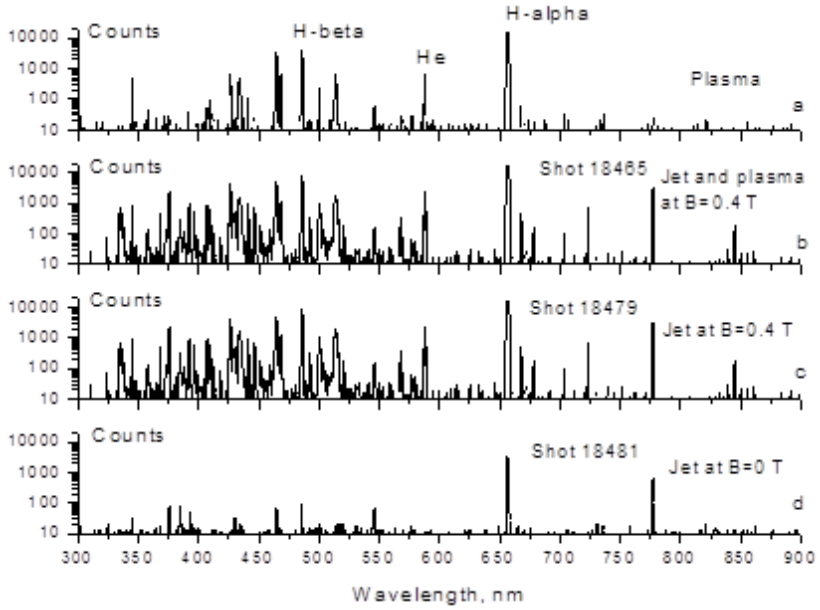

FIG. 23. Spectral radiations of jet and plasma in Globus-M before (a) and during (b) jet injection; (c)jet injected into vacuum chamber with magnetic field; (d)jet injected into vacuum chamber without magnetic field; sight along the source axis outlet the muzzle.

One could see evolution of these spectra before (a) and after (b) jet injection for the same shot. Similar spectrum of the jet was recorded without Globus-M plasma but with confined magnetic field (c). It is seen that pollution of the jet considerably reduces without magnetic field (d). Possibly in future experiments the plasma source should be placed at distance greater than 0.5 m from tokamak for efficient recombination of plasma jet into jet of neutrals before reaching the plasma core.

7. GAS STREAM INJECTION

To compare the efficiency of plasma jet injection with gas puffing, experiments were conducted with the first stage of the plasma gun used as gas generator. Test bed experiments showed the first stage is able to generate a fairly fast (1–5 km/s) neutral gas jet. This jet was injected into Globus-M and penetrated efficiently into the magnetic field. The density rise time of ~2.5 ms observed (Fig. 21) is shorter than that achieved customarily with conventional gas puffing (4–5 ms) while being much longer than that characteristic of plasma jet injection (<0.5 ms).

8. MODELLING OF JET PENETRATION

The model for gas jet penetration into the tokamak is applied for the high-velocity jets accelerated by plasma gun on Globus-M. The penetration of the jet into the core plasma required sophisticated theoretical consideration. For the jet penetration modelling the approach used was as described in [13]. The heating, expansion and ionization of the jet penetrating towards the tokamak centre are calculated for the typical density and temperature profiles measured by TS diagnostics. It is found that the initially neutral jet is ionized within $\tau_i = 0.5\ \mu s$, i.e. penetrates up to 5 cm assuming constant velocity.

Temporal evolution of the jet temperature is shown in Fig. 24. Note that the time scale of full ionization is of the same order as in experiments on Tore-Supra and ASDEX-Upgrade

[25, 26], where the jet with similar parameters was accelerated by pressure gradient through Laval nozzle.

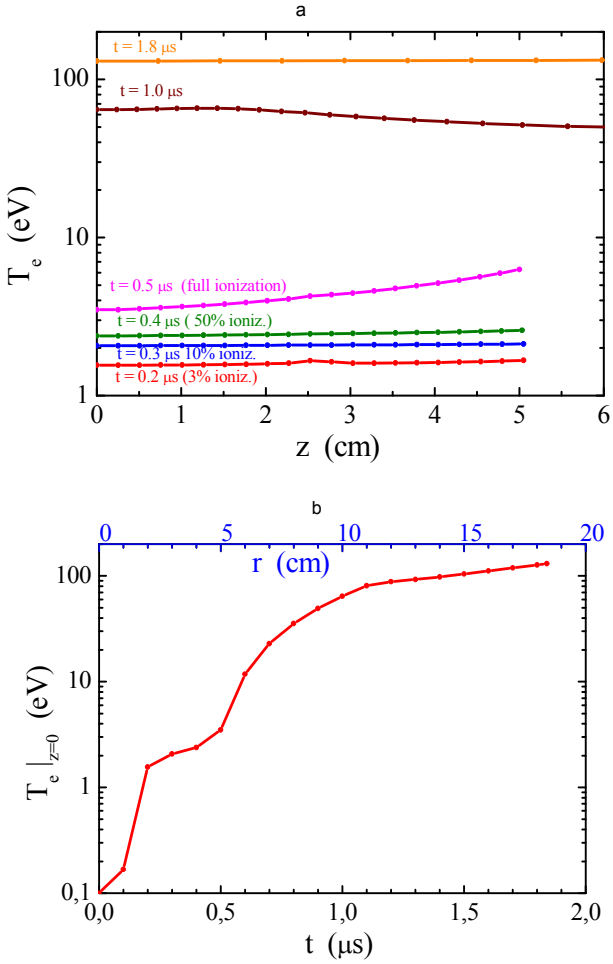

FIG. 24. Evolution of the jet temperature; (a) profiles along the magnetic field;(b) equatorial plane (z=0) temperature versus time.

The penetration of ionized jet in the injection direction is provided by polarization electric field $\vec{E}_0 = \left[\vec{B} \times \vec{V}_0\right] / B^2$ and $\vec{E} \times \vec{B}$ drift. However, this polarization (and jet velocity $\vec{V}_{jet}$) reduces due to currents in the Alfven wave emitted into the ambient plasma (the effect of so-called Alfven conductivity), and vertical ∇B induced currents.

Due to emission of Alfven wave the ionized jet decelerates exponentially and penetrates inside Globus-M plasma up to $V_0 \tau_\Sigma \approx 8$ cm, where $\tau_\Sigma \approx 0.8$ μs — characterizing deceleration time. Consequently, in the Globus-M deep penetration up to $V_0(\tau_i + \tau_\Sigma) \approx 12$ cm $\approx$ a/2 be possible, while on ASDEX-Upgrade $V_0 \tau_\Sigma \approx 1.5$ mm $<< a$, and jet practically could not cross the separatrix. The τ_Σ is inversely proportional to the sprout of ambient plasma density and proportional to the jet density, therefore for higher ambient plasma densities and lower jet density the penetration depth would be smaller.

The second process accelerates the jet towards the low field side. The ∇B induced current leads to acceleration towards the low field side. However, this current in the jet expanding along the magnetic field vanishes at time scale $R\sqrt{m_i/(T_e + T_i)}$ due to rotational transform, which leads to a displacement of the same order [27]. As both processes are taking place simultaneously consideration is more complex, but one can expect that significant part

of injected particles should be deposited inside the separatrix, mainly at the plasma periphery when the jet was injected from the equatorial plane. This does not contradict experimental observations. If one could imagine jet injection from high field side the depth of injection into the plasma column will increase significantly. The model predictions are consistent with experimental observations. It is demonstrated that with high velocities achieved by the plasma gun it is possible to get a deep jet penetration into the tokamak plasma.

9. DISCUSSION

A promising jet source (Fig. 1(b)) allows loading the fresh grains before each shot and produce stable and clean jets for many discharges. The developed more stable source generates gas and plasma jets with specific kinetic energies is in excess of those reached in an earlier study. The jet speed was increased up to 200 km/s and the jet density near the gun edge reached 2×10^{22} m^{-3}. This is sufficient for fuelling a tokamak such as Globus-M. But further increasing the source parameters will be required for large scale tokamaks. Coaxial gun accelerates the plasma by J×B force. Raising the discharge current between coaxial electrodes can increase not only kinetic energy of the jet but also the impurities. An attempt should be made to explore methods of increasing the magnetic field at a limited discharge current.

The experiments on discharge initiation by means of plasma jet both in conditions of single and double swing central solenoid operation regime showed that the current ramps up faster with the plasma gun initiation, than with traditional HF pre-ionization of the filling gas. Higher plasma current and earlier spectral lines excitation may confirm more intensive plasma heating at the initial stage of the discharge. This method could be used for efficient ignition of the discharges in fusion reactors.

Deep jet penetration into toroidal magnetic of the Globus-M was observed and a twofold density increase was achieved. Now it is clear that partly the effect of density increase can be attributed to the stream of neutrals penetrating into tokamak after plasma recombination during time-of-flight outside the tokamak vessel boundary. This is supported by test bed experiments with plasma jet penetration through transverse magnetic field (Fig. 8). We may recall that the jet velocity in these experiments was ~75 km/s, and the density measured at the gun edge, $\sim10^{22}$ m^{-3}. The transverse magnetic field of 0.3 T does not stop the jet that has passed a distance in excess of 75 cm. This may indicate transformation of a sizable fraction of the charged particle flux to a high-density flux of neutrals during the transit time ~10 μs. In a plasma jet with the parameters reached in test bed experiments ($n \sim 10^{21}$–10^{22} m^{-3}, T~1 eV), the rate of three-body radioactive recombination is very high [17]. To estimate the characteristic time of this process, precision measurements of the plasma jet concentration and temperature (transverse energy) would be required.

A straightforward estimation of the temperature made from plasma jet divergence measurements yields ~1 eV. This figure is not inconsistent with temperature data derived from the Hα/Hβ line intensity ratio. Assuming the measured transit time to be roughly equal to the characteristic three-body recombination time ($\tau_{rec} \approx 1.8\times10^{38}$ $T^{9/2}$ eV/n^2 $m^{-3} \approx 10^{-5}$ s), we obtain ~1 eV and $\sim4\times10^{21}$ m^{-3} for the parameters of the jet recombining in this time. The fairly low measurement accuracy and the order-of-magnitude character of the above calculations do not permit unambiguous identification of the mechanism by which the plasma jet penetrates across a magnetic field. At the same time, recombination of a plasma jet into the jet of neutrals appears a most likely candidate for the process resulting in efficient penetration of particles into a magnetic field.

The latest experiments with high speed jet injection into the Globus-M during current plateau phase showed efficient jet penetration into the plasma core. Analyzing spectral radiation one could conclude that such jet interacts with the walls of the chamber at confining magnetic field and pollutes the plasma. Possibly such plasma jet does not recombine completely into neutrals and is deflected by the magnetic field to the walls. Presently the source is not far enough from the tokamak (0.5 m), and experiments with longer recombination chamber (~1.5 m) are required.

Magnetic field penetration is a necessary, but not sufficient condition for deep plasma fuelling. The experiments with significantly decreased magnetic field did not show the deeper jet penetration into tokamak plasma. This means that the ratio of specific kinetic energy of the jet to magnetic field pressure does not play an exceptional role in interaction between the plasma jet and tokamak plasma confined by the magnetic field. Plasma pressure (temperature or density) could be an additional reason preventing penetration. It is experimentally established that the increase of the initial density of the target ohmic heating plasma decreased the jet penetration efficiency.

Modelling showed that both neutral jet and plasma jet penetration into the plasma core strongly depend on the jet velocity and ratio between jet and core densities (τ_Σ is inversely proportional to the sprout of ambient plasma density and proportional to the jet density). Therefore for higher jet velocity and density, and lower ambient plasma density the penetration depth would be higher. Important result of the simulations is the weak sensibility of particle deposition to the initial ionization degree of the jet. It is found that the initially neutral jet is ionized within $\tau_i = 0.5$ μs, i.e. penetrates up to 5 cm assuming constant velocity, so that the ionization time is smaller that any other characterizing time in the problem. So at the current stage of the research we can say about equal contribution of plasma jet and neutral jet components into the density raise effect recorded during injection experiments. But neutral jet is preferable because it penetrates more efficiently into confining magnetic field surrounding the plasma core. Simulations inside plasma show — ionization of jet and braking due to emission of Alfven waves and grad B drift accelerates jet towards low field side. Resulting effect allows the jet deposition inside separatrix, unlike the case of molecular supersonic beam, which is definitely deposited outside the separatrix

10. CONCLUSIONS

Investigations confirmed that developing DMP source has a potential means for nuclear fusion energy researches and applications. Novel type of clean plasma source for DMP production and acceleration has been successfully developed, investigated and tested in plasma fuelling experiments. Several modifications of the plasma gun were tested to get higher plasma jet parameters (velocity or density).

Optimization of pulsed coaxial accelerator parameters by means of analytical calculations has performed with the aim of achieving the highest flow velocity at fixed coaxial electrode length and stored capacitor energy. An experimental test bed was developed for investigation of intense plasma jet generation. Similar to the plasma focus technique the discharge was initiated along ceramic surface at the inlet of coaxial electrodes (muzzle) and accelerated along whole muzzle length to the electrode outlet. Such development allowed a doubling of the plasma flow velocity at the same muzzle length. An optimized source generated, during ≤50 μs clean, highly ionized hydrogen plasma with density of 2×10^{22} m^{-3}, total number of the accelerated particles $(1–5)\times10^{19}$ and flow velocity 30–200 km/s. It was

found that the highly ionized plasma jet recombines, during its time of flight, into a fast neutral flow and can penetrate the magnetic field. The jet of neutrals has kinetic energy higher than the hydrogen ionization potential.

Plasma startup in the tokamak with the help of the plasma gun showed better performance. The injection of plasma before the discharge created better conditions for breakdown and building up the plasma current at lower MHD activity as compared with ECR preionization and neutral gas prefill.

Experiments showed efficient jet penetration into the plasma core into the Globus-M during the current plateau phase. In 0.5 ms after a plasma gun shot, the density increases at all spatial points up to a radius $r \approx 0.3a$, thus evidencing deep plasma jet penetration. Such injection allowed a doubling of the plasma density in the tokamak. Gas flow injected with the first (gas producing stage) only penetrated into the trap during 4.5 ms.

The model for jet penetration into the tokamak is applied for the high-velocity jets accelerated by plasma gun on Globus-M. Numerical simulations showed that due to the large initial velocity such jets should penetrate deep (20cm) in the Globus-M plasma. The model predictions are consistent with experimental observations.

ACKNOWLEDGEMENTS

The authors wish to thank IAEA Staff, the scientific, technical and engineering staff of the MHD Phenomena and Hot Temperature Plasma Physics Laboratories.

REFERENCES

[1] GOUGE, M.J., Fuelling of ITER-scale fusion plasmas ANS Conference Nashville (1998) and http://www.ornl.gov/sci/fed/pellet/ornlpell_main.html.
[2] COMBS, S.K., Pellet injection technology, Rev. Sci. Instrum. 64 (1993) 1979.
[3] MILORA, S.L., et al., V Review paper: Pellet fuelling, Nucl. Fusion 35 (1995) 657.
[4] ITER PHYSICS BASIS EDITORS, Power and particle control, Physics of energetic ions Nucl. Fusion 39 (1999) 2416, 2521.
[5] RAMAN, R., et al., Experimental demonstration of tokamak fuelling by compact toroid injection, Nuclear Fusion 37 (1997) 964.
[6] DROBYSHEVSKY, E.M, ZHUKOV, B.G., SAKHAROV, V.A., IEEE. Trans. Magn. 31 (1) (1995) 299.
[7] SEMENOV, V.K, SPECTOROV, L.A., Investigation of stream of pulse-plasma discharge, Zh. Tekh. Fiz. 34 (5) (1964) 853.
[8] VASILJEVA, R.P., PERGAMENT, M.I., YAROSLAVSKY, A.I., Investigation of plasma-focus in coaxial injector Plasma Phys. and Controlled Nucl. Fusion Research IAEA Vienna 2 (1969) 39.
[9] VORONIN, A.V., HELLBLOM, K.G., Titanium-hydride gun for plasma injection into the T2- Reversed Field Pinch device, Plasma Physics and Controlled Fusion 41 (1999) 293.
[10] VORONIN, A.V., HELLBLOM, K.G., Generation of dense plasma clusters with high velocity, Plasma Phys. and Controlled Fusion 43 (2001) 1583.
[11] GUSEV, V.K., et al., Density limits and control in the Globus-M Spherical Tokamak, Nuclear Fusion 46 (2006) 584.

[12] GUSEV, V.K., et al, Plasma formation and first OH experiments in the Globus-M tokamak, Nuclear Fusion 41 (2001) 919.
[13] MARSHALL, J., Performance of hydromagnetic plasma gun, Phys. Fluids3(1960) 134.
[14] ABRAMOVA, K.B. et al, Injection of High-Density Plasma into the Globus-M Spherical Tokamak, Plasma Physics Reports 31 (2005).
[15] VORONIN, A.V. et al, High kinetic energy plasma jet generation and its injection into the Globus-M spherical tokamak, Nuclear Fusion 45 (2005).
[16] VORONIN, A.V., et al, High Kinetic Energy Dense Plasma Jet, Nukleonika51,2006) 85
[17] ARTSYMOVITCH, L.A. et al, Electrodynamic acceleration of plasma clusters, Soviet Journal of Experimental and Theoretical Physics 33 (1957) 3.
[18] KOLESNIKOV, P.M., Electrodynamics acceleration of plasma, Moscow: Atomizdat (1971) 198.
[19] IZVOZCHIKOV, A.V. et al., Multichennel analyser for simultaneous registration of energy spectres of hydrogen and deuterium atoms, Tech. Phys. 37(1992) 201.
[20] GUSEV, V.K. et al., Plasma jet source parameter optimisation and experiments on injection into Globus-M spherical tokamak, Proceedings of the 20th IAEA FEC, 20th IAEA Fusion Energy Conference 1–6 November 2004 Vilamoura, Portugal FT/P1-26 and http://www-naweb.iaea.org/napc/physics/fec/fec2004/datasets/index.html.
[21] GUSEV, V.K. et al., Plasma Heating and Fuelling in the Globus-M Spherical Tokamak, Proceedings of the 20th IAEA FEC, 20th IAEA Fusion Energy Conference 1–6 November 2004 Vilamoura, Portugal EX/P4-24 and http://www-naweb.iaea.org/napc/physics/fec/fec2004/datasets/index.html.
[22] GUSEV, V.K. et al., Overview of the Globus-M Spherical Tokamak Results, Proceedings of the 21th IAEA FEC, Chengdu, China, 16–21 October 2006.
[23] VORONIN, A.V. et al., High Kinetic Energy Jet Injection into Globus-M Spherical Tokamak, Proceedings of the 21th IAEA FEC, Chengdu, China, 16–21 October 2006 EX/P3-18.
[24] ROZHANSKY, V.A. et al., Penetration of supersonic gas jets into a tokamak, Nucl. Fusion 46 (2006) 367.
[25] BUCALOSSI, J. et al., Supersonic Molecular Beam Fuelling at ASDEX Upgrade, Proceedings of 29th EPS Conference on Contr. Fusion, Montreaux, 2002, ECA 26B, O-2.07 (2002).
[26] LANG, P.T., et al., Impact of a pulsed supersonic deuterium gas jet on the ELM behaviour in ASDEX Upgrade, Plasma Physics and Controlled Fusion 47 (2005), 1495.
[27] ROZHANSKY, V.A., et al. Mass deposition after pellet injection into a tokamak, Plasma Phys. Contr. Fusion 46 (2004) 575.
[28] HINNOV, E, HIRSCHBERG, J.G., Electron-Ion Recombination in Dense Plasmas, Phys.Rev. 125 (1962) 795.

LIST OF PARTICIPANTS

DUBROVSKI, A.	Pollution Free Sources of Ionizing Radiation Laboratory, Moscow Physical Society, Moscow, Russian Federation
GRIBKOV, V.	Department of dense magnetized plasma, Institute of Plasma Physics and Laser Microfusion, Warsaw, Poland
LUO, C.M.	The Department of Electrical Engineering and Applied Electronic Technology Tsinghua University, Beijing, China
OH, B.H.	Korean Atomic Energy Research Institute, Nuclear Fusion Lab, Daejeon, Republic of Korea
PIMENOV, V.	Effect of irradiation on metals Laboratory, A.A. Baikov Institute of Metallurgy and Material Science RAS, Moscow, Russian Federation
SCHOLZ, M.	International Center for Dense Magnetized Plasmas, Warsaw, Poland
SPRINGHAM, S.V.	National Institute of Education, Nanayang Technological University, Singapore
TARTARI, A.	Department of Physics, University of Ferrara, Ferrara, Italy
TOADER, E.I.	Department of Plasma Physics, Faculty of Physics, University of Bucharest, Bucharest-Magurele, Romania
UGASTE, Ü.	Department of Natural Sciences, Tallinn University, Tallinn, Estonia
VORONIN, A.V.	A.F. Ioffe Physico Technical Institute, St. Petersburg, Russian Federation

IAEA
International Atomic Energy Agency

Where to order IAEA publications

In the following countries IAEA publications may be purchased from the sources listed below, or from major local booksellers. Payment may be made in local currency or with UNESCO coupons.

AUSTRALIA
DA Information Services, 648 Whitehorse Road, MITCHAM 3132
Telephone: +61 3 9210 7777 • Fax: +61 3 9210 7788
Email: service@dadirect.com.au • Web site: http://www.dadirect.com.au

BELGIUM
Jean de Lannoy, avenue du Roi 202, B-1190 Brussels
Telephone: +32 2 538 43 08 • Fax: +32 2 538 08 41
Email: jean.de.lannoy@infoboard.be • Web site: http://www.jean-de-lannoy.be

CANADA
Bernan Associates, 4501 Forbes Blvd, Suite 200, Lanham, MD 20706-4346, USA
Telephone: 1-800-865-3457 • Fax: 1-800-865-3450
Email: customercare@bernan.com • Web site: http://www.bernan.com

Renouf Publishing Company Ltd., 1-5369 Canotek Rd., Ottawa, Ontario, K1J 9J3
Telephone: +613 745 2665 • Fax: +613 745 7660
Email: order.dept@renoufbooks.com • Web site: http://www.renoufbooks.com

CHINA
IAEA Publications in Chinese: China Nuclear Energy Industry Corporation, Translation Section, P.O. Box 2103, Beijing

CZECH REPUBLIC
Suweco CZ, S.R.O., Klecakova 347, 180 21 Praha 9
Telephone: +420 26603 5364 • Fax: +420 28482 1646
Email: nakup@suweco.cz • Web site: http://www.suweco.cz

FINLAND
Akateeminen Kirjakauppa, PO BOX 128 (Keskuskatu 1), FIN-00101 Helsinki
Telephone: +358 9 121 41 • Fax: +358 9 121 4450
Email: akatilaus@akateeminen.com • Web site: http://www.akateeminen.com

FRANCE
Form-Edit, 5, rue Janssen, P.O. Box 25, F-75921 Paris Cedex 19
Telephone: +33 1 42 01 49 49 • Fax: +33 1 42 01 90 90
Email: formedit@formedit.fr • Web site: http://www. formedit.fr

Lavoisier SAS, 145 rue de Provigny, 94236 Cachan Cedex
Telephone: + 33 1 47 40 67 02 • Fax +33 1 47 40 67 02
Email: romuald.verrier@lavoisier.fr • Web site: http://www.lavoisier.fr

GERMANY
UNO-Verlag, Vertriebs- und Verlags GmbH, Am Hofgarten 10, D-53113 Bonn
Telephone: + 49 228 94 90 20 • Fax: +49 228 94 90 20 or +49 228 94 90 222
Email: bestellung@uno-verlag.de • Web site: http://www.uno-verlag.de

HUNGARY
Librotrade Ltd., Book Import, P.O. Box 126, H-1656 Budapest
Telephone: +36 1 257 7777 • Fax: +36 1 257 7472 • Email: books@librotrade.hu

INDIA
Allied Publishers Group, 1st Floor, Dubash House, 15, J. N. Heredia Marg, Ballard Estate, Mumbai 400 001,
Telephone: +91 22 22617926/27 • Fax: +91 22 22617928
Email: alliedpl@vsnl.com • Web site: http://www.alliedpublishers.com

Bookwell, 2/72, Nirankari Colony, Delhi 110009
Telephone: +91 11 23268786, +91 11 23257264 • Fax: +91 11 23281315
Email: bookwell@vsnl.net

ITALY
Libreria Scientifica Dott. Lucio di Biasio “AEIOU”, Via Coronelli 6, I-20146 Milan
Telephone: +39 02 48 95 45 52 or 48 95 45 62 • Fax: +39 02 48 95 45 48
Email: info@libreriaaeiou.eu • Website: www.libreriaaeiou.eu

JAPAN
Maruzen Company Ltd, 1-9-18, Kaigan, Minato-ku, Tokyo, 105-0022
Telephone: +81 3 6367 6079 • Fax: +81 3 6367 6207
Email: journal@maruzen.co.jp • Web site: http://www.maruzen.co.jp

REPUBLIC OF KOREA
KINS Inc., Information Business Dept. Samho Bldg. 2nd Floor, 275-1 Yang Jae-dong SeoCho-G, Seoul 137-130
Telephone: +02 589 1740 • Fax: +02 589 1746 • Web site: http://www.kins.re.kr

NETHERLANDS
De Lindeboom Internationale Publicaties B.V., M.A. de Ruyterstraat 20A, NL-7482 BZ Haaksbergen
Telephone: +31 (0) 53 5740004 • Fax: +31 (0) 53 5729296
Email: books@delindeboom.com • Web site: http://www.delindeboom.com

Martinus Nijhoff International, Koraalrood 50, P.O. Box 1853, 2700 CZ Zoetermeer
Telephone: +31 793 684 400 • Fax: +31 793 615 698
Email: info@nijhoff.nl • Web site: http://www.nijhoff.nl

Swets and Zeitlinger b.v., P.O. Box 830, 2160 SZ Lisse
Telephone: +31 252 435 111 • Fax: +31 252 415 888
Email: infoho@swets.nl • Web site: http://www.swets.nl

NEW ZEALAND
DA Information Services, 648 Whitehorse Road, MITCHAM 3132, Australia
Telephone: +61 3 9210 7777 • Fax: +61 3 9210 7788
Email: service@dadirect.com.au • Web site: http://www.dadirect.com.au

SLOVENIA
Cankarjeva Zalozba d.d., Kopitarjeva 2, SI-1512 Ljubljana
Telephone: +386 1 432 31 44 • Fax: +386 1 230 14 35
Email: import.books@cankarjeva-z.si • Web site: http://www.cankarjeva-z.si/uvoz

SPAIN
Díaz de Santos, S.A., c/ Juan Bravo, 3A, E-28006 Madrid
Telephone: +34 91 781 94 80 • Fax: +34 91 575 55 63
Email: compras@diazdesantos.es, carmela@diazdesantos.es, barcelona@diazdesantos.es, julio@diazdesantos.es
Web site: http://www.diazdesantos.es

UNITED KINGDOM
The Stationery Office Ltd, International Sales Agency, PO Box 29, Norwich, NR3 1 GN
Telephone (orders): +44 870 600 5552 • (enquiries): +44 207 873 8372 • Fax: +44 207 873 8203
Email (orders): book.orders@tso.co.uk • (enquiries): book.enquiries@tso.co.uk • Web site: http://www.tso.co.uk

On-line orders
DELTA Int. Book Wholesalers Ltd., 39 Alexandra Road, Addlestone, Surrey, KT15 2PQ
Email: info@profbooks.com • Web site: http://www.profbooks.com

Books on the Environment
Earthprint Ltd., P.O. Box 119, Stevenage SG1 4TP
Telephone: +44 1438748111 • Fax: +44 1438748844
Email: orders@earthprint.com • Web site: http://www.earthprint.com

UNITED NATIONS
Dept. I004, Room DC2-0853, First Avenue at 46th Street, New York, N.Y. 10017, USA
(UN) Telephone: +800 253-9646 or +212 963-8302 • Fax: +212 963-3489
Email: publications@un.org • Web site: http://www.un.org

UNITED STATES OF AMERICA
Bernan Associates, 4501 Forbes Blvd., Suite 200, Lanham, MD 20706-4346
Telephone: 1-800-865-3457 • Fax: 1-800-865-3450
Email: customercare@bernan.com · Web site: http://www.bernan.com

Renouf Publishing Company Ltd., 812 Proctor Ave., Ogdensburg, NY, 13669
Telephone: +888 551 7470 (toll-free) • Fax: +888 568 8546 (toll-free)
Email: order.dept@renoufbooks.com • Web site: http://www.renoufbooks.com

Orders and requests for information may also be addressed directly to:

Marketing and Sales Unit, International Atomic Energy Agency
Vienna International Centre, PO Box 100, 1400 Vienna, Austria
Telephone: +43 1 2600 22529 (or 22530) • Fax: +43 1 2600 29302
Email: sales.publications@iaea.org • Web site: http://www.iaea.org/books

13-11411

INTERNATIONAL ATOMIC ENERGY AGENCY
VIENNA
ISBN 978–92–0–139110–0
ISSN 1011–4289